



National Library  
of Canada

Bibliothèque nationale  
du Canada

Canadian Theses Service

Services des thèses canadiennes

Ottawa, Canada  
K1A 0N4

## CANADIAN THESES

## THÈSES CANADIENNES

### NOTICE

The quality of this microfiche is heavily dependent upon the quality of the original thesis submitted for microfilming. Every effort has been made to ensure the highest quality of reproduction possible.

If pages are missing, contact the university which granted the degree.

Some pages may have indistinct print especially if the original pages were typed with a poor typewriter ribbon or if the university sent us an inferior photocopy.

Previously copyrighted materials (journal articles, published tests, etc.) are not filmed.

Reproduction in full or in part of this film is governed by the Canadian Copyright Act, R.S.C. 1970, c. C-30.

**THIS DISSERTATION  
HAS BEEN MICROFILMED  
EXACTLY AS RECEIVED**

### AVIS

La qualité de cette microfiche dépend grandement de la qualité de la thèse soumise au microfilmage. Nous avons tout fait pour assurer une qualité supérieure de reproduction.

S'il manque des pages, veuillez communiquer avec l'université qui a conféré le grade.

La qualité d'impression de certaines pages peut laisser à désirer, surtout si les pages originales ont été dactylographiées à l'aide d'un ruban usé ou si l'université nous a fait parvenir une photocopie de qualité inférieure.

Les documents qui font déjà l'objet d'un droit d'auteur (articles de revue, examens publiés, etc.) ne sont pas microfilmés.

La reproduction, même partielle, de ce microfilm est soumise à la Loi canadienne sur le droit d'auteur, SRC 1970, c. C-30.

**LA THÈSE A ÉTÉ  
MICROFILMÉE TELLE QUE  
NOUS L'AVONS REÇUE**

Search For Charge Symmetry Breaking in  
Neutron-Proton Elastic Scattering at 477 MeV

by

Richard R. Tkachuk

A Thesis Submitted in Partial Fulfillment of  
the Requirements for the Degree of  
Doctor of Philosophy

In  
Nuclear Physics  
Department of Physics

Edmonton, Alberta  
Spring, 1987

Permission has been granted to the National Library of Canada to microfilm this thesis and to lend or sell copies of the film.

The author (copyright owner) has reserved other publication rights, and neither the thesis nor extensive extracts from it may be printed or otherwise reproduced without his/her written permission.

L'autorisation a été accordée à la Bibliothèque nationale du Canada de microfilmer cette thèse et de prêter ou de vendre des exemplaires du film.

L'auteur (titulaire du droit d'auteur) se réserve les autres droits de publication; ni la thèse ni de longs extraits de celle-ci ne doivent être imprimés ou autrement reproduits sans son autorisation écrite.

ISBN 0-315-37670-8

The University of Alberta

Release Form

NAME OF AUTHOR : Richard R. Tkachuk

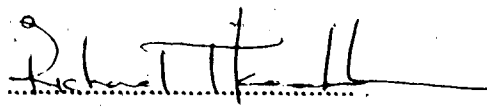
TITLE OF THESIS : Charge Symmetry Breaking in Neutron Proton  
Elastic Scattering at 477 MeV

DEGREE : Doctor of Philosophy

YEAR THIS DEGREE IS GRANTED : 1987

Permission is hereby granted to THE UNIVERSITY OF ALBERTA LIBRARY to reproduce single copies of this thesis and to lend or sell such copies for private, scholarly or scientific research purposes only.

The author reserves other publication rights, and neither the thesis nor extensive extracts from it may be printed or otherwise reproduced without the author's written permission.



(Student's Signature)

1508 - 11111 87th Avenue

Edmonton, Alberta

T6G 0X9

(Student's permanent address)

Date : March 11, 1987



THE UNIVERSITY OF ALBERTA

FACULTY OF GRADUATE STUDIES AND RESEARCH

The undersigned certify that they have read, and recommend to the Faculty of Graduate Studies and Research for acceptance, a thesis entitled Charge Symmetry Breaking in Neutron - Proton Elastic Scattering at 477 MeV submitted by Richard R. Tkachuk in partial fulfillment of the requirements for the degree of Doctor of Philosophy.

Gerald Roy  
Alan Smith  
H. J. K.

H. S. S. J.  
L. J. S. S. J.

F. Weizman  
R. M. J.

The University of Alberta

January, 1987

## Abstract

The effect of isospin violating, charge symmetry breaking (CSB) terms in the neutron - proton interaction has been observed by measuring the difference in the zero-crossing angles of the neutron and proton analyzing powers,  $A_n$  and  $A_p$ , at a neutron energy of 477 MeV at TRIUMF in Vancouver, B.C. The neutron (proton) analyzing power  $A_n$  ( $A_p$ ) was measured with a polarized (unpolarized) neutron beam incident on an unpolarized (polarized) proton target. Neutrons and protons were detected in coincidence over a  $10^\circ$  angular range. The interleaved measurements were made using the same apparatus to reduce systematic errors. Although designed as a null measurement where knowledge of absolute beam and target parameters were not fundamental to the final result, experimental parameters were determined as precisely as possible to reduce systematic errors associated with the experimental apparatus. All systematic errors not correlated with beam or target polarization reversals were removed to at least second order at the zero-crossing angle of the asymmetry. The target was of the 'frozen spin type' and contained  $55 \text{ cm}^3$  of butanol in a 2.6 kG magnetic field at 60 mK. Typical target polarizations of 0.75-0.85 with decay times of approximately 30 hours were attained throughout the duration of the experiment. Background originated mainly from the  $^{12}\text{C}(n, np)$  reaction and comprised approximately 1% of the total number of neutron - proton elastic events. From the difference in angles at which the two analyzing powers cross through zero the magnitude of  $\Delta A$  ( $= A_n - A_p$ ) has been determined as  $\Delta A = 0.0045 \pm 0.0018$  ( $\pm 0.0007$ ), where the second error represents systematic effects. This value is reasonably close to the latest theoretical calculations<sup>(1)</sup> which include CSB effects due to the n-p mass difference in  $\pi$ ,  $\rho$ , and  $2\pi$  exchange; electromagnetic coupling of the neutron anomalous magnetic moment to the proton current;  $\rho$ - $\omega$  meson mixing; and short and medium range effects of the up and down quark mass difference. This experiment represents the first unambiguous measurement of the class IV forces present in the nucleon-nucleon interaction.

## Acknowledgements

There are many to thank for the completion of this work. I would like to thank all the many members of the experimental group at the University of Alberta, TRIUMF and the University of Manitoba whose tireless efforts resulted in the success of a very difficult experiment. Also, the technical support staff at TRIUMF demonstrated very skilled ability in the operation of the TRIUMF cyclotron. In particular, I thank Dr. G. Roy, my thesis advisor, for his constant advice and encouragement throughout my work. Special plaudits go to Dr. L.G. Greeniaus whose task it was to introduce me to the experimental analysis and patiently listen to my constant questions. My enthusiastic appreciation goes to Dr. W.T.H. van Oers whose organizational and leadership skills were mainly responsible for directing the efforts and getting that extra 10% out of a large, diverse experimental group. My thanks are also extended to Dr. R. Abegg for the period during which I stayed at TRIUMF.

During my stay at the University of Alberta I enjoyed discussing the experiment with several of the other graduate students. Thanks go to R. Mitchell, K. Starko, G. Lotz, J. Johanssen and G. Edwards for advice, criticism and for demonstrating the finer points of some experimental techniques. Outside of the lab, I received unswerving support and encouragement from Jo-Anne Cameron. And finally, I must thank my parents for providing their support and direction.

## Table of Contents

Chapter 1	Introduction	1
Chapter 2	Theoretical Considerations	5
2.1	Charge Symmetry Breaking in Nucleon - Nucleon Elastic Scattering	5
2.2	Related Measurements in Charge Symmetry Breaking	9
2.3	Theoretical Considerations of Charge Symmetry Breaking in the Neutron - Proton Elastic Scattering System	12
Chapter 3	Experimental Apparatus	17
3.1	Introduction	17
3.2	Primary Beam Positioning	20
3.3	Primary Beam Energy and Polarization	21
3.4	Neutron Beam Production	27
3.5	Neutron Beam Collimation	27
3.6	Neutron Beam Polarization	36
3.7	Neutron Beam Profile Monitor and Polarimeter	30
3.8	Frozen Spin Type (FST) Target	33
3.8.1	Introduction and Operation	33
3.8.2	Target Magnetic Holding Field	36
3.8.3	Target Support Structure	39
3.9	Proton Detection Apparatus	39
3.9.1	Proton Boom	39
3.9.2	Delay Line Chambers	44
3.10	Neutron Detection and Calibration Apparatus	48
3.10.1	Neutron Detection Telescope	48
3.10.2	Neutron Scintillator Array	48
3.10.3	Neutron Position Determination	51

3.10.4	Neutron Time-of-Flight and Position Calibration	51
3.10.5	Neutron Scintillator Array Illumination	52
3.11	Trigger Logic	54
3.12	Phase Lock System	55
3.13	Data Collection	65
Chapter 4	Analysis	56
4.1	Introduction	56
4.2	Proton Beam Energy	56
4.3	Proton Beam Polarization	59
4.4	Proton Beam Intensity	62
4.5	Proton Beam Spatial Stability	62
4.6	Neutron Beam Polarization	64
4.7	Neutron Beam Intensity Profile	66
4.8	Target Position	70
4.9	Target Polarization	71
4.10	Proton Detection	72
4.10.1	Proton Time-of-Flight	72
4.10.2	Proton Track Reconstruction	73
4.10.3	FST Target Holding Field	80
4.10.4	Effect of Wedge-Shaped Absorber	82
4.11	Neutron Detection	83
4.11.1	Neutron Detection Array Calibration Technique	83
4.11.2	Neutron Position Determination	86
4.11.3	Neutron Bar Gain Stabilization	89
4.11.4	Effect of Neutron Polarization on Position Determination	91

4.11.5	Neutron Time-of-Flight	92
4.11.6	Neutron Detection Efficiency	92
4.12	Kinematic Observables and Data Constraints	93
4.12.1	Kinematic Observables	93
4.12.2	$\chi^2$ Calculations	96
4.12.3	Data Constraints	98
4.13	Elastic Neutron-Proton Asymmetry Calculation	103
4.13.1	Introduction	103
4.13.2	Asymmetry Slopes	107
4.13.3	Asymmetry Zero-Crossing Angles	108
4.13.4	Relationship of Asymmetry Slopes with Beam and Target Polarizations	111
4.13.5	$\chi^2$ Dependence of Asymmetry Calculation	112
4.13.6	Dependence of Asymmetry on Neutron Bar PHT Discrimination Threshold	113
4.13.7	Asymmetry Calculation Utilizing Outer Neutron Bars	113
4.13.8	Comparison of $A_n$ and $A_p$ Slopes with Observed Beam and Target Polarizations	114
4.14	Background Reduction	117
4.14.1	Background Sources and Effects	117
4.14.2	Background Fraction of Butanol Target Data	118
4.14.3	Background Asymmetry	128
Chapter 5	Conclusion	133
References		141
Appendices		
Appendix A	Systematic Errors	144
A.1	Introduction	144

A.2	Deviation of Proton Beam Spot on LD <sub>2</sub> Target	146
A.3	Angular Modulation of Proton Beam on LD <sub>2</sub> Target Multiple Scattering	148
A.4	Inequality of Up and Down Beam and Target Polarizations	148
A.5	Misalignment of Apparatus	149
A.6	Inequality of Up and Down Polarization and Misalignment of Apparatus	150
A.7	Target Holding Field Stability	151
A.8	Multiple Scattering	151
A.9	Incorrect Precession of Spin	153
A.10	Residual Neutron Polarization on Polarized Target	153
A.11	Neutron Beam Energy Stability	155
A.12	Relative Position of Target and Holding Field with Respect to Target Symmetry Axis	155
A.13	Neutron Detection Stability	157
A.14	Background	158
Appendix B	Experimental Overview	160
Appendix C	Experimental Proposal to Search for Charge Symmetry Breaking in the Neutron - Proton Elastic Scattering System at 350 MeV	164

## List of Tables

Table	Description	Page
1.1.1	Summary of Experimental Parameters	3
2.1.1	The separation of $2s+1L_J$ States in the Neutron - Proton System according to Isospin Conservation	6
2.1.2	Classification of Nuclear Potentials According to Isospin Behaviour	7
2.2.1	Low Energy $^1S_0$ Nucleon - Nucleon Elastic Scattering Parameters	9
3.3.1	Proton Beam Energy Monitor / Polarimeter Details	25
3.3.2	Proton Polarimeter Target Characteristics	26
3.8.1	Target Holding Field Line Integral	36
3.8.2	Target Materials in Neutron Beam Path	40
3.9.1	Positions of Proton Detection Apparatus Along Boom	44
3.9.2	Delay Line Chamber Construction Materials	45
3.10.1	Neutron Detection Apparatus	48
4.2.1	Average Primary Proton Beam Energies	57
4.3.1	Proton Polarimeter Instrumental Asymmetry	60
4.3.2	Polarimeter Target Carbon Correction Factors	61
4.3.3	Proton Beam Polarizations	61
4.4.1	Average Proton Beam Intensities	62
4.6.1	Vertical Neutron Polarizations	66
4.6.2	Horizontal Neutron Polarizations	66
4.7.1	Neutron Beam Intensity Profile Summary	67
4.8.1	Target Position Offsets	70
4.8.2	Target Volume and Fill Levels	71
4.9.1	Average Target Polarizations	71



Table	Description —	Page
4.10.1	Effect of Wedge-Shaped Absorber on Recoil Proton Angles	82
4.11.1	Neutron Detection Efficiency	92
4.13.1	Observed $A_n$ Slopes - Target Holding Field Up	107
4.13.2	Observed $A_n$ Slopes - Target Holding Field Down	107
4.13.3	Observed $A_p$ Slopes - Target Holding Field Up	107
4.13.4	Observed $A_p$ Slopes - Target Holding Field Down	108
4.13.5	Observed $A_n$ Zero-Crossing Angle - Target Holding Field Up	109
4.13.6	Observed $A_n$ Zero-Crossing Angle - Target Holding Field Down	109
4.13.7	Observed $A_p$ Zero-Crossing Angle - Target Holding Field Up	109
4.13.8	Observed $A_p$ Zero-Crossing Angle - Target Holding Field Down	110
4.13.9	Observed $\theta_{op}(A_n) - \theta_{op}(A_p)$ -- Target Holding Field Up	110
4.13.10	Observed $\theta_{op}(A_n) - \theta_{op}(A_p)$ -- Target Holding Field Down	110
4.13.11	Observed $\theta_{op}(A_n) - \theta_{op}(A_p)$ -- Averaged Over Target Holding Field	111
4.13.12	Neutron and Proton Angle Based Asymmetry Zero Crossing Angles	112
4.13.13	Asymmetry Zero-Crossing Angle as a Function of $\chi^2$ Constraints	112
4.13.14	Asymmetry Zero-Crossing Angles as a Function of Neutron Bar Pulse Height Discrimination	113
4.13.15	Asymmetry Zero-Crossing Angle With and Without Outer Neutron Bars	114
4.13.16	Asymmetry Slopes and Polarization Measurements	115

Table	Description	Page
4.14.1	Inelastic Event Fraction Form Graphite Target (Inner Bars, $\chi_i^2 < 5$ )	123
4.14.2	Graphite Target Inelastic Events Fraction as a Function of $\chi^2$ Cut (Inner Neutron Bars)	124
4.14.3	Carbon Mass in Butanol and Graphite Targets	124
4.14.4	Sources of Background in Target	125
4.14.5	Integrated Counts on SEM 4AM5 During $A_n$ Measurement	126
4.14.6	The Background Fraction (Inner Bars, $\chi_i^2 < 5$ )	127
4.14.7	Butanol Target Inelastic Event Fraction as a Function of $\chi^2$ Cut	128
4.14.8	Background Asymmetry as a Function of $\chi^2$ Constraint (Inner Bars, $\theta_n$ )	129
4.14.9	Background Asymmetry as a Function of $\chi^2$ Constraint (Inner Bars, $\theta_n$ )	129
5.1.1	Summary of Experimental $\theta_{op}(A_n) - \theta_{op}(A_p)$ Systematic Errors	134
5.1.2	Summary of Experimental $\theta_{on}(A_n) - \theta_{on}(A_p)$ Systematic Errors	134
5.1.3	Calculations of $\Delta A \times 10^{-4}$ at the Asymmetry Zero-Crossing Angle as a Function of Lab Energy by Miller, Thomas and Williams	138

## List of Figures

Figure	Description	Page
1.1.1	Method Used to Determine Difference Between $A_n$ Zero-Crossing Angle and $A_p$ Zero-Crossing Angle Based on Center of Mass Neutron Scattering Angle	1
2.1.1	Illustration of Charge Symmetry Constraints on Neutron - Proton Elastic Scattering	6
2.3.1	$\gamma$ NN Feynman Vertex	12
2.3.2	Contribution of Class (IV) Charge Symmetry Breaking by the Neutron - Proton Mass Difference in One-Pion Exchange	14
2.3.3	Isospin non-conserving $\rho - \omega$ Exchange in Neutron - Proton Elastic Scattering	15
3.1.1	Proton Beam Transport System	18
3.1.2	Coordinate System Definition	19
3.2.1	Secondary Emission Monitor Schematic	20
3.3.1	Beam Energy Monitor / Polarimeter Schematic	22
3.3.2	Beam Energy Monitor Range Counter Assembly	23
3.3.3	Rotation of Polarimeter Solid Angle Defining Counter to Reduce Changes in Solid Angle Associated with Movement of Primary Proton Beam	24
3.3.4	Schematic Diagram of Proton Polarimeter Electronics	25
3.6.1	Illustration of Neutron-Proton Polarization Transfer Process	29
3.6.2	Dipole Magnet 'CLYDE' Magnet Precession Curve	31
3.7.1	Neutron Profile Monitor / Polarimeter Schematic Diagram	32
3.8.1	Frozen Spin Type Target Diagram	34
3.8.2	Target Polarization Process	33
3.8.3	Target Magnetic Holding Field Line Integral	37

Figure	Description	Page
3.8.4	Contribution of Spin Precession Dipole Bonnie to Horizontal Component of Target Holding Field	38
3.8.5	Horizontal Components of Target Holding Field	39
3.9.1	Experimental Detection Equipment	42
3.9.2	Proton Boom Electronics	43
3.9.3	Delay Line Chamber Electronics	45
3.9.4	Delay Line Chamber 'Picket Fence' Spectra	46
3.9.5	Delay Line Chamber Delay Line Nonlinearity	47
3.10.1	Neutron Boom Electronics	49
3.10.2	Neutron Scintillator Array	50
3.10.3	Neutron Scintillator Array Illumination	53
3.11.1	Experimental Trigger Logic	54
4.2.1	Proton Beam Energy Distribution over First Data Taking Run	58
4.5.1	Secondary Emission Monitor Asymmetry Distribution	63
4.5.2	Method Used to Estimate Maximum Deflection of the Proton Beam Position on the LD <sub>2</sub> Target	64
4.7.1	Neutron Beam Profile Distributions	68
4.7.2	Neutron Beam Illumination of Target	69
4.10.1	Artificial Division of E-Counter During Analysis	72
4.10.2	Proton Track Reconstruction	75
4.10.3	Deviation between Reconstructed and Observed DLC coordinate for Front DLCs	76
4.10.4	Deviation between Reconstructed and Observed DLC coordinate for Back DLCs	77
4.10.5	Projection of Reconstructed Neutron - Proton Vertex Onto X = 0 Plane	78

Figure	Description	Page
4.10.6	Example of Neutron-Proton Vertex Reconstruction	79
4.10.7	Proton Angular Deflections Due to Target Holding Field	81
4.11.1	Neutron Array Calibration Proton TOF Spectrum	84
4.11.2	Neutron Array Calibration Proton Pulse Height Distribution	85
4.11.3	Neutron Array Calibration Proton Position Spectrum	87
4.11.4	Neutron Array TDIF Distribution	88
4.11.5	Scaled Neutron Event Pulse Height Distribution	90
4.12.1	Plot of the Neutron - Proton Energy Sum	94
4.12.2	Plot of the Total Transverse Momentum Sum	94
4.12.3	Plot of the Neutron - Proton Scattering Angle Sum	95
4.12.4	Plot of the Neutron - Proton Azimuthal Scattering Angle Sum	95
4.12.5	Neutron - Proton Polar Angle Sum $\chi^2$ as a function of Recoil Proton Angle	97
4.12.6	Sample Kinematic $\chi^2$ Distributions	99
4.12.7	Angular Distribution of Recoil Protons Coincident with Neutrons in Inner and Outer Neutron Bars	101
4.12.8	Neutron Bar Phototube ADC Distribution	102
4.13.1	Influence of Target Holding Field on Recoil Proton Angle	104
4.13.2	Typical Asymmetry Curve	106
4.14.1	Background Run Neutron-Proton Vertex Reconstruction	120
4.14.2	Top Half of Graphite Target Event $\chi^2$ Distribution	121
4.14.3	Bottom Half of Graphite Target Event $\chi^2$ Distribution	121
4.14.4	Elastic Event $\chi^2$ distribution.	121

Figure	Description	Page
4.14.5	Butanol Target Event Coplanarity	122
4.14.6	Butanol Target Event with Veto Signal Coplanarity	122
4.14.7	Graphite Target Event Coplanarity	122
4.14.8	Typical Background Asymmetry Curve	130
5.1.1	Comparison of Theory to Experiment	139
A.2.1	Deviation of Proton Beam on LD <sub>2</sub> Target	150
A.3.1	Modulation of Proton Beam on LD <sub>2</sub> Target	152
A.5.1	Misalignment of Apparatus	153

## Chapter 1 Introduction

A symmetry of any kind, either a nuclear force symmetry or that of a snowflake, provides evidence of deeper, more fundamental forces at work than those immediately visible. In the case of the snowflake, the hexagonal rotational symmetry provides a rich field of study of the behaviour of ice crystals, as well as an understanding of the meteorological conditions during which the snowflake was formed. In the case of charge symmetry, physicists may focus on weaker components of the nuclear force, such as  $\rho - \omega$  meson exchange, which are normally dwarfed by other larger components.

An extremely sensitive test of charge symmetry has been completed at the TRIUMF laboratory. The experiment was the first to look for evidence of isospin-nonconserving, class (IV) (of reference 2) charge symmetry breaking in the elastic neutron-proton scattering system. The difference in analyzing powers  $A_n - A_p$ , where the subscript denotes the polarized particle, was determined at the angle where the average analyzing power,  $\frac{1}{2}(A_n + A_p)$ , equals zero. The experiment is best described with the diagram illustrated in figure (1.1.1).

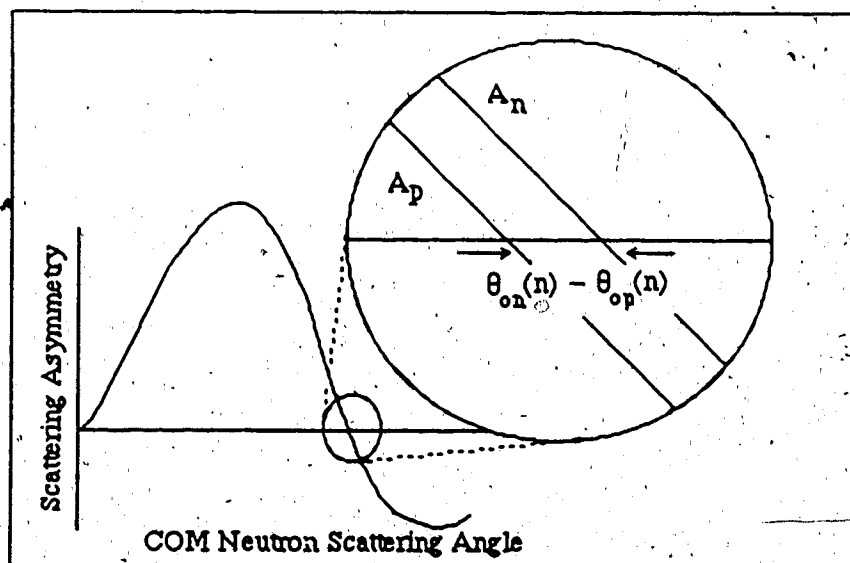


Figure (1.1.1) Method Used to Determine Difference Between  $A_n$  Zero-Crossing Angle and  $A_p$  Zero-Crossing Angle Based on the Center of Mass (COM) Neutron Scattering Angle.

A non-zero difference in zero-crossing angles of  $A_n$  and  $A_p$  signifies the presence of charge

symmetry breaking in the neutron-proton interaction. Any systematic errors inherent in measuring individual zero-crossing angles canceled when the difference was calculated. The measurement was of the 'null' variety. Consider the relations

$$\epsilon_p = P_p A_p = P_p ( \langle A \rangle - 1/2 \Delta A ) \quad (1.1.1)$$

$$\epsilon_n = P_n A_n = P_n ( \langle A \rangle + 1/2 \Delta A ), \quad (1.1.2)$$

where  $\langle A \rangle = 1/2 ( A_n + A_p )$ , and  $\Delta A = A_n - A_p$ . The observed difference in  $\epsilon_n$  and  $\epsilon_p$  is then

$$\Delta \epsilon = \epsilon_n - \epsilon_p = (P_n - P_p) \langle A \rangle - 1/2 \Delta A ( P_n + P_p ). \quad (1.1.3)$$

The first term is proportional to the difference in target and beam polarizations. If  $\Delta A$  is to be determined to  $\pm 10^{-4}$ , the differences in polarizations must be determined to the same accuracy. This presents extremely difficult experimental problems. But, if  $\Delta \epsilon$  is measured where  $\langle A \rangle = 0$ , at the neutron-proton asymmetry zero-crossing angle, the first term vanishes, leaving only the second. Then  $\Delta \epsilon$  is proportional to the average polarizations multiplied by  $\Delta A$ . A non-zero result is concrete evidence of the presence of charge symmetry breaking (CSB). The experimental parameters needed only to be kept constant throughout the measurements of  $A_n$  and  $A_p$ ; knowledge of absolute experimental parameters, such as target polarizations and beam energies, were not fundamental to the success of the experiment. However, care was taken to determine proton and neutron beam parameters as accurately as possible to understand all possible sources of systematic error. Unprecedented accuracy was achieved with experimental apparatus designed to reduce all systematic errors not correlated with target or beam polarization reversal to at most second order. In particular, a 'frozen spin type' polarizable target enabled the determination of  $A_n$  and  $A_p$  with the identical equipment.

The most pertinent experimental parameters are summarized below in table (1.1.1).



Table (1.1.1) Summary of Experimental Parameters

Neutron Beam Energy	477 MeV, 11 MeV FWHM
Average Neutron Beam Polarization	0.47
Target Volume	55 cm <sup>3</sup>
Average Target Polarization	0.78
Scattered Neutron Angular Detection Range	$27^\circ \leq \theta_n \leq 37^\circ$
Scattered Proton Angular Detection Range	$47^\circ \leq \theta_p \leq 57^\circ$

Other experiments relating to CSB are summarized in chapter two. One discovers, upon an examination of the literature, that conclusive proof of charge symmetry breaking has proved extremely elusive regardless of the forum of study. The experiment described here is the first to consider only class (IV) type interactions (see section 2.1) in the n-p system. There is no reason why class (IV) interactions do not contribute to binding energy differences between mirror nuclei. However, class (IV) forces vanish for s-wave interactions (such forces are typically of the form  $[\sigma(1) - \sigma(2)] \cdot L$ ) and therefore do not contribute to the binding energy difference between  $^3\text{H}$  and  $^3\text{He}$ . Binding energy differences between nuclei with  $A > 3$  are more difficult to explain in charge symmetry breaking terms; uncertainties in nuclear models tend to cloud the issue. Charge symmetry breaking tests in the neutron - proton system are advantageous in that the largest electromagnetic interaction is a coupling between the neutron magnetic moment and proton current; this interaction is smaller than the direct coulomb - coulomb interaction by approximately a factor of  $q/m$  (where  $q$  is the momentum transfer and  $m$  is the nucleon mass).

Several contributions to CSB in the neutron-proton system are briefly summarized and references to more detailed descriptions are provided in chapter three. Recent calculations indicate that the effect of the neutron-proton mass difference in one-pion-exchange dominates other effects but this is by no means the end of the story; several calculations of  $\Delta A$  have been made but as of writing no consensus has been achieved.

The high experimental accuracy required a high precision in the operation of all aspects of the proton beam, neutron beam, proton target, and detection apparatus. The desired experimental accuracy required that all possible systematic errors be reduced so that their effect on  $\Delta A$  did not exceed  $\approx 10^{-4}$  at the zero-crossing angle. In chapter three, the methods used to complete the experiment over several extended time periods maintaining uniform and precise experimental standards are discussed in detail. Design and performance of all experimental apparatus relevant to the experiment is described.

In chapter four the analysis of the experimental results is described. The

determination of the asymmetry zero-crossing angles was straightforward. The examination of the data for internal consistency and absence of error was not straightforward. The data was recorded on approximately 300 magnetic tapes. Each tape was spooled at least four times at just over one hour each time. The extraction of the data from the numerous data tapes is discussed along with the methods used to ensure its validity.

The experiment measured the difference between the zero-crossing angles of  $A_n$  and  $A_p$  as  $-0.175^\circ \pm 0.075^\circ$  ( $\pm 0.026^\circ$ ) based on the lab proton scattering angle, where the error in brackets is an estimate of the systematic error. Since the difference in asymmetries is the more pertinent number to theoreticians, it is presented in the conclusion. However, it must be stressed that the experiment measured the difference in zero-crossing angles and not asymmetries. The value of  $A_n - A_p$  was calculated by simply multiplying the result by the asymmetry slope as determined from the various phase shift fits to elastic neutron-proton scattering.

## Chapter 2 Theoretical Considerations

### 2.1 Charge Symmetry Breaking in Nucleon-Nucleon Elastic Scattering

Charge symmetry and charge independence were proposed as the first internal nuclear symmetries shortly after the discovery of the neutron. Neutrons and protons were viewed as two states of a single particle defined by the direction of a vector in isospin space. Charge independence implies the complete equivalence of hadronic forces with respect to arbitrary rotations of the isospin vector,  $T$ , in isospin space. In a manner entirely analogous to angular momentum algebra this relationship can be expressed as

$$[T, H_{\text{hadr}}] = 0 \quad (2.1.1)$$

where  $H_{\text{hadr}}$  represents the hadronic part of the nuclear Hamiltonian. In other words, the n-n, n-p and p-p hadronic or strong forces are indistinguishable in otherwise identical nuclear states. Charge symmetry is a similar but weaker symmetry than charge independence. Charge symmetry implies the equivalence of the hadronic force only with respect to  $180^\circ$  rotations in isospin space about the  $T_2$  axis. The charge symmetry operator,  $P_{\text{CS}}$ , is defined as

$$P_{\text{CS}} = \prod_{i=1}^N e^{i\pi T_{2i}} \quad (2.1.2)$$

for a system of  $N$  nucleons. Charge symmetry can apply even if charge independence fails, but the opposite is not true. If charge symmetry is valid, the charge symmetry operator commutes with the hadronic part of the Hamiltonian,

$$[P_{\text{CS}}, H_{\text{H}}] = 0 \quad (2.1.3)$$

The equivalence of the nuclear force with respect to the exchange of protons and neutrons is a consequence of CS, but does not alone define CS. CS also influences n-p states.

Analogous to a  $180^\circ$  angular rotation, the charge symmetry operation introduces an isospin related phase factor when operated upon a state,

$$P_{\text{CS}} |\alpha, T, T_3\rangle = (-1)^{T-T_3} |\alpha, T, -T_3\rangle \quad (2.1.4)$$

where  $\alpha$  represents all other nuclear quantum numbers. If the hadronic force is independent of charge symmetry breaking interactions, the hadronic neutron - proton Hamiltonian can not mix states of differing isospin. Otherwise the eigenvalue of the charge symmetry operator,  $P_{CS}$ , would flip sign. Therefore, both charge symmetry and charge independence prohibit transitions between  $n - p$  isosinglet and isotriplet states. If parity conservation is invoked, thereby prohibiting  $\Delta L=1$  transitions, transitions between spin triplet and singlet states are forbidden. A spin singlet-triplet transition observed in neutron - proton elastic scattering is a necessary and sufficient condition to demonstrate the presence of charge symmetry breaking. This is clearly illustrated in table (2.1.1).

**Table (2.1.1) The Separation of  $^{2S+1}L_J$  States in the Neutron - Proton System According to Isospin Conservation**

$T = 0$	$^1S_0, ^3P_{0,1,2}, ^1D_2, \dots$
$T = 1$	$^3S_1, ^1P_1, ^3D_{1,2,3}, \dots$

The ramifications of charge symmetry on the neutron-proton system is clearly evident in figure (2.1.1).

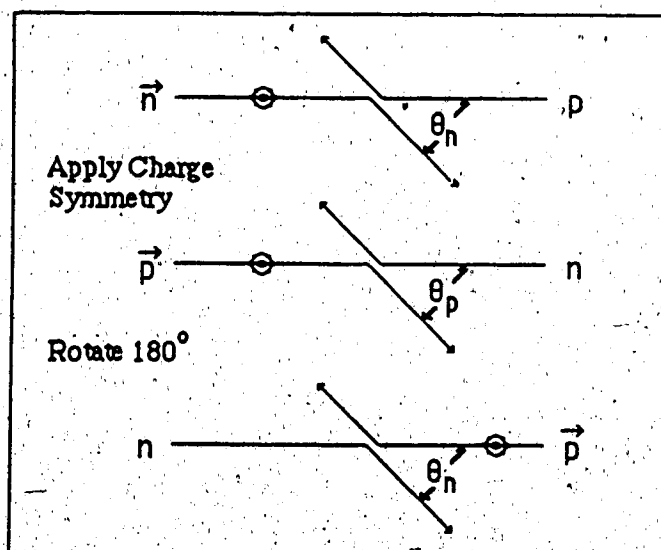


**Figure 2.1.1 Illustration of Charge Symmetry Constraints on Neutron - Proton Elastic Scattering**

If charge symmetry is valid, the differential cross section of polarized neutrons scattered from unpolarized protons is identical to unpolarized neutrons scattered from polarized protons; therefore,  $A_n = A_p$ .

Terms in the nucleon - nucleon potential have been classified according to their isospin behaviour in a review by E.M. Henley and G.A. Miller<sup>(2)</sup>.

**Table (2.1.2) Classification of Nuclear Potentials According to Isospin Behaviour**

Class	Example	Behaviour
(I)	$A + B \tau(1) \cdot \tau(2)$	Charge Symmetric Charge Independent
(II)	$C \tau_3(1) \tau_3(2)$	Charge Symmetric Charge Dependent
(III)	$D [\tau_3(1) + \tau_3(2)]$	Charge Asymmetric Charge Dependent
(IV)	$E [\tau(1) \times \tau(2)]_3 [\sigma(1) - \sigma(2)] \cdot L$ or $F [\tau_3(1) - \tau_3(2)] [\sigma(1) \times \sigma(2)] \cdot L$	Charge Asymmetric Charge Dependent Mixes states of differing Isospin

Class (I) forces are of the conventional type and obey both charge independence and charge symmetry. Class (III) potentials are charge symmetry breaking (CSB) but only affect n-n and p-p states and do not mix different isospin states. Class (IV) forces mix states of different isospin. Since  $\Delta J$  must equal zero, an isospin transition can arise only between the states  $^1P_1 - ^3P_1$ ,  $^1D_2 - ^3D_2$ , ...,  $^3L_J - ^1L_J$ . Class (IV) forces do not influence the S-state whatsoever. Note that CSB in n - p elastic scattering is due solely to class (IV) forces.

If we allow class (IV) CSB in the neutron - proton system an additional amplitude 'f' must be introduced to the conventional scattering matrix. The CSB M-matrix<sup>(3)</sup> now looks like

$$M_{fi} = (a+b) + (a-b)[\sigma(1) \cdot \sigma(2)] + (c+d) [\sigma(1) \cdot \mathbf{m}] [\sigma(2) \cdot \mathbf{m}] + (c-d) [\sigma(1) \cdot \mathbf{l}] [\sigma(2) \cdot \mathbf{l}] \\ + e [\sigma(1) + \sigma(2)] \cdot \mathbf{n} + f [\sigma(1) - \sigma(2)] \cdot \mathbf{n} \quad (2.1.5)$$

The unit vectors have the conventional form

$$l = \frac{\mathbf{k}_1 + \mathbf{k}_2}{|\mathbf{k}_1 + \mathbf{k}_2|} \quad m = \frac{\mathbf{k}_1 - \mathbf{k}_2}{|\mathbf{k}_1 - \mathbf{k}_2|} \quad n = \frac{\mathbf{k}_1 \times \mathbf{k}_2}{|\mathbf{k}_1 \times \mathbf{k}_2|} \quad (2.1.6)$$

Here,  $\mathbf{k}_1$  is the direction of the incident particle and  $\mathbf{k}_2$  is the direction of the scattered particle.

For future use the notation  $A_{ijkl}$  shall be adopted for spin related observables. The subscripts  $i$  and  $j$  denote polarization of the scattered and recoil particles respectively, and the subscripts  $k$  and  $l$  denote the polarization of the incident projectile and target particle. A '0' subscript denotes an unpolarized or unobserved polarization. In the density matrix formalism the expectation value,  $\langle A \rangle$ , of an operator  $A$  is defined as

$$\langle A \rangle = \text{Tr} (M^\dagger \rho_i M A), \quad (2.1.7)$$

where  $\rho_i$  is the initial neutron - proton density matrix. If the new scattering matrix,  $M_n$ , is inserted into (2.1.8), a non-zero difference would be observed between the asymmetry of unpolarized neutrons scattered from polarized protons ( $A_{000n}$ ) and the asymmetry of polarized neutrons scattered from an unpolarized proton target ( $A_{00n0}$ ). The evaluation of (2.1.7) yields

$$A_{000n} - A_{00n0} = \text{Tr} (M^\dagger \rho_i M \sigma_n \cdot \mathbf{n}) - \text{Tr} (M^\dagger \rho_i M \sigma_p \cdot \mathbf{n}). \quad (2.1.8)$$

The difference in asymmetries is related to the interference of the CSB amplitude  $f(E, \theta)$  with the conventional amplitudes as

$$\Delta A = A_{00n0} - A_{000n} = \frac{1}{2\sigma_0} \text{Re} (b^* f). \quad (2.1.9)$$

The scattering matrix  $M$  has been normalized according to  $\sigma_0 = 1/4 \text{Tr}(MM^\dagger)$ . An expression for  $f(E, \theta)$  is derived in section (2.3). A non-zero  $\Delta A$  is clear evidence of the presence of a class (IV) potential.

The CSB part of the n-p scattering matrix can also be determined by measuring the left-right scattering asymmetry of a beam and target initially polarized in perpendicular directions,

$$A_{00sk} - A_{00ks} = \frac{1}{2\sigma_0} \text{Im}(-c^* f). \quad (2.1.10)$$

The unit vector,  $s$ , is given by  $s = n \times k_1$ . The ten remaining CSB experiments (nine of which involve interference terms of the CSB amplitude,  $f(E, \theta)$ , with the conventional amplitudes; and the observable related to  $|f(E, \theta)|^2$ ) require the measurement of two or more polarizations among the incoming and outgoing particles. Such experiments involve rather formidable problems and are not currently feasible.

## 2.2 Related Measurements in Charge Symmetry Breaking

Low energy nucleon-nucleon scattering data clearly demonstrate strong evidence of charge independence breaking but do not unequivocally show effects of charge symmetry breaking. Scattering lengths and effective ranges of the nucleon-nucleon interactions are presented below in table (2.2.1) (reference 4 and other references therein).

Table (2.2.1) Low Energy  $^1S_0$  Nucleon-Nucleon Elastic Scattering Parameters

Interaction	$a$ (fm)	$r_0$ (fm)	
$n + p$	$-23.748 \pm 0.10$	$2.75 \pm 0.05$	
$n + n$	$-18.45 \pm 0.46$	$2.83 \pm 0.16$	$^2H(\pi^-, \gamma)2n$
	$-16.73 \pm 0.47$	$2.85 \pm 0.20$	$^2H(n, p)2n$
$p + p$	$-7.8098 \pm 0.0023$	$2.767 \pm 0.010$	raw experimental values
	$-17.9 \pm 1.0$	$2.82 \pm 0.03$	corrected for known electromagnetic (EM) effects

Clear evidence of charge independence breaking can be seen in the different  $n - p$  and  $n - n$  scattering lengths. The charge symmetry situation is more problematic. Any CSB effect is 10% the size of the theoretical correction made to the  $p - p$  scattering length. Definite evidence of CSB in low energy nucleon - nucleon scattering is limited by the accuracy which electromagnetic (EM) contributions can be extracted from  $p - p$  data. There also remains the question as to which  $a_{nn}$  value in table (2.2.1) is correct. Class (IV) forces vanish for s-wave interactions; therefore, the measurement of low energy  $n - p$ ,  $n - n$ , and  $p - p$  scattering parameters may indicate class (II) and class (III) forces but not class (IV) forces.

CSB can also be inferred from observed binding energy differences between mirror

nuclei, the Nolen - Schiffer effect<sup>(5)</sup>, remaining after all the uninteresting EM terms are subtracted. However, the extent to which charge symmetry is broken is dependent on the wavefunctions chosen and problems related to subtracting direct EM effects persist. As class (IV) forces only pertain to angular momentum states with  $L > 0$ , only evidence for the class (II) and (III) forces can be found in binding energy differences in the most easily understood mirror nuclei pair,  ${}^3\text{H}$  and  ${}^3\text{He}$ .

Investigation of CSB has also been extended to the  $\pi^\pm$  - d system<sup>(6-11)</sup>. Differences in the  $\pi^\pm$ -d total cross sections measured by Pedroni et. al.<sup>(6)</sup> in the energy range 70 - 370 MeV indicate maximal CSB effects on the order of 4% after the subtraction of Coulomb effects. The origin of the observed CSB is uncertain but can be parameterized in terms of different  $\Delta$ -isobar mass states in the elastic scattering channel. Masterson et. al.<sup>(7-9)</sup> measured the  $\pi^\pm$ -d differential cross sections at 143 MeV and 256 MeV. Masterson's results illustrated evidence of CSB after Coulomb contributions were removed and were in good agreement with those of Pedroni. Electromagnetic contributions to  $[\sigma(\pi^-d) - \sigma(\pi^+d)]$  experiments are much smaller than those of low energy nucleon-nucleon scattering studies. However, other significant EM contributions, such as direct coulomb - nuclear interference and the effective interaction energies of the  $\pi^\pm$  scattering from the deuteron, must first be determined and their contributions removed from the data.

CSB has also been investigated in the  $np - d\pi^0$  reaction<sup>(12-16)</sup>. Since a deuteron has isospin equal to zero and a pion has isospin equal to one, the reaction can go only in the  $T = 1$  channel. Therefore, the reaction mechanism must be identical to the  $pp - d\pi^+$  reaction where the identical particles in the incident channel require that the reaction be symmetric about  $90^\circ$  in the center of mass. Therefore, the forward-backward asymmetry defined by

$$A_{fb} = \frac{\sigma(0^\circ) - \sigma(180^\circ)}{\sigma(0^\circ) + \sigma(180^\circ)} \quad (2.2.1)$$

must identically be zero. In the  $np - d\pi^0$  reaction, the significance of an experimental result is not as heavily dependent on uninteresting coulomb effects. Cheung, Henley and Miller<sup>(16)</sup> have predicted that the reaction is driven mainly by  $\pi$ - $\eta$  meson meson mixing near the  $\Delta(3,3)$  resonance energy region and have estimated a forward-backward asymmetry of approximately -0.22%. Hollas et. al.<sup>(13)</sup> could find no evidence of a forward-backward asymmetry about  $90^\circ$  c.m. at 795 MeV at the level of  $\pm 0.50\%$ .

Pion scattering experiments<sup>(17)</sup> from  ${}^3\text{H}$  and  ${}^3\text{He}$  have also shown evidence of CSB. The ratios



$$r_1 = \frac{d\sigma(\pi^+ + {}^3\text{H})}{d\sigma(\pi^+ + {}^3\text{He})}, \text{ and } r_2 = \frac{d\sigma(\pi^- + {}^3\text{H})}{d\sigma(\pi^- + {}^3\text{He})} \quad (2.2.2)$$

were used to calculate the 'super-ratio'

$$R = r_1 r_2 \quad (2.2.3)$$

which must be unity if charge symmetry is valid. Nefkens et. al <sup>(17)</sup> observed a maximum value of  $R = 1.31 \pm 0.09$  scattering 180 MeV  $\pi^+$  and  $\pi^-$  from tritium and  ${}^3\text{H}$  targets. Explanations other than CSB have been offered. Deviations from the value of unity have been interpreted in terms of differing structures of  ${}^3\text{H}$  and  ${}^3\text{He}$  due to three - nucleon correlations caused by coulomb forces<sup>(18)</sup> and by direct coulomb interactions<sup>(19)</sup> rather than evidence of CSB forces.

Isospin conservation, and therefore charge symmetry, forbids the  $d + d \rightarrow {}^4\text{He} + \pi^0$  reaction since the initial and final state differ in isospin by unity. Experiments designed to detect this reaction have placed only an upper bound on the cross section. Upper limits of 900 pb / sr with a 404 MeV incident deuteron energy and where the alpha particle was detected at  $5.5^\circ$  <sup>(20)</sup>, 97 pb / sr at 460 MeV and  $8.7^\circ$  <sup>(21)</sup>, and 19 pb / sr at 787 MeV and  $11^\circ$  <sup>(22)</sup> have been measured in the past. The reaction is thought to be driven mainly by  $\pi - \eta$  and  $\pi - \eta'$  mixing<sup>(23)</sup>. The presence of a  $T = 1$  admixture in the  ${}^4\text{He}$  ground state could drive the reaction but no experimental evidence indicates the presence of such an admixture. Cheung <sup>(23)</sup> has estimated the forward angle differential cross-sections to be between 0.01 pb / sr and 0.1 pb / sr in the energy range 500 - 700 MeV. Coon and Freedom <sup>(24)</sup> have estimated the forward angle  $d + d \rightarrow {}^4\text{He} + \pi^0$  differential cross section to be approximately 0.12 pb / sr at 1.95 GeV.

An experiment measuring the existence of the class IV forces in the neutron - proton elastic scattering system is in process at IUCF<sup>(25)</sup> at an incident neutron beam energy 188 MeV. The experiment is similar to the TRIUMF experiment except that the beam and target are simultaneously polarized. The arguments are similar to those used earlier in that a non-zero asymmetry is direct evidence of the presence of class (IV) CSB forces. The IUCF experiment will not only measure the difference between the zero-crossing angles of  $A_n$  and  $A_p$  (equal to the asymmetry zero-crossing angle difference between parallel and antiparallel target and beam spin projections) but will also attempt to determine  $\Delta A$  over approximately  $30^\circ$  (lab) as well.

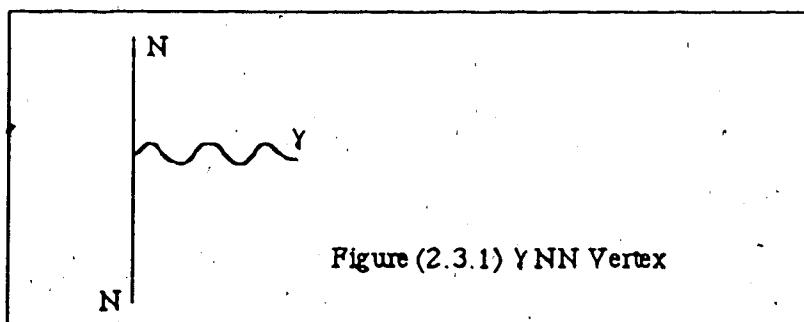
### 2.3 Theoretical Considerations of Charge Symmetry Breaking in Neutron-Proton Elastic Scattering

There are many sources of class (IV) contributions to charge symmetry breaking in the neutron - proton system, but until this TRIUMF experiment there had been no direct experimental evidence of the presence of such forces in the nucleon - nucleon interaction. Some of these CSB effects, such as the effect of the neutron - proton mass difference in one - pion exchange, are relatively straightforward and amenable to calculation. Three of the larger contributions to charge symmetry breaking are reviewed below. Other CSB class (IV) potential terms, such as those due to two-pion exchange and quark effects are not as large<sup>(1, 26)</sup> and are neglected here.

The  $\gamma NN$  vertex function is written as

$$\bar{u} [ e (F_1^s + F_1^v \tau_3) \gamma^\mu A_\mu - (F_2^s + F_2^v \tau_3) \frac{1}{2M} \sigma^{\mu\nu} F_{\mu\nu} ] u. \quad (2.3.1)$$

The graph associated with (2.3.1) is illustrated in figure (2.3.1).



The function  $F_{\mu\nu}$  represents the electromagnetic field strength tensor. The isoscalar (s) and isovector (v) parts of the nuclear electromagnetic form factors are given by <sup>(26)</sup>

$$F_1^s = \frac{1}{2} (F_1^{(p)} + F_1^{(n)}) \quad (2.3.2a)$$

$$F_1^v = \frac{1}{2} (F_1^{(p)} - F_1^{(n)}) \quad (2.3.2b)$$

$$F_2^s = \frac{1}{2} (\kappa_p F_1^{(p)} + \kappa_n F_1^{(n)}) \quad (2.3.2c)$$

$$F_2^v = \frac{1}{2} (\kappa_p F_1^{(p)} - \kappa_n F_1^{(n)}) \quad (2.3.2d)$$

The symbols  $\kappa_p$  and  $\kappa_n$  represent the magnetic moments of the proton and neutron. The first term corresponds to direct Coulomb interactions between two nucleons and can be neglected for the neutron - proton case. The second term of (2.3.1) depicts the coupling of the proton current to the neutron anomalous magnetic moment. This term is proportional to  $\mu \cdot B$  when a non-relativistic reduction is made. For zero momentum transfer the form factors reduce to

$$F_1^s(0) = F_1^v(0) = 1/2, \quad F_2^s(0) = -0.06, \quad F_2^v(0) = 1.85 \quad (2.3.2e)$$

If the form factors are reduced to their zero-momentum values, the contribution of the  $\gamma NN$  diagram to the proton - neutron elastic Lorentz invariant matrix is written as

$$M_{fi} = \bar{u}(p_1') e^2 [F_1^{(p)} \gamma_\mu - F_2^{(p)} \frac{1}{2M} \sigma_{\mu\nu} (p_1' - p_1)^\nu] u(p_1) \times \frac{1}{q^2 - ie} u(p_2') F_2^{(n)} \frac{1}{2M} \sigma^{\mu\nu} (p_2' - p_2)_\nu u(p_2) \quad (2.3.3)$$

The first - order contribution to the nucleon - nucleon scattering matrix can be determined by including the lowest order Feynman diagram in the non-relativistic approximation. The resultant class (IV) effective potential (in the Born approximation) can be found by taking the Fourier transform of the class (IV) part of (2.3.3). It is given by (2, 28)

$$V_{EM}^{iv}(r) = -\frac{e^2}{4\pi} \kappa^n [\tau_3(1) - \tau_3(2)][\sigma(1) \cdot \sigma(2)] \cdot L \frac{1}{r} \frac{d}{dr} \left( \frac{1}{r} \right), \quad (2.3.4)$$

where  $\kappa^n = -1.91$  represents the neutron magnetic moment in units of the nuclear magneton, and  $M$  is the nucleon mass.

The  $\pi NN$  vertex function is given by

$$ig \bar{u} \gamma_5 \tau \phi u \quad (2.3.5)$$

The one-pion-exchange graph is responsible for a class (IV) contribution to the  $M$  matrix

proportional to the difference in the nucleon masses.

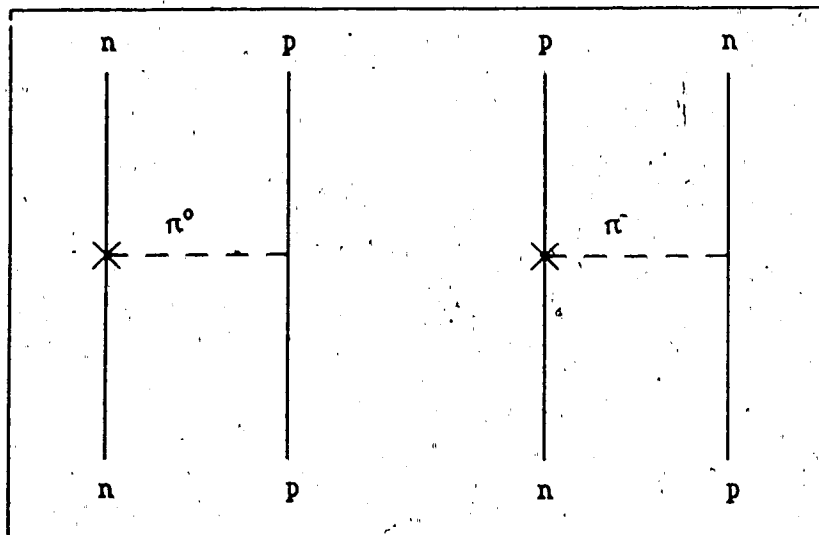


Figure (2.3.2) Contribution to class (IV) charge symmetry breaking by the neutron-proton mass difference in one-pion exchange

29) The class (IV) part of the effective potential (in the Born approximation) is then <sup>(28,</sup>

$$V^{IV}(r) = \frac{g^2}{4\pi} \frac{\delta}{m^2} [\tau(1) \times \tau(2)]_3 [\sigma(1) \times \sigma(2)] \cdot \mathbf{L} \frac{1}{r} \frac{d}{dr} \left[ \frac{1}{r} \exp(-m_\pi r) \right], \quad (2.3.6)$$

where  $m$  represents the average nucleon mass,  $\delta = (m_n - m_p) / (m_n + m_p)$ , and  $m_\pi$  is the pion mass.

CSB arises in  $\rho$  - exchange from the  $n$  -  $p$  mass difference. The  $\rho$ NN vertex function is given by

$$\bar{u} [ g_V \gamma^\mu + i f_V \sigma^{\mu\nu} q_\nu ] u \rho_\mu \quad (2.3.7)$$

the vector and tensor  $\rho$  meson - nucleon coupling constants are given by  $g_V$  and  $f_V$ , and  $q$  represents the four-momentum transfer. Calculations of  $\Delta A$  from this contribution are highly sensitive to uncertainties in the vector and tensor  $\rho$ -NN coupling constants. Estimates of this contribution<sup>(1)</sup> suggest that it is the second largest effect after the nucleon mass difference in

$\pi$ -exchange.

Isospin non-conservation, and therefore a potential of the class (IV) variety, can be induced by the electromagnetic mixing of mesons of different isospin. In particular, the mixing of the  $\rho$  - meson ( $T = 1$ ) with the  $\omega$  - meson ( $T = 0$ ) as in figure (2.3.3).

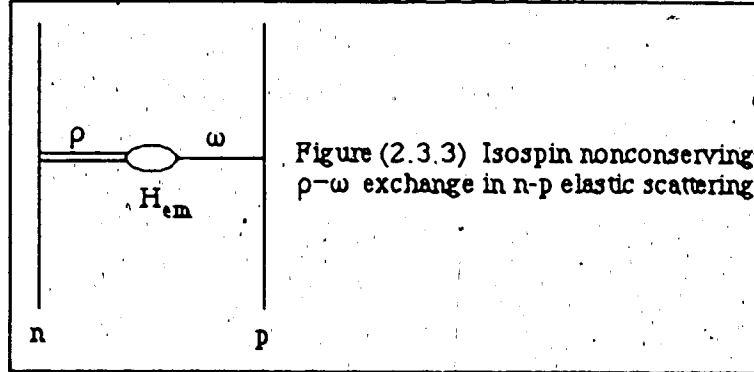


Figure (2.3.3) Isospin nonconserving  $\rho$ - $\omega$  exchange in n-p elastic scattering

The invariant amplitude,  $M_{fi}$ , in the Born approximation from this mixed - meson exchange can be expressed with the direct application of the Feynman rules,

$$M_{fi} = - \frac{g_\rho g_\omega \langle \omega^0 | H_{em} | \rho^0 \rangle}{(q^2 - m_\rho^2)(q^2 - m_\omega^2)} [\bar{u}(1)\tau_3(1) (\gamma^\mu + i\kappa^\nu \sigma^{\mu\nu} q_\nu) u(1) \bar{u}(2) \gamma_\mu u(2) + (1 \rightarrow 2; 2 \rightarrow 1)], \quad (2.3.9)$$

where  $\kappa^\nu$  represents the magnetic moment of the vector  $T = 1$  meson,  $m_\rho$  and  $m_\omega$  the masses of the two mesons,  $q$  the four-momentum transfer,  $g_\rho$  and  $g_\omega$  the meson-nucleon coupling constants and  $\langle \omega^0 | H_{em} | \rho^0 \rangle$  the electromagnetic overlap of the two meson states. The class (IV) part of the potential can be determined from the above by making the non-relativistic reduction and evaluating the Fourier transformation. One finds that<sup>(2, 28)</sup>

$$V_{\rho-\omega}^{(IV)} = - \frac{g_\rho g_\omega \langle \omega^0 | H_{em} | \rho^0 \rangle}{m_\omega^2 - m_\rho^2} \frac{\kappa^\nu [\sigma(1) - \sigma(2)] \cdot L}{4\pi M^2} \times \frac{1}{r} \frac{d}{dr} \left( e^{-\frac{m_\rho}{\hbar} r} - e^{-\frac{m_\omega}{\hbar} r} \right) \quad (2.3.10)$$

Accurately estimating the CSB contribution from  $\rho$ - $\omega$  mixing is difficult since calculations are sensitive to uncertainties in the meson - nucleon coupling constants and the electromagnetic mixing factor<sup>(1)</sup>. CSB effects in neutron - proton elastic scattering due to the mixing of the lighter  $\pi^0$ - $\eta$  mesons contribute only class (III) CSB forces<sup>(2)</sup>. Interference between vector and tensor parts of the vector isovector  $\rho$  meson and vector isoscalar  $\omega$  meson interaction causes the class (IV) type potential in  $\rho$ - $\omega$  meson mixing. These terms are absent in the  $\gamma^5$  interaction of the pseudoscalar isovector  $\pi$  meson and the pseudoscalar isoscalar  $\eta$  meson. However,  $\pi^0$ - $\eta$  meson mixing does contribute to class (IV) CSB in the  $n(p,d)\pi^0$  reaction through pion-production mechanisms<sup>(12)</sup>.

## Chapter 3 Experimental Apparatus

### 3.1 Introduction

This chapter is concerned with the design and calibration of the experimental equipment. For purposes of clarity, there is some repetition between this and the following chapter when discussion of the apparatus requires results of the analysis. Two other papers dealing with the experimental equipment have also been published (29, 30).

The experiment measured the difference between the zero-crossing angles of the scattering asymmetry of unpolarized neutrons scattered from a polarized target ( $A_p$ ) and of polarized neutrons scattered from an unpolarized proton target ( $A_n$ ). The interleaved experiments were made with identical apparatus designed to reduce all systematic errors not correlated with beam or target polarization reversal to at least second order. Any error in the positioning of experimental equipment could conceivably influence the measurement of  $A_n$  or  $A_p$ , but since the experimental geometry was common to both measurements any such effect must be identical; therefore, there could be no effect on the difference,  $A_n - A_p$ .

Details of the proton transport system<sup>(29)</sup> are illustrated in figure (3.1.1). The neutron beam originated from a liquid deuterium ( $LD_2$ ) neutron production target in the path of the primary proton beam. The dipole magnet 4AB2 swept away the unused portion of the incident proton beam. Neutrons were produced via the  $^2H(p,n)^2p$  reaction. Polarized (unpolarized) neutrons were produced with an polarized (unpolarized) proton beam. During the polarized beam portion of the experiment, the incident proton beam polarization was precessed into the (n,p) scattering plane to take advantage of the large transverse polarization transfer coefficient. The neutron polarization was precessed back into the vertical direction by two spin precession dipole magnets, 'Bonnie' and 'Clyde'. Neutrons were extracted at  $9^\circ$  (where the polarization transfer coefficient is at its largest) and collimated through a 3.37m long iron and lead collimator. Polarized (unpolarized) neutrons were scattered from an unpolarized (polarized) proton target to measure  $A_n$  ( $A_p$ ).

For future convenience, the experimental coordinate system is defined here. Left events are defined as events where neutrons were detected in the left neutron array. Coincident left event recoil protons must scatter to the right. The z-axis is defined along the incident neutron beam symmetry axis. The x-axis intersects the target in the horizontal plane. Positive is defined as emerging to the left of the target if the observer is looking downstream. The y-axis, not shown in figure (3.1.2), emerges vertically from the target.

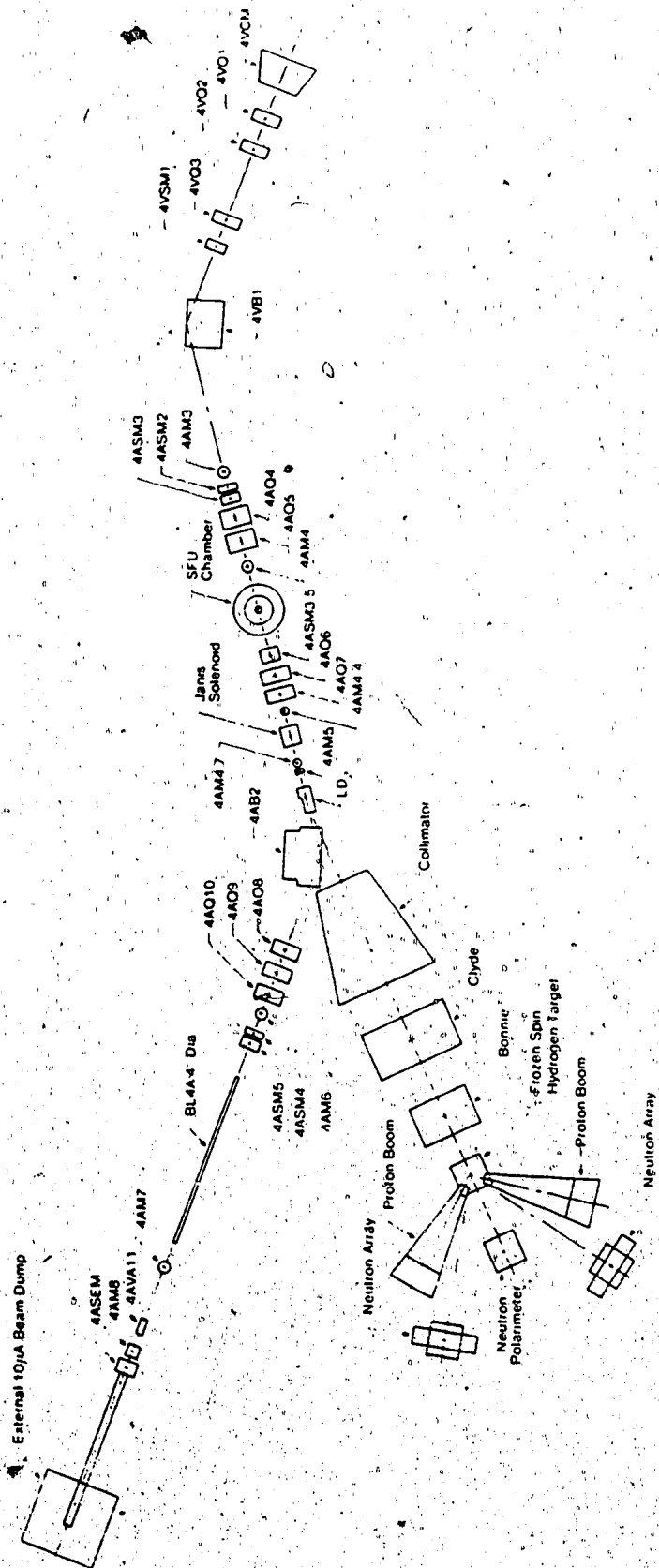


Figure (3.1.1) Proton Beam Transport System



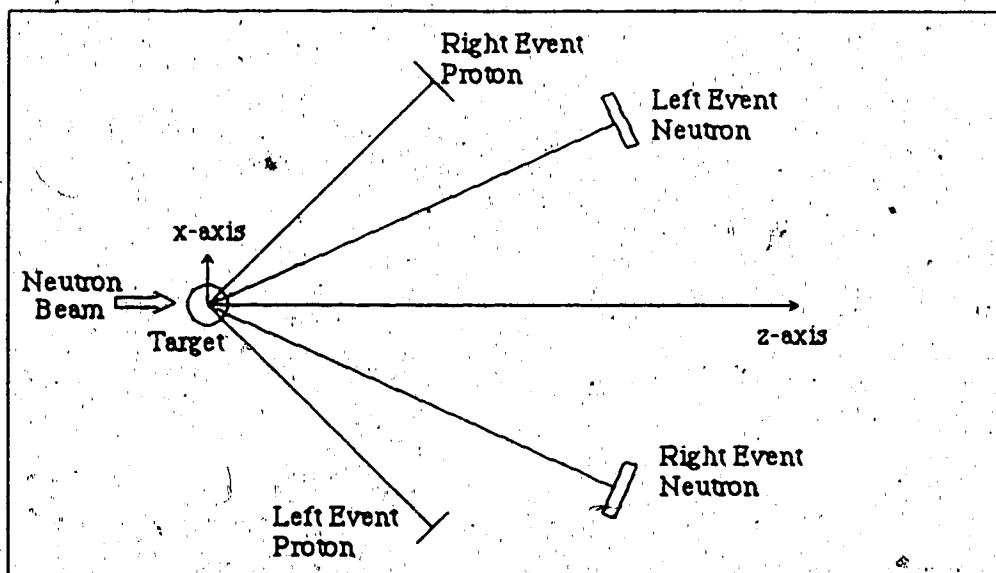


Figure (3.1.2) Coordinate System Definition

### 3.2 Primary Beam Positioning

The energy and position of the neutron beam at the FST target were sensitive to deviations in the proton beam position, angle and size at the LD<sub>2</sub> target. Both the polarized and unpolarized proton beams were extracted from the same ion source to reduce differences in the emittance properties between the three (up, down and off) proton beam polarization states. To maintain a consistent position of the primary proton beam on the LD<sub>2</sub> target, the vertical and horizontal positions of the proton beam were monitored with two pairs of split plate secondary emission monitors (SEMs)<sup>(31, 32)</sup> situated 0.86 m and 2.18 m upstream of the liquid deuterium neutron production target (shown as elements 4AM4.7 and 4AM4.4 in figure 3.1.1). A schematic diagram of the SEM assembly is illustrated in figure (3.2.1).

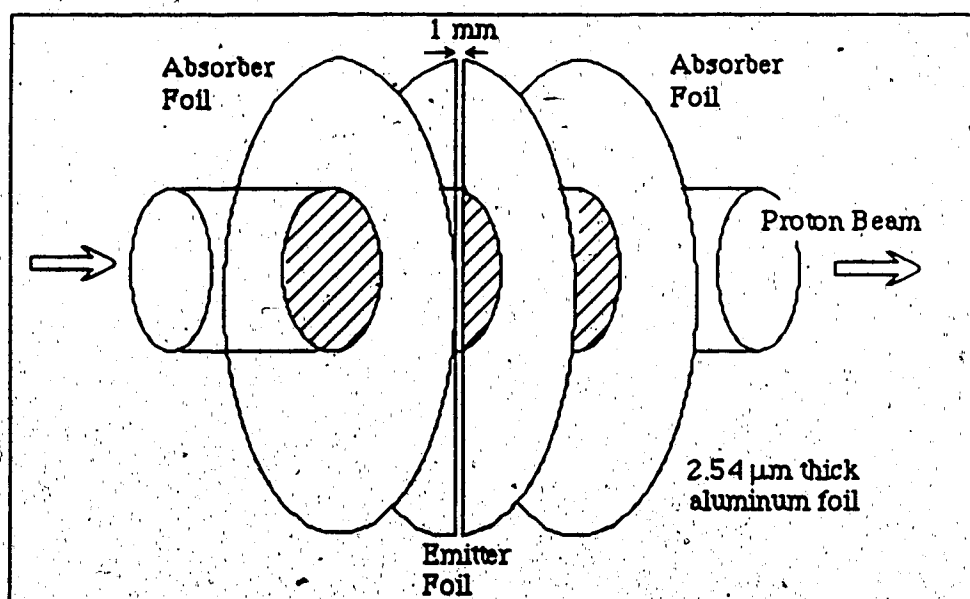


Figure (3.2.1) Schematic Diagram of Secondary Emission Monitor (SEM). Current from each semi-circular foil piece was integrated to calculate a left-right (in this figure) or up-down asymmetry. The asymmetry was used by a micro-processor to recalibrate horizontal and vertical steering magnets to maintain the proton beam position.

Each SEM consisted of three 2.54  $\mu\text{m}$  thick, 0.10 m diameter aluminum foils. The outer, or emitter, foils are separated from the inner, or absorber, foil by a 3.2 mm gap. The emitter foil is divided into two electrically isolated semi-circular halves. A +100 to +300 Volt potential on the absorber foil draws recoil electrons from the grounded absorber foils. Up /

down and left / right asymmetries were measured at each SEM location. SEM output signals were amplified and fed into a microprocessor system programmed to calculate appropriate beam element corrections. The feedback system employed the bending magnet 4VB1, the horizontal steering magnet 4ASM3, and the two vertical steering magnets 4VSM1 and 4ASM2. The SEMs were initially set to centre the proton beam on the LD2 target and were not altered over the duration of the experiment. The geometric centre of individual SEMs could be remotely positioned in vertical and horizontal directions to an accuracy of  $\pm 0.075$  mm. In total, the four SEMs were equivalent to 0.030 mm of aluminum in the proton beam path.

The profile of the proton beam was observed after every 24 hour period with the wire chamber 4AM5 (see figure 3.1.1) which had a 1 mm resolution. The width of the proton beam at the liquid deuterium production target was measured as 4.1 mm horizontal FWHM and 5.5 mm vertical FWHM.

### 3.3 Primary Beam Energy and Polarization

The experiment was designed so that an absolute calibration of the primary proton beam energy would not be needed. However, it was necessary to maintain the beam energy to within  $\pm 0.25$  MeV since the position of the zero-crossing angles is a weak function of the incident neutron energy (see appendix A). Since the accuracy of the asymmetry zero-crossing angle determination varies with the inverse of the beam and target polarizations, polarizations were monitored throughout and maintained as high as possible.

The proton beam energy and polarization were measured throughout the experiment<sup>(33)</sup> by inserting a thin kapton foil in the path of the beam 6.32 m upstream of the LD2 target. Protons scattered at  $\pm 17^\circ$ , where the p-p analyzing power approaches a maximum at the experimental energy, were detected in two transmission counter assemblies on either side of the beam. The detector assembly was completed with additional scintillator counters at  $\pm 68.9^\circ$  to detect recoil protons to reduce (p,2p) background. A schematic of the beam energy monitor BEM / polarimeter is illustrated in figure (3.3.1). Each assembly was composed of a scintillator telescope (polarimeter) followed by a large copper degrader and six scintillator sheets sandwiched within six 1 mm copper plates. A more detailed illustration of the range counter assembly is illustrated in figure (3.3.2). The proton beam energy was determined by counting the number of protons which stopped in each absorber sheet.

Normally, slight misalignments of the beam position could result in false

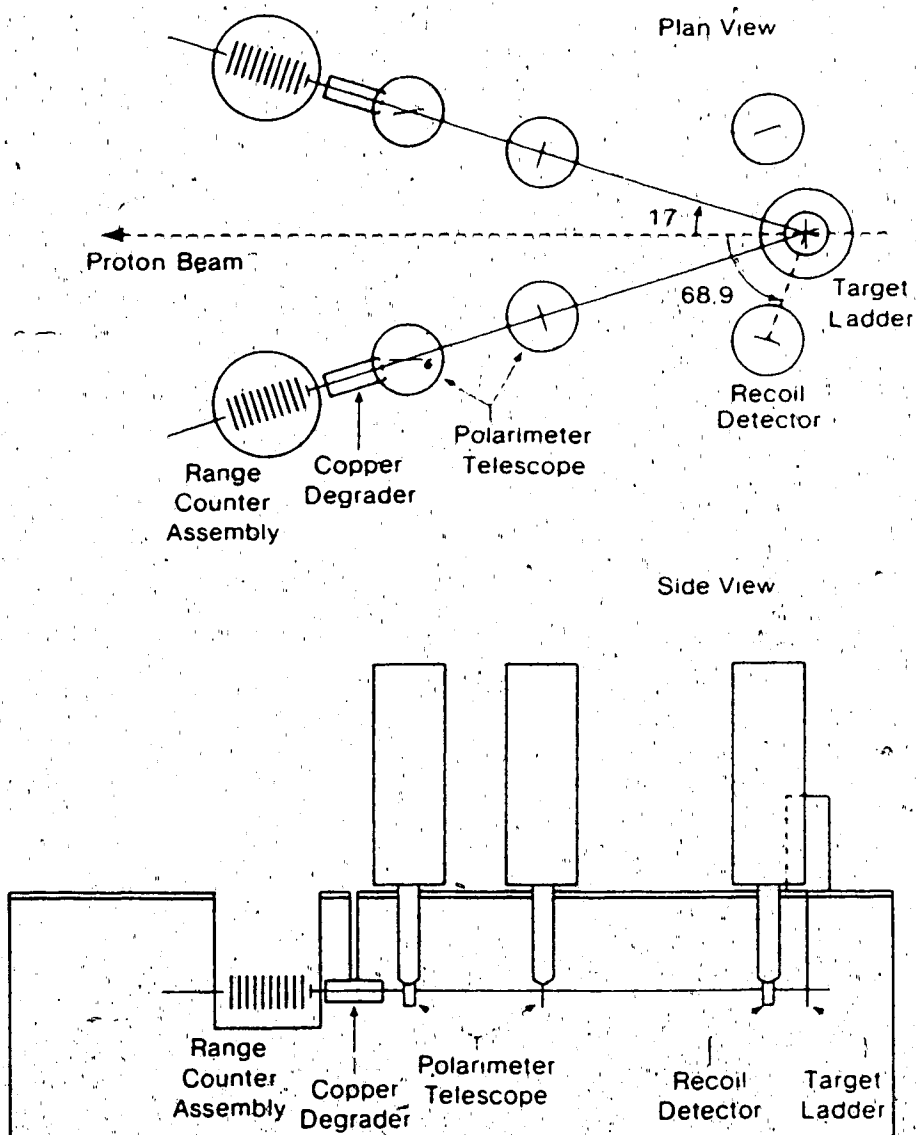


Figure (3.3.1) Schematic Diagram of Proton Polarimeter

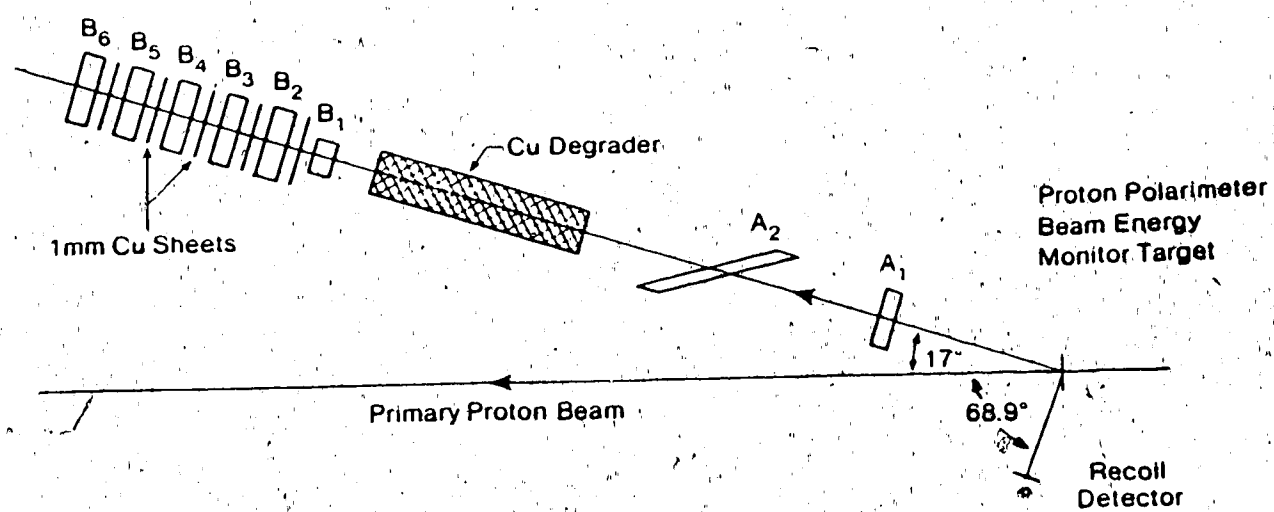


Figure (3.3.2) Beam Energy Monitor Range Counter Assembly

polarization<sup>(33)</sup> measurements due to changes in the left and right detector angular acceptance combined with changes in the p-p differential cross section as a function of proton recoil angle, and due to changes in the effective solid angle. The polarimeter was constructed to reduce such systematic errors by rotating the solid angle defining counter by  $68^\circ$ . This feature of the polarimeter design is illustrated in figure (3.3.3).

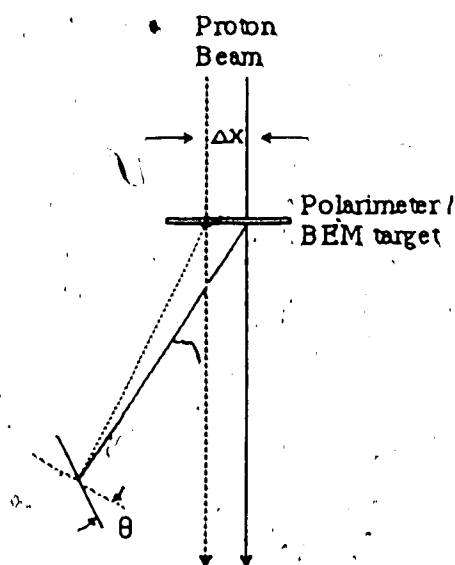


Figure (3.3.3) Rotation of polarimeter solid angle defining counter by  $\theta$  was designed to reduce changes in the solid angle associated with movement of the primary proton beam.

A schematic diagram of the proton polarimeter electronics is illustrated in figure (3.3.4)

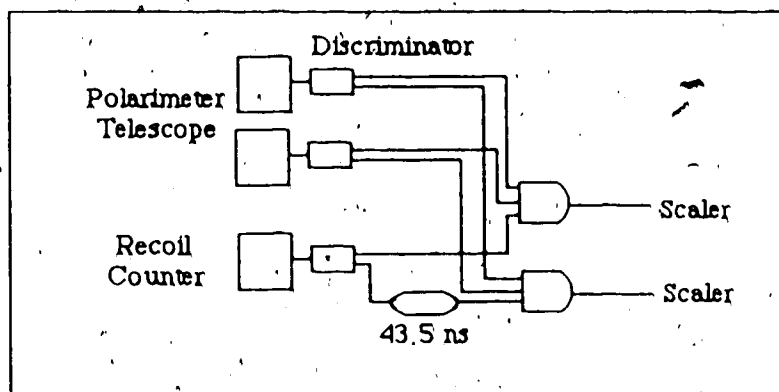


Figure (3.3.4) Schematic Diagram of Proton Polarimeter Electronics

The number of spurious, or accidental, polarimeter counts was determined by delaying the recoil counter signal by 43.5 ns thus excluding valid elastically scattered proton-proton pairs and satisfying the electronic logic requirements only by accident. The proton polarimeter instrumental asymmetry was measured constantly over the experiment by turning off the polarization one minute of every seven.

Details of the proton BEM / polarimeter are presented below in table (3.3.1).

Table (3.3.1) Proton BEM / Polarimeter Details

#### Defining Counter

Vertical Dimension	1.0 cm
Horizontal Dimension	2.5 cm
Distance to target	77.47 cm
Solid angle	0.16 msr
Polar angle Range	$\pm 0.37^\circ$
Azimuthal Range	$\pm 1.26^\circ$
Central Angle	$17^\circ$
Rotation Angle	$68^\circ$

#### Recoil Counter

Vertical Dimension	2.0 cm
Horizontal Dimension	1.0 cm
Distance to Target	20.32 cm
Solid Angle	4.84 msr
Polar Range	$\pm 1.41^\circ$
Azimuthal Range	$\pm 3.0^\circ$
Central Angle	$68.9^\circ$

Parameters of the proton polarimeter are listed in table (3.2.2) as measured with a 600 nA

beam. Although polyethylene ( $\text{CH}_2$ ) is more hydrogenous by a ratio of 5.24:1 than Kapton, the latter was chosen as the polarimeter / BEM target due to its greater resistance to radiation damage. Polyethylene and carbon targets were periodically inserted into the beam to monitor effects due to hydrogen loss in the kapton target and to measure the effect caused by the presence of carbon in the kapton foil. Kapton targets were replaced after approximately 30 - 60  $\mu\text{A}$  - hours.

**Table (3.3.2) Proton Polarimeter Target Characteristics**

	$\text{CH}_2$	Kapton
Relative p-p yield	5.24	1
% C(p,2p)	0.9%	4.0%
Random Rate	9.3%	22%
Instrumental Asymmetry	$-0.0166 \pm 0.0001$	$-0.0162 \pm 0.0002$

A 0.42 m long superconducting solenoid, 'Janus', precessed the proton polarization by  $90^\circ$  ( $\int \mathbf{B} \cdot d\mathbf{l} = 2.2\text{T}\cdot\text{m}$ ) into the scattering plane from the vertical direction to take advantage of the large  $^2\text{D}(\text{p},\text{n})2\text{p}$  polarization transfer coefficient  $(D_{\text{osso}}^2 + D_{\text{okso}}^2)^{1/2}$  at the  $\text{LD}_2$  target. The 'Janus' solenoid required thirty minutes of downtime daily to replenish liquid helium and nitrogen levels.



### 3.4 Neutron Beam Production

The neutron beam was produced via the  $^2\text{H}(p,n)^2\text{H}$  reaction. The target<sup>(29)</sup> contained liquid-deuterium ( $\text{LD}_2$ ) over a 21.6 K - 22.6 K temperature range and 24.2 - 24.6 psi pressure range with a mean density of  $0.167 \text{ g/cm}^3$ . The target was a 19.7 cm long, 50.8 mm diameter cylinder. The target end windows were 0.051 mm thick stainless steel and the target walls were 0.25 mm thick stainless steel. During cyclotron operation, the target was separated from the cyclotron vacuum by a 0.13 mm stainless steel barrier.

Critical to the experiment was the stability of the neutron beam energy over the duration of the experiment. Ideally, the neutron energy was directly correlated to the proton beam energy which was monitored throughout the experiment. However, the neutron beam energy may change if target density fluctuations result in significant changes in the proton beam energy loss within the liquid deuterium. The proton beam lost an average of 4.69 MeV in the liquid deuterium. Liquid deuterium changes density by  $\pm 0.6 \%$  over the observed  $\pm 0.5 \text{ K}$  variation in the target temperature. This causes a  $\pm 30 \text{ keV}$  change in the neutron energy. Such fluctuations in the neutron energy are well within the stringent limits required by the experiment (see appendix A). The absolute energy of the neutron beam was measured to be  $477 \pm 2 \text{ MeV}$  by time-of-flight techniques between the FST target and neutron profile monitor.

### 3.5 Neutron Beam Collimation

The neutron beam was extracted from the  $9^\circ$  port and collimated through a 3.37 m long collimator. The front face of the collimator was located 2.87 m from the center of the  $\text{LD}_2$  target. The collimator consisted of a pipe enclosed in solid lead and filled with 30.5 mm long cylindrical iron inserts with rectangular apertures. It consisted of two sections. The upstream section was 1.8 m long, 102 mm in diameter and contained six cylindrical inserts. The horizontal and vertical dimensions ranged in steps from 38.6 mm to 39.1 mm and from 18.2 mm to 25.2 mm, respectively. The downstream section was 1.5 m long, 127 mm in diameter and contained five inserts. The horizontal and vertical dimensions ranged from 43.2 mm to 45.6 mm and from 26.6 mm to 32.0 mm, respectively. The collimator inserts were positioned with a left-right asymmetry to correct for the asymmetric  $\text{LD}_2$  target

position. A secondary collimator was recessed 20 cm into the 1.6 m long gap in the dipole magnet 'Clyde'. The front face of the secondary collimator was positioned 7.26 m from the center of the LD<sub>2</sub> target. Lead bricks were stacked into the gap to form a 0.61 m long collimator with a 51.3 mm wide and 50.8 mm high aperture.

The collimator was designed to intersect the proton beam at the center of the LD<sub>2</sub> target ( $\pm 3$  mm). Neither the entrance nor exit foils of the LD<sub>2</sub> target were viewed by the frozen spin target.

### 3.6 Neutron Beam Polarization

The polarization of the incident proton beam was precessed into the scattering plane transverse to the beam direction to take advantage of the large transverse polarization transfer coefficient. The neutron beam polarization in the scattering plane is defined as

$$P_n = (d_{osso}^2 + d_{osko}^2)^{1/2} P_p \quad (3.6.1)$$

Here, the quantity  $d_{abcd}$  is the polarization transfer coefficient corrected for final state interactions where a, b, c and d represent the polarization of the scattered, recoil, beam and target particles. The unit vector  $\mathbf{k}$  represents the particle direction, and the vector  $\mathbf{s}$  is the direction perpendicular to particle motion and in the scattering plane. Figure (3.6.1) features a schematic diagram illustrating the polarization transfer process. Values for these coefficients were extracted from phase shift analyses of the p-n reaction and then corrected for final state interactions. Values of the spin transfer coefficients were taken as  $d_{osso} = -0.748$ ,  $d_{osko} = 0.079$  <sup>(34, 35)</sup> (see section 4.6). The main component of the neutron beam polarization emerging from the production target was a small angle,  $\phi = \tan^{-1}[d_{osko}/d_{osso}] = -6.3^\circ$ , away from the direction normal to the beam axis and in the scattering plane (see figure 3.6.1). In addition there existed a small, but nonetheless undesirable, vertical polarization component due to the reaction polarization coefficient  $A_{onoo} = -0.06$ . The polarization component in the scattering plane was precessed into the beam direction by the first dipole precession magnet 'Clyde'. The fringe field of the proton sweep magnet 4AB2 (noted in figure 3.2.1) precessed the neutron spin into the beam axis by a large degree so 'Clyde' ( $B_z = 9.903 \pm 0.23$  kG) had only to precess the spin by  $60^\circ$ . The second dipole precession magnet, 'Bonnie' ( $B_y = 15.71 \pm 0.76$  kG), precessed the neutron polarization by

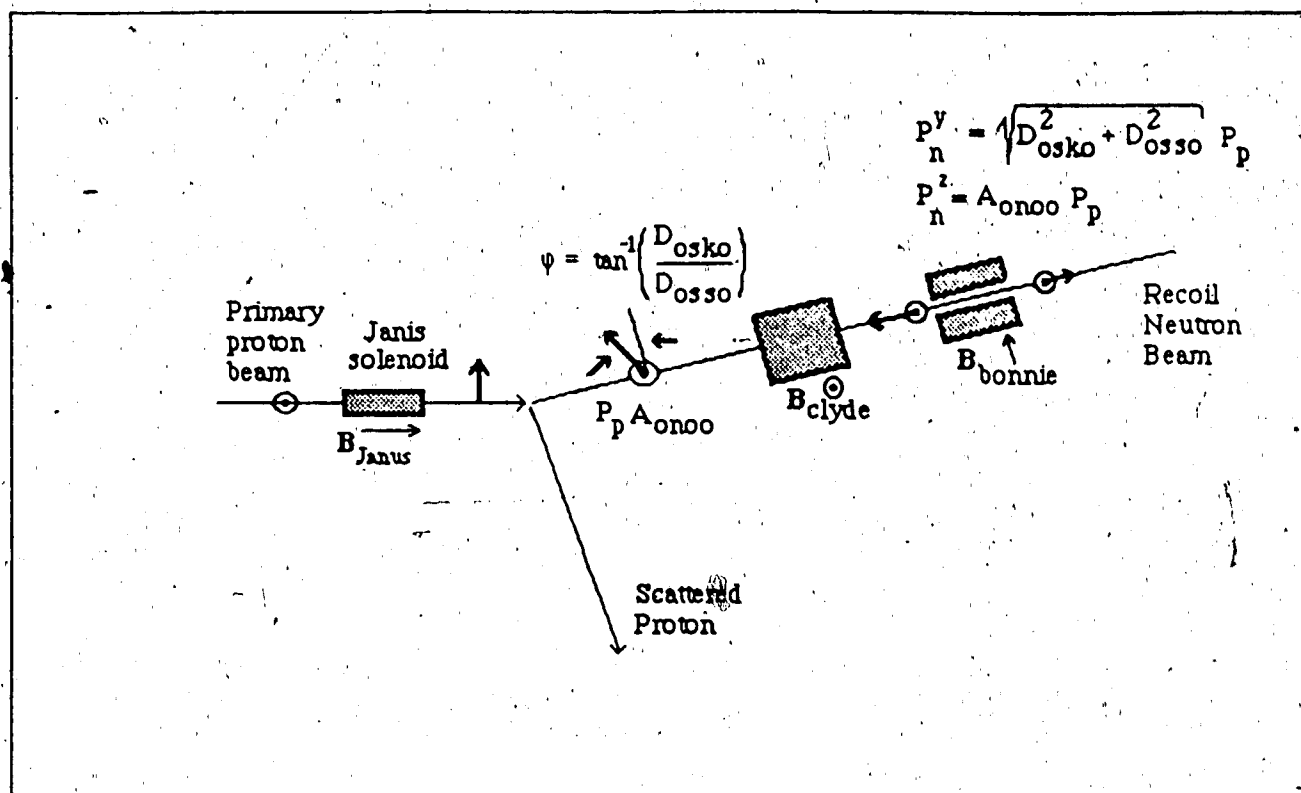


Figure (3.6.1) Depiction of Neutron Polarization Transfer and Precession Through Experimental Apparatus

90° into the vertical direction. 'Bonnie' also precessed the original vertical component of the neutron polarization, due to  $A_{onoo}$ , into the neutron beam axis. The two dipole magnets also served to sweep charged particles from the neutron beam.

The magnetic fields of both magnets were monitored and kept stable to within  $\pm 2$  G throughout the experiment with NMR probes. The dipole magnet 'Clyde' was calibrated by measuring the ratio of the left-right and up-down neutron asymmetry at the neutron polarimeter to the proton polarization as a function of Clyde's magnetic field setting. A plot of the ratio is illustrated in figure (3.6.2). The setting where the up-down asymmetry intersected the asymmetry axis where  $A = 0$  was selected as the experimental value. The precession curves indicates that uncertainty in the total neutron spin precession is  $\pm 5.8^\circ$ , much less than the acceptable limit of  $\pm 10^\circ$ .

### 3.7 Neutron Beam Profile Monitor and Polarimeter

The neutron beam profile monitor<sup>(36)</sup> was located 4.32 m downstream of the frozen spin target (16.90 m from the LD<sub>2</sub> target) and was used to monitor the vertical and horizontal intensity centroids and profiles of the neutron beam during data taking. A schematic diagram of the neutron profile monitor is illustrated in figure (3.7.1). Recoil protons from elastic  $^1\text{H}(n,p)n$  reactions within a 21.0 cm by 21.0 cm, 3.2 mm thick scintillator, termed the convertor-scintillator in figure (3.7.1), were traced back to their origin using information from two 20.3 cm by 20.3 cm delay line chambers (DLCs). The assembly was preceded by a 3.2 mm thick, 26 cm by 26 cm scintillator to veto charged particles in the neutron beam.

The neutron polarimeter was located just downstream of the neutron profile monitor as shown in figure (3.7.1). The neutron polarimeter consisted of four arms branching in the horizontal and vertical planes to measure left-right and up-down asymmetries of recoil protons produced by the  $^1\text{H}(n,p)n$  reaction scattered from a 5 cm thick, 15 cm by 15 cm scintillator ( $\text{CH}_{1.1}$ ) polarimeter target. The polarimeter target was preceded by a scintillator sheet used to veto charged particles in the neutron beam. Downstream of the target was an additional scintillator to detect all recoil charged particles. Each of the four arms contained a 10 cm by 10 cm scintillator sheet 50 cm from the target center spanning a solid angle of 0.040 sr to detect charged particles scattered from the polarimeter target. A wedge-shaped brass absorber (4.6 cm thick at small angles, 9.5 cm thick at large angles) was positioned upstream of each of the four scintillators to equalize the energies of scattered protons uniformly over the angular range subtended by each of the scintillators.

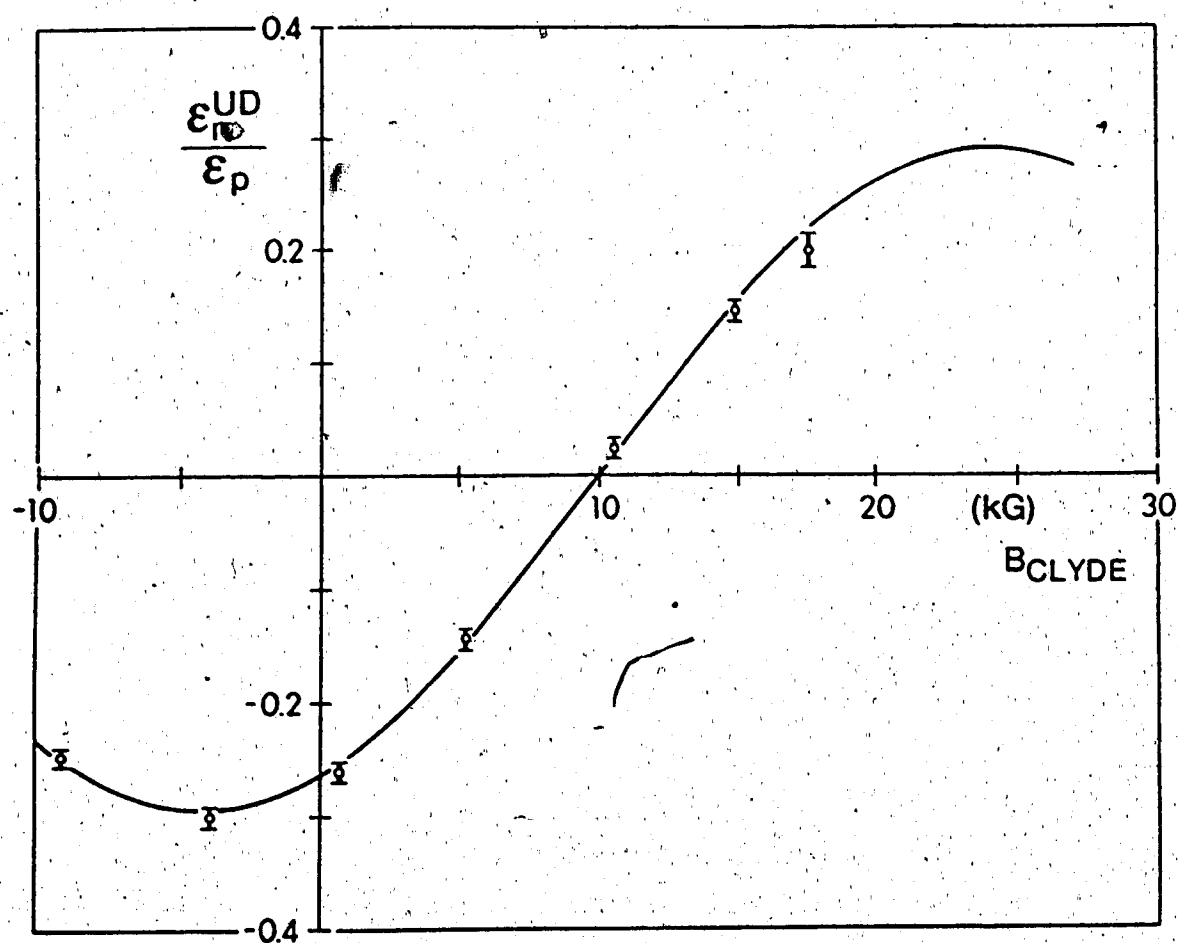


Figure (3.6.2) Ratio of Up-Down Neutron-Proton Scattering Asymmetry in Neutron Polarimeter to Proton Asymmetry in Proton Polarimeter as a Function of the Magnetic Field of the Dipole Precession Magnet 'Clyde'.

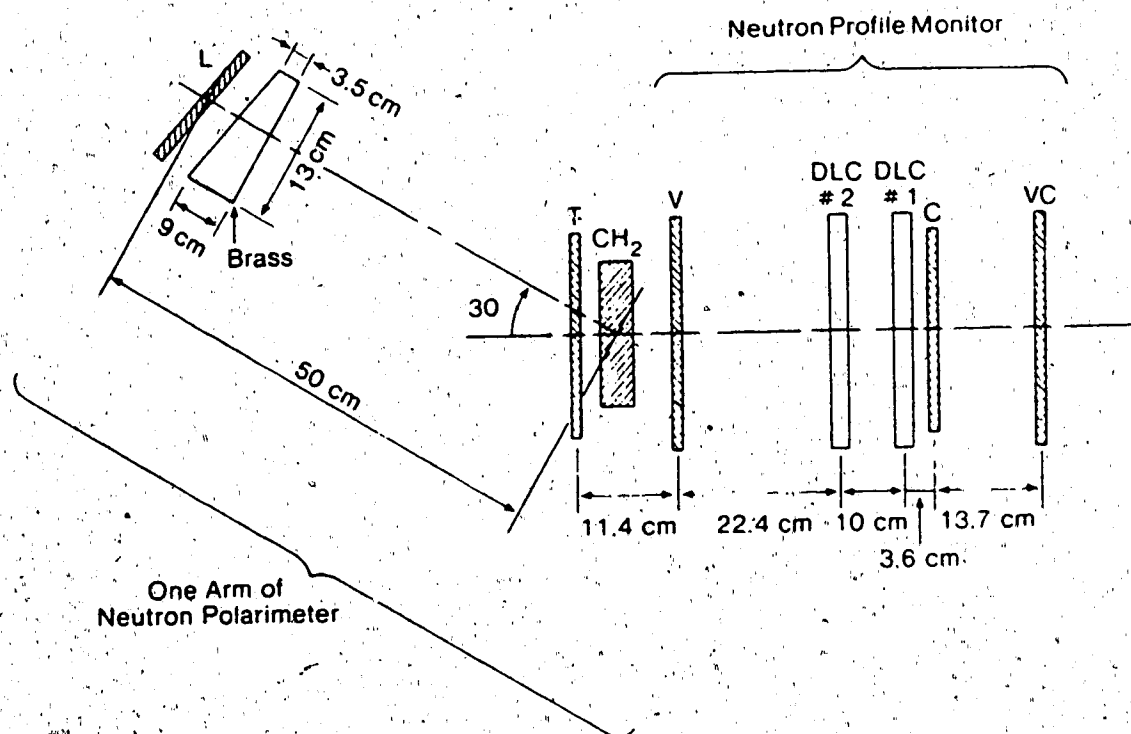


Figure (3.7.1) Schematic Diagram of Neutron Polarimeter / Profile Monitor

### 3.8 The Frozen Spin Target

#### 3.8.1 Introduction and Operation

A 'frozen spin type' (FST) polarizable proton target was built specifically for the experiment<sup>(37, 38)</sup>. This type of target allows a lower magnetic holding field to maintain target polarization. The target material is held at a very low temperature to 'freeze' the polarization in place. Typical polarizations of 0.8 with decay times of 30 days were attained in a magnetic holding field of 2.57 kG. A schematic diagram of the target and the support structure is shown in figure (3.8.1). The target cell was a 4.0 cm diameter, 4.5 cm high cylinder located 12.55 cm from the LD<sub>2</sub> neutron production target.

In a magnetic field the four-fold energy degeneracy of the electron-proton system disassociates into four distinct substates depending on the direction of the electron and proton spins. The polarization process is explained in figure (3.8.2).

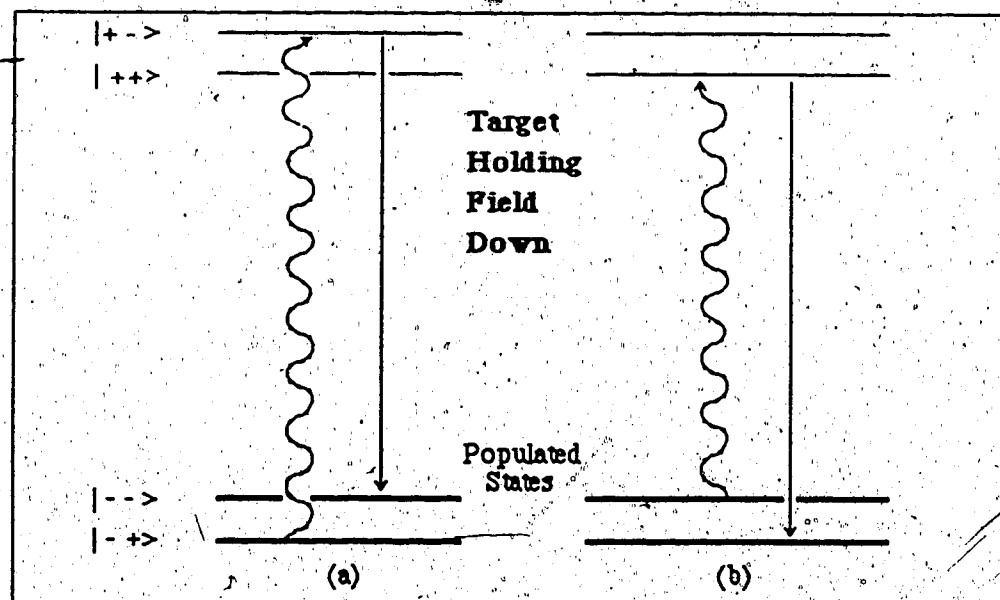


Figure (3.8.2) Target Polarization Process

Only the state with the electron magnetic moment aligned with the magnetic field is populated. Compared to the electron magnetic moment, the proton magnetic moment is smaller by the ratio of the electron to proton mass; therefore, its direction is not as significant. In (a), microwaves induce a double spin flip transition from  $|+->$  to  $|+->$ . The electron spin quickly reverts to its energetically favourable state but leaves the proton in its microwave induced state. The result is a net polarization. Note that the target polarization does not depend on the polarizing field direction.

# FROZEN SPIN TARGET ASSEMBLY

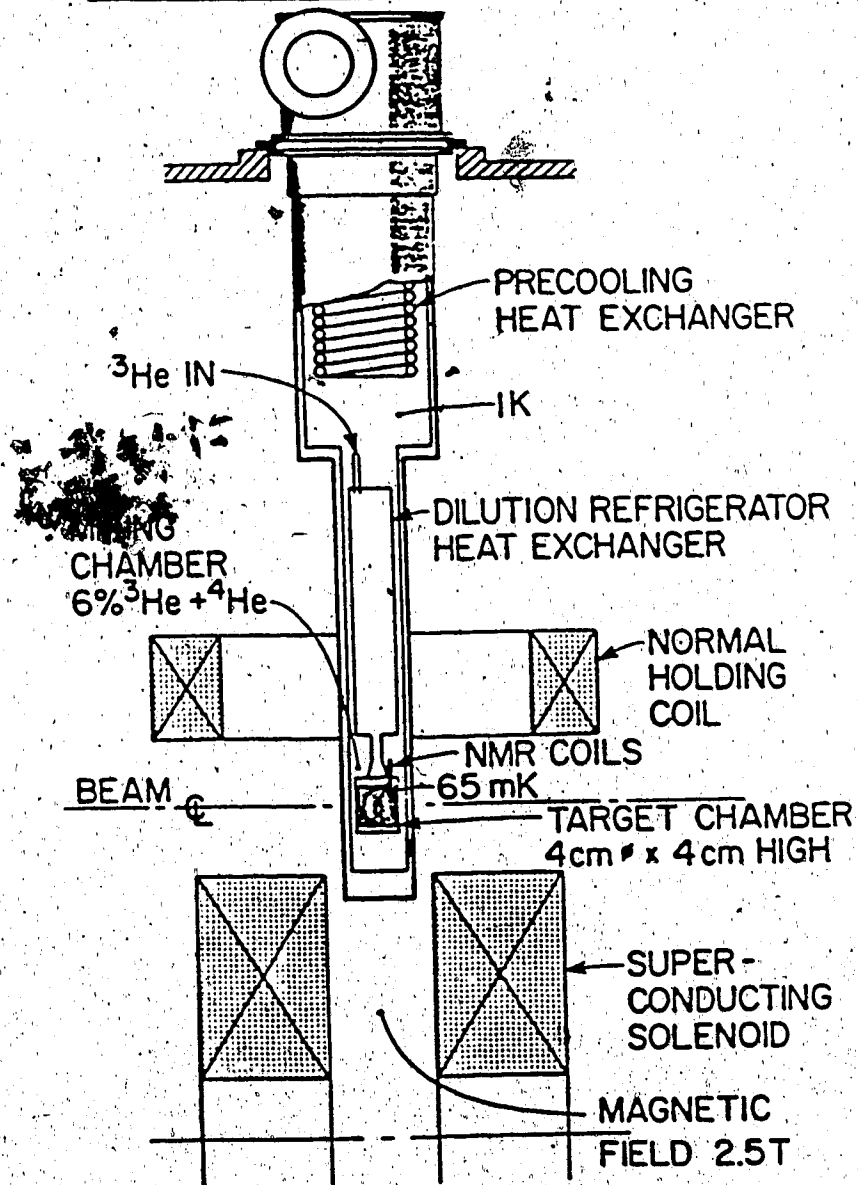


Figure (3.8.1) Schematic Diagram of Frozen Spin Type Target



Gross features of the energy level diagram are determined by the direction of the electron spin. Finer features are caused by the interaction of the proton spin with the external magnetic field and interactions between the proton and electron magnetic moments. Double spin flips are generally forbidden in the absence of an externally applied magnetic field. In the presence of a polarizing magnetic field, electron-proton spin states mix together in a manner which allows otherwise forbidden double spin flip transitions to occur. Microwave radiation can be applied to drive the double spin flip transitions. Electrons quickly revert to the lower energy state with their spin direction aligned parallel to the polarizing field direction, but protons maintain their new direction for a much longer period due to their smaller magnetic moment. The result is a net polarization. Note that the direction of the target polarizing field did not dictate the direction of the proton polarization.

Throughout the polarization process, the temperature had to remain very low. If thermal excitations, on the order of  $k_B T$ , exceeded the energy difference between any two neighbouring spin states, these spin states would become hopelessly mixed thereby ruining the polarization process. This process can be controlled with two possible mechanisms. The external magnetic holding field can be raised to such a value that the energy difference between neighbouring states is much larger than  $k_B T$ , or the temperature can be lowered. For the experiment for which the target apparatus was designed, it was important for the target holding field to be as low as possible.

Electron spin reversals drove the proton polarization process. The efficacy of the polarization depended on the distance between free electrons and protons, or equivalently, the number of free electrons in the target sample. A large concentration of free electrons was supplied by 'doping' the target material with an electron donor material. The relationship between the polarization decay time, temperature and holding field strength is given by

$$\lambda_p \approx \text{Constant} \times H^2 T^{-4} \quad (3.8.1)$$

The constant of the above relation is proportional to the inverse of the doping agent concentration. Temperatures during the operation of the polarized target remained below  $\approx 70$  mK, otherwise thermal excitations would have quickly destroyed any polarization. A high power refrigeration system was needed to cool the  $55 \text{ cm}^3$  target. The target assembly was mounted on a vertical dilution refrigerator with a cooling power of 100 mW at 0.5 K. An NMR coil inserted into the target was used to monitor the target polarization over the course of the experiment.

### 3.8.2 Target Magnetic Holding Field

During data collection a 2.57 kG holding field was maintained with a conventional solenoid above the target and a superconducting solenoid below. The superposition of the two fields provided a vertical field reproducible and stable to  $\pm 5$  G over a three week period. Both the superconducting and conventional magnets were continuously monitored with a pair of Hall probes. A sample plot of the vertical component of the target holding field line integral as a function of distance from the center of the target is illustrated in figure (3.8.3). Table (3.8.1) contains the integrated magnetic field between the center of the target over the extent of the proton detection apparatus (308 cm) for several horizontal planes above and below the neutron-proton scattering plane.

Table (3.8.1) Integrated Target Holding Field

Vertical Position (cm)	$\int B_y \cdot dz$ (kG-cm)	
	Holding Field Down	Holding Field Up
+2.54	-42.213	39.737
+1.27	-41.520	39.080
0.0	-41.178	38.698
-1.27	-41.138	38.829
-2.54	-41.512	39.094

The cyclotron fringe field contributed 5.0 G at the target center. Over the length of the proton detection apparatus the integrated cyclotron field was

$$\int B_{\text{fringe}} \cdot dl = -1.24 \text{ kG-cm} , \quad (3.8.2)$$

or, 3.2% of the target holding field alone. Horizontal field components were measured as  $11.4 \pm 0.8$  G in the central plane of the target. Measurements of  $A_n$  and  $A_p$  were made with the holding field in both vertical directions.

Before polarizing the FST, current to the conventional solenoid was reduced and the superconducting solenoid was raised around the target. Since the polarizing microwave frequency was a function of the magnetic field strength, there were strict requirements of  $10^{-4}$  on the homogeneity of the polarizing field. The superconducting magnet provided a 25

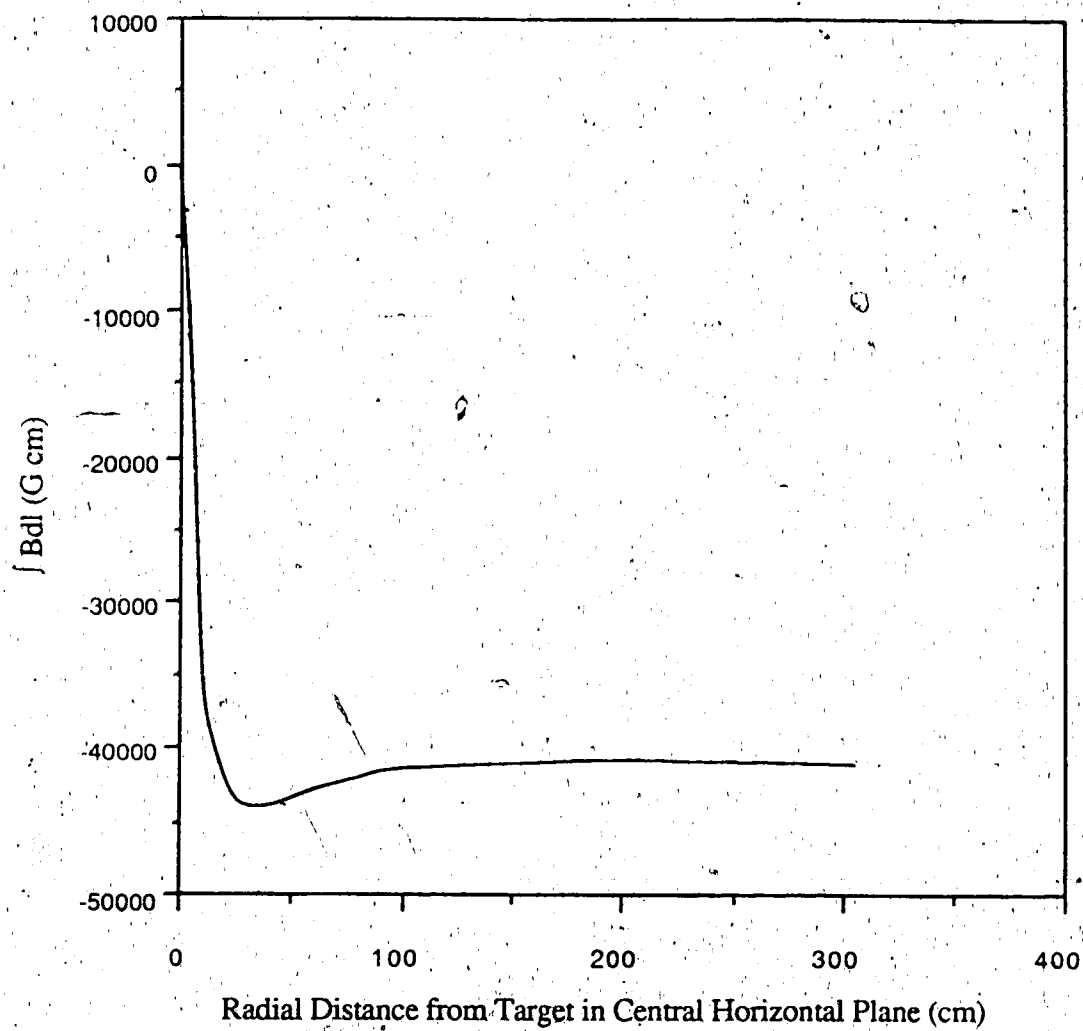


Figure (3.8.3) Integrated Holding Field as a Function of Radial Distance From Target in Central Horizontal Plane.

kG field with a homogeneity of  $\pm 50$  ppm over the volume of the target. The target was depolarized by trickling a small current through a  $10\Omega$  resistor located in the base of the target container to warm the target material. The target itself was never moved during the polarizing or depolarizing processes.

The contribution of the spin precession dipole magnet Bonnie to the horizontal components of the target holding field is illustrated in figure (3.8.4).

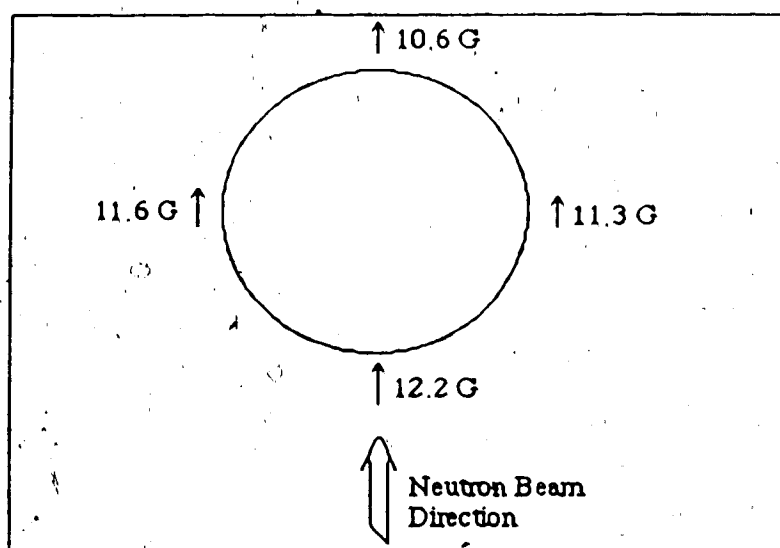


Figure (3.8.4) Contribution of Spin Precession Dipole Bonnie to Horizontal Component of Target Holding Field

The contribution of the spin precession dipole was constant throughout the experiment. The horizontal contribution to the target holding field from the holding field magnets alone was also measured. The results are illustrated in figure (3.8.5). Unlike the contribution from the spin precession dipole Bonnie, horizontal field components from the target holding field magnets reverse sign when the field is reversed.

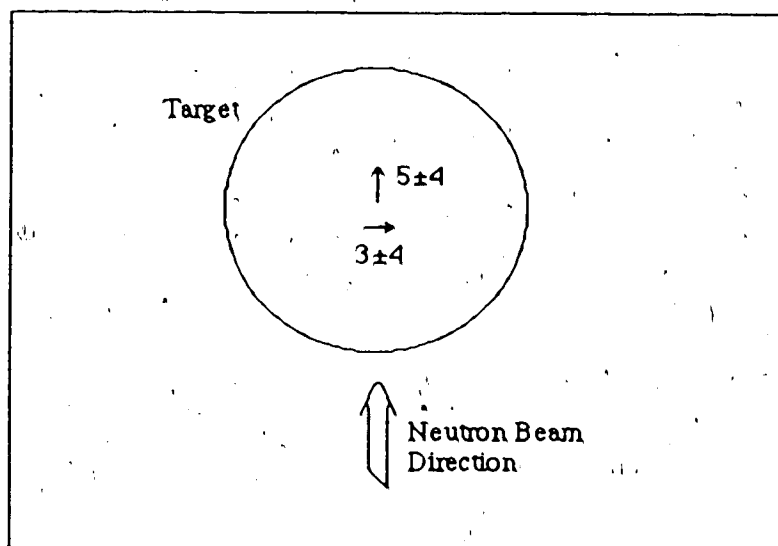


Figure (3.8.5) Target Holding Field Magnets Horizontal Components

Extra insulation was inserted in the room temperature coil during the first experimental run on two occasions: March 1, 1984 and April 9, 1984 as a result of a short-circuit between coils. The change in the magnetic field line integral caused by the insertion of the insulation in the magnet was estimated as  $\leq +0.6\%$ .

### 3.8.3 Target Support Structure

Insulation and support structure in the neutron beam path were kept to an absolute minimum to reduce background and proton multiple scattering. The butanol beads were uniformly illuminated over their entire volume. The target cell had two  $50 \text{ cm}^3$  vacuum spaces above and below the target material to keep as much material out of tails of the neutron beam flux. The outer vacuum shell was outside the main neutron flux. A  $10\text{-}\Omega$  carbon resistor and an NMR probe were located in the bottom of the target cannister. A list of the target material and the support structure around the target is tabulated in table (3.8.3).

Table 3.8.3 Target Materials in the Neutron Beam Path

Material Description	Distance from Target (cm)	Thickness (cm)	
Butanol	0.0	2.0	Target material $\approx 0.60$ packing fraction
He	0.0	2.0	Refrigerant fluid $\approx 0.40$ packing fraction
Copper	2.0	0.005	Microwave cavity
Teflon	2.0	0.013	Teflon Sleeve
Stainless Steel	2.2	0.038	Inner Vacuum shell
Kapton	2.4	0.001	Insulation
Copper	2.5	0.013	Inner heat shield
Kapton	2.5	0.003	Insulation
Aluminum	2.8	0.013	Middle heat shield
Kapton	3.4	0.013	Insulation
Aluminum	3.4	0.013	Outer Heat Shield
Aluminum	4.0	0.102	Outer Vacuum shell

All materials listed in table (3.8.2) are arranged in a concentric geometry around the target center.

The position and volume of the target material within the target were recorded with X-ray photographs. X-rays were taken of the target after data taking was completed for the first data taking run, and before and after data taking for the other data and background runs.

### 3.9 Proton Detection Apparatus

#### 3.9.1 Proton Boom

Proton detection assemblies were mounted on rigid booms and bolted to the floor at  $\pm 52^\circ$  to the left and right side of the neutron beam axis<sup>(39)</sup>. A diagram of the experimental apparatus layout is illustrated in figure (3.9.1). The two booms were mirror images of each other with respect to the neutron beam axis. All discussion will refer to both. Each boom held four delay line chambers<sup>(40)</sup> (DLC) to record horizontal and vertical proton track coordinates for proton track reconstruction, time-of flight (TOF) apparatus for energy determination, and a range counter assembly to isolate neutron-proton elastic events from high and low energy background.

The TOF assembly consisted of a thin scintillator (pTOF-start counter) located near the FST target and a large 67.0 cm by 67.0 cm scintillator sheet (E-counter) situated 3.4 m from the target. The proton TOF assembly did not view the front and back walls of the outer target chamber. The proton energy was determined from the proton TOF between the pTOF-start counter and E-counter. Individual phototubes viewed the top and bottom of the pTOF-start counter. The E-counter was viewed with a total of four phototubes; two were located at the top and two more at the E-counter base. In each case, individual phototube signals were fed into time to digital converters (TDCs) from constant fraction discriminators (CFDs) and the TOF was determined from the average. A schematic diagram of the proton boom electronics is illustrated in figure (3.9.2).

A wedge-shaped absorber (wedge) was positioned just upstream of the E-counter, with the thick edge positioned at the small angle side, to absorb low energy background and to reduce elastically scattered protons to an energy independent of their scattering angle. Downstream of the E-counter, a 6.4 mm thick brass absorber was positioned designed to absorb elastically scattered protons. A final scintillator sheet (veto-counter) was located downstream of the absorber to discriminate against high energy background.

A 'pattern counter' was inserted in each proton boom to provide precision in DLC calibration. The pattern counter consisted of seven 30.0 mm diameter and 3.2 mm thick scintillator disks imbedded in a lucite sheet of the same thickness. DLC positions of protons passing through the scintillator disks provided a convenient coordinate reference system. On occasion, a DLC had to be dismantled for maintenance. Repositioning DLCs required an accuracy of  $\pm 0.35$  mm. Detecting passing charged particles in the pattern counter allowed an absolute DLC position determination to 0.3 mm over a data-taking period of 6 h.

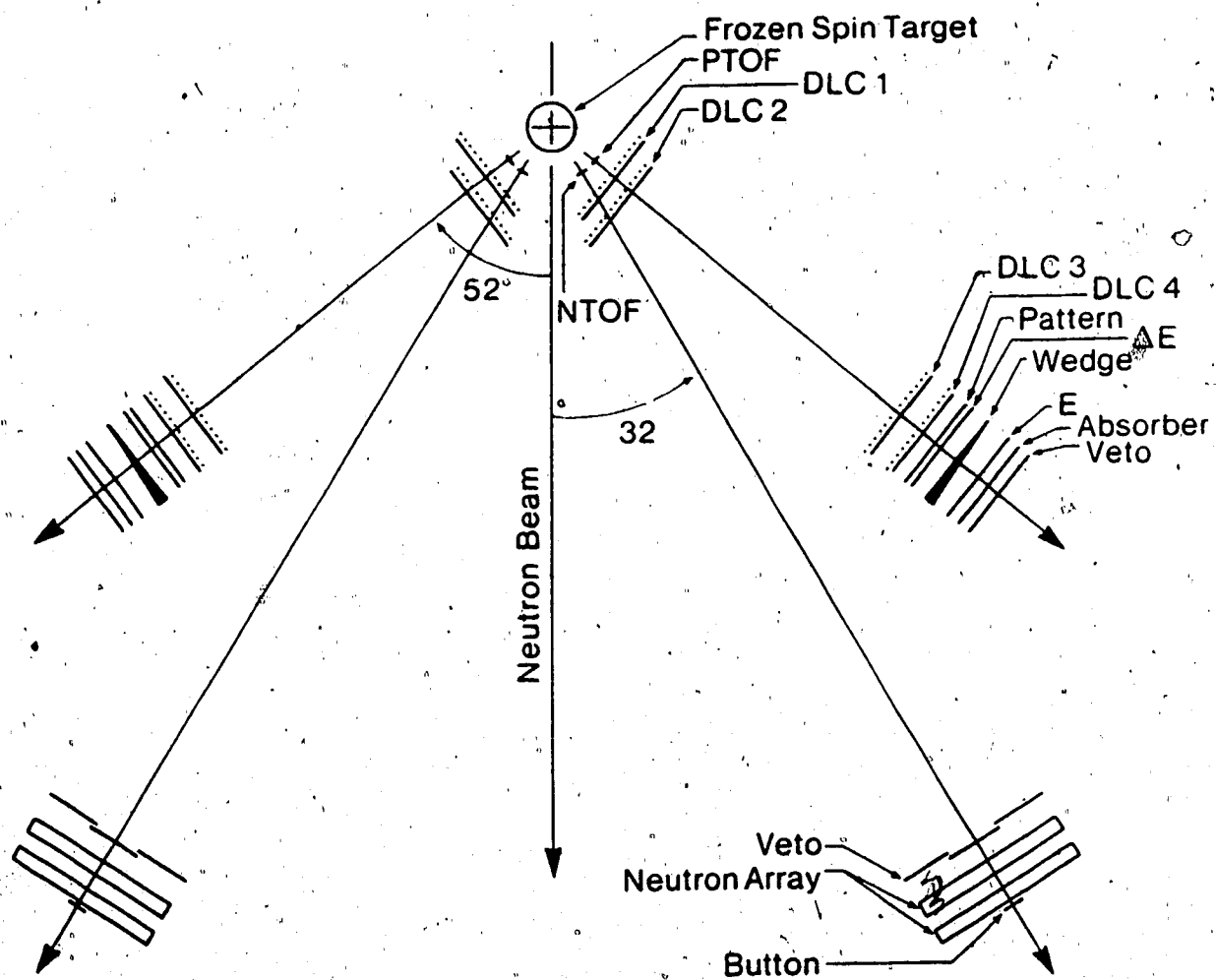


Figure (3.9.1) Detection Equipment



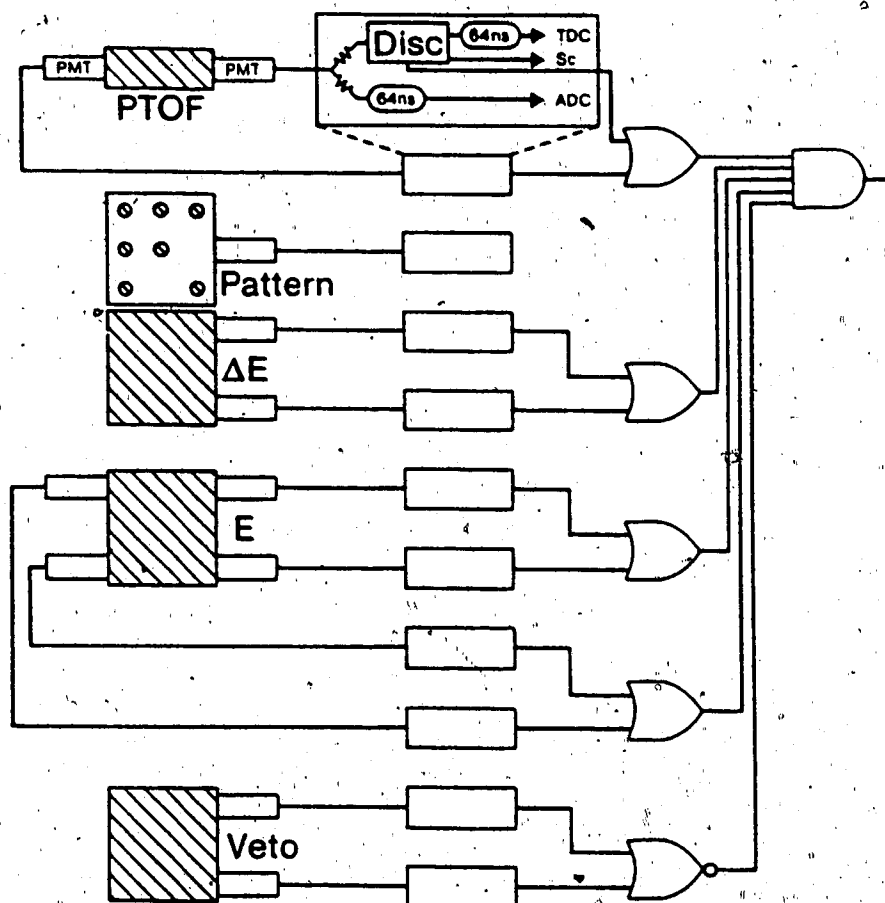


Figure (3.9.2) Proton Boom Electronics

The expanded box illustrates how the Scaler, ADC, and TDC values are taken from the photomultiplier.

Details of apparatus along the proton boom are listed in table (3.9.1).

**Table (3.9.1) Positions of Proton Detection Apparatus Along Boom**

Item	Distance (mm)		Thickness(mm)		Dimensions (cm)	
	Left	Right	Left	Right	Horizontal	Vertical
Time-of-Flight Start	340	335	0.8	0.8	14.0	14.0
DLC 1	517	518			67.0	67.0
DLC 2	679	678			67.0	67.0
DLC 3	2833	3003			67.0	67.0
DLC 4	2997	3003			67.0	67.0
Pattern Counter	3111	3114	3.2	3.2	67.0	67.0
$\Delta E$ -counter	3137	3139	6.4	6.4	67.0	67.0
Wedge			16.3 <sup>†</sup>	15.7 <sup>†</sup>	69.0	69.0
E-counter	3444	3444	6.4	6.4	67.0	67.0
Absorber					67.0	67.0
Veto	3598	3595	6.4	6.4	67.0	67.0

<sup>†</sup> Absorber wedge thicknesses were measured at center. Thickness changed with horizontal position by 0.046 mm/mm.

All distances are relative to the distance from the center of the FST target to the center plane of the listed item. Left and right are defined as the direction of the scattered neutron if the observer faces downstream. DLC 2 of table (3.9.1) was offset 75 mm to keep its frame out of the 10° angular bite subtended by the neutron detection apparatus.

### 3.9.2 Delay Line Chambers

The kinematic acceptance of elastically scattered neutron - proton pairs was determined by the DLC furthest from the target on each proton boom. Each of the DLCs measured 67 cm by 67 cm in the horizontal and vertical directions with an active area of 58 cm by 58 cm. They were composed of an anode plane sandwiched between two cathode planes. Anode planes were composed of 291 vertical 20  $\mu$ m gold plated tungsten wires separated by 2.0 mm at a +4550 V potential. Cathode planes were constructed of many 3.5 mm wide, 20  $\mu$ m thick copper strips separated by 0.5 mm on mylar backing. The cathode strips extended horizontally on one cathode plane and vertically on the other. The materials which a recoil proton must pass through are listed in table (3.9.2)<sup>(41)</sup>.

Table 3.9.2 DLC Construction

Material	Thickness	Thickness (mg/cm <sup>2</sup> )
Aluminized mylar	25 $\mu$ m	3.3
Magic Gas	14-20 mm	3.4
Mylar	25 $\mu$ m	3.3
Copper Cathode Strip	20 $\mu$ m	18.0
Magic Gas	6 mm	1.2
Tungsten Anode Wire	20 $\mu$ m	38.0
Magic Gas	6 mm	1.2
Copper Cathode Strip	20 $\mu$ m	18.0
Mylar	25 $\mu$ m	3.3
Magic Gas	14-20 mm	3.4
Aluminized mylar	25 $\mu$ m	3.3

The thickness of the magic gas is listed as 14-20 mm because of bulging in the DLC centre. Note that in the above table that the cathode copper strips cover 80% of the active area and the anode wires only 1%. Efficiencies of each chamber coordinate were typically >98%.

Magic gas<sup>(42)</sup> (an admixture of 30% isobutane, 30% a mixture of 1% freon in argon, and 40% a mixture of argon bubbled through methylal) was continuously fed in at rate of 100 cc / min into each of the chambers with a pressure to match the electrostatic attraction between the anode and cathode planes to keep a constant 6 mm spacing between the two.

A simplified schematic diagram of the DLC electronics is illustrated in figure (3.9.3).

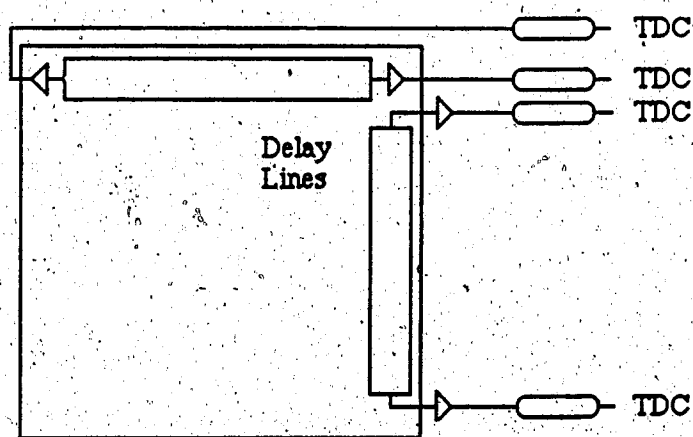


Figure (3.9.3) DLC electronics. A amplifier-discriminator circuit is attached at each end of the delay line.

The cathode strips passed through the gas seal and were capacitively coupled to the delay line. Delay lines mounted on the vertical and horizontal frames of the chamber were of the Perez-Mendez type<sup>(44, 45)</sup>. Delay line propagation speed was approximately 28 ns/cm. A discriminator board was mounted at each end of the delay line. The time interval between detection of the propagated signals at either end of the delay line was related to the position where the signal was induced along the delay line; therefore, position information was taken from time difference, or TDIF, spectra.

No interpolation can be made between adjacent anode wires, nor can the side of the anode wire where a proton passed be distinguished. DLC resolution, in the horizontal plane, was restricted to the anode wire spacing, 2 mm. Individual anode wires were easily distinguished in horizontal TDIF spectra as sharp peaks. These anode wire peaks formed a 'picket fence' signature. A portion of a typical 'picket fence' spectrum is illustrated in figure (3.9.4).

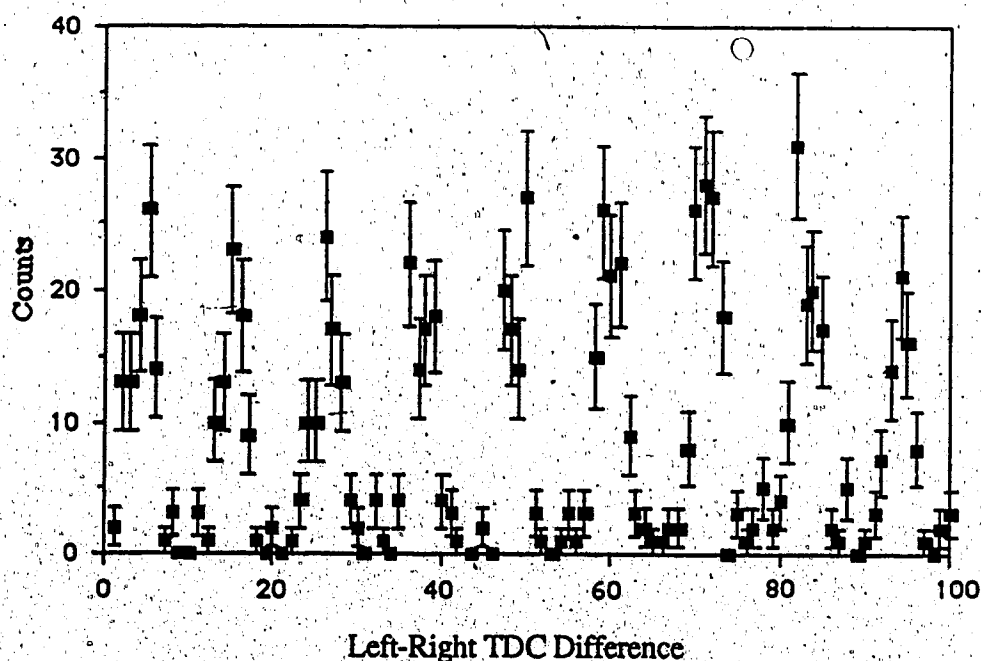


Figure (3.9.4) Raw TDC Differences Between Left and Right Ends of Horizontal Delay Line Illustrating 'Picket Fence' Structure Due to Vertically Running Anode Wires.

Individual peaks can be associated on a one-to-one correspondence with anode wires. A calibration table was constructed relating time delay to absolute position. Calibrations were not as easily made

in the vertical dimension where no such 'picket fence' spectra existed (the wires run vertically so that horizontal spectra are discrete but the vertical are continuous). DLCs were calibrated by placing each group of four as close together and as far as possible from the target so that the entire active area of each was illuminated. The first and third chambers were rotated by  $90^\circ$  so that their vertical, now horizontal, coordinate could be calibrated against the picket fence spectra of the second and fourth chambers and vice versa for the second and fourth chambers. This calibration process revealed non-linearities in the delay line behaviour. An example is illustrated in figure (3.9.5). How such nonlinearities were handled in the analysis is discussed in detail in the following chapter.

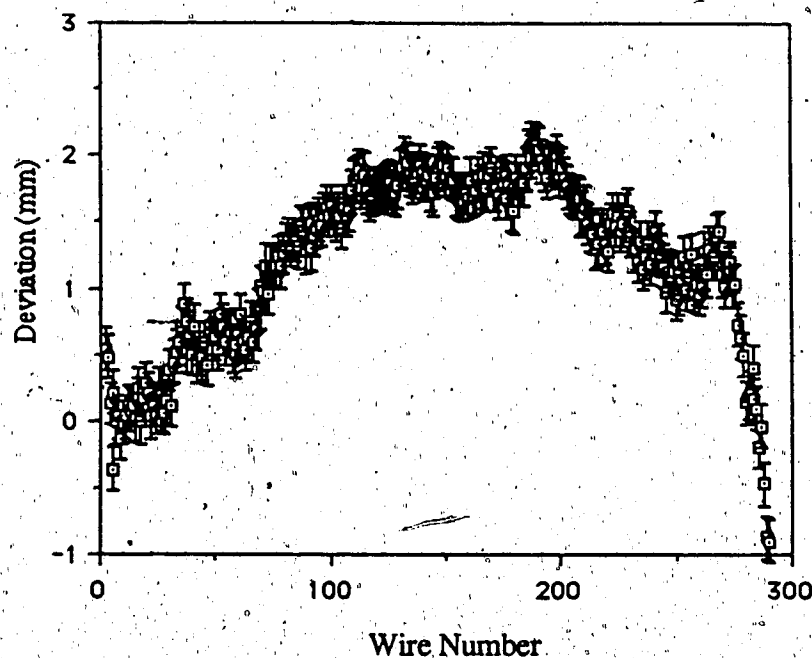


Figure (3.9.5) Delay Line Nonlinearity. The plot illustrates the difference between the actual wire position and the wire position as calculated if a constant signal wire propagation speed is used.

Each chamber contained 4 BNC inputs for pulser signals to be fed in near both ends of each delay line, with a separation of  $552.5 \pm 0.7$  mm. These pulses were fed in directly to 1.6 mm thick copper strips which were capacitively coupled to the cathode plane. The positions of pulser DLC events were used to monitor and correct for small drifts in the delay line timing over the course of the experiment.

### 3.10 Neutron Detection and Calibration Apparatus

#### 3.10.1 Neutron Detection Telescope

Each neutron detection assembly was centered at  $\pm 32^\circ$  relative to the neutron beam symmetry axis and subtended  $11.5^\circ$ . Scattered neutrons were detected in a large scintillator array. Preceding the scintillator array was a veto counter to discriminate against charged particles. The veto-counter was comprised of three overlapping rectangular scintillator sheets. Neutron TOF was determined as the difference between the detection time of events in the neutron scintillator array and the reconstructed time of the neutron-proton scattering vertex from information taken from the proton detection system. A schematic diagram of the neutron boom electronics is illustrated in figure (3.10.1). Included in the neutron detection system were apparatus designed to continuously calibrate scintillator photomultipliers.

The positions of the scintillator arrays relative to other experimental apparatus is illustrated in figure (3.9.1). Details of the neutron scintillator array are listed in table (3.10.1).

Table (3.10.1) Neutron Detection Apparatus

Scintillator	Distance (mm)		Thickness (mm)	Dimensions (mm)	
	left	Right		Horizontal	Vertical
Neutron TOF Start	326	320	0.8	14.	14.
Veto	5064	5080	6.4	1050. <sup>†</sup>	1050. <sup>†</sup>
Front Bank	5225	5225	150.0	1050.	1050.
Back Bank	5415	5426	150.0	1050.	1050.
Button	5540	5559	7.0	70.	

<sup>†</sup> Constructed with three overlapping scintillator sheets

All distances in table (3.10.1) are from the center of the FST to the center of the listed item. Using the established convention, left and right refer to the scattered neutron direction if the observer is looking downstream.

#### 3.10.2 Neutron Scintillator Array

Scattered neutrons were detected in two large 1.05 m wide, 1.05 m high and 0.30 m

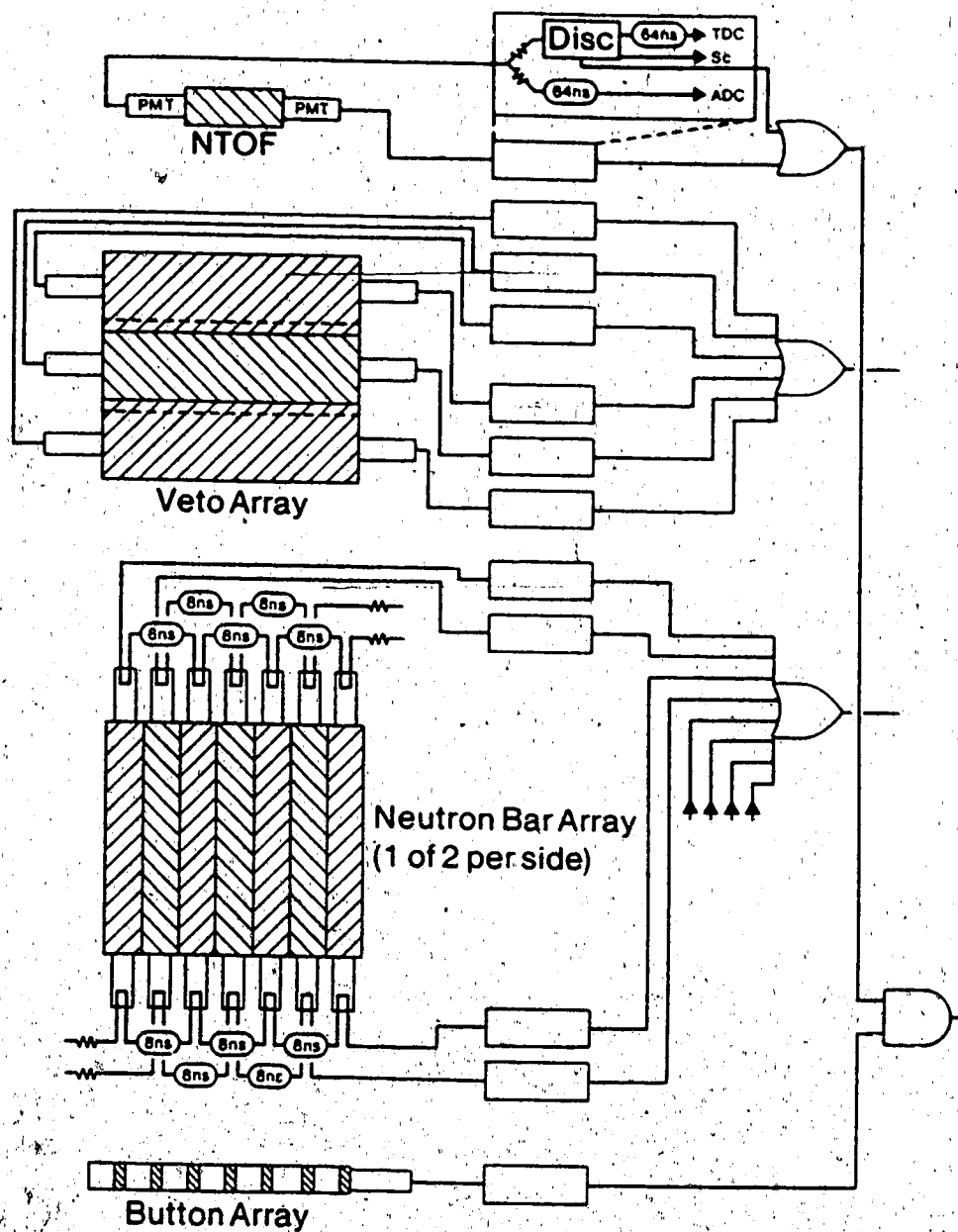


Figure (3.10.1) Neutron Boom Electronics

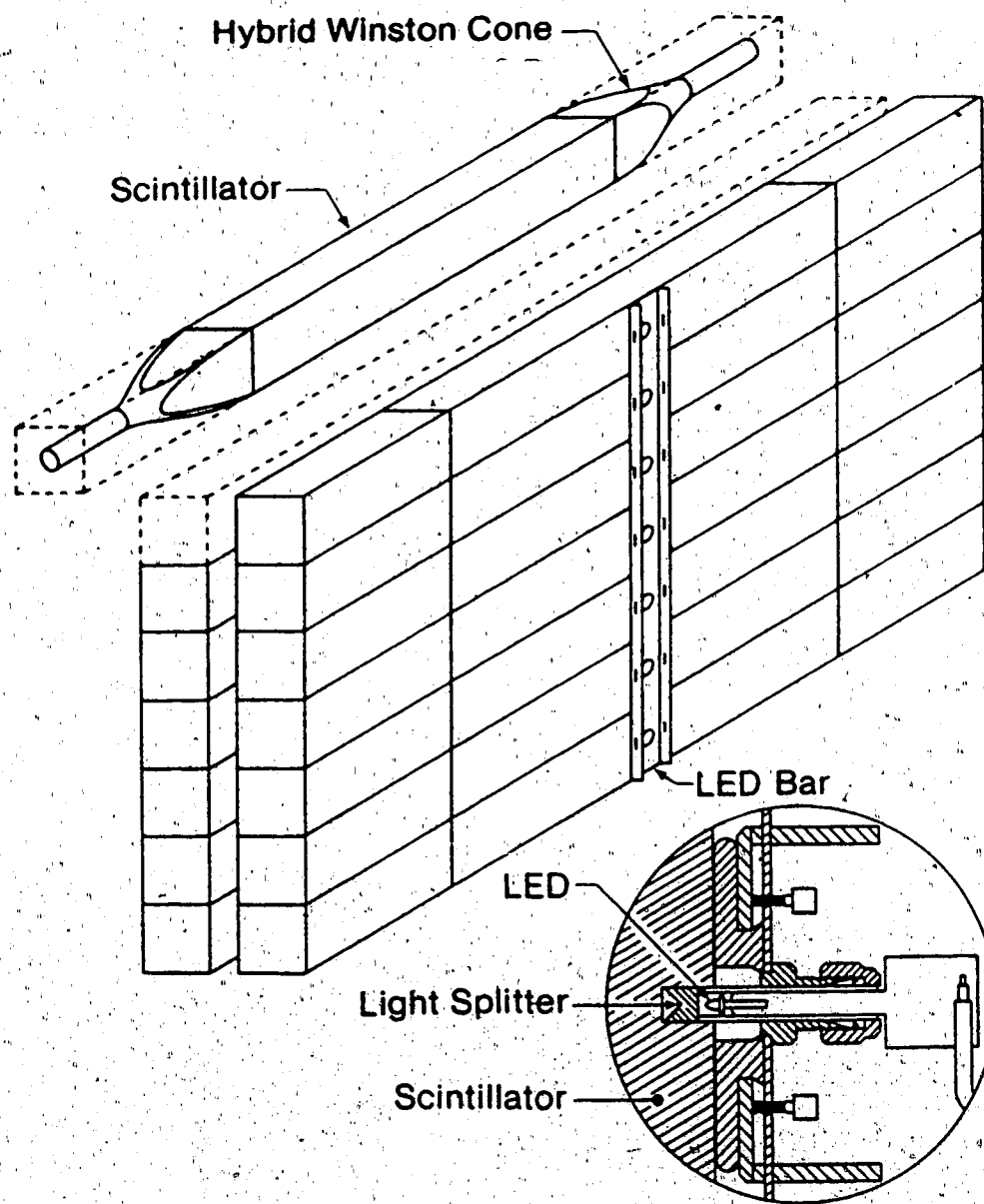


Figure (3.10.2) Schematic Diagram of Neutron Scintillator Array



thick NE110 scintillator arrays. The two arrays were identical to one another; all discussion refers to both. A schematic drawing of a scintillator array is illustrated in figure (3.10.2). Each array was constructed of two stacks of seven 1.05 m wide, 0.15 m deep and 0.15 m high scintillator bars. Both ends of each scintillator bar were fitted with a modified Winston cone light collector and photomultiplier designed to accept light reflected from scintillator bar inside surfaces at angles less than  $\approx 15^\circ$ . Delay lines connected groups of four and three nonadjacent bars in the front and back stacks, as in figure (3.10.1), to reduce otherwise prohibitive electronic costs associated with separate electronic systems for each of the fifty-six neutron bars. Signals from the neutron array delay lines were fed into a CFD - TDC combination to provide neutron position and TOF information.

### 3.10.3 Neutron Position Determination

Identification of struck scintillator bars and the event horizontal coordinate were made from the timing difference (TDIF) between the left and right side delay line signals. Double hits within bars daisy-chained on the same delay line were identified by the time sum (TSUM) of the left and right delay line signals. Vertical coordinates were taken as the vertical center of the neutron bar, thereby limiting the vertical resolution to  $\pm 7.5$  cm.

### 3.10.4 Neutron Time-of-Flight and Position Calibration

Seven small 'button' scintillator counters were located at the downstream side of each scintillator array (see figure 3.10.1). Protons passing through the scintillator array and a 'button' counter were used to continuously calibrate photomultipliers attached to the scintillator bars. For the sake of brevity, such protons are termed 'button' events in the remainder of the text. Elastically scattered protons striking button scintillators deposited 54.6 MeV (62.3 MeV) in the front (back) scintillator bars releasing a constant amount of light against which the photomultipliers were calibrated. Each photomultiplier button event analog to digital converter (ADC) signal was monitored after every two hour period of data taking throughout the experiment. Drifts in the magnitude of phototube ADC signals were corrected for by adjusting the high voltage to individual phototubes. Photomultiplier high voltages were controlled by a terminal located outside the experimental area. Individual phototube ADC signals were allowed to drift within  $\pm 10\%$  of their nominal value before voltage corrections were applied. Such small changes could be easily corrected for during

the analysis by scaling the ADC signals by the button event ADC values, but larger drifts were not permitted for fear that changes in absolute detection efficiency might ensue.

Drifts in the timing characteristics of individual phototubes were corrected by observing the difference between the actual and apparent button proton event position. Timing corrections were added to the raw neutron bar delay line TDIF to force the difference to equal zero.

Light pulses were injected into the back of each neutron array with light emitting diodes (LEDs) attached to the back side array (see figure 3.10.1). The LEDs were designed to detect any timing drifts in the neutron scintillator array phototubes influencing position measurements. In fact, it was discovered that the apparent positions of the button events allowed a more accurate monitor of phototube timing drifts than the light pulsers.

### 3.10.5 Neutron Scintillator Array Illumination

The geometric detection limit of elastically scattered neutron-proton pairs was defined by the DLC furthest from the FST target. The  $11.5^\circ$  angular bite subtended by the neutron detector was sufficient to detect elastically scattered neutrons coincident with protons detected in the proton detection assembly regardless of the holding field configuration. The extent of the illuminated area of the neutron scintillator array is illustrated in figure (3.10.3). The effects of multiple scattering have not been included in the illustration. Multiple scattering smeared the edges of the illuminated area by approximately  $0.8^\circ$  or equivalently, 7 cm. The target holding field deflected elastically scattered recoil protons by approximately  $\pm 1.2^\circ$  thereby shifting the illuminated portion of the neutron array 1.1 cm to the left or right, depending on the holding field direction and to which direction the neutron scattered. The left and right edges of the neutron array were never fully illuminated. Only a very small fraction of the top and bottom neutron scintillator bars were illuminated.

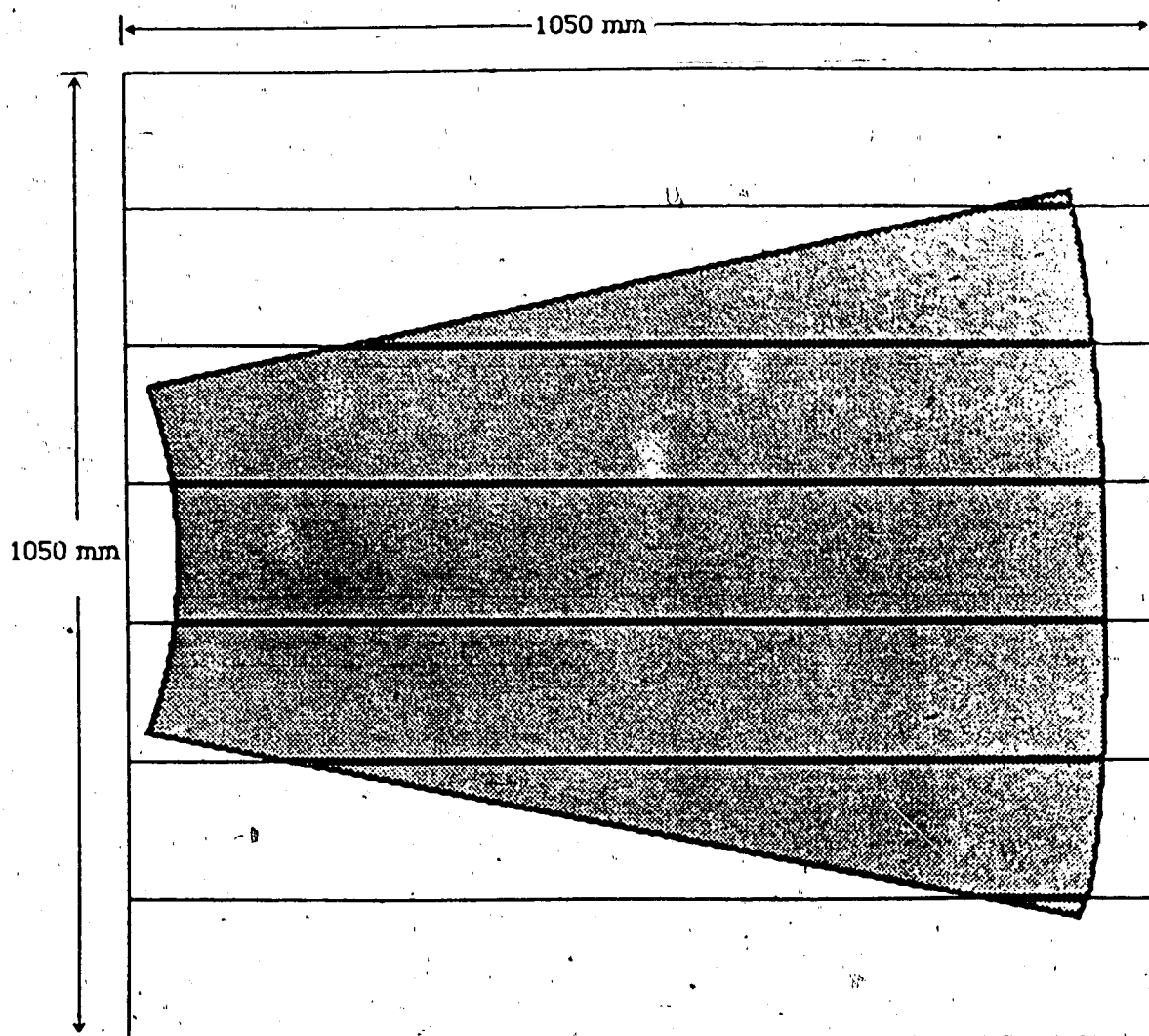


**Figure (3.10.3) Neutron Scintillator Array Illumination**

The DLC furthest from the FST target defined the kinematic acceptance of the experimental apparatus. Only a very small portion of the top and bottom bars were illuminated by neutron-proton elastic events. The illuminated area shifted to the left or right by  $\sim 1.2^\circ$  (11 cm) when the target holding field was applied. The edges of the illuminated area were smeared by  $0.8^\circ$  (7 cm) by proton coulomb multiple scattering in the target material.

### 3.11 Trigger Logic

The trigger system used in the experiment is illustrated in figure (3.11.1).

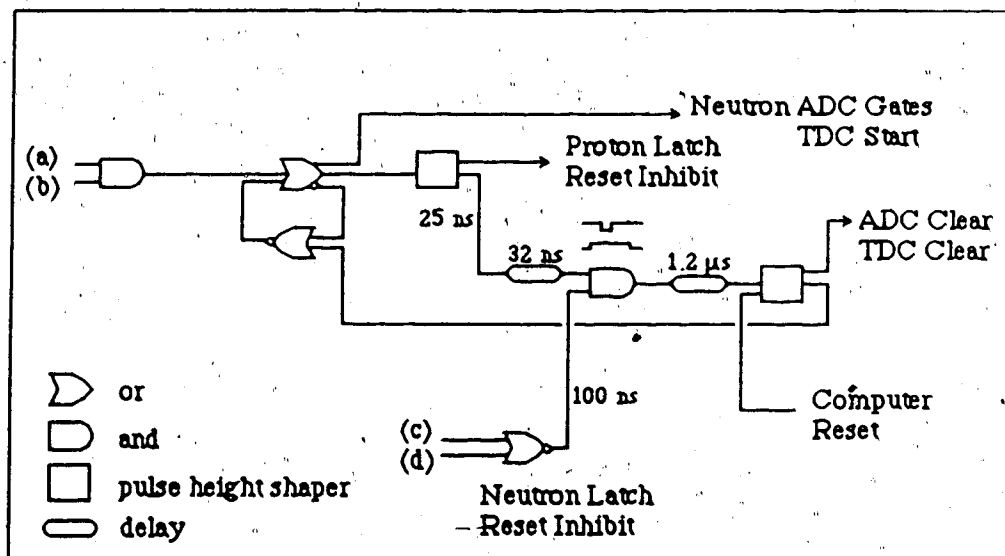


Figure (3.11.1) Experimental Trigger Logic.

The neutron trigger is shown here. The latch is set by a (a) neutron detected in the scintillator array and (b) no veto signal. The neutron TDCs are started and the ADC gate is strobed. Unless the latch is inhibited by (c) the proton side of the electronics (neutron latch reset inhibit) or by (d) a button event, the latch releases itself and clears the ADCs and TDCs.

A successful neutron latch trigger requires the neutron scintillator array to fire, or the nTOF, Veto and button counter to fire simultaneously (signifying a 'button' proton). The neutron latch trigger starts the TDCs and strobes the ADC gates. A signal from the proton latch (the neutron latch reset inhibit in the diagram) must arrive within 100 ns of the neutron latch trigger otherwise the latch is freed and 1.2  $\mu$ s later the latch returns to its waiting state. Once the latch is set, the electronics waits until the computer has finished processing the event before the computer reset is triggered, the ADCs and TDCs cleared, the latch freed and returned to its waiting state.

A successful proton latch trigger (the proton latch is not shown here) requires the pTOF counter,  $\Delta E$ -counter, E-counter to fire with no signal from the Veto counter.

### 3.12 Phase Lock System

Timing with respect to the cyclotron radio-frequency (RF) system was sensitive to cyclotron tune dependent phase shifts between the RF and arrival of each proton beam burst. A scintillation detector was inserted in the  $6^\circ$  port of the neutron collimator 5750 mm from the center of the  $\text{LD}_2$  target. The residual field of the proton beam sweep magnet 4AB2 (see figure 3.1.1) and a 44 mm thick brass plug inserted in the  $6^\circ$  port assure that the scintillator detected only neutral particles originating at the  $\text{LD}_2$  target. The beam burst signal was continuously corrected by the time difference between the RF and  $6^\circ$  port signals.

### 3.13 Data Collection

During the experiment, the direction of the proton polarization and holding field were selected on the basis of a four day cycle. The target was polarized each morning for the  $A_n$  measurement and depolarized each evening for the  $A_p$  measurement. A complete cycle covering all permutations of target polarizations, beam polarizations and holding field directions was completed in four days and then repeated. More beam time was allotted to the polarized neutron beam, or  $A_n$ , portion of the experiment since the accuracy of the  $A_n$  ( $A_p$ ) zero-crossing angle measurement depended on the inverse of the beam (target) polarization. The higher target polarizations were not without cost, however, since polarizing the target required a daily four hour period during which data taking had to be suspended.

The experiment was completed over four separate data taking periods, each lasting approximately two weeks, and a four day background measurement. Each of the four data taking periods was subdivided into the number of data tapes required to store the collected data. Each data tape was assigned a run number. A typical run collected data between one and four hours depending on the neutron flux. Discussion of the experimental analysis will frequently refer to measurements made on a run-to-run basis.

Signals from the detection apparatus were fed into fast electronics and interfaced to a Data General Eclipse computer through a CAMAC interface. All data was written to tape at 1600 bpi.

## CHAPTER 4 - ANALYSIS

### 4.1 Introduction

The behaviour of the experimental apparatus was monitored throughout by on-line checks and a more detailed analysis was made later during the off-line analysis. The analysis consisted of four parts: determining good n-p elastic events, isolating possible sources of systematic errors, measuring the percentage of background data and its contribution to the asymmetry, and the calculation of asymmetry zero-crossing angles from the data. The current chapter describes the results of each aspect of the experimental analysis.

Coincident neutron-proton pairs were detected in two pairs of mirror - symmetric neutron and proton detection apparatus. Following the established convention, coincident neutron - proton pairs will be referred to as left or right n-p events, where left or right is defined by which side of the neutron beam the neutron scattered from the point of view of an observer looking downstream (see figure 3.1.2).

### 4.2 Proton Beam Energy

The primary proton beam energy was measured at the proton beam energy monitor (BEM, see section 3.3 and reference 33). The average proton energy was calculated using the relation

$$E_p = \frac{\sum_{i=1}^5 a_i (N_i - N_{i+1})}{\sum_{i=1}^5 (N_i - N_{i+1})} \quad (4.2.1)$$

where  $N_i$  is the number of counts detected in the  $i^{\text{th}}$  BEM scintillator (there were six in total), and  $a_i$  is the average energy (calculated) of a proton whose range extends only as far as the  $i^{\text{th}}$  1mm copper absorber. The BEM had left and right detector arms. The true proton energy was taken as the average of the left and right values to reduce effects associated with lateral movement of the beam on the BEM / polarimeter target.

BEM scalers were read every five minutes and proton beam energies were averaged

over two hour periods. The results for the five runs are summarized below in table (4.2.1). The average difference from the mean is presented as well as the standard deviation of the energy distribution since the distribution of proton energies could not be accurately described by a gaussian distribution. The observed proton beam energies during the first experimental run are illustrated in figure (4.2.1)

**Table (4.2.1) Average Primary Proton Beam Energies**

Run	Average Energy (MeV)	Standard Deviation (MeV)	Average Difference from Energy Mean (MeV)	Range of Deviation from Mean (MeV)	
				Minimum	Maximum
1	497.763	0.072	0.066	497.512±0.083	497.888±0.083
2	498.090	0.133	0.100	497.810±0.070	498.341±0.061
3	497.745	0.081	0.067	497.554±0.070	497.979±0.071
4	497.704	0.106	0.089	497.563±0.061	497.842±0.053
background	497.671	0.067	0.046	497.833±0.044	497.552±0.044

The largest standard deviation of the energy distribution observed during the experiment was 0.133 MeV and the largest observed deviation of a single energy over a two hour period from the mean was 0.280 MeV. The allowable limit of the proton energy distribution standard deviation was calculated as 0.25 MeV (see appendix A on systematic errors). The 0.35 MeV increase in the energy of the second run does not introduce systematic errors if  $\Delta A$  is calculated for each run and averaged over all four. No run was excluded on the basis of an energy far from the nominal mean.

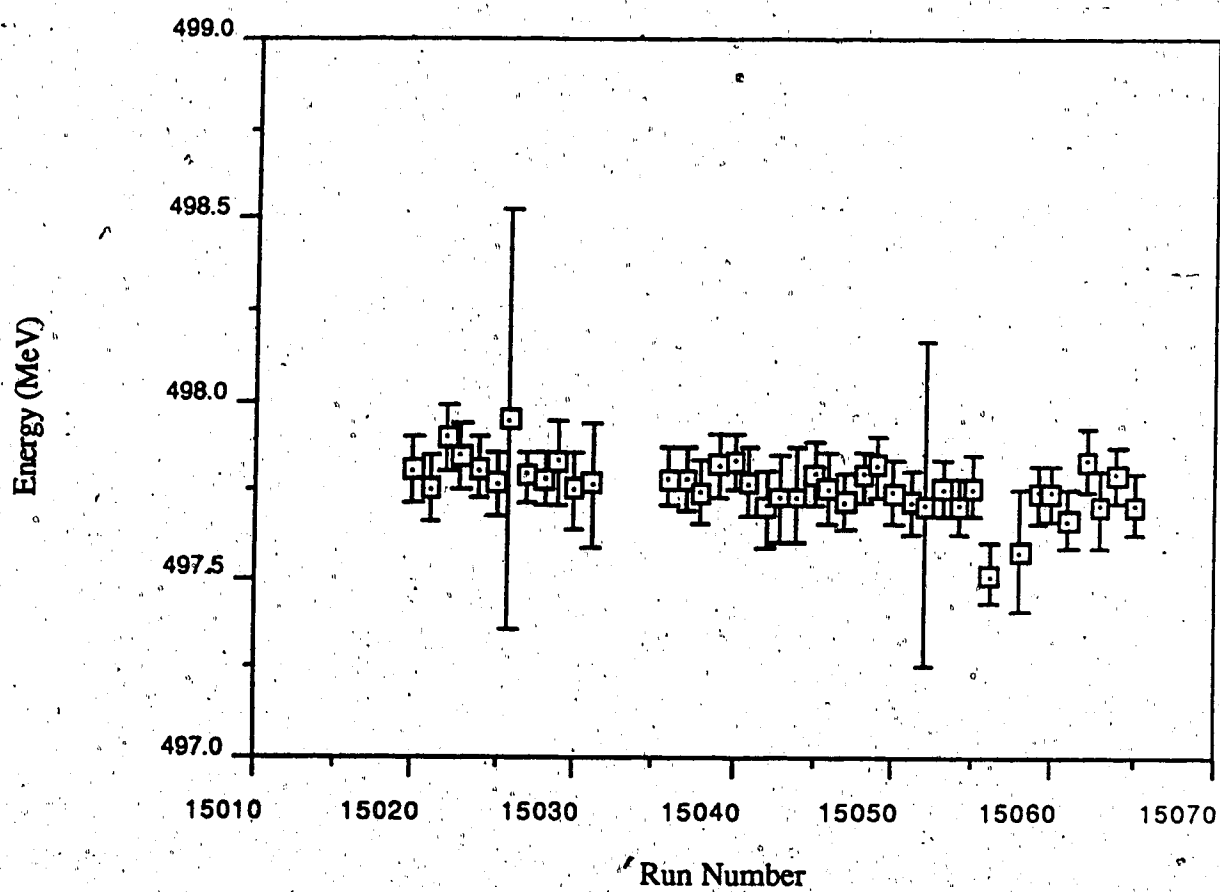


Figure (4.2.1) Proton Beam Energy During the First Data-Taking Run.



### 4.3 Proton Beam Polarization

The primary proton beam polarization was measured in the BEM / polarimeter combination. For particulars of the device, see section (3.3). Raw left-right asymmetries were taken from the polarimeter scalers every five minutes and averaged over every two hour period of data taking. The proton polarization reverted to the unpolarized state for one minute out of every seven to continuously monitor the instrumental asymmetry. Raw left-right asymmetries were corrected for the polarimeter instrumental asymmetry, from non-elastically scattered proton-proton pairs, and from non-hydrogenous contaminants in the target. The observed number of accidentals in each of the left and right detectors was subtracted directly from the number of observed events,

$$L' = L - L^{\text{acc}} \quad , \quad (4.3.1a)$$

$$R' = R - R^{\text{acc}} \quad , \quad (4.3.1b)$$

where, L and R are the observed number of events detected in the left and right sides of the polarimeter apparatus,  $L^{\text{acc}}$  and  $R^{\text{acc}}$  are the number of observed accidentals, and L' and R' are the number of counts after the correction for accidentals has been applied. The raw asymmetry was then calculated as

$$\epsilon_{u,d}^{\text{raw}} = \frac{L_{u,d}' - R_{u,d}'}{L_{u,d}' + R_{u,d}'} \quad (4.3.2)$$

The subscripts 'u' and 'd' represent measurements and corrections made for the positive and negative vertical proton polarization states. The proton polarization flipped between the three states 'up', 'down' and 'off' during the  $A_n$  measurement. The proton instrumental asymmetry was measured while the proton polarization was in the 'off' state. Proton polarizations were corrected by subtracting the measured instrumental asymmetry averaged over the period during which the polarization was measured. The corrected asymmetry is then

$$\epsilon_{u,d}^{\text{m}} = \epsilon_{u,d}^{\text{raw}} - \epsilon_0 \quad (4.3.3)$$

Here,  $\epsilon_0$  is the instrumental asymmetry and  $\epsilon_{u,d}^m$  is the asymmetry after corrections have been applied for accidental counts and instrumental asymmetry. The average proton polarimeter instrumental asymmetry for each of the four data taking runs and the background run are illustrated in table (4.3.3).

**Table (4.3.1) Proton Polarimeter Instrumental Asymmetry**

Run	Instrumental Asymmetry
1	-0.019
2	-0.019
3	-0.012
4	-0.006
background	-0.015

Statistical errors of the instrumental asymmetries are negligible.

The true asymmetry was then calculated as

$$\epsilon_{u,d} = \frac{\epsilon_{u,d}^m - r \epsilon_b}{1 - r} \quad (4.3.4)$$

where  $r$  represents the ratio of (p,2p) events to the total observed, and  $\epsilon_b$  is the background asymmetry. The  $^{12}\text{C}(p,2p)$  background asymmetry was measured as  $\epsilon_b = 0.139 \pm 0.014$  with a  $11.0 \text{ mg/cm}^2$  carbon polarimeter target. The fraction of events originating from  $^{12}\text{C}$ ,  $r$ , was measured by inserting the same carbon target into the polarimeter. The number of  $^{12}\text{C}(p,2p)$  events from a polyethylene target was determined by scaling the number of events observed with the  $^{12}\text{C}$  target in place by the relative amounts of carbon in the two targets, the target thicknesses, and integrated beam current on each of the targets,

$$r_{\text{CH}_2} = \frac{\frac{C}{(L_{\text{net}} + R_{\text{net}})} \frac{\text{CH}_2}{\Delta x} \frac{[X]}{[X]^C} \frac{\text{CH}_2}{N_{\text{SEM}}}}{\frac{\text{CH}_2}{(L_{\text{net}} + R_{\text{net}})} \frac{\text{CH}_2}{\Delta x} \frac{[X]^C}{[X]} \frac{C}{N_{\text{SEM}}}} \quad (4.3.5)$$

Here,  $L_{\text{net}}$  and  $R_{\text{net}}$  represent the number of events detected in the left and right arms of the polarimeter assembly (after accidental subtraction),  $\Delta x$  is the thickness of the polarimeter target,  $[X]$  is the amount of non-hydrogenous materials in the target, and  $N_{\text{SEM}}$  is the number of counts detected in the final SEM located in the primary proton beam downstream of the  $\text{LD}_2$  target (see figure 3.2.1). The superscripts 'C' and ' $\text{CH}_2$ ' denote the carbon and  $\text{CH}_2$  polarimeter targets, respectively. The above expression assumes that the  $^{16}\text{O}(p,2p)$  and  $^{13}\text{N}(p,2p)$  reactions are similar to  $^{16}\text{C}(p,2p)$  quasi-elastic reactions. Table (4.3.2) shows the ratio of the actual to observed asymmetry for the various polarimeter targets used over the course of the experiment.

**Table (4.3.2) Polarimeter Carbon Correction Factors**

Target Material	Chemical Composition	Density (gm/cm <sup>3</sup> )	$\epsilon_f / \epsilon_m$
Kapton	$\text{C}_{22}\text{H}_{10}\text{N}_2\text{O}_5$	1.42	1.025
Polyethylene	$\text{CH}_2$	0.95	1.006
Mylar	$\text{C}_5\text{H}_4\text{O}_2$	1.39	1.015

The carbon correction factors changed the observed asymmetry by less than 3%.

Table (4.3.2) below shows the average proton beam polarizations measured in each of the four data taking and background runs.

**Table (4.3.3) Proton Beam Polarizations**

Run	Proton Beam Polarization	
	Up	Down
1	0.636	-0.664
2	0.644	-0.649
3	0.661	-0.658
4	0.659	-0.664
background	0.660	-0.659

A change in the proton polarization direction required several seconds for transient currents within the polarized ion source to settle into equilibrium. During these moments, the ion source delivered a busy signal to the experimental electronics.

#### 4.4 Proton Beam Intensity

Knowing the solid angle subtended by the polarimeter, the p-p differential cross section and the thickness of the polarimeter target, a proton beam intensity can be calculated. Average proton beam intensities for unpolarized and polarized beam portions calculated in the above manner are listed below in table (4.4.1).

Table (4.4.1) Average Proton Beam Intensities (nA)

Run Number	A <sub>n</sub> Measurement			A <sub>p</sub> Measurement
	Proton Polarization State Up	Down	Off	Proton Polarization State Off
1	304	313	308	789
2	371	424	416	681
3	480	484	460	482
4	447	450	533	538
background	771	732	712	-----

#### 4.5 Proton Beam Spatial Stability

Asymmetries measured by the secondary emission monitors<sup>(31, 32)</sup> (SEMs), beamline elements 4AM4.4 and 4AM4.7 illustrated in figure (3.2.1), were used to continuously adjust beamline correction magnets to ensure a stable proton beam position on the neutron production target. Typical proton beam left / right and up / down positional asymmetries are illustrated in figure (4.5.1). Widths of the SEM asymmetry distributions were directly correlated to the stability of the proton beam position. Given that the SEMs each contained a 1 mm spacing between two semi-circular plates, and the proton beam spot was measured with a 4.1 mm horizontal and a 5.5 mm vertical FWHM (see section 3.2) the magnitude of the motion of the proton beam on each SEM can be estimated. The asymmetries correspond to a beam width of  $\sigma_x = 0.06$  mm and  $\sigma_y = 0.05$  mm at the first SEM location and  $\sigma_x = 0.12$  mm and  $\sigma_y = 0.05$  mm at the SEM following the spin precession solenoid, Janus. There were no significant differences in the SEM asymmetries for different proton beam polarization states.

The worst case uncertainty of the proton position and incident angle on the LD<sub>2</sub> target can be estimated by linearly extrapolating the beam position from the SEMs to the

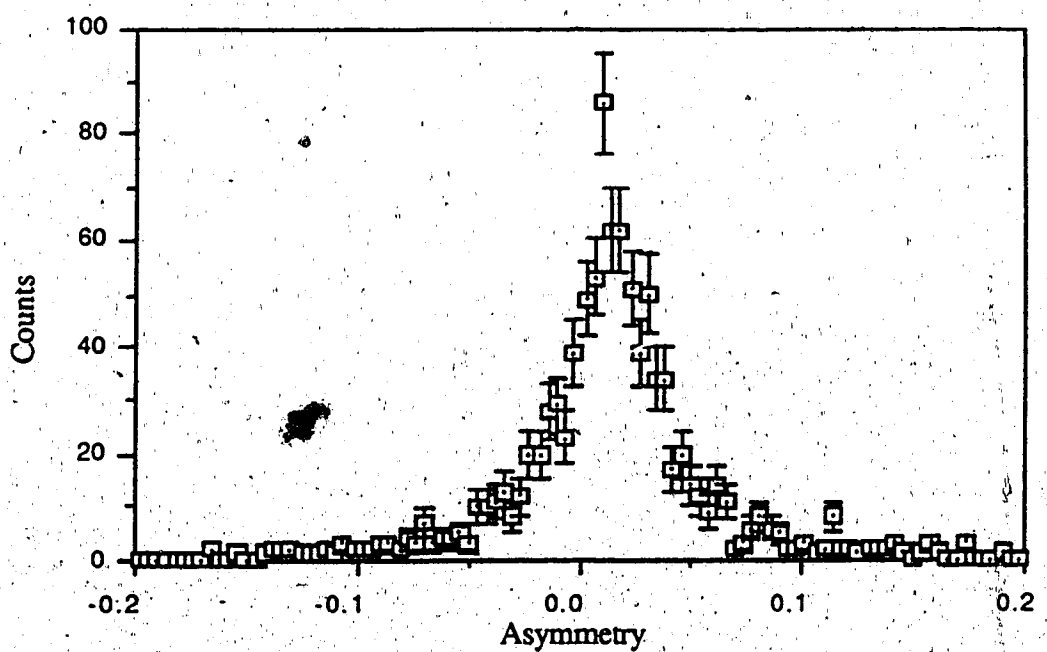
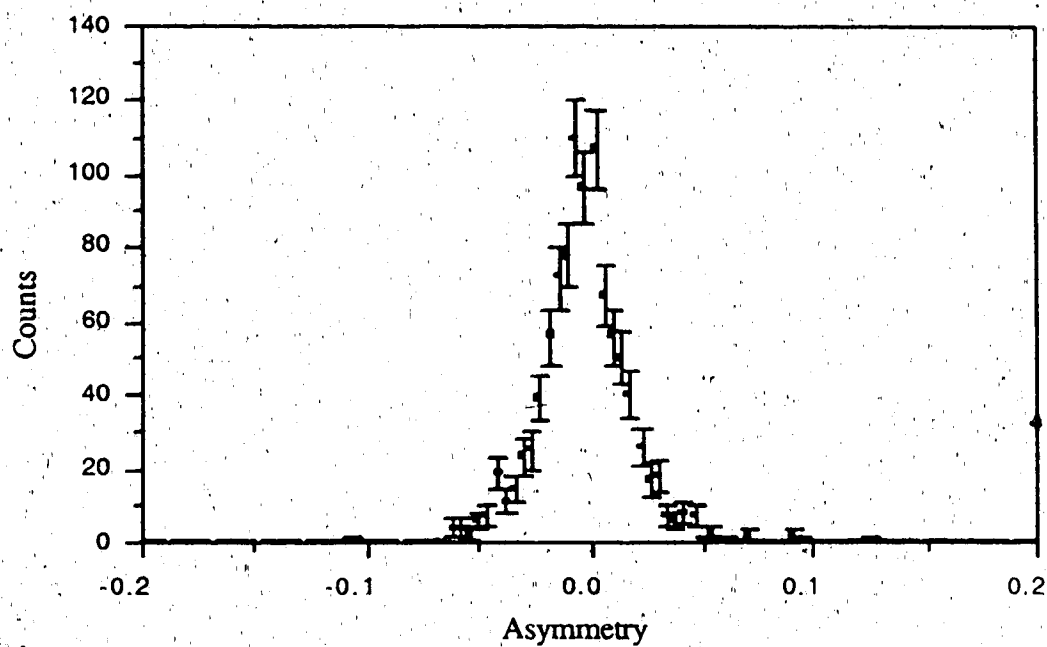


Figure (4.5.1) Raw left-right (top) and up-down (bottom) asymmetries measured in SEM 4AM4.7 (see figure 3.2.1). An asymmetry of 0.1 represents a displacement of 0.24 mm.

target.

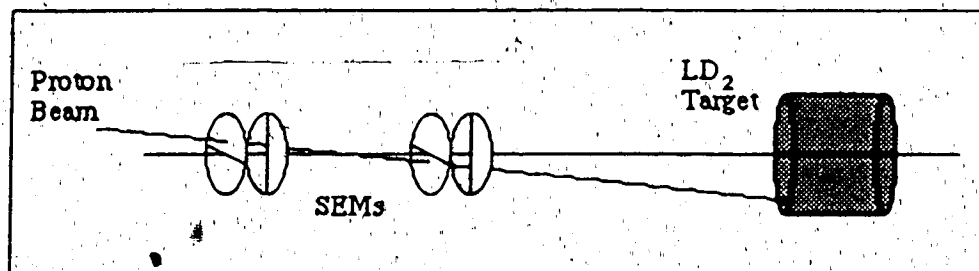


Figure (4.5.2) Estimate of Maximum Deflection of the Proton Beam Position On the LD<sub>2</sub> Target.

Such a calculation shows that the maximum estimates of the position and angular uncertainties of the primary beam at the LD<sub>2</sub> target were  $\sigma_x < 0.2$  mm,  $\sigma_y < 0.2$  mm,  $\sigma_x^\theta < 0.009^\circ$  and  $\sigma_y^\theta < 0.013^\circ$ . These values are less than the 0.33 mm that the proton beam could be allowed to move across the LD<sub>2</sub> target before systematic errors would have effected the asymmetry measurement at the zero - crossing angle at the  $10^{-4}$  level (see appendix A on systematic errors).

#### 4.6 Neutron Beam Polarization

Neutron polarizations were measured at the neutron polarimeter (see section 3.7). The neutron polarization is the proton polarization, as measured in the proton polarimeter (see section 4.3), multiplied by the  $^2\text{D}(\text{p},\text{n})2\text{p}$  polarization transfer coefficient. The neutron polarimeter effective left-right and up-down analyzing powers were determined<sup>(43)</sup> by measuring the ratio of the proton polarization multiplied by the polarization transfer coefficient to the observed neutron asymmetry,

$$A_{\text{eff},n} = \frac{[d_{\text{osso}}^2 + d_{\text{okso}}^2]^{1/2} P_p}{\epsilon_n} \quad (4.6.1)$$

where

$$P_p = \frac{\epsilon_p}{A_{\text{osno}}} \quad (4.6.2)$$

The subscripts on the polarization transfer coefficients are as those defined in section (3.4). Here, the expression within the square root of (4.6.1) is the  $^2D(p,n)2p$  transverse polarization transfer coefficient at  $90^\circ$  including final state interactions,  $A_{\text{oono}}$  is the proton-proton analyzing power at  $17^\circ$  (lab),  $\epsilon_p$  is the observed proton-proton scattering asymmetry at the proton polarimeter, and  $\epsilon_n$  is the neutron-proton scattering asymmetry at the neutron beam polarimeter. D.V.Bugg et. al.<sup>(35)</sup> have calculated a values  $D_{\text{osso}} = -0.6992$  and  $D_{\text{osko}} = 0.0905$  at  $90^\circ$  for free n-p scattering, and  $d_{\text{osso}} = -0.7379$  and  $d_{\text{osko}} = 0.0778$  for quasi-free n-p scattering after corrections for final state interactions. Calculations using the phase shifts of R. Arndt<sup>(3.3)</sup> yield  $D_{\text{osso}} = -0.7181$  and  $D_{\text{osko}} = 0.0449$ . A value for  $[d_{\text{osso}}^2 + d_{\text{osko}}^2]^{1/2}$  of 0.7496 was used as the average of these two results. The analysis of R. Arndt yields a free p-p analyzing power at  $17^\circ$  of  $A_{\text{oono}} = 0.507$ , and the calculations of D.V.Bugg yield  $A_{\text{oono}} = 0.519$ . An average value of  $A_{\text{oono}} = 0.513$  was used.

The left - right neutron polarimeter effective analyzing power was measured while the spin precession dipoles were at their definitive experimental settings to precess the neutron spin into the vertical direction. The up - down analyzing power was measured while the horizontal field was set to precess the neutron spin into the scattering plane and perpendicular to the beam direction. The following values were measured,

$$A_{n,\text{eff}}^{\text{up,down}} = 0.201 \pm 0.013 \quad (4.6.2)$$

and

$$A_{n,\text{eff}}^{\text{left,right}} = 0.195 \pm 0.012 \quad (4.6.3)$$

The difference between the effective left-right and up-down analyzing powers, if significant, may reflect the differences in the horizontal and vertical neutron beam widths. The wider horizontal width may result in the n-p analyzing power being integrated over a wider angular range thus diluting the final average.

Neutron beam polarizations were continuously monitored throughout the experiment. Vertical neutron polarizations measured in the neutron polarimeter, after corrections for instrumental asymmetry, are listed in table (4.6.1)

Table (4.6.1) Vertical Neutron Polarizations

Run	Polarization State		Instrumental Asymmetry
	Positive	Negative	
1	$0.462 \pm 0.005$	$-0.489 \pm 0.005$	-0.042
2	$0.467 \pm 0.004$	$-0.476 \pm 0.003$	-0.046
3	$0.472 \pm 0.009$	$-0.483 \pm 0.002$	-0.044
4	$0.490 \pm 0.003$	$-0.490 \pm 0.004$	-0.044
Background	$0.483 \pm 0.002$	$-0.488 \pm 0.001$	-0.044

The observed horizontal neutron polarizations, as measured in the vertical arms of the neutron polarimeter, are listed in table (4.6.2).

Table (4.6.2) Horizontal Neutron Polarizations

Run	Polarization State		Instrumental Asymmetry
	Positive Vertical Proton Polarization	Negative Vertical Proton Polarization	
1	$0.003 \pm 0.003$	$-0.004 \pm 0.003$	-0.004
2	$-0.015 \pm 0.004$	$-0.011 \pm 0.003$	-0.001
3	$0.002 \pm 0.003$	$-0.001 \pm 0.002$	-0.003
4	$0.007 \pm 0.002$	$-0.009 \pm 0.002$	-0.003
Background	$-0.001 \pm 0.001$	$-0.002 \pm 0.002$	-0.004

The stability of the horizontal and vertical polarimeter instrumental asymmetries provides an illustration of the stability of the neutron beam on the neutron polarimeter.

#### 4.7 Neutron Beam Intensity Profile

A change in the neutron beam position would result in false angular measurements of outgoing scattered neutron and proton pairs. Such a change could be due to changes in the position, angle or profile of the proton beam on the LD<sub>2</sub> target, movement of the LD<sub>2</sub> target itself, or a shift in the neutron beam collimator position. Since the stability of the neutron beam position was of great importance, the neutron beam intensity profile and horizontal and vertical centroids were determined on a daily basis using the neutron profile monitor / polarimeter located 16.90 m from the liquid deuterium neutron production target (see section 3.7). A typical measurement of the vertical and horizontal neutron beam profiles are illustrated in figures (4.7.1). The results of the



neutron profile measurements on a run-to-run basis are listed in table (4.7.1).

**Table (4.7.1) Neutron Beam Intensity Profile**

Run	Centroid Variance (mm)				Beam Width (FWHM) (mm)	
	$\langle x \rangle$	$\sigma_x$	$\langle y \rangle$	$\sigma_y$	Horizontal	Vertical
1	2.0	0.4	-0.9	0.3	95.3	72.2
2	2.0	1.3	-1.2	0.9	97.7	72.9
3	1.0	1.1	-1.4	0.9	97.9	72.2
4	-0.7	0.3	-2.8	0.3	95.8	69.5
background	-0.5	0.3	-2.8	0.6	95.4	69.3

If the  $\text{LD}_2$  target is treated as a fixed neutron source around which the neutron beam pivots, the incident neutron beam angle stability can be extrapolated to  $\pm 0.005^\circ$  on the FST. The neutron beam profile is illustrated in figure (4.7.1). The neutron beam was 73 mm wide and 55 mm high (FWHM) at the target. The entire target material is illuminated. The empty 50  $\text{cm}^3$  spaces at the top and bottom of the inner target canister prevented illumination of the surrounding target support structure. The neutron beam illuminated the 4 cm diameter, 5 cm high inner target cannister but not the outer 8 cm diameter, 12 cm high aluminum vacuum shell as illustrated in figure (4.7.2).

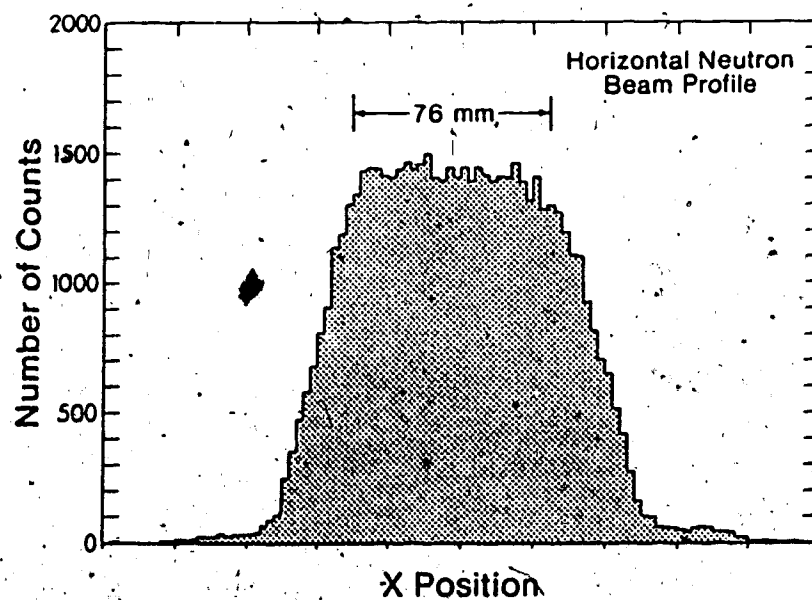
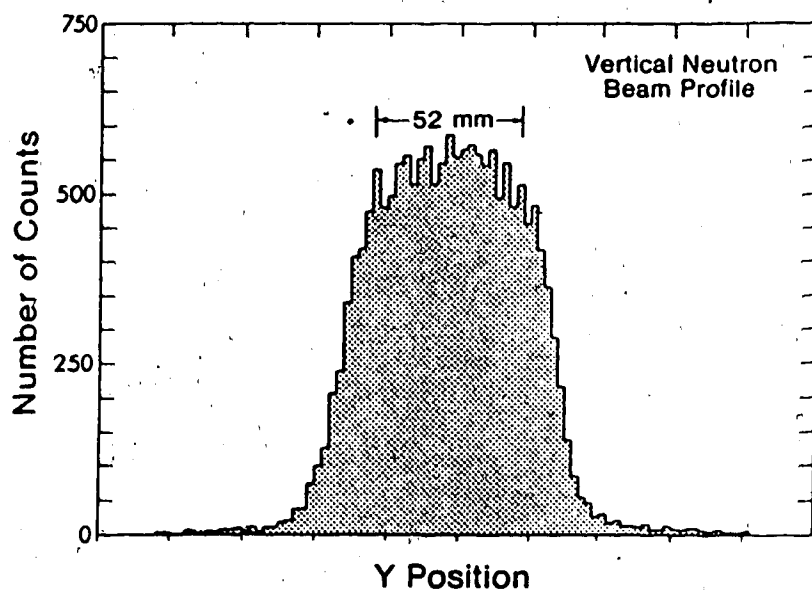


**Figure (4.7.1) Horizontal and Vertical Neutron Beam Profiles.**  
 The vertical neutron beam profile distribution (top) had a flat top 52 mm wide at the neutron polarimeter target. The flat portion of the horizontal neutron beam profile distribution (bottom) was 76 mm wide.

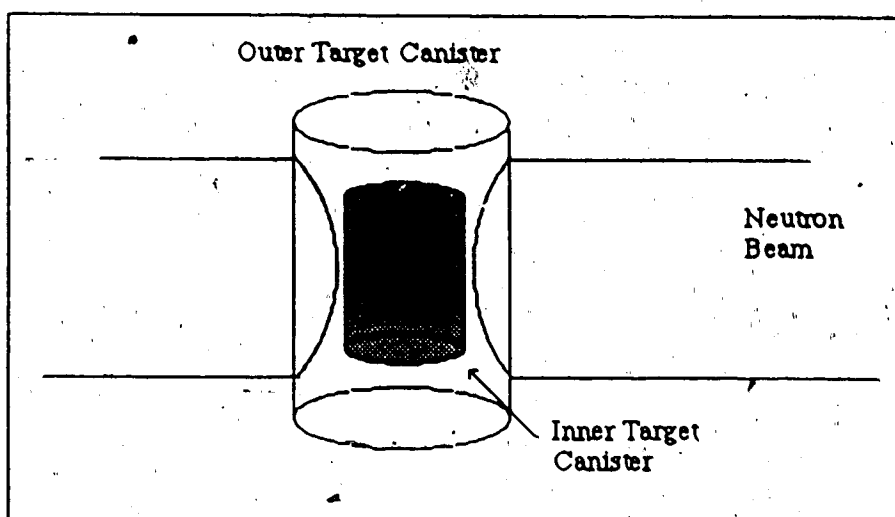


Figure (4.7.2) Neutron Beam illumination of FST target.

## 4.8 Target Position

Undetected changes in the target position would have resulted in an inaccurate reconstruction of the proton and neutron scattering angles because of changes in the magnetic holding field line integral between the neutron-proton scattering vertex out to the proton E-counter. Unless such deviations in the target position were correlated with the  $A_n$  and  $A_p$  measurements there would be no net effect on the zero-crossing angle measurements. Nonetheless, the target position was remeasured on several occasions over the duration of the experiment. The lateral and longitudinal positions of the FST with respect to the pivot position are shown in table (4.8.1).

**Table (4.8.1) Frozen Spin Target Position Offsets**

Run	Measurement Date	x - offset (mm)	z - offset (mm)
1	No Measurements		
2	4 Aug 84	$-1.4 \pm 0.7$	$0.0 \pm 0.7$
	22 Aug 84	$0.1 \pm 0.7$	$-0.9 \pm 0.7$
	5 Sep 84	$-1.6 \pm 1.0$	$0.9 \pm 1.0$
3	26 Sep 84	$-1.1 \pm 0.7$	$1.0 \pm 0.7$
	17 Oct 84	$-1.0 \pm 0.7$	$1.4 \pm 0.7$
4	4 Dec 84	$1.1 \pm 0.7$	$0.7 \pm 0.7$
	24 Dec 84	$1.1 \pm 0.7$	$0.7 \pm 0.7$
background	8 Jan 85	$1.0 \pm 0.7$	$1.0 \pm 0.7$
	11 Jan 85	$1.3 \pm 0.7$	$1.8 \pm 0.7$

No target position measurements were made during the first data taking run. The x-position is to the left of the pivot as seen by the LD<sub>2</sub> target, and the z - position is defined positive from the pivot towards the neutron profile monitor. Target positions were determined from x-ray photographs taken of the target. Offsets were measured of the inner target cylinder with respect to the outer target can. The outer target can was part of the rigid target support structure and was assumed to remain rigidly fixed. The central vertical axis of the magnetic field with respect to the target axis was offset by 1.0 mm downstream of the target position during the first three runs, and by 0.5 mm upstream of the target position during the final data taking and background runs.

The volumes occupied by the butanol beads and the heights of the beads in the target

cannister as measured by X-ray photographs are shown in table (4.8.2).

**Table (4.8.2) Target Volume and Fill Level**

Run	Target Volume (cm <sup>3</sup> )	Fill Level (mm)
1	Not Measured	
2	55	46
3	50	41
4	55	46
background	43.4	41

The values of the height of the butanol beads in the canister in the above table were averaged over the run. Although the target volume was not recorded after the first data taking run, the volume was estimated as 55 cm<sup>3</sup>.

#### 4.9 Target Polarizations

Target polarizations were measured with a nuclear magnetic resonance (NMR) system. An NMR coil was located in the bottom half of the inner target cannister. Polarizations were calibrated with calculated thermal equilibrium values in the target field near 1K. NMR polarization measurements were made when the target was located in the high 25 kG polarizing field before and after the daily polarized target runs. Average target polarizations taken during the four data runs are listed below.

**Table 4.9.1 Average Target Polarizations (NMR)**

Run	Target Polarization
1	0.677±0.011
2	0.846±0.014
3	0.804±0.010
4	0.789±0.015

Polarization decay times ranged between 24 and several hundred hours. Such a variation was due to a very strong dependence between polarization decay time and target temperature. At the beginning of the experiment the target temperature was held between 81 mK - 88 mK. Target temperatures gradually fell over the course of the experiment reaching the low 50s as the cryogenics personnel grew more experienced with the target apparatus.

## 4.10 Proton Detection

### 4.10.1 Proton Time-of-Flight

Proton energies are determined from the time-of-flight between the pTOF scintillator and E-counter. The pTOF signal was taken as the simple average of the two timing signals from the top and bottom of the counter. Four phototubes viewed the E-counter from above and below. The E-counter was divided into five sections<sup>(46)</sup> with different conditions for each.

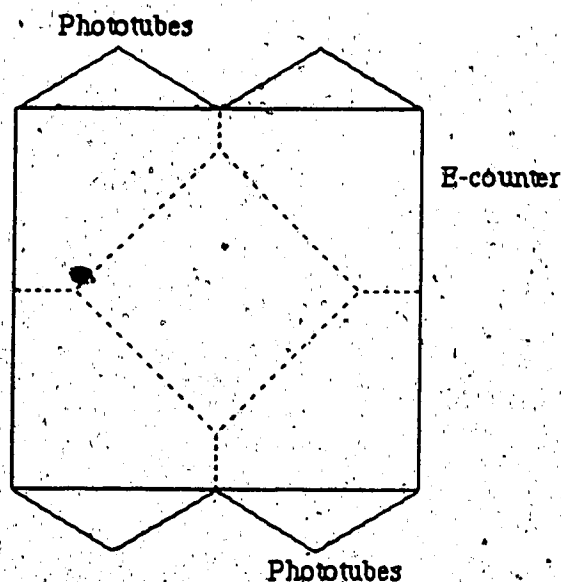


Figure (4.10.1) Artificial division of proton E-counter for proton time-of-flight calculations

The central region accepted timing signals from all phototubes. Valid events within the central region required all four phototubes to fire. Events in the corners were treated differently. The timing signal from a phototube was observed to be unreliable if the proton track intersected the corner of the E-counter horizontally across from the phototube. The timing information was rejected whether or not the phototube fired. Events occurring in the corners were used only when the other three phototubes fired.

The sum of the TDC signals was corrected for the time necessary for the light to

travel from the event position to each of the three or four phototubes used in the proton TOF calculation. The E-counter was artificially divided into an  $18 \times 28$  element array. The time required for light to travel from each of the 504 array elements to the four phototubes was measured and recorded. The proton trajectory was extrapolated to the E-counter. When the proton struck the central region of the E-counter, the time required for the light to reach all four phototubes was subtracted from the phototube TDC sum. When the proton struck a corner of the E-counter, the time required for light to reach the three phototubes used in the TOF calculation was subtracted from the TDC sum. The apparent proton TOF was taken as the corrected TDC sum averaged over the three or four phototubes.

Corrections were made for proton energy losses in the target and wedge-shaped absorber by subtracting a proton TOF dependent variable from the apparent proton TOF. A TOF constant was added to account to each of the five regions of figure (4.10.1) to account for electronic delays. This constant was determined to force energies of elastically scattered protons to their kinematically accepted values. A random value between -0.5 and 0.5 was added to all measured TOF values to avoid histogramming errors caused by the granularity of the raw TOF data.

#### 4.10.2 Proton Track Reconstruction

Horizontal and vertical positions were determined from four delay line chambers (DLCs) along each proton boom. The difference between the TDC signals (TDIF) from opposite ends of the vertical and horizontal delay lines determined the position of the intersection of the proton path with each DLC. The apparent horizontal position was calculated as

$$x_a = dx / dt (T - T_{RP}) + C_x \quad (4.10.1)$$

Here,  $T$  is the TDC difference (TDIF) between the arrival of the signal at the left and right ends of the delay line, and  $T_{RP}$  is the left-right TDIF of the pulser located on the right end of the delay line,  $C_x$  is a position dependent correction to account for delay line non-linearities (see section 3.9), and  $dx / dt$  is the number of millimeters a signal travels along the delay line per TDC channel,

$$dx / dt = \frac{x_{RP} - x_{LP}}{T_{RP} - T_{LP}} \quad (4.10.2)$$

where,  $x_{RP}$  and  $x_{LP}$  are defined as the positions of the pulsers on the right and left side of the delay line. The actual horizontal coordinate is then taken as the anode wire position closest to the apparent position from the 'picket fence' spectrum (see section 3.9.3).

Since no such discrete, 'picket fence' spectra existed in the vertical dimension, a different system was used. A vertical position was calculated as

$$y_a = (T - T_{BP}) \, dy/dt + C_y \quad (4.10.3)$$

where  $C_y$  is a position dependent correction to account for vertical delay line non-linearities, and  $dy/dt$  is evaluated as

$$dy / dt = \frac{y_{TP} - y_{BP}}{T_{TP} - T_{BP}} \quad (4.10.4)$$

where,  $y_{TP}$  and  $y_{BP}$  are the vertical coordinates of the pulsers on the top and bottom of the delay line. The pulser TDIF variables  $T_{RP}$ ,  $T_{LP}$ ,  $T_{TP}$  and  $T_{BP}$  of (4.10.2) and (4.10.4) were reevaluated offline after every two hour period to correct for minor fluctuations in the delay line timing.

The horizontal track position resolution of 2.0 mm FWHM was limited by the anode wire spacing. Events which caused avalanches to occur on two neighbouring anode wires could not be distinguished between events which caused single avalanches. The vertical track position resolution of 0.7mm FWHM was somewhat better since the vertical coordinate was not limited by the granularity of the picket fence spectrum.

Acceptable tracks required at least a single horizontal and vertical position in the front and back group of two DLCs. A proton track was reconstructed from the available DLC information as in figure (4.10.2).



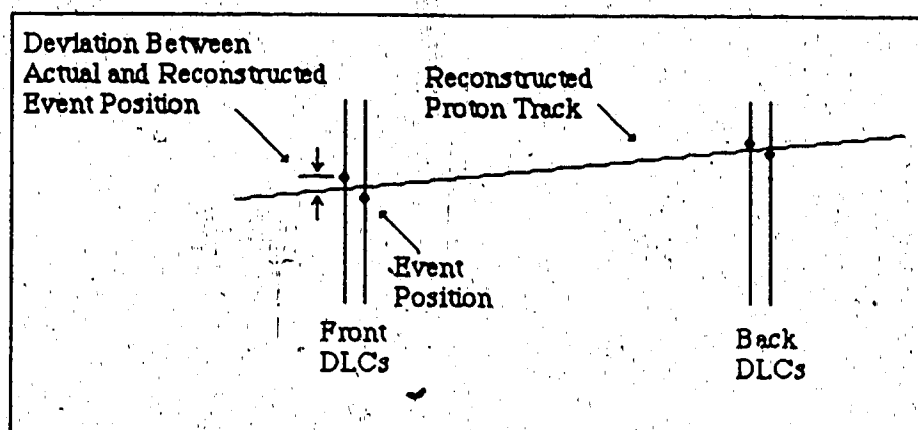


Figure (4.10.2) Proton Track Reconstruction

Typical deviations between reconstructed and observed track coordinates for front DLCs is illustrated in figure (4.10.3), and for back DLCs in figure (4.10.4).

The efficiency of each DLC coordinate exceeded 98%. Since only a horizontal and vertical coordinate in each of the front and back DLCs were required for an acceptable track, the net DLC efficiency was approximately 99%.

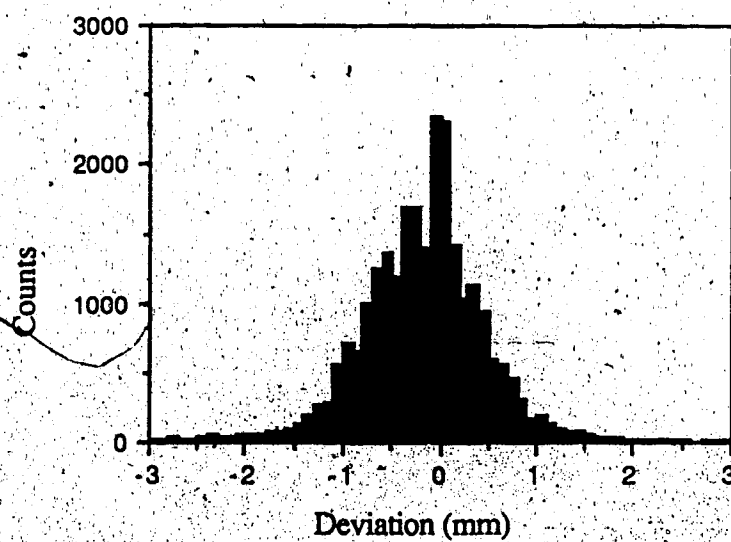
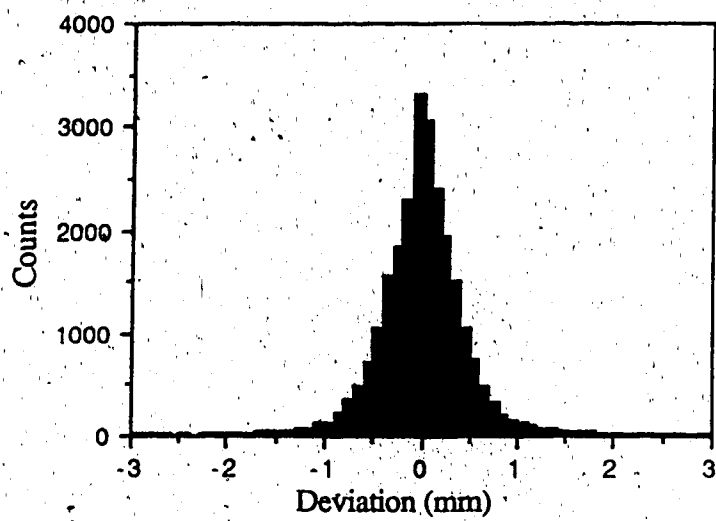


Figure (4.10.3) Deviation Between Observed and Reconstructed Horizontal (top) and Vertical (bottom) Coordinates for Front DLCs

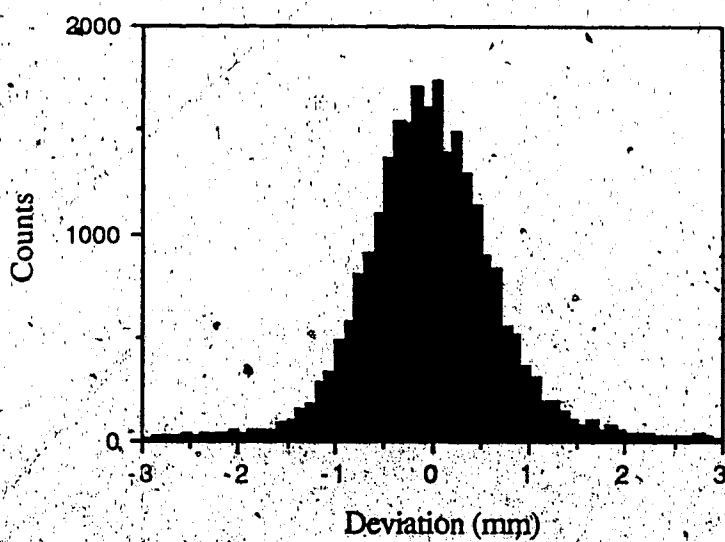
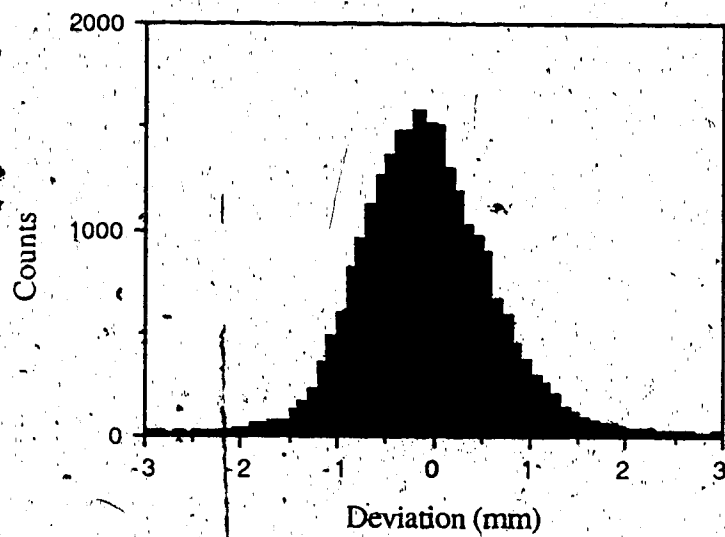


Figure (4.10.4) Deviation Between Observed and Reconstructed Horizontal (top) and Vertical (bottom) Back DLC Coordinates

Proton tracks were traced back to the FST target. Since the neutron track was not reconstructed, neutron - proton vertex positions were projected onto the  $x = 0$  plane as in figure (4.10.5) (the coordinate frame was defined in section 3.1).

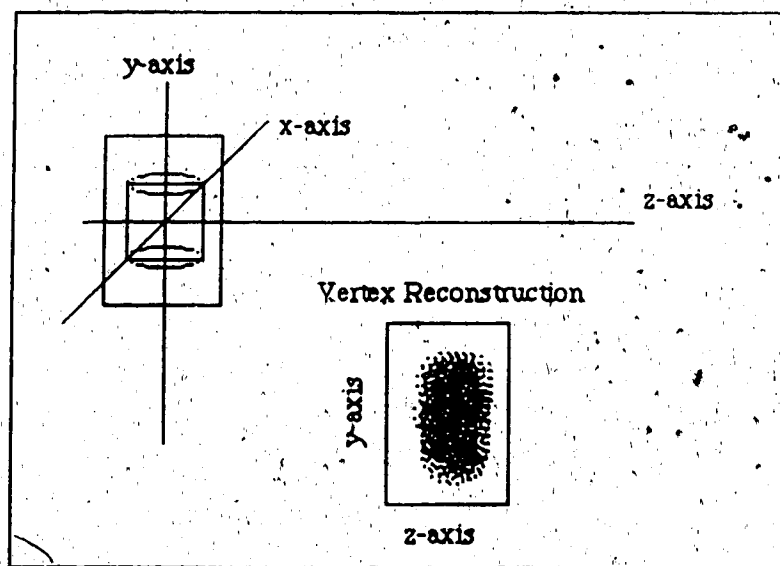


Figure (4.10.5) Projection of Reconstructed Vertex onto  $z=0$  Plane

A typical plot of the neutron - proton vertex reconstruction is illustrated in figure (4.10.6). Vertex positions were not corrected for the deflection of the recoil protons in the target holding field; therefore, z-vertex positions shifted by  $\pm 7.2$  mm depending on the holding field direction. Consequently, loose constraints were placed on the z-vertex position.

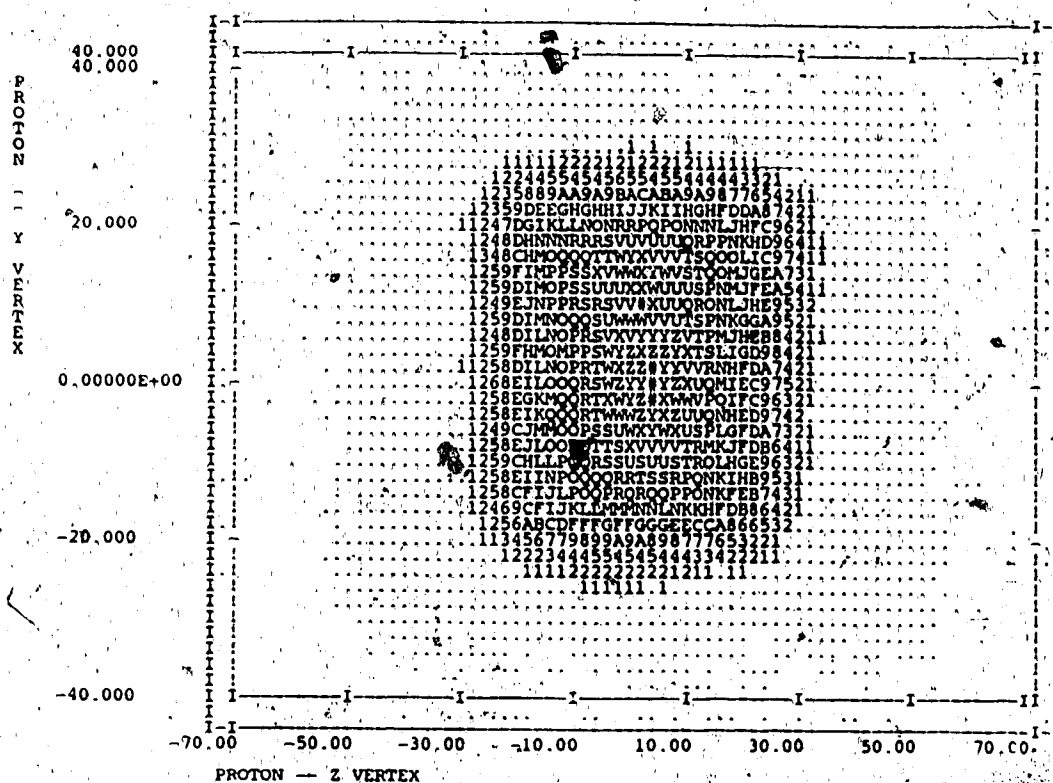


Figure (4.10.6) Reconstructed Neutron-Proton y-z Vertex.

All axis coordinates are in mm. The smallest bin is denoted by a '.'. As the number of events increases, the scale extends from 1 to 10 and then through the alphabet. The maximum number of events within a single bin is denoted by a '#'.

### 4.10.3 FST Target Holding Field

Proton angles were corrected for horizontal angular deflections caused by the target holding field. Angular deflections depended on holding field direction, neutron-proton vertex position within the target, proton recoil energy, and proton energy loss in the target material and support structure.

Magnetic field mappings were made before the beginning of the experiment in several planes above and below the median plane. These measurements were used to determine the line integral of the magnetic field,  $\int B \cdot dl$ , as a function of proton angle and vertex position. A plot of the magnetic field line integral in the median plane as a function of distance from the center of the target is illustrated in figure (3.8.3). The field maps were used to evaluate proton angular deflections. The angular deflection of a proton in a magnetic field is

$$\Delta\theta = \frac{e}{pc} \int B_y dl \quad (4.10.8)$$

if the proton scatters in the plane defined by  $y = 0$ . Here,  $B_y$  is the vertical component of the magnetic field as a function of distance from the target and  $dl$  is the incremental distance from the target. The simple relation (4.10.8) could not be used since the magnetic field extended well outside the target area and beyond the first DLC 520 mm from the target. Reconstructed proton tracks would not be identical to the path deflected by the magnetic field. This is illustrated in figure (4.10.7).

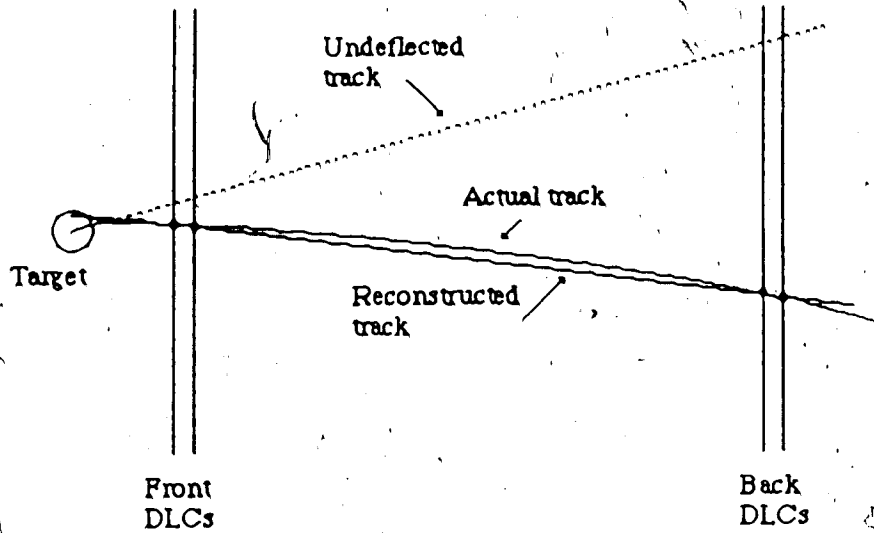


Figure (4.10.7) Proton Angular Deflections due to Target Holding Field

A computer code was used to simulate the flight of protons from their vertex position in the target through the DLCs in the target holding field. Proton energy loss was included in the calculations. A least squares fit was made to the points where the proton flight path intersected the DLCs. The angular correction used in the analysis was taken as the difference between the original proton recoil angle and the angle reconstructed with DLC information.

The final angular correction to the reconstructed proton track was approximated with the function

$$\Delta\theta = \Delta\theta_0 + A\Delta x + B \left( \frac{1}{p} - \frac{1}{p_0} \right). \quad (4.10.9)$$

Here, the holding field deflection and proton momentum at  $\theta_p = 52^\circ$  are given by  $\Delta\theta_0$ , and  $p_0$ , respectively,  $B$  relates the angular deflection to the inverse of the proton momentum,  $\Delta x$  is the lateral offset of the FST from the centre of the magnetic field, and  $A$  is a constant relating angular deflection to lateral target offset. The magnitude of  $\Delta\theta_0$  was taken as  $1.21^\circ$  ( $1.29^\circ$ ) when the target holding field was in the positive (negative) vertical direction (the sign of  $\Delta\theta_0$  depended on the direction of the holding field and the proton scattering direction). The difference between the two values was due to the contribution of the cyclotron magnetic field in the experimental area. The horizontal components of the target holding field (section 3.8) were small and neglected in the

analysis.

#### 4.10.4 Effect of the Wedge Shaped Absorber

Additional angular corrections were made to the proton angles to correct for offsets caused by the wedge-shaped absorber, the target holding field and multiple scattering in the target. Protons which multiple scattered to the thicker side of the wedge had a larger probability of absorption through nuclear reactions than those which multiple scattered to the thinner side. The result was a small bias in the observed proton recoil angle distribution. Reversing the holding field direction affected the magnitude of the angular shift by sweeping higher or lower energy protons into the wedge-shaped absorber. A uniform additive angular correction was applied to all proton angles to account for this angular shift. The corrections are reproduced in table (4.10.1)

**Table (4.10.1) Observed Effect of Wedge-Shaped Absorber on Recoil Proton Angles**

Proton Direction	Average bias of Proton Angular Distribution Holding Field Direction	
	up	down
Right	-0.07°	0.17°
Left	0.13°	-0.07°

The angular corrections were taken from the observed shifts in the neutron-proton opening angle distributions. The shifts were simulated with a Monte Carlo program. The results of the simulation accurately reproduced the centroids of the observed neutron - proton opening angles as a function of holding field direction and recoil angle. The observed biases in the experimental proton angular distributions were not perfectly symmetric between left-HF up and right-HF down events and between left-HF down and right -HF up events since the magnetic field line integral between the FST target and the E-counter differed by 3.2% (table 3.8.1) between the two holding field configurations, and since the left and right wedge thicknesses differed by 3% (table 3.9.1).

A bias in the proton angular distribution toward larger or smaller angles can not influence the results of the experiment. The experiment was designed to measure differences in the  $A_n$  and  $A_p$  zero-crossing angles. An angular bias in the proton angular distribution shifts both asymmetry distributions by an identical amount but does not influence the differences between zero-crossing angles.



## 4.11 Neutron Detection System

### 4.11.1 Neutron Detection Array Calibration Techniques

The analysis of button protons, so-called because of 7 cm by 7 cm counters situated in the back of the neutron array, provided calibrations for both the gain and timing characteristics for the 56 photomultipliers attached to the neutron detection scintillator array. Button events were extracted from the experimental data and analyzed in a first pass through the data to provide the necessary calibrations.

Cuts were placed on the button proton TOF between the 'neutron' start counter and the veto-counter. A typical button proton TOF spectrum is illustrated in figure (4.11.1). Cuts were employed to exclude pions. The actual energy of the button protons was unimportant. Only a stable button proton energy spectrum was required.

Neutron detection efficiency was dependent on the photomultiplier analog to digital converter (ADC) discrimination threshold. An undetected shift in the photomultiplier gain without a corresponding scaling in the software discrimination threshold would change the neutron detection efficiency (see appendix A on systematic errors). Button events provided a stable signal from the photomultipliers against which gains were calibrated. Typical button pulse height distribution spectra, after pedestal (the phototube response without an event in the neutron bar) subtraction, are illustrated in figure (4.11.2). Upstream (downstream) button phototube centroids were positioned in channel 320 (368) by manipulating the phototube high voltages. Upstream and downstream phototube pulse height distributions were typically 90 and 115 channels wide (FWHM), respectively. The wider phototube ADC signal distribution in the back bars of the neutron array was caused by proton energy straggling in the front neutron bars. A sufficient number of button protons were collected during each run to determine the location of the 56 phototube button event ADC centroids to within  $\pm 0.3\%$ .

The target holding field caused small angular deflections to the path of the button protons which caused protons with slightly different energies for the two holding field configurations. The energy deposited in the scintillator bars, and therefore the phototube signal triggered by passing button protons, was dependent on the button proton energy. Button event photomultiplier signals were scaled up or down by approximately 0.7% to account for this effect.

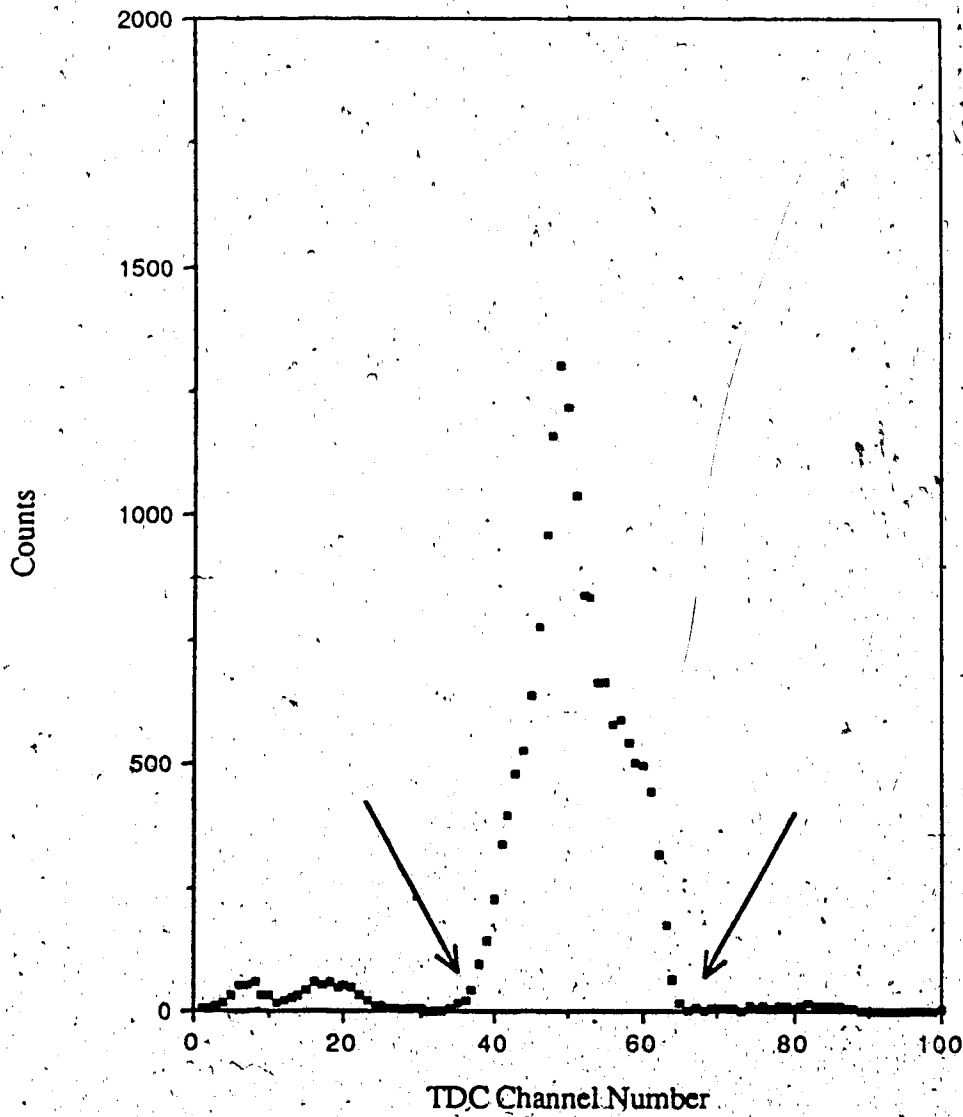


Figure (4.11.1) Button Proton Time-of-Flight Distribution  
Time increases from left to right and 1 TDC channel is equivalent to 50 ps.  
The positions of the cuts employed in the analysis are displayed.

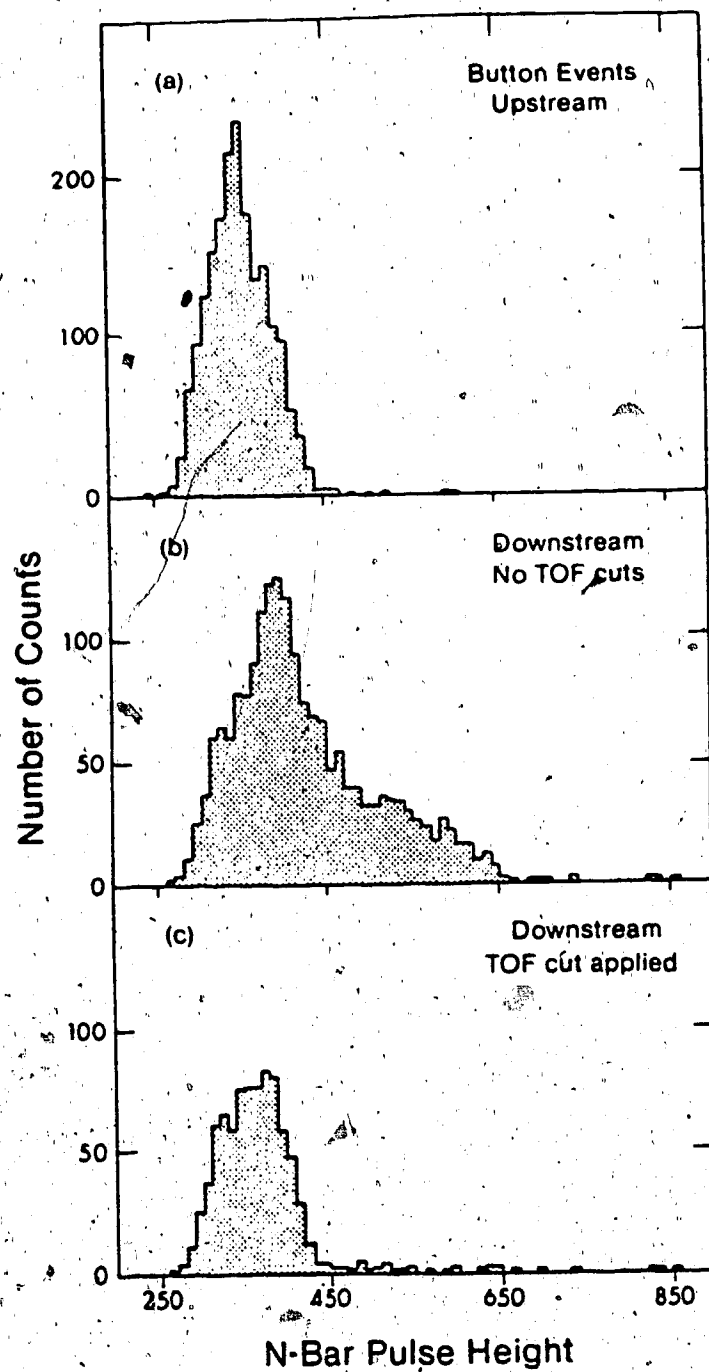


Figure (4.11.2) Button Proton Event Upstream and Downstream Neutron bar Pulse Height Distribution.

The absolute positions of button proton events in the neutron scintillator array were known. Differences between apparent and actual button proton positions in each neutron scintillator bar revealed any timing drifts in the neutron array phototubes. A typical button proton position distribution is illustrated in figure (4.11.3). The apparent positions of button protons were determined by the difference in time of signals at opposite ends of the neutron bar,

$$x_b = \frac{[(T_L - T_S) + T_C] L}{\Delta T} \quad (4.11.1)$$

Here,  $T_L$  and  $T_S$  are the pulse arrival times at the opposite ends of the neutron bar,  $L$  is the physical length of the neutron bar,  $\Delta T$  is the time required for light to traverse the entire neutron bar length, and  $T_C$  is a correction to account for shifts in PHT timing on a run-to-run basis. The variable  $T_C$  was reevaluated each run by requiring apparent button positions to be within  $\pm 15$  mm (approximately 4 TDC channels) of their physical position in the neutron bar. Apparent button proton positions,  $x_b$ , were determined to within  $\pm 0.4$  mm each experimental run. The apparent button proton position is later used to correct apparent neutron positions (see section 4.11.3).

#### 4.11.2 Neutron Position

Drifts in timing differences between photomultipliers of the same neutron bar were corrected by monitoring the difference between apparent and actual button proton positions (section (4.11.1)). The struck neutron bar was identified by the TDIF between the delay lines attached to each end of the neutron array. Each bar has its own TDIF signature. A typical neutron bar delay line TDIF spectrum is illustrated in figure (4.11.4). Each peak represents an individual bar and the position of an event in the TDIF plateau determines its position.

The neutron horizontal position,  $x_n$ , was calculated as

$$x_n = \frac{[(T_L - T_S) + T_C] L}{\Delta T} - x_b \quad (4.11.3)$$

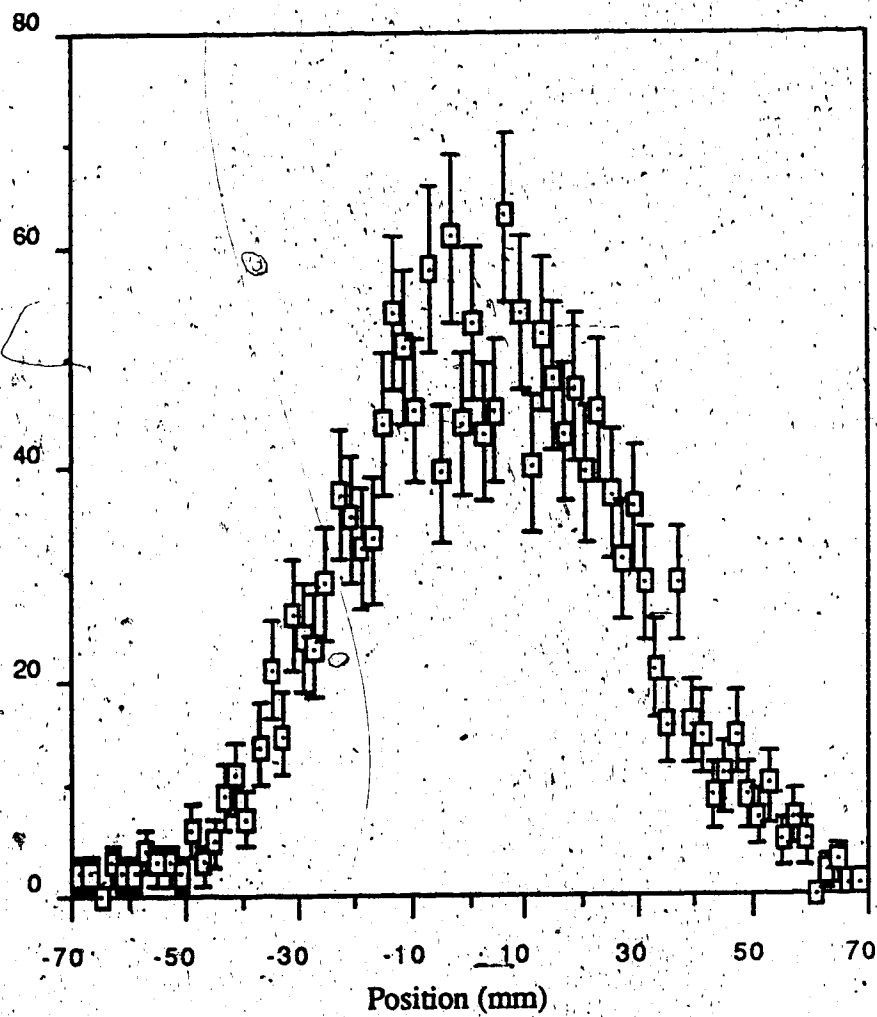


Figure (4.11.3) Apparent Button Proton Position Spectrum

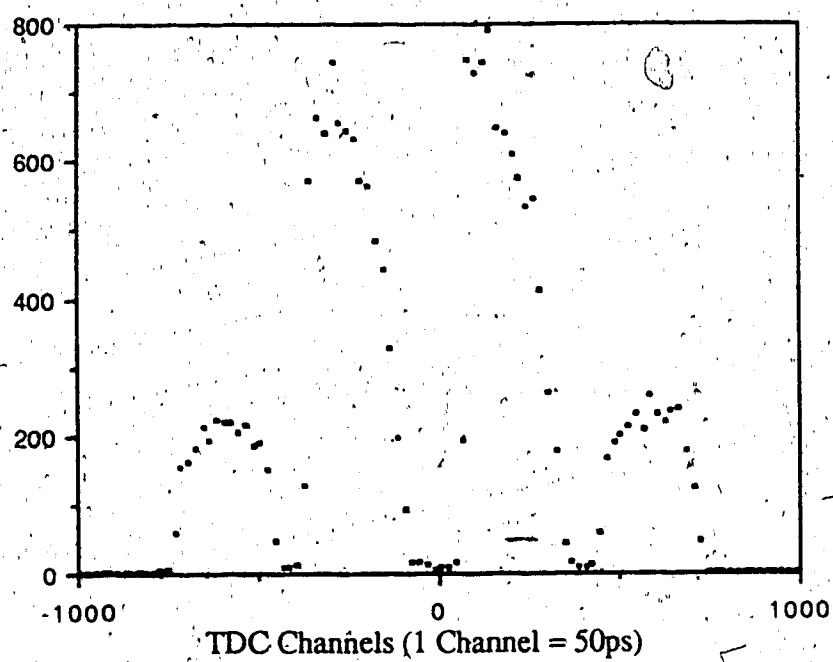


Figure (4.11.4) Large Angle-Small Angle Neutron Array  
Delay Line Time Difference

where the symbols are identical to those in section (4.11.1). Shifts in photomultiplier timing were corrected with the apparent button centroid position,  $x_b$ . The timing width of the neutron bars was determined by uniformly illuminating the entire width of the bar with recoil particles from the target. The coincident proton requirement was removed since the kinematic acceptance of the detection apparatus was defined by the active area of the DLCs (see section 3.10.5). The TDC channel width of each neutron bar was determined as  $\Delta T = 13.2 \pm 0.2$  ns. Care was taken to exclude events close to the hardware detection threshold. Such events had very poor position resolution and would have caused a less accurate position resolution if included. An error in the neutron bar TDC width scales the observed difference in  $A_n$  and  $A_p$  zero-crossing angles. The error has been included in the estimate of the experimental systematic error (see chapter 5).

The neutron vertical and longitudinal position resolution both were limited to  $\pm 7.5$  cm by the 15 cm height and depth of the neutron bars. The horizontal position resolution was estimated as  $\pm 30$  mm FWHM by the difference in the observed front and back positions of button protons.

Neutrons events were not accepted if non-adjacent neutron bars were struck in coincidence. The delay line assembly did not permit the identification of which bar was struck first.

#### 4.11.3 Neutron Bar ADC Gain Stabilization

The amplitude of neutron induced photomultiplier signals was scaled to remove effects of neutron bar electronic gain changes by using the formula

$$PHT_f = (PHT_i - Ped) * \frac{Scale}{PHT_{button}} \quad (4.11.2)$$

The variable 'Ped' is the ADC pedestal and represents the photomultiplier signal when no energy is deposited in the bars (typically 5 - 15 channels of 1024 full scale), 'Scale' represents a constant scaling factor equal to 320 for front bars and 368 for back bars, 'PHT<sub>button</sub>' is the observed button event phototube ADC centroid (section 4.11.1). A typical neutron phototube ADC distribution is illustrated in figure (4.11.5)

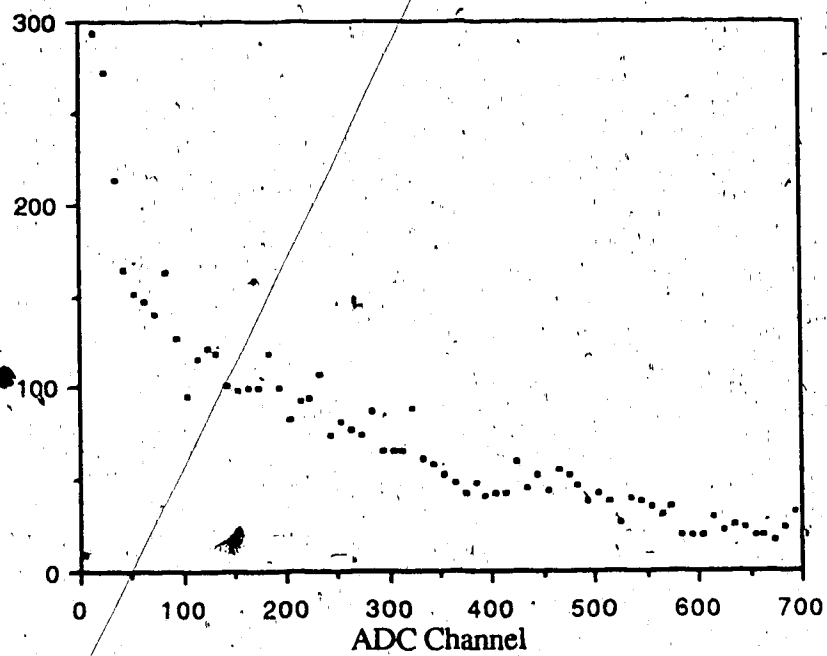


Figure (4.11.5) Scaled Neutron Bar Photomultiplier Pulse Height Distribution



#### 4.11.4 Effect of Neutron Polarization on Position Determination

Apparent neutron positions detected in the scintillator array are influenced by neutron polarization since the direction of polarization defines a left or right scattering preference. Since the final neutron polarization was different for neutrons produced from the  $A_n$  and  $A_p$  measurements, the observed neutron angles were shifted by a different amount when the neutron based measurements were used.

Scattered neutrons during the  $A_n$  measurement had the polarization

$$P_{nf}(A_n) = \frac{P_{ni}D_{nono} \pm A_{oono}}{1 \pm P_{ni}A_{oono}} \quad (4.11.4)$$

and scattered neutrons during the  $A_p$  measurement had the polarization

$$P_{nf}(A_p) = \frac{P_{pi}D_{noon} \pm A_{oonn}}{1 \pm P_{pi}A_{oonn}} \quad (4.11.4)$$

Here,  $P_{ni}$  is the initial neutron polarizations,  $D_{nono}$  is the depolarization coefficient,  $D_{noon}$  is the depolarization transfer coefficient, the abbreviation ' $\pm$ ' represents scattering to the left (+) or right (-), and  $A_{oono}$  and  $A_{oonn}$  are the (n,p) analyzing powers. The deviation from the actual position is given by

$$\Delta_x(\theta) = \frac{R}{2} P_{nf} A \sin\theta_p \quad (4.11.6)$$

Where  $R$  is the range of the recoil proton in the scintillator array,  $\theta_p$  is the proton recoil scattering angle in the struck neutron scintillator bar, and  $A$  is the free neutron-proton analyzing power at the angle  $\theta_p$ . This calculation assumes that all light detected is from the end of the recoil proton track and is therefore an overestimation of the effect.

After averaging the deviation between the apparent and actual positions given by equation (4.11.6) over all proton recoil angles,  $\theta_p$ , the average shift was calculated to be below the  $10^{-4}$  degree level for both the  $A_n$  and  $A_p$  measurements. In addition, the angular shift does not affect the zero-crossing angle measurement to first order. This effect can be safely neglected.

#### 4.11.5 Neutron Time - of - Flight

Neutron time-of-flight (TOF) information was taken from the average of the timing signals from each end of the struck neutron bar and the reconstructed time of the scattering within the FST using proton TOF information. Additive timing corrections were calculated for each neutron bar on a run-to-run basis by forcing the average neutron energy to the value expected by free neutron-proton elastic scattering kinematics. Electronics did not allow unambiguous identification of the neutron bar struck if adjacent neutron bars fired coincidentally. The neutron TOF was taken as the average and a distance on the order of 40 mm was added to the neutron flight path. This extra distance was added to bring the energies of such coincident events into agreement with energies expected from free neutron - proton elastic scattering kinematics. It can be viewed as a correction to account for the distance travelled by recoil particles from one neutron bar to the other.

#### 4.11.6 Neutron Detection Efficiency

A Monte-Carlo code<sup>(47)</sup> was used to estimate the neutron detector efficiency. Efficiencies as a function of threshold discrimination are presented in table (4.11.1).

Table (4.11.1) Neutron Detection Efficiency

Discrimination Threshold (ADC Channel)	MeV electron equivalent <sup>†</sup>	Single Bar Efficiency	Detector Efficiency
0	0	0.165	0.303
10	0.6	0.161	0.296
15	0.8	0.159	0.293
20	1.1	0.156	0.288

The overall detector efficiency was the efficiency of two identical bars where one was located directly behind the other (the geometry of the neutron detector array). The overall detector efficiency,  $E$ , was calculated as

$$E = 2E_{\text{single}} - E_{\text{single}}^2, \quad (4.11.8)$$

where  $E_{\text{single}}$  represents the single bar efficiency. The cut used in the analysis was at channel 20 (or at 1.1 MeVee).

## 4.12 Kinematic Observables and Data Constraints

### 4.12.1 Kinematic Observables

The experiment was four times kinematically overdetermined to allow neutron-proton elastic events to be distinguished from inelastic background. Simple elastic neutron-proton scattering places tight constraints on the energies and scattering angles of the two outgoing particles. The energy sum was formed as

$$E_{\text{sum}} = E_p + E_n \quad (4.12.1)$$

A typical energy sum histogram is illustrated in figure (4.12.1). The small low energy tail of the histogram was caused by the low energy component in the incident neutron energy distribution and by (n,np) background.

The transverse momentum sum was determined with the relation

$$P_x = P_p \cos \theta_p \sin \phi_p + P_n \cos \theta_n \sin \phi_n \quad (4.12.2)$$

A sample histogram of the transverse momentum sum is illustrated in figure (4.12.2). Since the original transverse momentum sum of the incident neutron beam was zero, conservation of momentum dictates that the total transverse momentum of the scattered neutron-proton pair be zero also.

The deviation between the observed and kinematically expected neutron-proton opening angle was calculated by

$$\theta_{\text{sum}} = \theta_n + \theta_p - 84.41^\circ + 0.122 (\theta_n - 32.0^\circ) + 0.0016 (\theta_n - 32.0^\circ)^2 \quad (4.12.3)$$

The linear and quadratic terms were included to account for the variation of the opening angle as a function of neutron scattering angle. A typical opening angle distribution is illustrated in figure (4.12.3). The majority of the width of the distribution is due to proton coulomb multiple scattering within the FST.

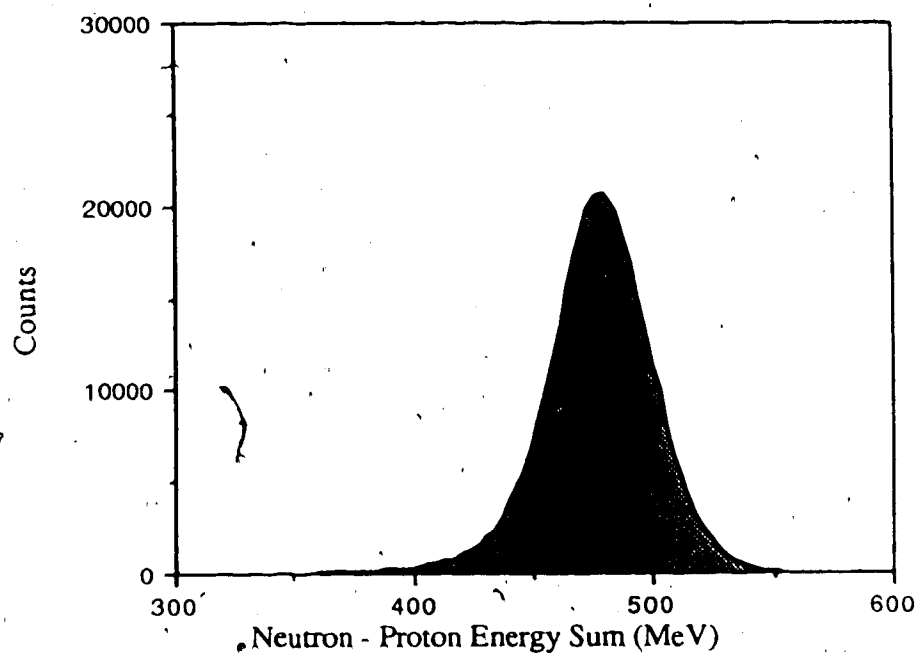


Figure (4.12.1) Neutron-Proton Energy Sum. The energy resolution of the E-sum distribution was approximately 20 MeV.

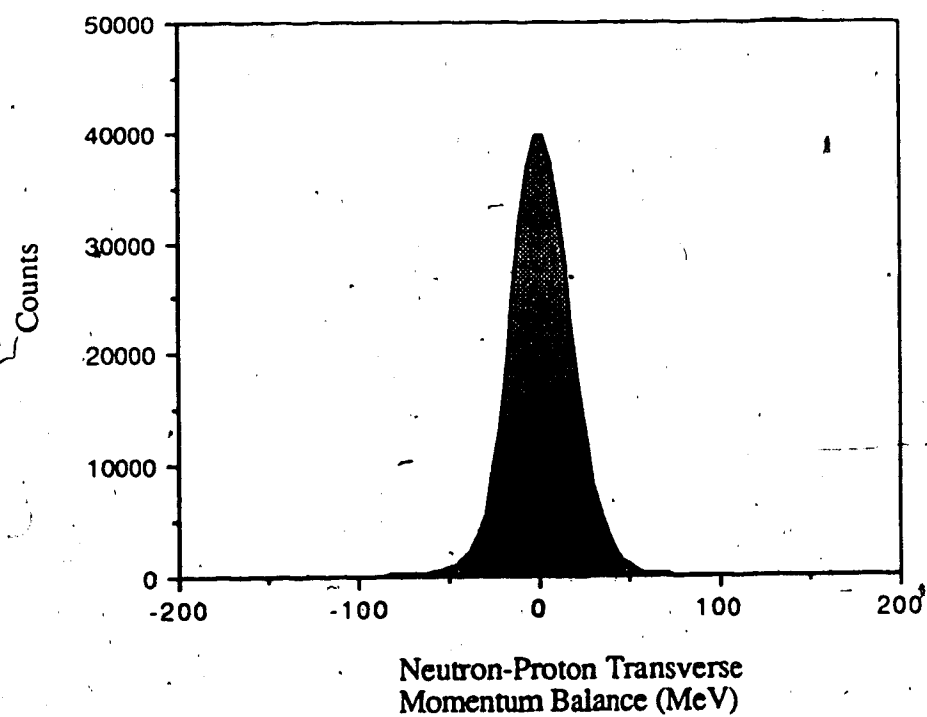


Figure (4.12.2) Transverse Momentum Balance. The resolution of the the transverse momentum balance was approximately 17 MeV.

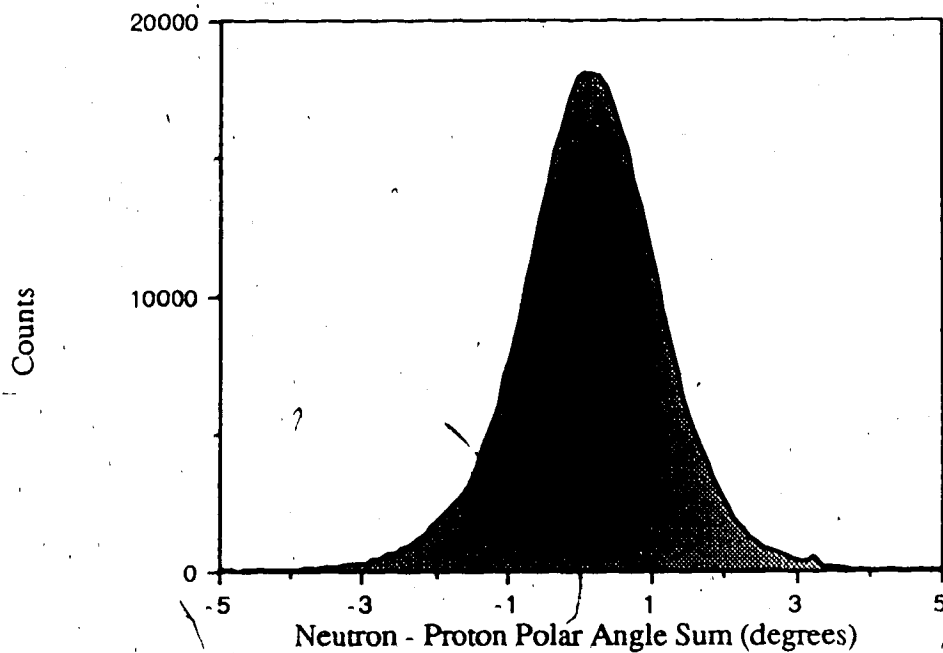


Figure (4.12.3) Opening Angle Distribution.  
The angular resolution of the opening angle distributions was approximately  $0.8^\circ$ .

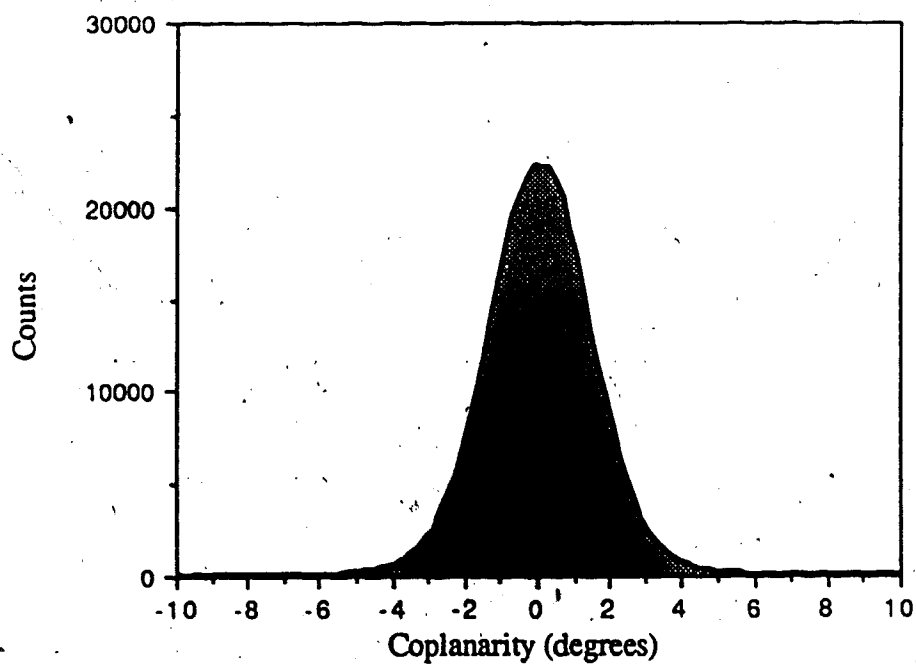


Figure (4.12.4) Neutron-Proton Coplanarity Distribution  
The angular resolution of the coplanarity distribution was typically  $\sigma = 1.4^\circ$ .

The proton-neutron coplanarity was calculated with the relation

$$\varphi_{\text{sum}} = \varphi_n - \varphi_p - 180^\circ, \quad (4.12.4)$$

Conservation of the vertical component of the total momentum dictated that the coplanarity be zero. An example histogram of the neutron-proton coplanarity is illustrated in figure (4.12.4). The width of the coplanarity histogram originated from proton multiple scattering and the inherent  $\pm 7.5$  cm uncertainty in the neutron vertical position.

#### 4.12.2 $\chi^2$ Calculations

The square of the observed difference from the kinematically expected value was calculated for each of the four kinematic observables and divided by the standard deviation of the observed distribution to form the kinematic  $\chi^2$ .

$$\chi_i^2 = \frac{(A_i - \langle A_i \rangle)^2}{\sigma_i^2} \quad (4.12.5)$$

where the index  $i$  represents one of the four kinematic observables (E-sum,  $p_x$ -sum,  $\varphi$ -sum, and  $\theta$ -sum);  $\langle A_i \rangle$  represents the expected value, and  $\sigma_i$  is the standard distribution. The standard distributions were determined from the data. A  $1/P_p$  dependence was used to describe the observed dependence of the standard distribution,

$$\sigma_i = \sigma_0 + B_i \left( \frac{1}{P_p} - \frac{1}{P_0} \right) \quad (4.12.6)$$

Here,  $P_0$  is the proton momentum at the center of the angular acceptance,  $P_p$  is the observed proton momentum, and  $\sigma_0$  is the standard deviation at  $P_p = P_0$ . The standard deviation used in the calculation of the kinematic  $\chi^2$  was correlated to the proton momentum to ensure the consistency of the  $\chi^2$  calculations over the full angular range. Upper and lower limits to the standard deviations were set according to minimum and maximum experimental proton momenta. In figure (4.12.5) the centroids of the opening angle  $\chi^2$  variable distribution as calculated with a constant standard deviation and with a momentum dependent standard deviation are plotted as a function of proton recoil angle.

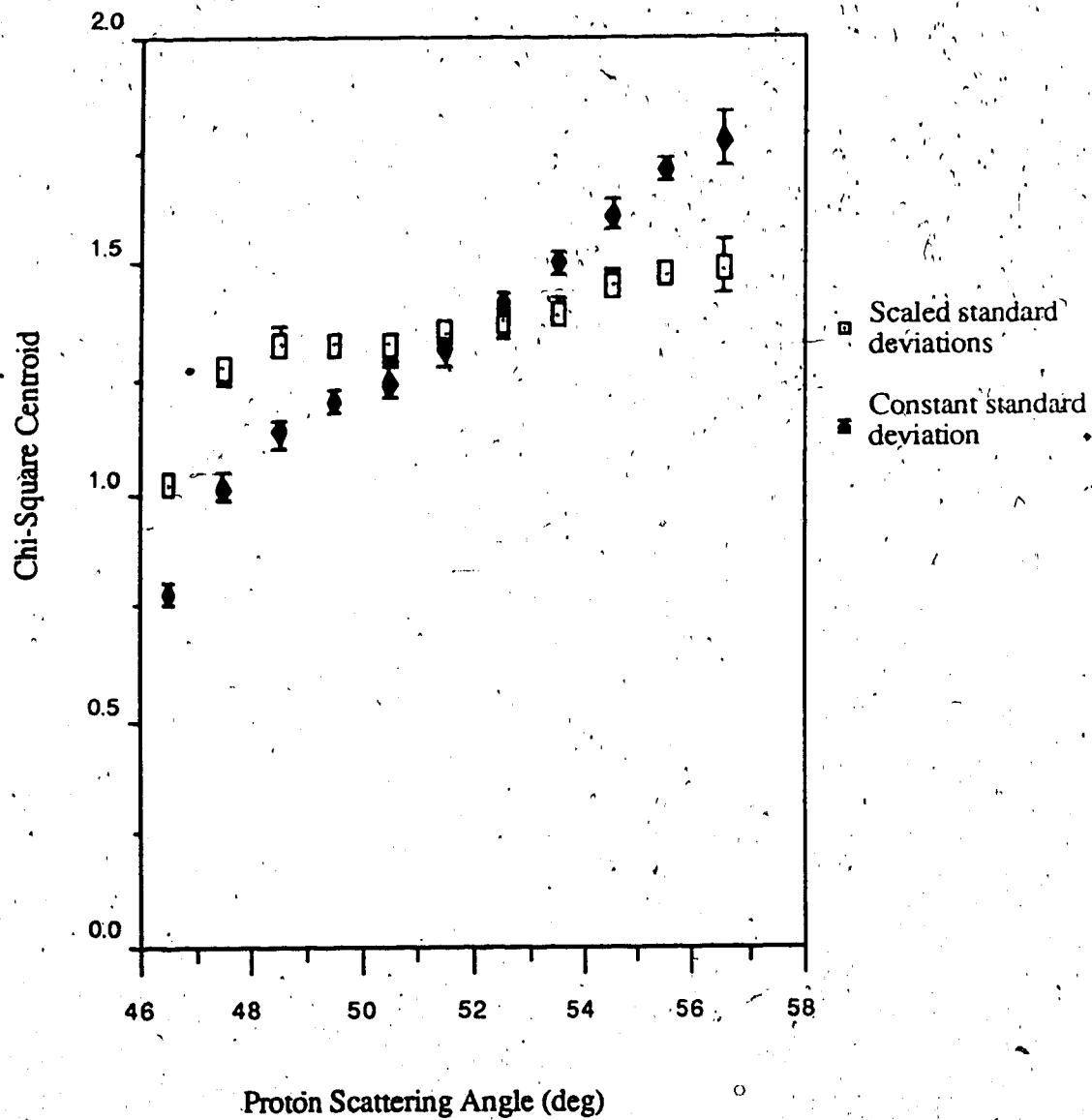


Figure (4.12.5) Centroid of opening angle chi-square distributions as a function of recoil proton angle.

Note the angular dependence of the  $\chi^2$  variable distribution if a constant standard deviation is used. The scaled standard deviation substantially decreases the angular dependence. The standard deviations ranged about their average value by approximately 10%.

#### 4.12.3 Data Constraints

Various constraints were applied to the calculated kinematic  $\chi^2$  variables. In some cases, all  $\chi^2$  variables were forced to be less than a specific value. This condition is expressed as ' $\chi_i^2 < x$ ', where  $x$  represents the position of the cut. Alternatively, constraints may be applied to the sum of the four kinematic  $\chi^2$  variables, the event  $\chi^2$  variable. This constraint is expressed as ' $\Sigma \chi_i^2 < x$ '. Several cuts were employed in the determination of the asymmetry zero-crossing angles. Distributions of the event  $\chi^2$  variable and of a single kinematic  $\chi^2$  variable are illustrated in figure (4.12.6). The positions of the several cuts employed in the analysis,  $\Sigma \chi_i^2 < 10, 15$ , and  $20$  and  $\chi_i^2 < 4, 5$ , and  $7.5$ , are also illustrated in the diagram. The displayed  $\chi^2$  distributions do not reflect ideal  $\chi^2$  distributions because of non-gaussian multiple scattering in the target, a low energy component in the incident neutron energy distribution and the presence of (n,np) background.

The quality of the DLC proton track reconstruction was determined by calculating the variable

$$\Delta^2 = \frac{\sum (x_{\text{recon}} - x_{\text{observed}})^2}{(\text{\#coords-used} - 4)} \quad (4.12.7)$$

Here,  $x_{\text{recon}}$  and  $x_{\text{observed}}$  are the reconstructed and observed DLC coordinates. The sum in equation (4.12.7) extended over the number of valid horizontal and vertical DLC coordinates of the possible eight. A cut was placed at  $\Delta^2 \leq 40$  which rejected approximately 6% of the recorded events. This loose cut was used to avoid unnecessary rejection of events due to proton multiple scattering in individual DLCs; kinematic constraints were used to reject unwanted events.



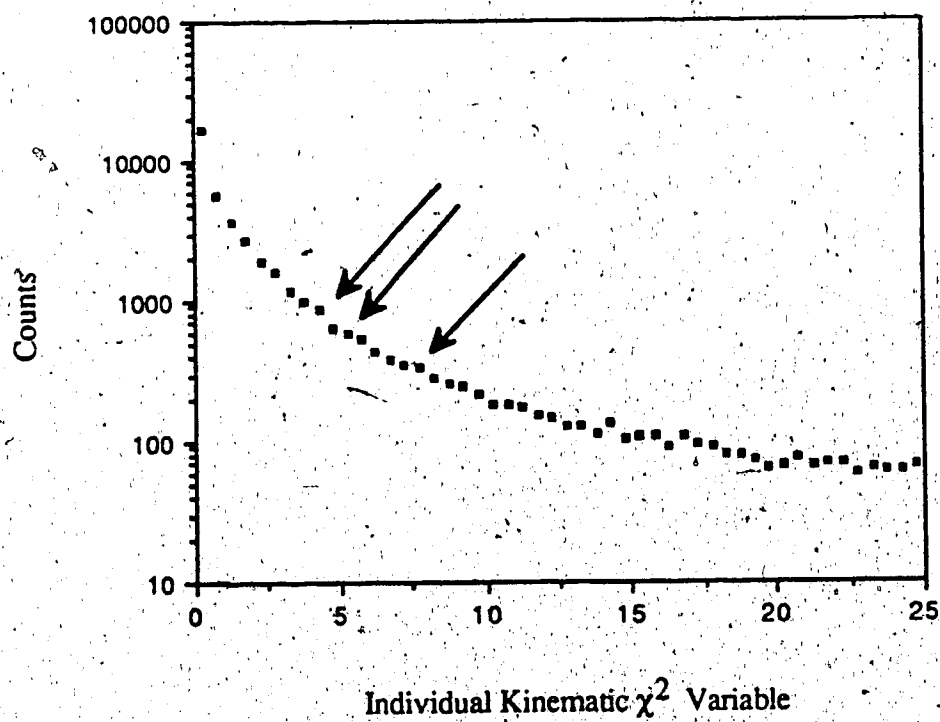
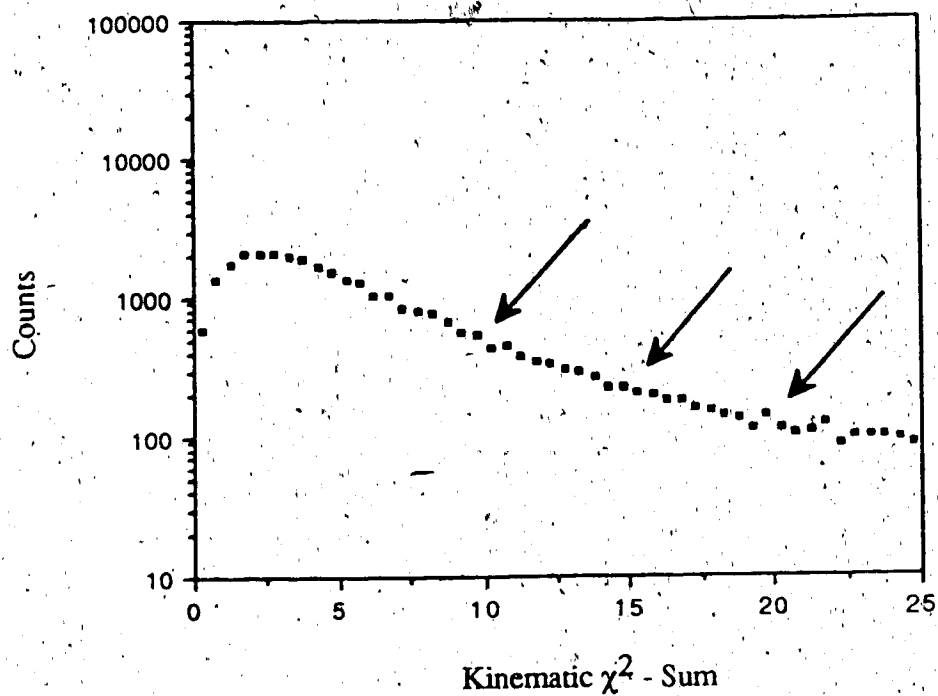


Figure (4.12.6) Sample Distributions of the Kinematic  $\chi^2$  Sum (top) and an Individual Kinematic  $\chi^2$ . The positions of several cuts on the kinematic  $\chi^2$  variable employed in the analysis are shown.

The z-y projection (where y represents the vertical direction and z is the direction of the neutron beam) of the neutron-proton vertex position was calculated with the DLC proton track information. Cuts were placed at

$$-30\text{mm} \leq y_{\text{vertex}} \leq +30\text{mm} \quad (4.12.7a)$$

and

$$-35\text{mm} \leq z_{\text{vertex}} < +35\text{mm}, \quad \text{at } x = 0. \quad (4.12.7b)$$

The cuts on the target image z-coordinate were purposely left rather loose since no corrections were applied to the vertex reconstruction to account for magnetic holding field effects. The vertex image moved by  $\pm 7.2$  mm along the z-direction depending on the holding field direction.

Only a small portion of the outer neutron bars was illuminated by elastically scattered neutrons because of the constraints placed on the experimental solid angle acceptance of the proton detection apparatus. In figure (4.12.7), the angular distribution of protons in coincidence with neutrons detected in the outer neutron bars is compared with the angular distribution of protons detected in coincidence with neutrons observed in the inner five neutron bars. Since fewer elastically scattered events were observed in the outer neutron bars, the proportion of inelastic events to elastic events must be much larger than in the inner neutron bars. Therefore, all events detected in outer neutron bars were excluded from the data set used to calculate the asymmetry zero-crossing angles.

A typical renormalized neutron scintillator bar pulse height distribution is illustrated in figure (4.12.8). The hardware discrimination threshold can be seen near the origin where the pulse height distribution peaks. In order to investigate any possible systematic errors associated with neutron scintillator signals near the hardware discrimination threshold, asymmetry zero-crossing angles were calculated as a function of several cuts on neutron scintillator bar pulse heights as indicated in figure (4.12.8). Cuts were applied at the ADC channels 0, 15, 20 and 25. The results are discussed in section (4.13).

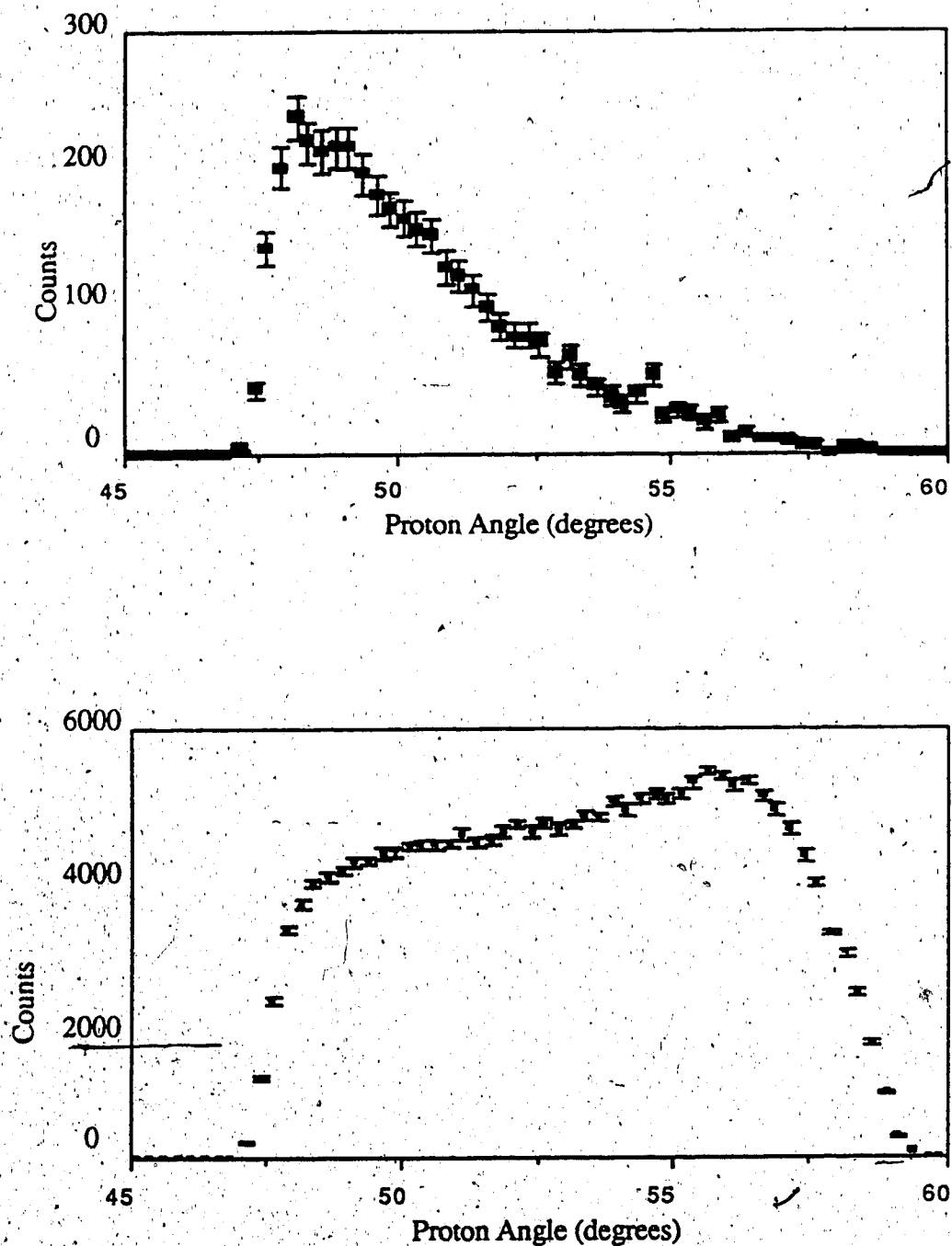


Figure (4.12.7) Detected Proton Angular Distribution with Coincident Neutrons in Outer Neutron Bars (top) and with Coincident Neutrons in Inner Bars (bottom). The peak at small angles of the former distribution is due to the limits on the solid angle acceptance defined by the proton detection apparatus.

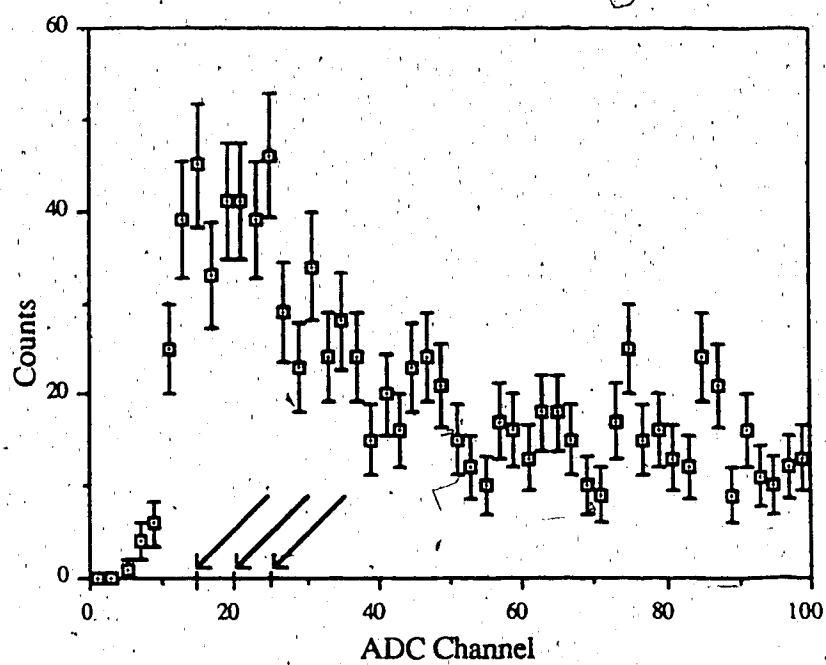


Figure (4.12.8) Single Neutron Bar Phototube ADC Distribution  
The position of the cuts employed in the analysis are displayed.

## 4.13 Elastic Neutron-Proton Scattering Asymmetry Calculation

### 4.13.1 Introduction

The neutron-proton elastic scattering asymmetry was determined from the ratio

$$r = \left( \frac{L^+ R^-}{R^+ L^-} \right)^{1/2} \quad (4.13.1)$$

The superscript represents the proton (neutron) polarization direction for measurements of  $A_p$  ( $A_n$ ). The scattering asymmetry was then

$$\varepsilon = \frac{r - 1}{r + 1} \quad (4.13.2)$$

Errors in asymmetries were calculated from the function

$$\Delta\varepsilon = \left( \frac{r^2}{(1+r)^4} \left( \frac{1}{L^+} + \frac{1}{L^-} + \frac{1}{R^+} + \frac{1}{R^-} \right) \right)^{1/2} \quad (4.13.3)$$

Asymmetries were averaged over both holding field configurations. This method of calculation reduced all systematic errors not associated with target or beam polarization reversals to at most second order near the asymmetry zero-crossing angle. However, the angular region common to protons scattered to the left and right was reduced to approximately  $8.1^\circ$  by the action of the target holding field (see figure 4.13.1). This type of calculation is termed the 'overlap' calculation.

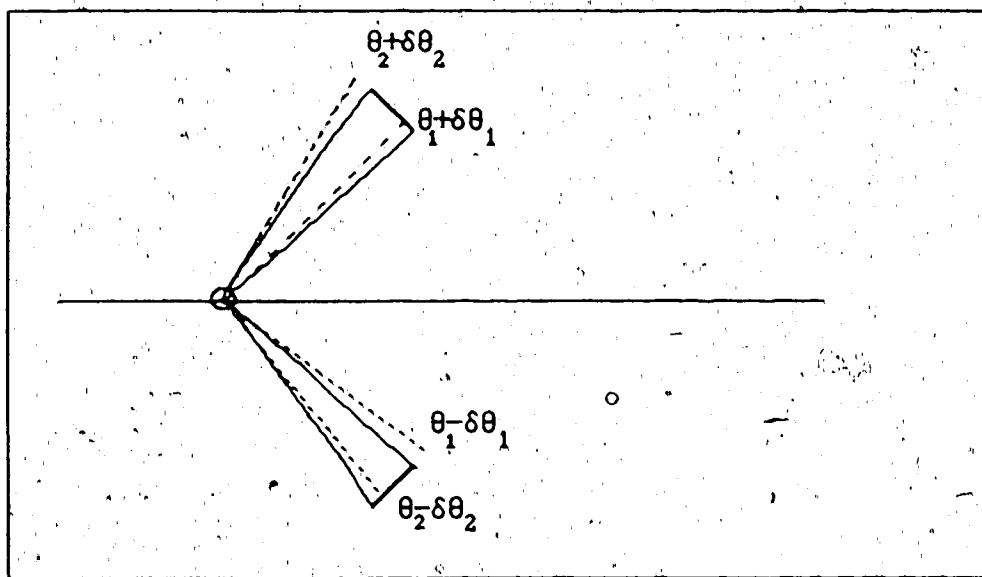


Figure (4.13.1) Schematic Illustration of the Influence of the Target Holding Field on Recoil Proton Angles. The detection apparatus encompasses the angular range  $(\theta_2 - \theta_1)$ . The common angular region to the left and right detection systems is  $(\theta_2 - \theta_1) - (\delta\theta_2 + \delta\theta_1)$ .

Alternatively, asymmetries could be calculated for the entire angular range subtended by the experimental apparatus. This calculation was called the non-overlap calculation. Asymmetries calculated in this manner benefit from improved statistics but are more susceptible to systematic errors. A comparison of the asymmetry calculated via the two methods provides a means of testing consistency among the left and right sets of experimental apparatus. The scattering asymmetry was calculated as

$$\epsilon_L = \frac{L^+ - aL^-}{-L^+ + aL^-} \quad (4.13.4)$$

on the left, and

$$\epsilon = \frac{R^+ - aR^-}{R^+ + aR^-} \quad (4.13.5)$$

on the right. Here, the constant 'a' is the ratio of the total number of left and right events detected for polarization up compared to polarization down in the overlap region,

$$a = \frac{L^+ + R^+}{L^- + R^-} \quad (4.13.6)$$

Events were histogrammed in  $0.25^\circ$  angular bins for  $\theta_p$  and  $\theta_n$ . All calculations required a minimum of 50 events in each bin to guarantee the applicability of gaussian statistics. A typical asymmetry plot for one of the four data-taking runs is illustrated in figure (4.13.2). Asymmetry slopes and zero-crossing angles were calculated with a least squares fit to a straight line. The slope of the observed asymmetry is expressed as  $e'_n$ , where the subscript represents the polarized particle, and the zero-crossing angles are represented as  $\theta_{op}(A_n)$ , where the subscript on the zero-crossing angle,  $\theta_o$ , represents the reference particle from which the asymmetry was determined. For example,  $\theta_{op}(A_n)$  represents the  $A_n$  zero-crossing angle determined from the proton angular distribution.

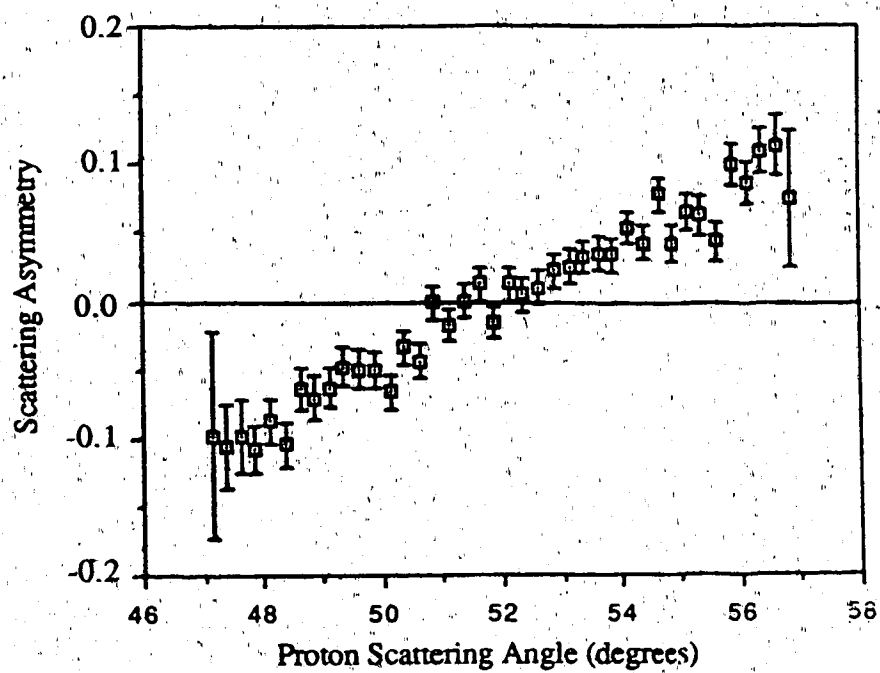


Figure (4.13:2) Typical Asymmetry Curve



### 4.13.2 Asymmetry Slopes

In the following tables, all fits to the asymmetry slopes are presented. Results obtained with the non-overlap calculation are presented beside the result obtained using the overlap calculation of equation (4.13.1). All results displayed were determined with the chi-square constraint  $\chi^2 < 5$ , and with the cut on the neutron scintillator pulse height at  $\text{PHTmin} > 20$ .

Table (4.13.1)  $A_n$  Measurement Asymmetry Slopes  
Target Holding Field Up  
Proton Angle Based,  $\chi^2 < 5$ ,  $\text{PHTmin} > 20$

Run	Left	Right	Non-Overlap	Overlap	NOV - OV
1	0.0143(11)	-0.0137(11)	0.0140(8)	0.0145(10)	-0.0005(6)
2	0.0123(10)	-0.0130(10)	0.0127(7)	0.0117(9)	0.0010(6)
3	0.0130(8)	-0.0128(8)	0.0129(6)	0.0132(7)	-0.0003(4)
4	0.0139(10)	-0.0148(10)	0.0144(7)	0.0142(9)	0.0002(6)

Table (4.13.2)  $A_n$  Measurement Slopes  
Target Holding Field Down  
Proton Angle Based,  $\chi^2 < 5$ ,  $\text{PHTmin} > 20$

Run	Left	Right	Non-Overlap	Overlap	NOV - OV
1	0.0122(10)	-0.0137(10)	0.0130(7)	0.0127(10)	0.0003(6)
2	0.0126(13)	-0.0124(13)	0.0125(9)	0.0133(12)	-0.0008(6)
3	0.0135(8)	-0.0139(8)	0.0137(6)	0.0128(7)	0.0009(4)
4	0.0148(13)	-0.0140(12)	0.0144(9)	-0.0156(11)	-0.0012(6)

Table (4.13.3)  $A_p$  Measurement Slopes  
Target Holding Field Up  
Proton Angle Based,  $\chi^2 < 5$ ,  $\text{PHTmin} > 20$

Run	Left	Right	Non-Overlap	Overlap	NOV - OV
1	0.0175(12)	-0.0191(12)	0.0183(8)	0.0178(11)	0.0005(8)
2	0.0211(10)	-0.0201(10)	0.0206(7)	0.0216(9)	-0.0010(6)
3	0.0202(9)	-0.0190(9)	0.0196(6)	0.0198(8)	-0.0002(5)
4	0.0204(12)	-0.0184(13)	0.0194(9)	0.0200(11)	-0.0006(6)

Values in brackets represent the error of the last digits of each value, and NOV - OV represents the difference between the two types of calculation. The quoted statistical error of the NOV - OV value is representative of the difference in the amount of data used between the two calculations.

**Table (4.13.4)  $A_p$  Measurement Slopes  
Target Holding Field Down  
Proton Angle Based,  $\chi_i^2 < 5$ , PHTmin > 20**

Run	Left	Right	Non-Overlap	Overlap	NOV - OV
1	0.0203(11)	-0.0190(11)	0.0196(8)	0.0208(10)	-0.0012(6)
2	0.0195(15)	-0.0209(14)	0.0202(8)	0.0210(13)	-0.0008(10)
3	0.0199(9)	-0.0189(9)	0.0194(6)	0.0196(8)	-0.0002(6)
4	0.0202(11)	-0.0195(11)	0.0198(8)	0.0210(10)	-0.0012(6)

Results of the asymmetry slope measurements illustrate the consistency between the average of the left and right side measurements utilizing the entire angular range and the overlap calculation using only the  $8^\circ$  angular region common to the left and right detection assemblies. The agreement indicates, but does not prove, that systematic errors do not contribute to the asymmetry calculation.

#### 4.13.3 Asymmetry Zero-Crossing Angles

Asymmetry zero-crossing angles from the four data taking runs calculated from equation (4.13.1) for the overlap region, and the zero-crossing angle calculated as in equation (4.13.4) for the non-overlap region are presented in the tables below.

**Table (4.13.5)  $A_n$  Zero-Crossing Angle**  
**Target Holding Field Up**  
**Proton Angle Based,  $\chi_i^2 < 5$ , PHTmin > 20**

Run	Left	Right	$\theta_{op}(A_n)$ Non-Overlap	Overlap	OV - NOV
1	51.54(23)	51.56(27)	51.55(18)	51.52(19)	-0.03(8)
2	51.81(24)	51.72(26)	51.76(18)	51.76(20)	0.00(8)
3	51.89(18)	51.98(21)	51.93(14)	51.96(14)	0.03(6)
4	51.59(21)	51.60(22)	51.60(15)	51.62(16)	-0.02(6)

**Table (4.13.6)  $A_n$  Zero-Crossing Angle**  
**Target Holding Field Down**  
**Proton Angle Based,  $\chi_i^2 < 5$ , PHTmin > 20**

Run	Left	Right	$\theta_{op}(A_n)$ Non-Overlap	Overlap	OV - NOV
1	52.30(28)	52.18(22)	52.24(18)	52.23(19)	-0.01(6)
2	52.27(34)	51.91(31)	52.09(23)	52.04(22)	-0.05(6)
3	52.09(20)	52.28(17)	52.20(13)	52.25(14)	0.05(5)
4	52.33(28)	52.16(26)	52.30(19)	52.22(18)	-0.08(6)

**Table (4.13.7)  $A_p$  Zero-Crossing Angle**  
**Target Holding Field Up**  
**Proton Angle Based,  $\chi_i^2 < 5$ , PHTmin > 20**

Run	Left	Right	$\theta_{op}(A_n)$ Non-Overlap	Overlap	OV - NOV
1	52.19(20)	52.25(21)	52.22(15)	52.18(15)	-0.02(4)
2	51.81(14)	52.09(17)	51.92(11)	51.93(11)	0.01(3)
3	52.13(14)	52.33(17)	52.21(11)	52.23(11)	0.02(3)
4	52.01(18)	52.10(23)	52.04(14)	52.00(14)	-0.04(4)

**Table (4.13.8)  $A_p$  Zero-Crossing Angles  
Target Holding Field Down  
Proton Angle Based,  $\chi^2_i < 5$ , PHTmin > 20**

Run	Left	Right	$\theta_{op}(A_p)$ Non-Overlap	Overlap	OV - NOV
1	52.42(18)	52.18(17)	52.30(12)	52.25(12)	-0.05(3)
2	52.54(25)	52.06(21)	52.26(16)	52.32(16)	0.06(3)
3	52.09(15)	52.09(14)	52.09(10)	52.07(11)	-0.02(3)
4	52.40(18)	52.08(16)	52.22(12)	52.21(12)	-0.01(3)

The ratio method is consistent with values obtained using the left and right apparatus individually.

Differences between  $A_n$  and  $A_p$  zero-crossing angles as a function of holding field direction are listed in tables (4.13.9) and (4.13.10).

**Table (4.13.9)  $\theta_{op}(A_n) - \theta_{op}(A_p)$   
Target Holding Field Up  
Proton Angle Based,  $\chi^2_i < 5$ , PHTmin > 20**

Run	Left	Right	$\theta_{op}(A_n) - \theta_{op}(A_p)$ Non-Overlap	Overlap	OV - NOV
1	-0.65(30)	-0.69(34)	-0.67(23)	-0.66(24)	0.01(5)
2	-0.01(28)	-0.37(31)	-0.17(21)	-0.17(23)	0.00(5)
3	-0.24(22)	-0.34(27)	-0.28(17)	-0.28(18)	0.00(5)
4	-0.42(28)	-0.50(32)	-0.46(21)	-0.38(21)	0.08(5)

**Table (4.13.10)  $\theta_{op}(A_n) - \theta_{op}(A_p)$   
Target Holding Field Down  
Proton Angle Based,  $\chi^2_i < 5$ , PHTmin > 20**

Run	Left	$\theta_{op}(A_n) - \theta_{op}(A_p)$ (degrees) Right	Non-Overlap	Overlap	
1	-0.12(34)	0.00(28)	-0.05(22)	-0.02(22)	0.03(5)
2	-0.27(43)	-0.15(37)	-0.20(28)	-0.29(28)	-0.09(5)
3	-0.00(25)	+0.19(22)	+0.11(17)	+0.19(18)	0.08(5)
4	-0.06(34)	+0.09(31)	+0.02(23)	+0.01(22)	-0.01(5)

The measurements made with different holding fields are consistent internally but the two groups are separated by approximately two standard deviations. Any systematic error associated with

holding field direction cancels to second order when results obtained with the holding field in both directions are averaged together. These values are presented in table (4.13.11).

**Table (4.13.11)  $\theta_{op}(A_n) - \theta_{op}(A_p)$  - Averaged Over Target Holding Field  
Proton Angle Based,  $\chi^2_1 < 5$ , PHTmin > 20**

Run	Asymmetry Slope				
	Left	Right	Non-Overlap	Overlap	OV - NOV
1	-0.39(23)	-0.34(22)	-0.366(158)	-0.328(163)	0.038(40)
2	-0.14(26)	-0.26(24)	-0.200(176)	-0.219(176)	-0.019(19)
3	-0.12(17)	-0.08(17)	-0.100(121)	-0.051(126)	0.049(35)
4	-0.24(22)	-0.20(22)	-0.226(155)	-0.190(154)	0.036(18)
<b>Weighted Average</b>			<b>-0.205(74)</b>	<b>-0.175(76)</b>	

The two calculations are consistent with one another.

#### 4.13.4 Neutron and Proton Angular Based Asymmetry Calculations

Both outgoing particle angles were recorded. The asymmetry can be expressed as a function of the neutron or proton angle. In order not to confuse the particle angle which the asymmetry calculation was based upon with the particle which was originally polarized, the asymmetries will be referred to as neutron or proton based asymmetry. The consistency between the neutron and proton based asymmetry provides another experimental consistency test. Proton angles were used to calculate the final result. The neutron based calculation was susceptible to additional systematic errors (see the conclusion for a complete summary) which the proton angle based calculation was not. Table (4.13.12) below illustrates the difference in the  $A_n$  and  $A_p$  zero-crossing angles based on the neutron and proton angular distributions.

**Table (4.13.12) Neutron and Proton Angle Based Asymmetry Zero-Crossing Angle**  
 $\chi_i^2 < 5$ , PHTmin > 20

Run Number	Zero-Crossing Angle	
	$\theta_{op}(A_n) - \theta_{op}(A_p)$	$\theta_{on}(A_n) - \theta_{on}(A_p)$
1	-0.328(163)	+0.341(149)
2	-0.219(176)	+0.214(157)
3	-0.051(126)	+0.094(114)
4	-0.190(154)	+0.229(145)
Wtd Average	-0.175(76)	+0.201(69)

The proton and neutron angle based results can not be compared directly because of the slope of the analyzing power is dependent on the scattering angle chosen.

#### 4.13.5 Chi-Square Dependence of Asymmetry Calculations

Asymmetries were determined over a wide range of  $\chi^2$  - cuts. A zero-crossing angle independent of  $\chi^2$  demonstrates the insensitivity of the experiment with respect to background contamination. The  $\chi^2$  - cuts were selected to accept a large percentage of n-p events while keeping the background down to a level where it would have a minimum effect on the asymmetry calculation. Table (4.13.13) below shows the results of differing constraints on the data set.

**Table (4.13.13) Asymmetry Zero-Crossing Angle as a Function of  $\chi^2$  Constraints**  
 Proton Angle Based, PHTmin > 20

Run Number	$\chi_i^2 < 4$	$\chi_i^2 < 5$	$\chi_i^2 < 7.5$	$\chi_i^2 < 9$
1	-0.401(174)	-0.328(163)	-0.332(150)	-0.361(149)
2	-0.292(180)	-0.219(176)	-0.202(162)	-0.232(159)
3	-0.006(160)	-0.051(126)	-0.048(116)	-0.081(114)
4	-0.199(160)	-0.190(154)	-0.195(145)	-0.204(142)
Wtd Average	-0.190(79)	-0.175(76)	-0.173(70)	-0.198(69)

There is no significant dependence on the result as a function of  $\chi^2$  - cut.

#### 4.13.6 Dependence of Asymmetry on Neutron Bar PHT Discrimination Threshold

Effects associated with cuts on the neutron software discrimination threshold were investigated by comparing results obtained with a number of cuts. Table (4.13.14) contains the differences in the zero-crossing angles as a function of cuts on the ADC channel of the neutron bar PHT signal.

**Table (4.13.14) Asymmetry Zero-Crossing Angle as a Function of Neutron Bar Pulse Height Cut**  
Proton Angle Based,  $\chi_i^2 < 5$

Run Number	No PHT cut	Channel 15 (0.84 MeVee)	Channel 20 (1.12 MeVee)	Channel 25 (1.4 MeVee)
1	-0.347(156)	-0.315(159)	-0.328(163)	-0.332(166)
2	-0.188(164)	-0.221(171)	-0.219(176)	-0.194(179)
3	-0.036(120)	-0.004(124)	-0.051(126)	-0.083(129)
4	-0.178(150)	-0.162(151)	-0.190(154)	-0.190(155)
Wtd Average	-0.165(72)	-0.150(74)	-0.175(76)	-0.183(77)

The definitive cut used in the asymmetry calculation was positioned at the ADC channel 20 after pedestal subtraction and PHT signal calibration. This cut was just beyond the hardware discrimination threshold (this can be seen in figure 4.12.8) in order to achieve maximum detection efficiency but not to include possible behaviour defects at or near the hardware threshold. Table (4.13.14) reveals no trends in the results as a function of neutron bar threshold discrimination.

#### 4.13.7 Asymmetry Calculation Utilizing Outer Neutron Bars

The outer neutron bars were outside the experimental acceptance for n-p events with no proton multiple scattering (see section 4.12). Neutrons striking the outer bars either singly or in coincidence with adjacent bars were not included in the analysis. Their inclusion

would result in an increased background to elastic event ratio.

**Table (4.13.15) Asymmetry Zero-Crossing Angle with  
and without Outer Neutron Bars  
Proton Angle Based,  $\chi^2 < 5$ , PHTmin > 20**

Run Inner	Neutron Bars	Outer Neutron Bars	All Neutron Bars
1	-0.328(163)	-0.4(40)	-0.290(160)
2	-0.219(176)	+0.2(12)	-0.179(170)
3	-0.051(126)	-2.7(46)	-0.042(125)
4	-0.190(154)	-2.4(20)	-0.201(152)
Wtd Average	-0.175(76)	-0.6(17)	-0.160(74)

The 50 event per bin requirement was relaxed to 10 events per bin for the outer bar asymmetry calculation because of the fewer number of outer bar events which passed the  $\chi^2$  constraints. Results obtained with the outer neutron bars alone are consistent within the given statistical accuracy with those obtained with inner bars alone. Including the outer bars increases the solid angle subtended by the neutron detection array by 7 / 5 but does not increase the number of observed elastic events by a similar factor because the outer bars are outside the angular acceptance defined by the proton detection assembly.

#### 4.13.8 Comparison of $A_n$ and $A_p$ Slopes with Measured Beam and Target Polarizations

The observed slope of the scattering asymmetry is related to the beam or target polarization by

$$\epsilon_n' = P_n A_n' \quad (4.13.7a)$$

and

$$\epsilon_p' = P_p A_p' \quad (4.13.7b)$$

where the subscripts represent the polarized proton or neutron and the prime denotes the slope with respect to the proton scattering angle. The neutron polarization was related to the primary proton beam polarization with the relation



$$P_n = P_p (d_{okko}^2 + d_{okso}^2)^{1/2} \quad (4.13.8)$$

Here,  $P_p$  is the primary proton beam polarization,  $P_n$  is the neutron beam polarization and  $(d_{okko}^2 + d_{okso}^2)^{1/2}$  is the magnitude of appropriate Wolfenstein polarization transfer coefficient corrected for final state interactions at  $90^\circ$  in the lab. As discussed in section (4.6), the magnitude of the polarization transfer coefficient can be taken as  $(d_{osso}^2 + d_{okso}^2)^{1/2} = 0.7496$ . The slope of the scattering asymmetry with respect to the lab proton scattering angle was taken as  $A' = 0.0263^{(3.3)}$ . Relations (4.13.7a) and (4.13.7b) can be combined to give

$$\frac{(d_{osso}^2 + d_{okso}^2)^{1/2} P_p A'_n}{P_p A'_p} = \frac{\epsilon_n}{\epsilon_p} \quad (4.13.9)$$

In this manner, the ratio of the measured asymmetry slopes can be compared to the observed proton beam and target polarizations. Differences between  $A'_n$  and  $A'_p$  due to charge symmetry breaking effects are very small and were neglected. Values of asymmetry slopes and average beam and target polarizations are shown in table (4.13.16) for each of the four data taking runs. Each run is divided according to the direction of the target holding field.

**Table (4.13.16) Asymmetry Slopes and Polarization Measurements**  
Proton Angle Based,  $\chi_i^2 < 5$ , PHTmin > 20

Run	Holding Field	$P_{beam}$	$P_{target}$	$P_n / P_{target}$	$\epsilon_p / \epsilon_n$	Difference
1	up	0.658	0.670±0.016	1.334±0.032	1.23±0.16	0.10(16)
	down	0.623	0.643±0.016	1.352±0.034	1.64±0.19	-0.29(19)
2	up	0.646	0.853±0.020	1.730±0.041	1.85±0.22	-0.12(22)
	down	0.647	0.847±0.020	1.716±0.040	1.58±0.24	0.14(24)
3	up	0.660	0.830±0.014	1.648±0.027	1.50±0.14	0.15(14)
	down	0.659	0.784±0.014	1.559±0.028	1.53±0.14	0.03(14)
4	up	0.660	0.751±0.021	1.491±0.042	1.41±0.17	0.08(17)
	down	0.665	0.820±0.021	1.616±0.041	1.35±0.17	0.27(17)

Statistical errors associated with the proton beam polarization were negligible. Target polarizations were determined with a nuclear magnetic resonance system. The weighted average of ratios from the above table is  $0.966 \pm 0.014 \pm 0.04$ , where the first quoted error is statistical, and the second systematic. Systematic errors are due to uncertainties in the p-p

analyzing power (at  $17^\circ$ ,  $A = 0.513$ , see section 4.6) and in the neutron beam spin precession ( $\pm 5^\circ$ ). The good agreement between the two measurements provided a convenient check on the internal consistency of the experiment.

## 4.14 Background Reduction

### 4.14.1 Background Sources and Effects

The experiment was designed to measure the difference in the  $A_n$  and  $A_p$  zero-crossing angles. Even a small contribution to the asymmetry from neutron-proton pairs originating from processes other than elastic scattering could have shifted the apparent neutron-proton scattering asymmetry zero-crossing angle. To measure the fraction of (n,np) background and its effect on the elastically scattered neutron-proton asymmetry zero-crossing angle, the target was filled with graphite beads and the resultant asymmetry was measured.

Hardware and software restrictions reduced the number of neutron-proton events originating from quasi-elastic reactions in the target material and support structure. The background event rate was reduced with the wedge-shaped energy degrader which only transmitted protons with energies in the range of recoil elastically scattered protons and above. Overly energetic protons were flagged in a veto-counter (see section 3.9.1) following the E-counter and an additional absorber. The sides of the outer target canister were not illuminated by the collimated neutron beam. The proton TOF start counters (see section 3.9.1) were designed not to view the outer target canister entrance and exit walls. Two 50 cm<sup>3</sup> empty spaces were located above and below the target container to keep a large part of the target support structure out of the main neutron beam flux. Constraints on kinematic observables further reduced quasi-elastic contamination.

Inelastic processes influence the  $A_n$  measurement if any of the quasi-elastic scattering asymmetries, such as  $^{12}\text{C}(n,np)$ ,  $^4\text{He}(n,np)$ , and  $^{16}\text{O}(n,np)$  are non-zero. The presence of background results in a non-zero shift in  $A_n$  at the zero-crossing angle equal to

$$\Delta A_n = r_b A_b \quad (4.14.1)$$

Here,  $r_b$  represents the ratio of background to observed events satisfying a given  $\chi^2$  condition, and  $A_b$  is the background asymmetry. This factor must remain below  $10^{-3}$  (see appendix A) if background effects on  $\Delta A$  are to remain negligible compared to the experimental statistical accuracy.

Since an unpolarized neutron beam impinging on unpolarized target contaminants can not in itself cause a left - right scattering asymmetry, inelastic contamination decreased

the slope of the  $A_p$  asymmetry curve, effectively lessening the FST polarization, but caused no shift in the  $A_p$  zero-crossing angle.

Background events consisted of (n,np) reactions from  $^4\text{He}$  refrigerant,  $^{12}\text{C}$  and  $^{16}\text{O}$  within butanol ( $\text{C}_4\text{H}_9\text{OH}$ ) and from the target support structure. A closer inspection of the background role in the  $A_n$  measurement was made by replacing the conventional target butanol beads with graphite beads. Replacing the conventional butanol beads with graphite beads removed most of the hydrogen from within the target but left the relative mass ratios of the various background sources approximately intact.

Conventionally, button protons ( see sections 3.10.4 and 4.11.1) were used to continuously calibrate neutron detector photomultiplier gains and timing characteristics. However, such button protons could not be used during the background run for two reasons. First, there were an insufficient number for the accuracy needed. Second, and more important, the energy distribution from button protons produced via the  $^{12}\text{C}(\text{n},\text{Xp})$  reaction differed from the energy distribution of button protons from simple (n,p) scattering; therefore, a calibration to the background button protons would provide a false calibration. An alternate method was found to calibrate the neutron detectors. Halfway through the background run, a polyethylene ( $\text{CH}_2$ ) collar was attached to the FST. Button protons were collected to provide the necessary calibrations.

#### 4.14.2 Background Fraction of Butanol Target Data

To calculate the effect of the background on the  $A_n$  measurement, the contamination fraction must first be determined. It is impossible to determine this fraction from the butanol data alone. Even at large  $\chi^2$ , background events cannot be distinguished from neutron-proton elastic scattering events. Non-Gaussian proton multiple scattering, as well as the low energy tail in the incident neutron energy distribution cause the observed event chi-square distribution to deviate from the ideal. The number of background events within the butanol data satisfying  $\chi_i^2 < 5$  (see section 4.12) was estimated by scaling the number satisfying the equivalent condition in the graphite target data by the ratios of relative carbon concentrations and integrated neutron fluxes. Inelastic events in the graphite data must first be distinguished from elastic events or else the butanol target inelastic fraction will be over-estimated.

Events originating from small amounts of hydrogen dominate the number of

observed events because of the larger elastic scattering cross section. The depolarizing resistor located in the base of the target cannister (see section 3.8) contained approximately 11 mg of hydrogen. As illustrated in figure (4.14.1), the location of the resistor is clear on the neutron-proton vertex image taken during the background run. For this reason, the target was artificially divided during the analysis. Only events originating from the top half of the target were used during the analysis.

Event  $\chi^2$  distributions of events detected from the top and bottom halves of the graphite bead filled target are illustrated in figures (4.14.2) and (4.14.3). A sample  $\chi^2$  distribution from the butanol target is shown in figure (4.14.4) for comparison. Note the pronounced elastic peak in the histogram taken from the bottom half of the target. If the distribution from the top half is subtracted from the bottom half, after a suitable normalization to account for the volume difference, the result closely resembles the chi-square distribution from the butanol target data. This elastic peak is clear evidence that a large percentage of the graphite target events are truly inelastic and not poorly calibrated elastics.

An unknown fraction of the graphite target events satisfying  $\chi_i^2 < 5$  are neutron-proton elastic events originating from the hydrogenous target insulation. This fraction must be calculated. Consider plots of the neutron-proton coplanarity (the neutron-proton azimuthal angle sum) produced from the butanol and graphite targets (figures 4.14.5 and 4.14.7). All events in the two histograms satisfied the  $\chi^2 < 5$  condition for the other three kinematic observables. Events from all neutron bars were accepted. The graphite target histogram consists of an elastic peak atop a wide, nearly flat background. The flat background distribution is similar in shape to the coplanarity distribution of events which triggered the proton boom veto counter illustrated in figure (4.14.6). Events which triggered the veto counter passed through a brass absorber which stopped elastically scattered protons. A polynomial fit to the background is illustrated. The number of inelastic events was estimated by integrating under the fit between limits defined by the cut on the coplanarity  $\chi^2$  variable. The number of background events from the inner neutron bars only was calculated by scaling the number from all neutron bars by a factor of 5 / 7 to account for the difference in solid angle.

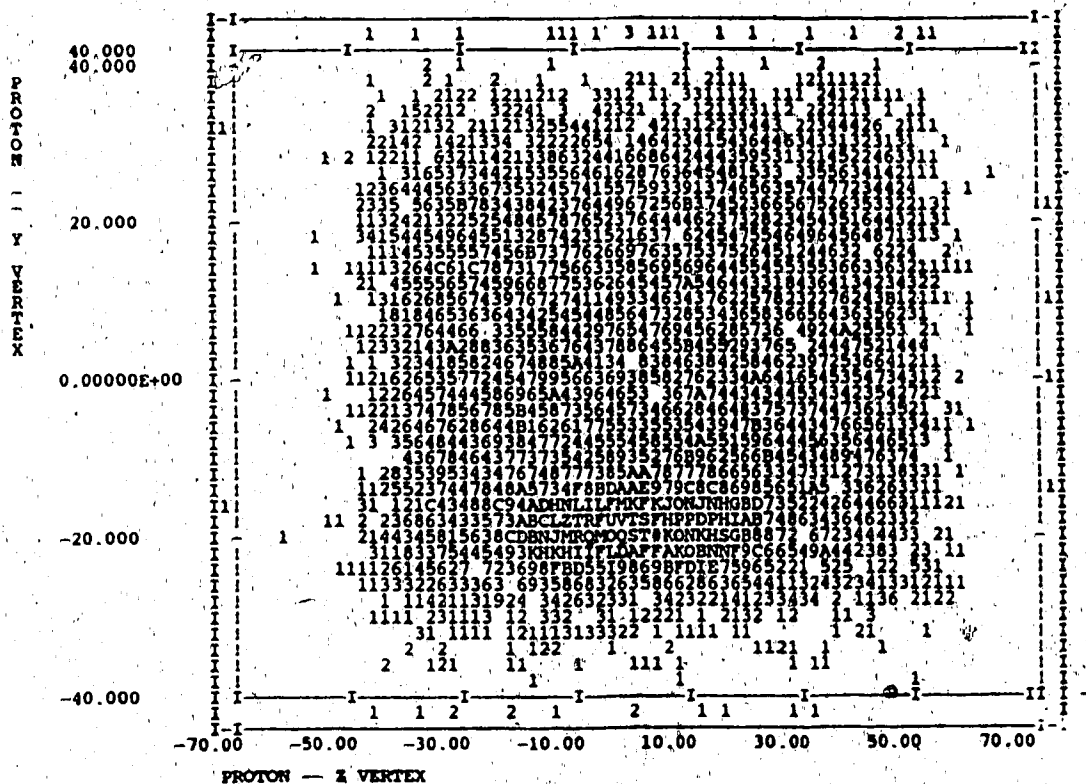


Figure (4.14.1) Background Run Target Neutron-Proton Vertex Image  
 Note the clear peak in the base of the target cannister showing the  
 location of the hydrogen-rich depolarizing resistor.

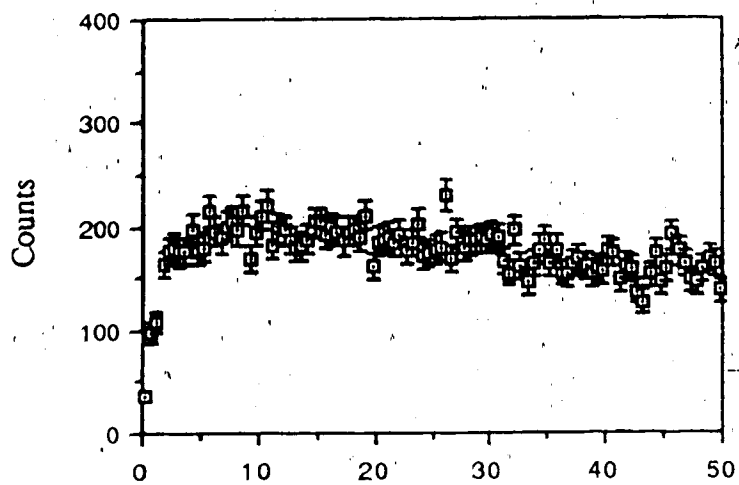


Figure (4.14.2) Top Half of Graphite Target  
summed  $\chi^2$  Distribution

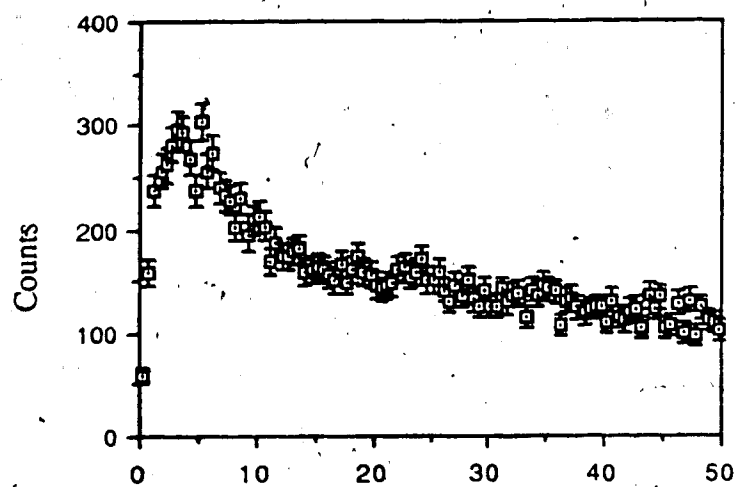


Figure (4.14.3) Bottom Half of Graphite Target  
Summed  $\chi^2$  Distribution

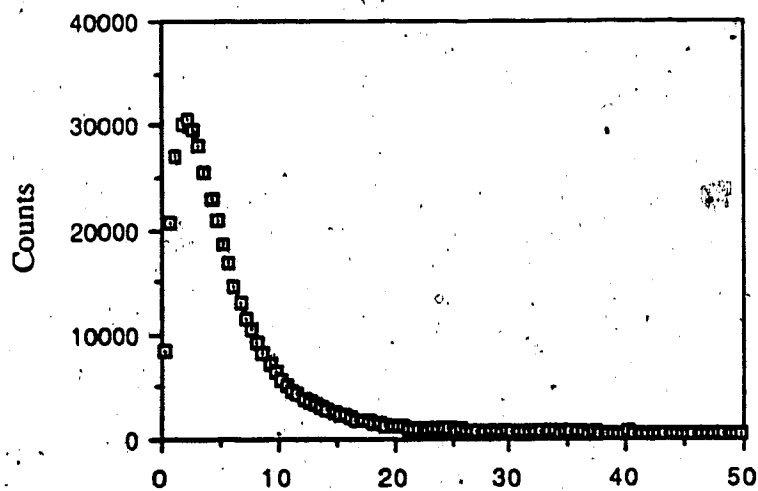


Figure (4.14.4) Butanol Target Summed  $\chi^2$   
Distribution

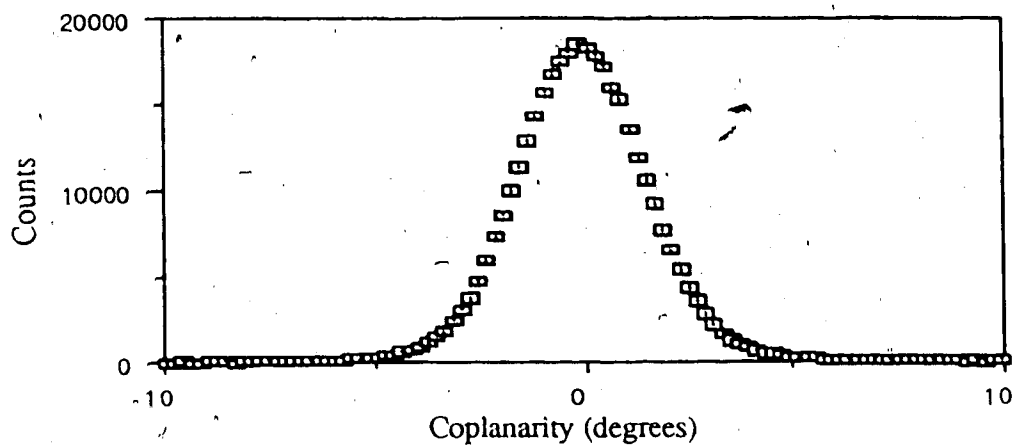


Figure (4.14.5) Butanol Target Elastic Event Coplanarity Distribution

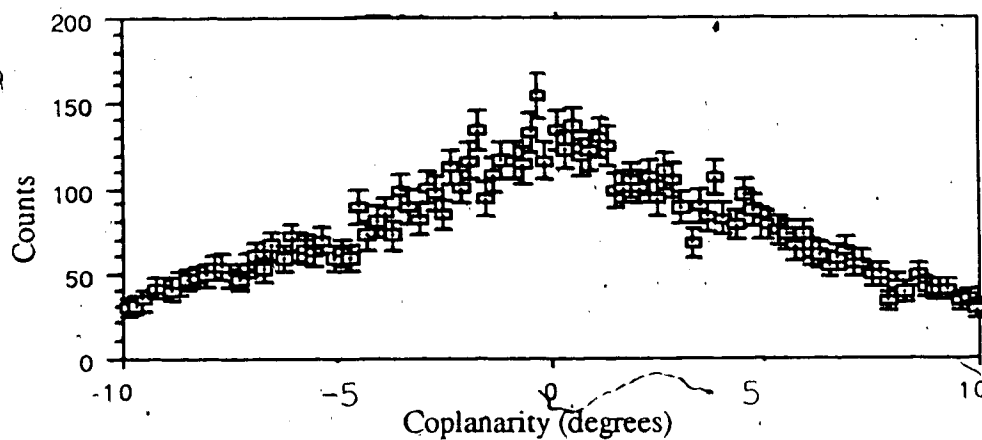


Figure (4.14.6) Butanol Target Veto-Event Coplanarity Distribution

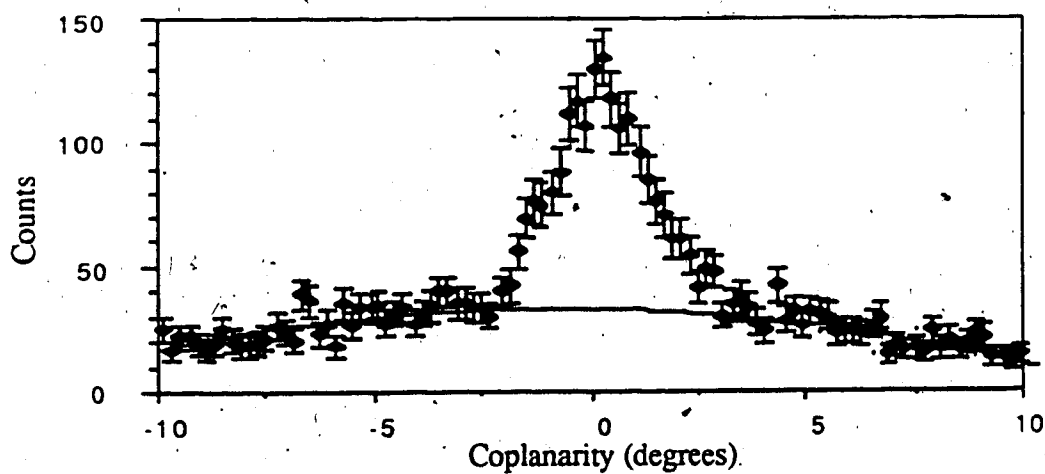


Figure (4.14.7) Observed Background Event Coplanarity Distribution with Top Half of Graphite Target



TABLE (4.14.1) Inelastic Event Fraction from Graphite Target  
(inner bars,  $\chi^2 < 5$ )

Event Type	Holding Field	Total Observed Events	Inelastic Events	Elastic Events	Inelastic Event Fraction
Left	Up	2966	885±130	2080	0.30±0.04
Right	Up	2555	664±100	1891	0.26±0.04
Left	Down	1913	636±100	1277	0.33±0.05
Right	Down	2158	686±100	1472	0.32±0.05

Errors associated with the number of inelastic events were calculated on the basis of results obtained with various fits to the data. The ratio of the number of inelastic events to the total obtained with the graphite target in place are needed in the section pertaining to the inelastic asymmetry calculation. Since the angular acceptance of the left and right apparatus differed because of the action of the target holding field, and since the two magnetic field configurations were not perfectly symmetric because of the cyclotron fringe field, estimates were made of the background fraction for both holding field directions and for both left and right event types (left and right event types follow the convention defined in section 3.1).

An estimate of the background fraction as a function of  $\chi^2$  cut can be made. The ratio of neutron-proton elastic events which pass the  $\chi^2 < 5$  constraint to any other constraint can be estimated from the butanol target data. Given this ratio, the number of elastic graphite target events can be determined as follows,

$$\frac{\text{elastic } N(\chi^2 < A)_{\text{Graphite Target}}}{\text{elastic } N(\chi^2 < 5)_{\text{Graphite Target}}} = \frac{\text{elastic } N(\chi^2 < A)_{\text{Butanol Target}} [1 - f_b(\chi^2 < A)]}{\text{elastic } N(\chi^2 < 5)_{\text{Butanol Target}} [1 - f_b(\chi^2 < 5)]} \quad (4.14.2)$$

where  $N(\chi^2 < A)$  represents the number of elastically scattered neutron-proton pairs satisfying a given  $\chi^2$  constraint,  $N(\chi^2 < A)$  represents the total number of events satisfying the given  $\chi^2$  constraint, and  $f_b(\chi^2 < A)$  represents the fraction of background events to the total observed while the butanol target was in place. As yet,  $f_b(\chi^2 < A)$  is unknown. However, such correction factors are small (this is shown later) and can be neglected.

The background fractions as a function of  $\chi^2$  constraint are shown in table (4.14.2).

Since table (4.14.1) shows that the background fraction does not noticeably depend on the target holding field direction, it is neglected in table (4.14.2).

**Table (4.14.2) Graphite Target Inelastic Event  
Fraction as a Function of  $\chi^2$  Cut (inner neutron bars)**

Chi-Square Constraint	Number of Graphite Target Events	$\frac{N(\chi^2 < A)}{N(\chi^2 < 5)}$ elastic	Number of Elastics	Number of Inelastics	Graphite Target Inelastic Fraction
$\chi_i^2 < 4$	7667	0.889	5975	1692	0.22
$\chi_{i2}^2 < 5$	9592	1.000	6721	2871	0.30±0.04
$\chi_{i2}^2 < 7.5$	14150	1.155	7763	6387	0.45
$\chi_i^2 < 9$	16750	1.206	8106	8644	0.52
$\Sigma \chi_{i2}^2 < 10$	11257	1.091	7332	3925	0.35
$\Sigma \chi_{i2}^2 < 15$	16499	1.218	8186	8314	0.50
$\Sigma \chi_i^2 < 20$	21650	1.277	8583	13067	0.60

The amounts of carbon in the butanol and graphite targets are shown in table (4.14.3).

**Table (4.14.3) Carbon Mass in Butanol and Graphite Target Material**

Run	Carbon Mass (gm)
1	26.0±4.0
2	26.0±2.0
3	23.0±2.0
4	26.0±2.0
background	29.7±0.02

The butanol bead density was taken  $0.9 \text{ gm/cm}^3$  (48) and a packing fraction of 0.6 was assumed. The  $^{12}\text{O}$  within butanol ( $\text{C}_4\text{H}_9\text{OH}$ ) was treated as  $^{12}\text{C}$  in the carbon mass calculation. The graphite bead density was measured as  $0.684 \pm 0.001 \text{ gm/cm}^3$  including the packing fraction. The average amount of carbon in the butanol target, weighted according to the neutron beam flux on the FST target during each of the four butanol target  $A_n$  measurements, was  $24.8 \pm 1.3 \text{ gm}$ . Other sources of background within the FST target common to all runs viewed by the proton time-of-flight system are listed in table (4.14.4).

**TABLE (4.14.1) Inelastic Event Fraction from Graphite Target**  
(inner bars,  $\chi^2 < 5$ )

Event Type	Holding Field	Total Observed Events	Inelastic Events	Elastic Events	Inelastic Event Fraction
Left	Up	2966	885±130	2080	0.30±0.04
Right	Up	2555	664±100	1891	0.26±0.04
Left	Down	1913	636±100	1277	0.33±0.05
Right	Down	2158	686±100	1472	0.32±0.05

Errors associated with the number of inelastic events were calculated on the basis of results obtained with various fits to the data. The ratio of the number of inelastic events to the total obtained with the graphite target in place are needed in the section pertaining to the inelastic asymmetry calculation. Since the angular acceptance of the left and right apparatus differed because of the action of the target holding field, and since the two magnetic field configurations were not perfectly symmetric because of the cyclotron fringe field, estimates were made of the background fraction for both holding field directions and for both left and right event types (left and right event types follow the convention defined in section 3.1).

An estimate of the background fraction as a function of  $\chi^2$  cut can be made. The ratio of neutron-proton elastic events which pass the  $\chi^2 < 5$  constraint to any other constraint can be estimated from the butanol target data. Given this ratio, the number of elastic graphite target events can be determined as follows,

$$\begin{array}{c} \text{elastic} \\ N(\chi^2 < A) \\ \text{Graphite} \\ \text{Target} \end{array} = \begin{array}{c} \text{elastic} \\ N(\chi^2 < 5) \\ \text{Graphite} \\ \text{Target} \end{array} \frac{\begin{array}{c} N(\chi^2 < A) [1 - f_b(\chi^2 < A)] \\ \text{Butanol} \\ \text{Target} \end{array}}{\begin{array}{c} N(\chi^2 < 5) [1 - f_b(\chi^2 < 5)] \\ \text{Butanol} \\ \text{Target} \end{array}} \quad (4.14.2)$$

where  $N(\chi^2 < A)$  represents the number of elastically scattered neutron-proton pairs satisfying a given  $\chi^2$  constraint,  $N(\chi^2 < 5)$  represents the total number of events satisfying the given  $\chi^2$  constraint, and  $f_b(\chi^2 < A)$  represents the fraction of background events to the total observed while the butanol target was in place. As yet,  $f_b(\chi^2 < A)$  is unknown. However, such correction factors are small (this is shown later) and can be neglected.

The background fractions as a function of  $\chi^2$  constraint are shown in table (4.14.2).

Where  $m_B$  is the mass of the target structure viewed by the proton time-of-flight apparatus plus the average mass of carbon present in the target butanol,  $m_G$  is the mass of the target and the graphite contained within during the background run, and  $f_t$  is the fraction of background originating from the top half of the target.

The neutron flux on the FST target was directly proportional to the proton current on the liquid deuterium target. The primary beam current was measured with two devices, the BEM-Proton polarimeter assembly, and the SEM downstream of the neutron production target (see figure 3.1.1). The SEM results were used in the background calculations since they were not affected by hydrogen loss, nor were they altered throughout the experiment. The polarimeter target thickness and composition was frequently changed. The integrated SEM counts for the  $A_n$  measurement is shown in table 4.14.5. All three proton polarization states were used in the  $A_p$  measurement, and only unpolarized protons were used in the  $A_n$  measurement.

**Table (4.14.5) Integrated Counts on SEM 4AM5 During  $A_n$  Measurement**

Run Number	Integrated SEM Counts ( $\times 10^7$ )					
	Holding Field Up			Holding Field Down		
	Up	Down	Off	Up	Down	Off
1	6.31	6.43	2.27	7.05	6.73	2.17
2	8.77	8.30	3.12	4.62	6.00	1.77
3	16.63	16.40	6.01	15.60	15.47	4.96
4	9.17	8.95	3.52	5.70	5.72	2.32
<b>Butanol Total</b>	<b>40.88</b>	<b>40.08</b>	<b>14.92</b>	<b>32.97</b>	<b>33.92</b>	<b>11.15</b>
<b>Graphite Total</b>	<b>11.57</b>	<b>10.54</b>	<b>3.56</b>	<b>7.87</b>	<b>7.73</b>	<b>2.42</b>

Unpolarized beam was used to calibrate the proton and neutron polarimeters during the  $A_n$  measurement. Statistical errors in the SEM counts are completely negligible, but the relation between SEM counts and the neutron flux on the FST target could be influenced by small changes in the cyclotron beam tune. The cyclotron was retuned on a daily basis while changing from polarized to unpolarized beam. The influences of the frequent changes in beam tune can be investigated by comparing the ratio of the number of neutron-proton elastic scattered pairs to the SEM count over a single run. Data from separate runs can not be directly compared because of changes in target volume.

The fraction of inelastic to elastic events is given by the relation,

$$f_b = \frac{\text{SEM Butanol Target}}{\text{SEM Graphite Target}} \cdot \frac{m_b}{f_t m_G} \cdot \frac{\text{Background } N(\chi_i^2 < 5) \text{ Graphite Target}}{\text{Background } N(\chi_i^2 < 5) \text{ Butanol Target}} \quad (4.14.4)$$

The results are shown in table (4.14.6).

**Table (4.14.6) The Background Fraction**  
(inner neutron bars,  $\chi_i^2 < 5$ )

Event Type	Holding Field Direction	Mass Normalization (But / Graphite)	SEM Normalization (But / Graphite)	Graphite Target Background Events	Butanol Target Events	Background Fraction
Left	Up	1.79±0.14	3.73	885±130	6.417e+5	0.009±0.003
Right	Up	1.79±0.14	3.73	664±100	5.722e+5	0.008±0.003
Left	Down	1.79±0.14	4.33	636±100	4.598e+5	0.011±0.003
Right	Down	1.79±0.14	4.33	686±100	5.237e+5	0.010±0.003

Approximately one percent of the data used in the asymmetry calculation is from inelastic reactions. Packing fractions were identical for both target materials.

An estimate of the background fraction in the butanol target data can be made based on the results in table (4.14.3) and (4.14.6).

**Table (4.14.7) Butanol Target Inelastic Event  
Fraction as a Function of Chi-Square Cut**

Chi-Square Cut	Butanol Target Inelastic Fraction
$\chi_i^2 < 4$	$0.007 \pm 0.002$
$\chi_i^2 < 5$	$0.010 \pm 0.003$
$\chi_i^2 < 7.5$	$0.015 \pm 0.004$
$\chi_i^2 < 9$	$0.017 \pm 0.005$
$\Sigma \chi_i^2 < 10$	$0.012 \pm 0.003$
$\Sigma \chi_i^2 < 15$	$0.017 \pm 0.005$
$\Sigma \chi_i^2 < 20$	$0.020 \pm 0.006$

#### 4.14.3. Background Asymmetry

The zero-crossing angles of  $A_n$  and  $A_p$  from the butanol target data were determined under the  $\chi^2$  conditions

$$\chi_i^2 < 5 \quad i = \begin{array}{l} \text{Energy Sum} \\ \text{Transverse momentum balance} \\ \text{Opening Angle} \\ \text{Coplanarity} \end{array} \quad (4.14.5)$$

The graphite target background data should be evaluated under the identical conditions. The graphite target asymmetry at the neutron-proton zero-crossing angle is listed as a function of kinematic  $\chi^2$ -cut in table (4.14.8.). Unlike the neutron-proton elastic scattering asymmetry zero-crossing angle, the proton and neutron based background asymmetry need not be correlated. The background asymmetry has been calculated as a function of both angular distributions and are presented in tables (4.14.8) and (4.14.9). The average proton (neutron) based neutron-proton scattering asymmetry zero-crossing angle was determined to be  $51.95 \pm 0.06$  ( $32.03 \pm 0.06$ ). The values in the two following tables only include events from the inner five neutron bars of each array of seven.

**Table (4.14.8) Background Asymmetry as a function of  $\chi^2$  Constraint at  $\theta_p = 52^\circ$**   
(inner bars, PHTmin > 20, proton angle based)

Constraint	Holding Field		Average
	Up	Down	
$\chi_i^2 < 4$	+0.004±0.019	+0.008±0.022	+0.006±0.014
$\chi_i^2 < 5$	-0.006±0.017	+0.007±0.019	0.000±0.013
$\chi_i^2 < 7.5$	-0.001±0.014	+0.003±0.016	+0.001±0.011
$\chi_i^2 < 9$	+0.007±0.013	-0.002±0.014	+0.004±0.010

**Table (4.14.9) Background Asymmetry as a function of  $\chi^2$  Constraint at  $\theta_p = 32^\circ$**   
(inner bars, PHTmin > 20, neutron angle based)

Constraint	Holding Field		Average
	Up	Down	
$\chi_i^2 < 4$	+0.002±0.019	-0.008±0.022	-0.003±0.014
$\chi_i^2 < 5$	-0.010±0.017	-0.007±0.019	-0.008±0.013
$\chi_i^2 < 7.5$	-0.007±0.014	-0.003±0.015	-0.005±0.011
$\chi_i^2 < 9$	+0.003±0.013	-0.003±0.014	0.000±0.010

The background asymmetry was calculated with the ratio method of equation (4.13.2). A typical plot of the background asymmetry as a function of proton recoil angle is illustrated in figure (4.14.9). At least ten counts were required in each angular bin before an asymmetry was calculated. Asymmetry calculations for the data from the conventional butanol target required a minimum of fifty counts per  $0.025^\circ$  angular bin to ensure gaussian statistics, but this was reduced for the graphite target calculations because of its smaller data set. An insufficient number of experimental counts remained if additional constraints were applied. Allowing a higher percentage of poor  $\chi^2$  events does not appear to influence the asymmetry at the neutron-proton zero-crossing angle. The background asymmetry, within the experimental accuracy, is consistent with zero.

The background asymmetry may be determined from the relation

$$\epsilon_T = r_c \epsilon_c + r_b \epsilon_b \quad (4.14.8)$$

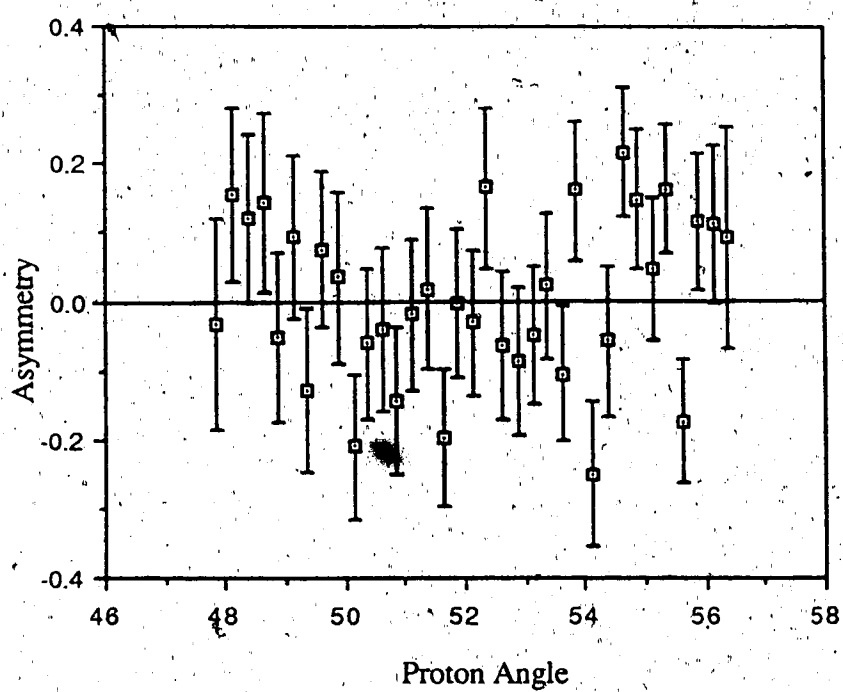


Figure (4.14.8) Observed Background Asymmetry  
(Target Holding Field Down,  $\chi^2_1 < 5$ , All Neutron Bars)



where  $\epsilon$  represents the asymmetry,  $r$  is the ratio of the number of detected events to the total, and subscripts represent total, elastic and background events. At the zero-crossing angle  $\epsilon_e = 0$ . The observed proton angle based asymmetry of inner bar events satisfying the  $\chi_i^2 < 5$  condition was

$$\epsilon_T(\theta_p) = r_b \epsilon_b(\theta_p) = 0.000 \pm 0.013, \quad (4.14.9a)$$

and the neutron angle based asymmetry was

$$\epsilon_T(\theta_n) = r_b \epsilon_b(\theta_n) = -0.008 \pm 0.013 \quad (4.14.9a)$$

The ratio of background to those detected during the graphite target run was  $r_b = 0.30 \pm 0.04$ . Therefore, the proton angle based background asymmetry was

$$\epsilon_b(\theta_p) = 0.000 \pm 0.043, \quad (4.14.10a)$$

and similarly, the neutron angle based background asymmetry was

$$\epsilon_b(\theta_n) = -0.027 \pm 0.043, \quad (4.14.10b)$$

The average proton polarization during the background run was 0.660 (with negligible error). If the polarization transfer coefficient is taken as  $(d_{osso}^2 + d_{osko}^2)^{1/2} = 0.75$ , the proton angle based inelastic background analyzing power was

$$A_b(\theta_p) = 0.000 \pm 0.087, \quad (4.14.11a)$$

and the neutron angle based inelastic background analyzing power was

$$A_b(\theta_n) = -0.054 \pm 0.087, \quad (4.14.11a)$$

The ratio of inelastic to total events detected satisfying  $\chi_i^2 < 5$  with the butanol target was calculated as  $r_b = 0.010 \pm 0.003$ . The inelastic events shifted the zero-crossing angle  $\theta_{op}(A_n)$

by

$$\Delta \theta_{op}(A_n) = \frac{-P_p (d_{osso}^2 + d_{osko}^2)^{1/2} r_b A_b}{\frac{dA}{d\theta_p}} \quad (4.14.13a)$$

and shifted the zero-crossing angle  $\theta_{on}(A_n)$  by

$$\Delta \theta_{on}(A_n) = \frac{-P_p (d_{osso}^2 + d_{osko}^2)^{1/2} r_b A_b}{\frac{dA}{d\theta_n}} \quad (4.14.13b)$$

where  $P_p$  now represents the average proton beam polarization over the butanol target runs,  $dA/d\theta_p$  is the slope of the asymmetry with respect to the proton recoil angle in the lab,  $dA/d\theta_n$  is the slope of the asymmetry with respect to the neutron scattering angle in the lab and  $r_b$  is the butanol target background fraction. Substituting  $P_p = 0.654$ ,  $(d_{osso}^2 + d_{osko}^2)^{1/2} = 0.7496$  and  $r_b = 0.010 \pm 0.003$ ,  $dA/d\theta_p = +0.0237$  and  $dA/d\theta_n = -0.0256$  one finds that the contribution to the proton and neutron angle based zero-crossing angles from background inelastic reactions was

$$\Delta \theta_{op}(A_n) = 0.000^\circ \pm 0.018^\circ \quad (4.14.13a)$$

and

$$\Delta \theta_{on}(A_n) = -0.010^\circ \pm 0.016^\circ \quad (4.14.13a)$$

## Chapter 5 Conclusion

The experimental difference in the  $A_n$  and  $A_p$  asymmetry zero-crossing angles based on the laboratory proton scattering angles was determined to be

$$\theta_{op}(A_n) - \theta_{op}(A_p) = -0.175^\circ \pm 0.076^\circ \left( \begin{array}{c} +0.030^\circ \\ -0.025^\circ \end{array} \right) \quad (5.1)$$

and based on lab neutron scattering angles as,

$$\theta_{on}(A_n) - \theta_{on}(A_p) = +0.212^\circ \pm 0.069^\circ \left( \begin{array}{c} +0.027^\circ \\ -0.031^\circ \end{array} \right) \quad (5.2)$$

where the first error is statistical and the second systematic. Corrections have been applied to the neutron lab scattering angle based result to account for polarization dependent neutron detection effects in the neutron scintillator array (see section 4.11.4) and to account for the presence background (see section 4.14). The two results (5.1) and (5.2) can not be directly compared since the slopes of the asymmetry as a function of lab neutron and proton angles are not equal (hence the inequality of the statistical errors).

The systematic error was calculated by summing the squares of the deviations of  $\theta_{op}(A_n) - \theta_{op}(A_p)$  from the quoted result after (i) the  $\chi^2$  constraint was varied between  $\chi^2 < 4$  to  $\chi^2 < 7.5$ , (ii) the cut on the neutron scintillator bar pulse height distribution was varied between  $PHT_{min} > 15$  to  $PHT_{min} > 25$ , and (iii) calculating the uncertainty associated with background subtraction. The systematic errors are summarized in table (5.1.1).

**Table (5.1.1) Summary of Experimental  $\theta_{op}(A_n) - \theta_{op}(A_n)$   
Systematic Errors**

Item	Difference About Definitive $\theta_{op}(A_n) - \theta_{op}(A_n)$	
	Minimum	Maximum
$\chi^2$ constraint	-0.015°	+0.002°
Neutron Bar Discrimination Threshold	-0.008°	+0.025°
Background Subtraction	-0.018°	+0.018°
<b>Total<sup>†</sup></b>	<b>-0.025°</b>	<b>+0.030°</b>

<sup>†</sup> Summed in quadrature

Two additional values must be evaluated in the calculation of the systematic error associated with the calculation of  $\theta_{on}(A_n) - \theta_{on}(A_n)$ . First, any uncertainty in the evaluation of the neutron bar TDC length must be included. A deviation in this value scales the value of  $\theta_{on}(A_n) - \theta_{on}(A_n)$  by the identical percentage. Second, an error in the evaluation of the effect of the scattered neutron polarization on neutron position determination must also be included. These two systematic errors associated with the neutron angle based calculation have no proton angle based counterpart.

**Table (5.1.2) Summary of Experimental  $\theta_{on}(A_n) - \theta_{on}(A_n)$   
Systematic Errors**

Item	Difference About Definitive $\theta_{on}(A_n) - \theta_{on}(A_n)$	
	Minimum	Maximum
$\chi^2$ constraint	-0.000°	+0.019°
Neutron Bar Discrimination Threshold	-0.026°	+0.008°
Background Subtraction	-0.016°	+0.016°
Neutron Bar TDC Length	-0.003°	+0.003°
<b>Total<sup>†</sup></b>	<b>-0.031°</b>	<b>+0.027°</b>

<sup>†</sup> Summed in quadrature

The difference  $A_n - A_p$  was not directly measured but can be calculated by multiplying the result (5.1) by the slope of the analyzing power with respect to the laboratory

proton scattering angle,

$$A_n - A_p = -[\theta_{op}(A_n) - \theta_{op}(A_p)] \frac{dA}{d\theta_p} \quad (5.3)$$

or by multiplying (5.2) by the slope of the analyzing power with respect to the lab neutron scattering angle,

$$A_n - A_p = -[\theta_{on}(A_n) - \theta_{on}(A_p)] \frac{dA}{d\theta_n} \quad (5.4)$$

The Arndt et. al.<sup>(34)</sup> phase shift results give  $dA/d\theta_p = +0.0263$  and  $dA/d\theta_n = -0.0284$ . The Saclay-Geneva<sup>(49)</sup> analysis are  $dA/d\theta_p = +0.0277$  and  $dA/d\theta_n = -0.0300$ . Differences in the slope of the analyzing powers between the two phase shift fits are negligible compared to the experimental statistical uncertainty. The results of Arndt et. al. were used in the calculation. Therefore, the difference in the two analyzing powers at the neutron-proton elastic scattering asymmetry zero-crossing angle is then,

$$A_n - A_p = +0.0046 \pm 0.0020 (\pm 0.0007), \quad (5.5)$$

based on the lab proton scattering angle results, and

$$A_n - A_p = +0.0060 \pm 0.0020 (\pm 0.0008), \quad (5.6)$$

based on lab neutron scattering angles. The proton based result has been accepted as the definitive experimental result because of the slightly larger systematic errors associated with the neutron angle based result.

CSB effects on the n-p transition matrix can be calculated within the framework of the DWBA formalism. The transition matrix can be written as

$$T_{CSB} = T_0 + \delta T, \quad (5.7)$$

where  $T_0$  represents the charge symmetric transition matrix. The CSB part is then

$$\delta T_{fi} = -\frac{M}{4\pi} \langle k_f^- | V_{CSB} | k_i^+ \rangle \quad (5.8)$$

The  $(-)$  and  $(+)$  superscripts indicate the asymptotic behaviour of the distorted waves as time goes to negative and positive infinity, respectively. If the transition to the LSJ basis is made, the distorted states can be expressed as

$$|k_i^+\rangle = \frac{1}{(2\pi)^{3/2}} \sum_{LJM} 4\pi i^L R_{JLS}(r) Y_{Lm}(\hat{p}) e^{i\delta_{JLS}} |Ls_i; JM\rangle \langle Ls_i; JM | Lm s_i m_i \rangle \quad (5.9a)$$

$$= \frac{1}{(2\pi)^{3/2}} \sum_{LJM} \sqrt{4\pi(2L+1)} i^L R_{JLS}(r) e^{i\delta_{JLS}} |Ls_i; JM\rangle \langle Ls_i; JM | L0 s_i m_i \rangle \quad (5.9b)$$

and

$$|k_f^-\rangle = \frac{1}{(2\pi)^{3/2}} \sum_{LJM} 4\pi i^L R_{JLS}(r) Y_{Lm}^*(\hat{p}') e^{-i\delta_{JLS}} |Ls_f; JM\rangle \langle Ls_f; JM | L0 s_f m_f \rangle \quad (5.9c)$$

The functions  $R_{JLS}(r)$  are the radial solutions to the Schrodinger equation in the presence of a charge symmetric neutron - proton potential. Class (IV) CSB forces effect transitions between  $S=0$  and  $S=1$  states only (if total angular momentum and parity are conserved); therefore, angular momentum decompositions of the incident and final states in the above equation need only contain those partial waves for which  $L = J$ .

If the class (IV) CSB potential is given by

$$V_{CSB}^{(IV)} = f(r) (\sigma(1) - \sigma(2)) \cdot L, \quad (5.10)$$

is substituted into (5.8) with (5.9b) and (5.9c), then one finds that for  $s_i = 0$  and  $s_f = 1$ ,

$$\delta T_{fi} = -\frac{M}{(2\pi)^3} \sum_J \sqrt{2} (2J+1) G_J e^{i(\delta_{JJ0} + \delta_{JJ1})} e^{-im_f \phi} P_J^1(\cos \theta). \quad (5.11a)$$

where  $\theta$  and  $\phi$  are the polar and azimuthal scattering angles in the center of mass system.

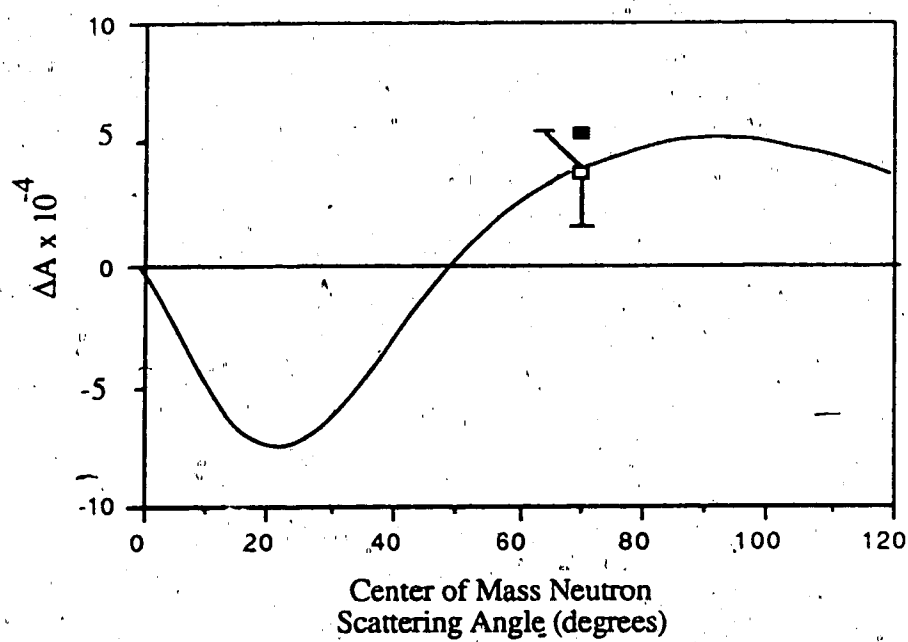


Figure (5.1) Comparison of Theory to Experiment  
 The experimental result (hollow point with error bars) is compared to the calculations of Svenne (curve, reference 53) and of Miller, Thomas and Williams (dark point, reference 1).

future.

The experimental result is not inconsistent with theory, but the variety of results between different calculations points towards the need for more theoretical work.

Experimentally, a proposal has been submitted and accepted to remeasure the extent to which charge symmetry is broken in neutron - proton elastic scattering at 350 MeV at TRIUMF. The proposal itself is reproduced in appendix C. The discrepancy between theory and experiment at 477 MeV may be due to problems with the energy dependence of the terms or due to terms which have yet to be included. The additional measurement will provide an important constraint on existing and future calculations as well as help unravel the energy dependence of the various terms.



## Reference List

- (1) G. A. Miller, A.W.Thomas, A.G.Williams, Phys. Rev. Lett. 56 2567, 1986
- (2) E.M.Henley and G.A.Miller, in Mesons in Nuclei, edited by M.Rho and D.Wilkinson, (North Holland, Amsterdam, 1979), Vol. I, p. 405.
- (3) J. Bystricky, F. Lehar and P. Winternitz Le Journal de Physique 39 (1978) 1
- (4) O.Dumbrajs et. al., Nucl. Phys. B216, 277 (1983)
- (5) J.A. Nolen and J.P. Schiffer, Ann. Rev. Nucl. Sci. 19 (1969) 471
- (6) E.Pedroni et. al., Nucl. Phys A300, 321 (1978)
- (7) T.G.Masterson et. al., Phys. Rev. Lett. 47 (1981) 220
- (8) T.G.Masterson et. al., Phys. Rev. C 26 (1982) 2091
- (9) T.G.Masterson et. al., Phys. Rev. C 30 (1984) 2010
- (10) B. Balestri et. al., NP A392 217 (1983)
- (11) K. Galathuler et. al. NP A392 253 (1980)
- (12) C.Y.Cheung, E.M.Henley and G.A.Miller, Phys. Rev. Lett. 43 1215 (1979)
- (13) C.L. Hollas et. al., Phys. Rev. C 24 (1981) 1561
- (14) D.F. Bartlett et. al., Phys. Rev. D 1 1984 (1970)
- (15) S.S. Wilson et. al., Phys. Lett. 35B 83 (1971)
- (16) C.Y.Cheung, E.M.Henley and G.A.Miller, NP A305 342 (1978)
- (17) B.M.K.Nefkens, Phys. Rev. Lett. 52 735 (1984)
- (18) S.Barshay and L.M.Shegal, Phys Rev C 31 2133 (1985)
- (19) Kr. T. Kim, Y. E. Kim, R. H. Landau, Submitted to Phys Rev. Lett. Sep, 1986
- (20) Yu.K.Akimov et al., Sov. Phys. JETP 14, 512 (1962)
- (21) A. Poirer and M. Pripstein, Phys. Rev. 122, 1917 (1961)
- (22) J. Benaigs et. al. Phys. Lett. 53B, 390 (1974)
- (23) C.Y.Cheung, Phys. Lett. 119B, 47 (1982)
- (24) S.A.Coon and D.M.Predom, Phys. Rev. C, 32, 1448 (1985)

- (25) S.E. Vigdor et. al., Proc. Fifth Intl. Symp. on Polarization Phenomena in Nuclear Physics (Sante Fe, August, 1980), edited by G.G. Ohlsen et. al. (AIP, New York, 1981) Vol. II, p. 1455.
- (26) K. Brauer, E.M. Henley, and G.A. Miller, Phys. Rev. C 34 (1986) 1779
- (27) L. Bjorken and S. Drell, Relativistic Quantum Mechanics, McGraw-Hill Book Company, Inc., New York, 1964.
- (28) C.Y. Cheung, Charge Symmetry Breaking in the Neutron-Proton System, Ph.D. thesis, University of Washington, 1979
- (29) R. Abegg, J. Birchall, E. Cairns, H. Coombes, C.A. Davis, N.E. Davison, P.W. Green, L.G. Greeniaus, H.P. Gubler, W.P. Lee, W.J. McDonald, C.A. Miller, G.A. Moss, G.R. Plattner, P.R. Poffenberger, G. Roy, J. Soukup, J.P. Svenne, R. Tkachuk, W.T.H. Van Oers and Y.P. Zhang, The Neutron Beam Facility at TRIUMF, NIM A234 (1985) 11 - 19
- (30) R. Abegg, J. Birchall, E. Cairns, H. Coombes, C.A. Davis, N.E. Davison, P.W. Green, L.G. Greeniaus, H.P. Gubler, W.P. Lee, W.J. McDonald, C.A. Miller, G.A. Moss, G.R. Plattner, P.R. Poffenberger, G. Roy, J. Soukup, J.P. Svenne, R. Tkachuk, W.T.H. Van Oers and Y.P. Zhang, Detection Equipment for a Test of Charge Symmetry Breaking, NIM A234 (1985) 20 - 29
- (31) J. Marko and R. Morewood, Report on the Use of Secondary Emission Monitors in a Particle Beam Positioning Feedback Loop, Internal TRIUMF Report (1979)
- (32) R. Morewood and J. Marko, Secondary Emission Monitors as a Beam Steering Device, Internal TRIUMF Report (1979)
- (33) L.G. Greeniaus and J. Soukup, Polarimeter - Beam Energy Monitor, Internal TRIUMF Report TRI-DNA-81-1 (1981)
- (34) R. Arndt, Interactive Dial - In Program SAID (from phase shift dial-in program, Solution C500, Fall 1986)
- (35) D.V. Bugg and C. Wilkin, private communication; D. Axen, R. Dubois, R. Keeler, G.A. Ludgate, C.J. Oram, L.P. Robertson, N.M. Stewart, C. Amsler, D.V. Bugg, J.A. Edgington, W.R. Gibson, N. Wright and A.S. Clough, Phys. Rev. C21, (1982) 998.
- (36) H. Gubler, Internal TRIUMF Report (1981)
- (37) R. Abegg, D. Bandyopadhyay, J. Birchall, E. Cairns, H. Coombes, C.A. Davis, N.E. Davison, P.P.J. Delheigh, P.W. Green, L.G. Greeniaus, H.P. Gubler, D.C. Healey, C. Lapointe, W.P. Lee, W.J. McDonald, C.A. Miller, G.A. Moss, G.R. Plattner, P.R. Poffenberger, W.D. Ramsay, G. Roy, J. Soukup, J.P. Svenne, R. Tkachuk, W.T.H. Van Oers, G.D. Wait, and Y.P. Zhang, Proton Target Polarization with a Polarized Neutron Beam at 477 MeV, Submitted letter to NIM.

- (38) P.P.J. Delheij, D.C. Healey and G.D. Wait, The Frozen Spin Polarized Proton Target at TRIUMF for Intermediate Energy Neutron Scattering, Submitted to NIM.
- (39) N.E. Davison, Proton Booms for Experiment 121 "Test of Charge Symmetry" TRIUMF Internal Report TRI-DN-83-2 (1983)
- (40) G. Charpak and F. Sauli, NIM 162 (1979) 405
- (41) P. Poffenberger, A Pedestrian's Guide to the CSB Delay Line Chambers TRIUMF Internal Report TRI-DN-84-30 (1984)
- (42) F. Sauli, Principles of Operation of Multiwire Proportional and Drift Chambers, CERN Internal Report 77-09 (1977)
- (43) H. Gubler, Internal TRIUMF Note (1981)
- (44) R. Grove, I. Ko, B. Leskivar and V. Perez-Mendez, NIM 99 (1972) 381
- (45) R. Grove, V. Perez-Mendez and J. Sperinde, NIM 106 (1973) 407
- (46) C. Lapointe, Internal University of Alberta Note, 1985
- (47) R.A. Cecil, B.D. Anderson and R. Madey NIM 161 (1979) 439
- (48) S. Mango, O. Runolfsson and M. Borghini NIM 72 (1969) 45
- (49) J. Bystricky, C. Lechanoine and F. Lehar, Private Communication.
- (50) G.A. Miller, Private Communication, 1985
- (51) L. Ge and J.P. Svenne, Phys. Rev. C, 33 (1986) 417; L. Ge Charge Symmetry Breaking in Neutron Proton Scattering, M.Sc. Thesis, University of Manitoba, 1985; J.P. Svenne, Private Communications
- (52) R. Holzenkamp, K. Holinde and A.W. Thomas, Private Communication
- (53) J. Iqbal, R. Woloshyn and J. Thaler, Submitted to Phys. Rev. C.
- (54) J. Birchall, Internal TRIUMF Report (1980)

## Appendix A - Summary of Systematics

### A.1 Introduction

The nature of the experiment removes most errors to first order in the determination of the analyzing power,  $A$ , and to second order in the determination of  $\Delta A = A_n - A_p$ , where the subscript represents the polarized particle, at the zero-crossing angle. Absolute knowledge of beam intensity, target and beam polarization are not needed in the final calculations. Sources of error caused by differences between left and right detection apparatus are diminished by the manner in which the analyzing power is determined from experimental data. The following notes summarize the major sources of error and a calculation of their effects on the measured asymmetries under the most pessimistic of conditions. It must be stressed from the outset that  $A_n$  and  $A_p$  are independent quantities and are measured in two different, but concurrent, experiments utilizing the one set of equipment. Systematic errors may affect one or both analyzing power measurements. With this in mind errors in individual asymmetries will be denoted  $\delta A_{n,p}$  and errors in the difference  $A_n - A_p$  will be specified as  $\delta \Delta A$ . The errors calculated here follow the outline of an earlier note<sup>(54)</sup>.

It is convenient to adopt a general notation which can be referred to throughout this note. The observed count rates in the left and right side detection apparatus can be written as

$$L^+ = \sigma^+(1 + P^+ A_l^+) \quad (A.1.1a)$$

$$R^+ = \sigma^+(1 - P^+ A_r^+) \quad (A.1.1b)$$

$$L^- = \sigma^-(1 - P^- A_l^-) \quad (A.1.1c)$$

$$R^- = \sigma^-(1 + P^- A_r^-) \quad (A.1.1d)$$

The '+' superscripts represent the direction of the target or beam polarization for measurements of  $A_p$  or  $A_n$ . The asymmetries are determined from the data as

$$\varepsilon = (r-1)/(r+1) \quad (A.1.2)$$

where  $r^2 = L^+R^- / L^-R^+$

$$= [\sigma_1^+ \sigma_r^- (1 + P^+ A_1^+) (1 + P^- A_r^-)] / [\sigma_1^- \sigma_r^+ (1 - P^- A_1^-) (1 - P^+ A_r^+)]. \quad (A.1.3)$$

In the complete absence of any experimental errors (A.1.3) reduces to (A.1.4),

$$r_0^2 = \left( \frac{1 + PA}{1 - PA} \right)^2 \quad (A.1.4)$$

The differential cross section, as a function of angle, has been assumed to differ from its nominal value due to slight geometric or other imperfections,

$$\sigma_{lr}^\pm = \sigma(1 + s_{lr}^\pm), \quad (A.1.5)$$

and/or the observed asymmetry changes by ,

$$A_{lr}^\pm = A + a_{lr}^\pm, \quad (A.1.6)$$

and the magnitude of the polarization changes between up and down states by

$$P^\pm = P \pm \alpha.$$

(A.1.7)

Inserting the expanded expressions (A.1.4), (A.1.5) and (A.1.6) into (A.1.2) one finds that the parameter  $r^2$ , to second order in terms of the  $s$ ,  $a$  and  $\alpha$ , changes by,

$$\begin{aligned} r^2 = r_0^2 & \left[ 1 + \frac{1}{\sigma} (s_1^+ + s_r^- - s_1^- - s_r^+) \right. \\ & + P(a_1^+ + a_r^- + a_1^- + a_r^+) - AP^2(a_1^+ + a_r^- - a_1^- - a_r^+) \\ & + \alpha(a_1^+ - a_r^- + a_1^- + a_r^+) - 2PA\alpha(a_1^+ - a_r^- - a_1^- + a_r^+) + 4PA^3\alpha^2 \\ & \left. + P^2(a_1^+ a_r^- + a_1^- a_r^+) \right]. \quad (A.1.8) \end{aligned}$$

The error in the measured asymmetry can be rewritten with the relation,

$$\begin{aligned} \delta A = \frac{1}{4P} \left[ \frac{1}{\sigma} (s_1^+ + s_T^- - s_1^- - s_T^+) \right. \\ + P (a_1^+ + a_T^- + a_1^- + a_T^+) - AP^2 (a_1^+ + a_T^- - a_1^- - a_T^+) \\ + \alpha (a_1^+ - a_T^- + a_1^- + a_T^+) - 2PA\alpha (a_1^+ - a_T^- - a_1^- + a_T^+) + 4PA^3\alpha^2 \\ \left. + P^2 (a_1^+ a_T^- + a_1^- a_T^+) \right]. \end{aligned} \quad (A.1.9)$$

## A.2 Deviation of Beam Spot on LD<sub>2</sub> Target

A change of the proton beam spot position will alter the angle of the neutron beam on the frozen spin target (FST) which in turn influences the direction of the scattered and recoil particles from the FST. The measured n-p asymmetry is not affected by minor drifts of the proton beam in the vertical direction, but deviations in the horizontal position are directly related to both the polar scattering angles of the elastic n-p pair and therefore the observed asymmetry.

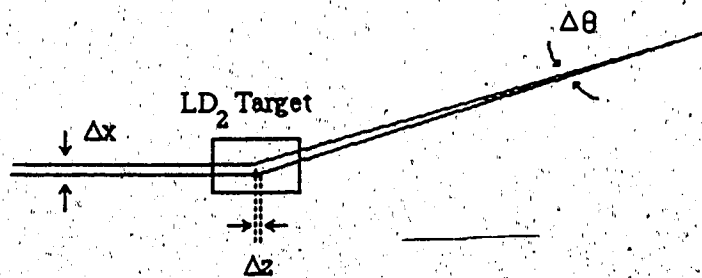


Figure (A.2.1) Horizontal Deviation of Proton Beam on LD<sub>2</sub> Target

The FST is situated 12.55 m from the center of the LD<sub>2</sub> target. A change in the x-position of  $\Delta x = 2\text{mm}$  could alter the angle of the neutron beam incident on the FST by  $\Delta\theta = 1.5 \times 10^{-3}$  degrees. Since  $\Delta\theta$  will be very small the expansions of (A.1.5) and (A.1.6)

need be taken to only first order :

$$\begin{aligned} a_l^+ &= \Delta\theta A', & a_r^+ &= -\Delta\theta A', \\ a_l^- &= \Delta\theta A', & a_r^- &= -\Delta\theta A', \end{aligned} \quad (A.2.1)$$

$$\begin{aligned} s_l^+ &= \Delta\theta \sigma'/\sigma, & s_r^+ &= -\Delta\theta \sigma'/\sigma, \\ s_l^- &= \Delta\theta \sigma'/\sigma, & \text{and} & & s_r^- &= -\Delta\theta \sigma'/\sigma. \end{aligned} \quad (A.2.2)$$

Where  $A' \approx -0.027$  /deg,  $\sigma \approx 6.9$  mb, and  $\sigma' \approx -0.39$  mb/deg at the zero-crossing angle. Therefore, after substitution into (A.1.9) one gets :  $\delta A \approx \delta\Delta A \approx 0$ .

If the deviation of the beam spot on the LD2 target is correlated with beam polarization (A.1.9) changes into

$$\delta A_n = \phi\sigma' + \phi A' \approx 10^{-4} \text{ at } A = 0. \quad (A.2.3)$$

As  $A_p$  is not effected by correlated deviations in proton beam position with beam polarization reversals  $dA_p = 0$ . Therefore  $\delta\Delta A = \delta A_n \approx 10^{-4}$ . This value is likely a pessimistic overestimation of the error as the neutron collimator defines the acceptance region of neutrons originating at the LD<sub>2</sub> target.

Changes in the beam spot position also cause an energy change in the scattered neutron beam. The neutron collimator axis intersects the center of the LD<sub>2</sub> target at nine degrees to the proton beam axis. The average length the proton beam passes through the target,  $\Delta z$  in figure A.2.1, will depend on where the collimator axis intersects the proton beam. Protons of 477 MeV will lose approximately 0.04 MeV /mm. The asymmetry zero-crossing angle changes as a function of energy as  $\partial\theta_{zc}/\partial E = -0.011$  deg/MeV (lab). Therefore, a change in the proton beam position on the LD<sub>2</sub> target by 1.0 mm causes a change to the path lengths of those protons which produce the neutron beam by  $\Delta z = 6.3$  mm thereby reducing the neutron beam energy by 0.25 MeV. This results in a change in the zero-crossing angle of  $2.8 \times 10^{-3}$  degrees or, equivalently, a change in the asymmetry at the nominal zero-crossing angle by  $0.7 \times 10^{-4}$ . To keep  $\delta A \leq 10^{-4}$ , the proton beam position on the LD2 target must be kept to within  $\pm 1.2$  mm.

### A.3 Modulation of Proton Beam on LD<sub>2</sub> Target

Changes in the direction of the proton beam on the LD<sub>2</sub> target effectively alters the energy of the outgoing neutron beam. At the 90° neutron beam exit port,  $\partial E / \partial \theta_{\text{recoil}} = 3.36$  MeV/deg (lab). At 480 MeV the  $\theta_{\text{zc}}$  does not change appreciably with neutron energy;  $\partial \theta_{\text{zc}} / \partial E = -0.011$  deg/MeV.

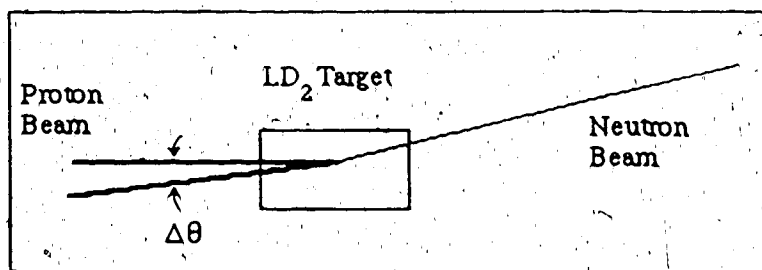


Figure (A.3.1) Modulation of Proton Beam on LD<sub>2</sub> Target

Since  $\partial A / \partial \theta = -0.027$  /deg the observed asymmetry changes with neutron recoil angle at the LD<sub>2</sub> target as  $\partial A / \partial \theta_{\text{recoil}} = 1.0 \times 10^{-3}$  /deg. A modulation of the beam direction on the LD<sub>2</sub> target of  $|\theta^+ - \theta^-| = 0.1^\circ$  (here, the superscript represents proton polarization) correlated with primary beam polarization results in a systematic deviation of  $\delta \Delta A = 1 \times 10^{-4}$ .

### A.4 Inequality of Up and Down Polarization

If the beam or target polarization differs in magnitude between up and down states as  $P^\pm = P \pm \alpha$ , then one finds from (A8) that  $\delta A_{n,p} = A^3 \alpha^2$ . At  $A=0$ ,  $\delta A_{n,p} = 0$  and  $\delta \Delta A = 0$ . At the limits of the detection apparatus the analyzing power approaches a value of  $A = 0.2$  and taking the difference in up and down beam or target polarization states as 0.2 (that is,  $\alpha = 0.1$ )  $\delta \Delta A = \delta A_{n,p} = 8 \times 10^{-5}$ .



### A.5 Misalignment of Apparatus

If the apparatus is misaligned by

$$\theta_L = \theta - \varphi, \text{ and } \theta_R = \theta + \varphi, \quad (\text{A.5.1})$$

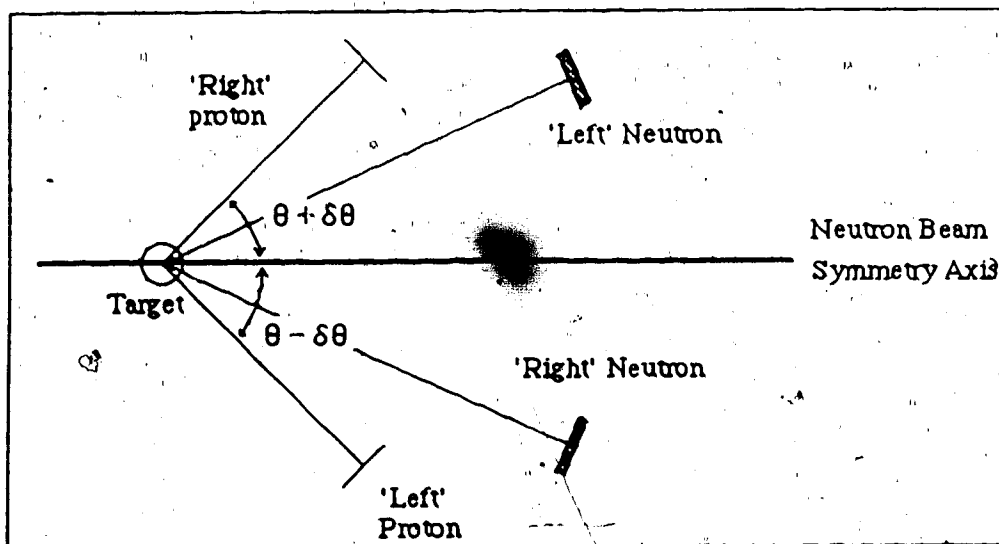


Figure (A.5.1) Misalignment of Apparatus

then the variables of (A.1.5) and (A.1.6) are

$$a_1^+ = \varphi A' + \varphi^2 A''/2$$

$$a_r^+ = \varphi A' + \varphi^2 A''/2$$

$$a_1^- = -\varphi A' + \varphi^2 A''/2$$

$$a_r^- = -\varphi A' + \varphi^2 A''/2$$

(A.5.2)

$$s_1^\pm = \pm (\varphi \sigma' + \varphi^2 \sigma''/2)$$

(A.5.3)

$\sigma$

$$s_r^\pm = \pm (-\varphi \sigma' + \varphi^2 \sigma''/2)$$

$\sigma$

All first order errors in the asymmetry cancel to first order leaving second order systematics

$$\delta A = \phi^2 A'' / 2, \quad (A.5.4)$$

$$-8 \times 10^{-4} \text{ deg}^{-2} \leq A'' \leq 8 \times 10^{-4} \text{ deg}^{-2},$$

giving  $\delta A \ll 10^{-4}$  throughout the angular range for a misalignment of  $0.1^\circ$ . The proton and neutron detection booms were located to an accuracy of  $\pm 0.02^\circ$  and  $\pm 0.05^\circ$  respectively during the experiment.

#### A.6 Inequality of Up and Down Polarization and Misalignment of Apparatus

Let the detectors be misaligned as in (A.5.1), and the beam or target polarizations differ in magnitude between opposite spin states as (A.1.7). Substituting (A.5.1) and (A.1.7) into (A.1.9) one finds that

$$\delta A_{n/p} = -2A\alpha\phi A' + \frac{\phi^2 A''}{2} + A^3 \alpha^2. \quad (A.6.1)$$

Since the proton and neutron detectors can be located to an accuracy of  $\pm 0.02^\circ$  and  $\pm 0.05^\circ$  respectively, in estimating the maximum effect on  $\Delta A$  a value of  $|\theta_l - \theta_r| = 0.1^\circ$  will be used. The asymmetry changes with angle by

$$A' = -0.027 / \text{deg} \quad (A.6.3)$$

$$|A''| \leq 0.0008 / \text{deg}^2. \quad (A.6.4)$$

At the extreme limits of detection the expression for  $\delta A$  is dominated by the term proportional to  $A$ . Inserting  $P = 0.7 \pm 0.1$ , that is  $\alpha = 0.1$ , into (A.6.1) one finds that  $\delta A \approx (6 \times 10^{-4})A$ . As  $A$  approaches a value of 0.2 at the limits of the angular acceptance one finds that  $\delta A \approx 10^{-4}$ . Where  $A_n \approx 0$ , all terms in (A.6.1) contribute since  $A_p$  is in the range of  $4 \times 10^{-3}$ . Here,  $\delta A < 10^{-5}$ .

There will be a slight contribution to  $\delta \Delta A$  as  $A_n' \neq A_p'$  due to slight CSB effects. The magnitude of the inequality can only be estimated on the basis of theoretical

contributions to  $\Delta A$  illustrated in figure (2.3.1). From Miller, Thomas and Williams<sup>(1)</sup>,

$$A_n - A_p \leq 5 \times 10^{-5} / \text{deg (lab)} \quad (\text{A.6.5})$$

One sees immediately that such contributions to  $\delta \Delta A$  are insignificant.

### A.7 Reproducibility of Target Holding Field

Small changes in the magnitude of the holding field cause changes in the extent to which the holding field bends recoil proton trajectories. The holding field will bend n-p elastic trajectories at the large angle limit of the detection system by  $1.8^\circ$  and to the small angle detection limit by  $1.2^\circ$ . The target holding field at the centre of the target is 2.57 kG and the line integral  $\int \mathbf{B} \cdot d\mathbf{l}$  seen by a proton originating in the centre of the target is 44 kG-cm. One finds that at  $\theta_p = 53^\circ$ ,  $p_p = 549 \text{ MeV}/c$ ,  $\partial \theta_{hf} / \partial B_{hf} = 4.8 \times 10^{-4} \text{ deg/Gauss}$ . The magnitude of the holding field fluctuations can be estimated as  $\sigma_{hf} = 2.6 \text{ G}$ . If target holding field deviations are not correlated with spin direction  $\delta A = \delta \Delta A = 0$ . If the holding field deviations are directly correlated with target polarization then  $\delta \theta_{zc} = 1.2 \times 10^{-3} \text{ degrees}$  corresponding to  $\delta \Delta A = 3 \times 10^{-5}$  at  $A = 0$ .

### A.8 Multiple Scattering

Multiple scattering smears the angles of recoil protons emerging from the target. Assuming that the multiple scattering follows a Gaussian distribution

$$L^\pm(\theta) = \int \sigma(\theta + \delta) [1 \pm PA(\theta)] \exp(-\delta^2 / \delta_0^2) d\delta. \quad (\text{A.8.1})$$

and a similar equation for  $R^\pm$ . The parameter  $\delta_0$  is related to the magnitude of multiple scattering as  $\delta_0 = \sqrt{2} \sigma_{ms}$ . Expanding  $\sigma(\theta)$  and  $A(\theta)$  as a function of  $\theta$  as

$$\sigma(\theta) = \sigma(\theta_0) + \delta \sigma'(\theta_0) + \frac{\delta^2}{2} \sigma''(\theta_0) + \dots, \quad (\text{A.8.2})$$

and integrating the first three terms of the combined Taylor expansion of  $L^\pm$  and  $R^\pm$ , (A.8.1) can be rewritten as

$$L^\pm(\theta) \approx L^\pm(\theta_0) + \frac{\delta_0^2}{4} (\sigma''(1 \pm PA) \pm \sigma PA'' \pm 2P\sigma'A') \quad (\text{A.8.3a})$$

$$R^\pm(\theta) \approx R^\pm(\theta_0) + \frac{\delta_0^2}{4} (\sigma''(1 - PA) - \sigma PA'' - 2P\sigma'A'). \quad (\text{A.8.3b})$$

These expressions can be expressed in terms of the more familiar notation of (A.1.9) as

$$a_1^+ = \frac{\delta_0^2}{4\sigma} (\sigma A'' + 2\sigma'A'). \quad (\text{A.8.4a})$$

$$a_R^+ = \frac{\delta_0^2}{4\sigma} (\sigma A'' + 2\sigma'A') \quad (\text{A.8.4b})$$

$$a_L^- = \frac{\delta_0^2}{4\sigma} (\sigma A'' + 2\sigma'A') \quad (\text{A.8.4c})$$

$$a_R^- = \frac{\delta_0^2}{4\sigma} (\sigma A'' + 2\sigma'A') \quad (\text{A.8.4d})$$

Inserting the above results into the expression (A.1.9), one gets

$$\delta A = \frac{\delta_0^2}{4} (A'' + 2\frac{\sigma'}{\sigma} A') \quad (\text{A.8.5})$$

Near the zero-crossing angle,

$$\begin{aligned} A' &= -0.027 / \text{deg} \\ |A''| &\leq 5 \times 10^{-4} \\ \sigma &= 6.9 \text{ mb (lab)} \\ \sigma' &= -0.39 \text{ mb/deg (lab)} \\ \delta_0 &\leq 0.8 (= \sqrt{2}\sigma_{\text{ms}}) \end{aligned} \quad (\text{A.8.6})$$

Substituting into (A.8.5) one gets  $\delta A = 5 \times 10^{-4}$ , at  $A = 0$ .

### A.9 Incorrect Precession of Spin

Any residual proton polarization perpendicular to the horizontal plane left after the proton spin precession can only result in a neutron polarization also perpendicular to the horizontal plane. Such a neutron polarization component is rotated into the beam axis by the dipole magnets Bonnie and Clyde and cannot in itself result in a false asymmetry. However, an error in the proton spin precession leaving a residual vertical component coupled with an error in the neutron spin precession can cause a error in the measured asymmetry. Assuming an error in both the proton and neutron spin precession by  $\omega_p = 5^\circ$  and  $\omega_n = 5^\circ$ , there would exist an additional vertical component to the neutron polarization at the FST which would change sign with flips in the beam polarization as

$$\Delta P_n^\pm = \frac{[P \pm (d_{osso}^2 + d_{osko}^2)^{1/2} P_p \sin \omega_p] \sin \omega_n}{(1 \pm P_p A)} \quad (A.9.1)$$

where the  $(d_{osso}^2 + d_{osko}^2)^{1/2} = 0.75$  and the polarization, equal to the analyzing power,  $P = A = -0.06$ . One finds that the extra component to the neutron vertical polarization is exceedingly small. It has been shown earlier that differing up/down polarizations do not contribute to false asymmetries if  $|P^+ - P^-| < 0.1$ .

### A.10 Residual Neutron Polarization on Polarized Target

A residual neutron polarization can couple to the target polarization and cause a false asymmetry measurement. The polarized target state left and right count rates would (after dropping common factors) be

$$L^+ = [1 + A(P_p^y + P_n^y) + P_p^y P_n^y A_{yy} + A_{zx}(P_n^z P_p^x + P_n^z P_p^x) + A_{zz} P_n^z P_n^x] \quad (A10.1a)$$

$$L^- = [1 - A(P_p^y - P_n^y) - P_p^y P_n^y A_{yy} - A_{zx}(P_n^z P_p^x + P_n^z P_p^x) - A_{zz} P_n^z P_n^x] \quad (A10.1a)$$

$$R^+ = [1 - A(P_p^y + P_n^y) + P_p^y P_n^y A_{yy} - A_{zx}(P_n^z P_p^x + P_n^z P_p^x) + A_{zz} P_n^z P_n^x] \quad (A10.1a)$$

$$R^- = [1 + A(P_p^y - P_n^y) - P_p^y P_n^y A_{yy} + A_{zx}(P_n^z P_p^x + P_n^z P_p^x) - A_{zz} P_n^z P_n^x] \quad (A10.1a)$$

Note that the residual neutron beam polarization does not reverse sign when the target polarization is reversed. Adopting the usual notation of (A.1.6) one gets

$$a_1^+ = \frac{1}{P_p^y} [A_y P_n^y + P_p^y P_n^y A_{yy} + A_{zx}(P_n^z P_p^x + P_n^z P_p^x) + A_{zz} P_n^z P_n^x] \quad (A10.2a)$$

$$a_1^- = \frac{1}{P_p^y} [-A_y P_n^y + P_p^y P_n^y A_{yy} + A_{zx}(P_n^z P_p^x + P_n^z P_p^x) + A_{zz} P_n^z P_n^x] \quad (A10.2b)$$

$$a_1^+ = \frac{1}{P_p^y} [A_y P_n^y - P_p^y P_n^y A_{yy} + A_{zx}(P_n^z P_p^x + P_n^z P_p^x) - A_{zz} P_n^z P_n^x] \quad (A10.2c)$$

$$a_1^- = \frac{1}{P_p^y} [-A_y P_n^y - P_p^y P_n^y A_{yy} + A_{zx}(P_n^z P_p^x + P_n^z P_p^x) - A_{zz} P_n^z P_n^x] \quad (A10.2d)$$

The spin correlation parameters  $A_{yy}$  and  $A_{zz}$  do not change sign on the left and right sides, i.e. they do not cause a left-right asymmetry. The largest contribution to a false asymmetry is

$$\delta A_p = \delta \Delta A \approx \frac{1}{P_p^y} A_{zx} (P_n^z P_p^x + P_n^z P_p^x). \quad (A10.3)$$

Neutrons created from an unpolarized proton beam on the LD2 target have a maximum vertical polarization determined by the np asymmetry at  $9^\circ$ . The maximum component of the neutron polarization in the scattering plane would then be  $P_n^z = 0.06$ . The spin correlation parameter is equal to  $A_{zx} = -0.02$  ( $E_n = 477$  MeV,  $70^\circ$  cm, Arndt '86 phase shifts). The vertical proton polarization is  $P_p^y = 0.8$ , the maximum component of the proton target polarization in the scattering plane is determined by the error in the direction of the target holding field; this was estimated as  $\pm 1.0^\circ$  from the vertical. Therefore,  $P_p^x \leq 0.8 \sin(1.0^\circ) = 0.014$ . The maximum effect on  $A_p$  is then

$$\delta A_p = \delta \Delta A \leq 0.3 \times 10^{-4}. \quad (A10.4)$$

### A.11 Neutron Energy Stability

Asymmetry changes with incident neutron energy. At  $E_n = 477$  MeV, and  $\theta_n = 72.0^\circ$

$$\frac{\partial \Delta}{\partial \theta} = -0.027 / \text{MeV (lab)} \quad (\text{A.11.1})$$

$$\frac{\partial \theta_{zc}}{\partial E} = -0.011 \text{ deg/MeV (lab)} \quad (\text{A.11.2})$$

Absolute knowledge of the beam energy is unimportant to a approximately a few MeV as long as it does not change by approximately 0.25 MeV between data taking runs.

### A.12 Relative Position of Target and Holding Field with Respect to Symmetry Axis

Deviations in target position and/or the holding field with respect to the symmetry axis will cause shifts between actual scattering angles and those measured for the tracks. The main contributor to the resultant angular deviations is the different  $\int B \cdot dl$  which protons see due to the shifted holding field. As such, shifts of the target position are similar in effect to shifts in the holding field.

The position of the target cell was determined within  $\pm 0.5$  mm from X-rays of the FST taken at least once per data taking period.

#### (a) Lateral Target Deviations

Let the target move to one side by  $dx$ . Protons to one side will pass through a larger  $\int B \cdot dl$  and be bent through a larger angle, and those to the other side will pass through a smaller  $\int B \cdot dl$  and be deflected by a smaller angle. The left/right change in asymmetries and cross section of (A.1.3) and (A.1.4) are related by

$$a^+_l = a^-_l = a^+_r = a^-_r = a \quad (\text{A.12.1})$$

and

$$s^+_l = s^-_l = -s^+_r = -s^-_r = s. \quad (\text{A.12.2})$$

Estimating the parameters  $a$  and  $s$  as from

$$a = \frac{\partial \Delta}{\partial \theta} \frac{\partial \theta}{\partial x} \text{ hf } dx, \quad s = \frac{1}{\sigma} \frac{\partial \sigma}{\partial \theta} \frac{\partial \theta}{\partial x} \text{ hf } \quad (\text{A.12.3})$$

The change in magnetic field deflection can be determined as

$$\frac{\partial \theta}{\partial x} \text{ hf } \approx 5 \times 10^{-3} \text{ deg mm}^{-1} \text{ at } \theta = 53^\circ \text{ and at the target center,} \quad (\text{A.12.4})$$

and

$$\frac{1}{\sigma} \frac{\partial \sigma}{\partial \theta} = 5.6 \times 10^{-2} \text{ deg}^{-1}, \quad (\text{A.12.5})$$

to find that

$$\delta A \approx 2.8 \times 10^{-4} dx \quad (\text{A.12.6})$$

throughout the angular range. Lateral deviations should be kept to within  $\pm 0.5$  mm.

#### (b) Longitudinal Target Deviations

Target deviations along the symmetry axis cause recoil protons to have a larger or lower  $\int B \cdot dl$ , depending on the direction of the shift. One discovers that the angular shift is of the same magnitude for protons scattered to the left or right, but towards larger angles on one side and towards lesser angles on the other. Consequently in the notation of (A.1.3):  $a^\pm_l = -a^\pm_r$  and  $s^\pm_l = s^\pm_r$ .

$$a^\pm_l = PA \frac{\partial \Delta}{\partial \theta} \frac{\partial \theta}{\partial l} \quad (\text{A.12.7})$$

$$\text{at } 53^\circ, \quad \frac{\partial \theta}{\partial l} \approx 3 \times 10^{-3} \text{ deg mm}^{-1} \quad (\text{A.12.8})$$



Substituting into (A.1.9) one finds that  $\delta A \ll 10^{-4}$  close to where  $A = 0$ . If such deviations are correlated with spin flips,  $\Delta A = 4 \times 10^{-5}$  dl. Therefore the upper limit on longitudinal displacements is  $\pm 0.7$  mm.

### (c) Vertical Target Displacement

For vertical displacements we have  $a_{\pm}^{\pm} = -a_{\mp}^{\pm}$ ,  $s_{\pm}^{\pm} = s_{\mp}^{\pm}$ . At the zero-crossing, fluctuations in vertical position are not critical. If vertical displacements are correlated with spin flips  $\Delta A = 1.2 \times 10^{-4}$  dy (in mm). Vertical deviations should be kept within  $\pm 0.8$  mm.

## A.13 Neutron Detection Stability

A higher threshold on neutron detection effectively discriminates against a percentage of otherwise detected np pairs. If the efficiency of a left or right neutron bar increases or decreases by a fixed specific percentage  $s$ , then

$$s_L^{\pm} = s, \quad \text{and} \quad s_R^{\pm} = 0, \quad \Delta A = 0. \quad (\text{A.13.1})$$

If the efficiency changes randomly as  $\epsilon \pm \Delta \epsilon$  as the experiment progresses the estimation of  $\Delta A$  is somewhat more involved. If the spin of the beam or target is flipped  $N$  times (consider only the target as its polarization is flipped far less often) the average difference in the efficiency between the time with the target in the down direction and the target in the up direction is inversely proportional to the square root of the number of times the target spin was reversed and directly proportional to the standard deviation of the efficiency. The time scale at which the efficiency drifts is also important, but as this is not known the worst case will be selected - that the efficiency drifts cyclically comparable to the frequency of target polarization reversal. Then if all of the eight threshold discriminators on both of the neutron arrays have long term random instabilities to within  $\pm \Delta \epsilon$ , the uncertainty in each of the parameters  $s_{\mp}^{\pm}$  of equation (A.1.5) is

$$\frac{\Delta s_{\mp}^{\pm}}{(2\sqrt{N})} = \Delta \epsilon \quad (\text{A.13.2})$$

Substituting (A27) into (A9) one finds that

$$\delta A \approx \frac{\Delta \epsilon}{4P\sqrt{N}} \quad (\text{A.13.3})$$

With  $P = 0.6$ ,  $N = 8$  target polarization flips,  $\delta A \approx 0.15\Delta\epsilon$ .

The efficiency can change due to photomultiplier gain shifts. Estimates of  $\epsilon$  can be made based on the experimental results. Experiment #121 had neutron software cuts at roughly 1.1 MeV electron equivalent (MeVee). At this energy the neutron bar efficiency changed with respect to the energy threshold by  $0.0039 / \text{MeV}$ . The absolute efficiency of the neutron bars was  $\approx 30\%$ . To keep  $\delta A < 10^{-4}$ , changes in efficiency should have been kept within  $\pm 6 \times 10^{-4}$  (Equation A.13.3). Therefore the software cut at 1.12 MeVee must not change by 0.06 MeVee, or 5%. Since changes in software thresholds are directly proportional to photomultiplier gains, an equivalent condition to the stability of thresholds to  $\pm 5\%$  is that photomultiplier gains should also be kept to within  $\pm 5\%$ .

## A.14 Background

### (i) Polarized Neutron Beam

Let  $f$  = the fraction of target nuclei which can cause quasifree scattering of cross section  $\sigma_b$ . If the analysing power for the background is  $a_b$  the count rates for a polarised neutron run are,

$$L^+ = \sigma(1+PA) + f\sigma_b(1+Pa_b) \quad (\text{A.14.1a})$$

$$R^+ = \sigma(1-PA) + f\sigma_b(1-Pa_b) \quad (\text{A.14.1b})$$

$$L^- = \sigma(1-PA) + f\sigma_b(1-Pa_b) \quad , \text{ and} \quad (\text{A.14.1c})$$

$$R^- = \sigma(1+PA) + f\sigma_b(1+Pa_b) \quad (\text{A.14.1d})$$

Adopting the notation of (A.1.6) one gets

$$a_L^+ = \frac{f\sigma_b}{P\sigma}(1 + Pa_b) , \quad (A.14.2a)$$

$$a_R^+ = \frac{-f\sigma_b}{P\sigma}(1 - Pa_b) , \quad (A.14.2b)$$

$$a_L^- = \frac{-f\sigma_b}{P\sigma}(1 - Pa_b) , \text{ and} \quad (A.14.2c)$$

$$a_R^- = \frac{f\sigma_b}{P\sigma}(1 + Pa_b) . \quad (A.14.2d)$$

Then, substituting the above into (A.1.9) :

$$\delta A_n = \frac{f\sigma_b}{\sigma} a_b \quad (A.14.3)$$

To keep the effects on  $\delta A_n$  due to the background to within  $\pm 10^{-4}$ , the percentage of background counts to real n-p elastic counts multiplied by the background asymmetry must be kept within  $\pm 10^{-4}$ . An upper limit on the ratio of background to real n-p elastic events as  $\approx 1\%$ .

## (ii) Polarized Target

A background merely serves to lessen the asymmetry since the contents of the target other than  $^1\text{H}$  cannot be polarized. One finds that  $\delta A_p = 0$ .

## Appendix B Experimental Overview

Conventionally, a Ph.D. candidate in experimental nuclear physics must take responsibility for the design, construction, observation and analysis of an experiment. Physics is changing. Today, some experiments require the resources of large groups of physicists together with teams of technicians. Although there is great opportunity for graduate students to learn from such large-collaborations, attention must be paid to whether or not the responsibilities chosen by a student justify a postgraduate degree.

Although all aspects of the experiment are fully described in this work, it is the result of a cooperative effort of many people. The charge symmetry breaking experiment was first proposed in 1978 and funding was granted two years later. In 1982 the author joined the existing experimental collaboration.

There were distinct divisions of labour among smaller groups within the experimental group itself. The construction and operation of the frozen spin target was, for the most part, carried out by the cryogenics staff at TRIUMF. One of the two neutron scintillator arrays had been used previously. All other equipment was constructed specifically for the experiment. The neutron beam facility at TRIUMF was modified to meet the strict demands of the CSB experiment. The design work of the apparatus was subdivided among the group and constructed by the TRIUMF technical support staff. During this time the author was only peripherally involved.

Due to the high operating cost of the TRIUMF cyclotron the experiment ran 24 hours each day. Schedules were established so that three or four persons were always on duty in staggered eight hour shifts. During the actual data collection the author was responsible for most of the duties required to keep a complex experiment running.

Before the beginning of each experimental run a proper beam tune was established. This was the duty of the TRIUMF technical support staff under the guidance of a group member. Once the beam tune was satisfactory the SEM (see section 3.2) feedback loop was slowly turned on to maintain a constant proton beam position on the  $LD_2$  target. The proper SEM - beam correction magnet system matrix elements were required before the feedback system was operational.

High voltages were applied to each of the neutron bar scintillator array photomultipliers (see section 3.10.4 and 4.11.1). Since each photomultiplier response changed drastically between each of the four data-taking runs a few days were required before the proper calibration was achieved. Recalibrating the photomultipliers required fast analysis of the data collected before the appropriate corrections to the photomultiplier bias could be applied. Once the proper calibration was established, continuous checks of the data

were necessary to monitor neutron bar photomultiplier signal gain shifts. Corrections were applied whenever required. Additional analysis checks were required to identify and remove corrupted components of the elaborate experimental electronics.

The position and dimensions of the neutron beam at the neutron beam polarimeter location were measured. The stability of the neutron beam parameters was required otherwise systematic errors would overwhelm the experiment on the level of the design precision.

The stability of the neutron and proton hardware detection thresholds were absolutely necessary for an accurate measurement. A change in the detection thresholds could conceivably alter the  $A_n$  measurement differently than the  $A_p$  measurement and thereby introduce systematic errors. These thresholds were monitored on a regular basis.

The target vessel had to be filled with frozen butanol beads and cooled to 65 mK. This procedure was completed by the cryogenics subgroup. Once the target was operational, the temperature and polarization were monitored throughout the experiment. Liquid helium and nitrogen refrigerant were supplied on a daily basis. The target holding field and polarization direction were frequently reversed on the basis of a four day cycle (see section 3.13). This lengthy process required four hours during which data collection was suspended.

The  $^4\text{He}$  levels of the spin precession superconducting solenoid Janis were constantly monitored and maintained to ensure the refrigeration system operated properly.

A new proton polarimeter target foil had to be cut, weighed and installed in the polarimeter before each new run and replaced if radiation damaged.

Broken delay line chamber anode wires needed to be replaced. This task required disassembling the chamber, identifying and replacing the broken anode wire, and replacing the chamber in its original position. The accuracy of the experiment required high precision while replacing the chamber. Apparatus was specifically designed to ensure that the delay line chambers were repositioned accurately.

An NMR signal from the neutron spin precession dipoles Bonnie and Clyde were constantly monitored to ensure a stable magnetic field. Additional Hall probes were located in the target holding field room temperature and superconducting magnets. These were constantly monitored and charted over the duration of the experiment to check the stability of the target holding field.

It was not until the data collection was completed that the author assumed the major portion of his duties. The author was responsible for all aspects of the analysis. The experiment was an extremely accurate measurement where all possible systematic errors affecting  $\Delta A$  had to be identified to the  $10^{-4}$  level during the analysis. Initially he worked

together with one other group member and gradually assumed complete control of the data analysis. Before an experimental result was released, all aspects of the experiment had to be completely understood. Several subtle effects and their influence on the measurement were identified by the author.

The Fortran computer code specific to the experiment required to analyze the data was approximately 10,000 lines long. The author wrote a large percentage of the software and debugged it all. The analysis is described in full detail in the fourth chapter.

The analysis itself was labour intensive. Over two hundred and fifty magnetic tapes were collected. Each tape required an initial pass to establish the calibration constants (see section 4.11) and another to extract the asymmetry curves. A complete analysis cycle required two months of shift work to process all the data tapes. A preliminary run through the data was made without the participation of the author. A second and third analyses were made to study the data searching for effects overlooked during the data collection. The final analysis was then completed with a more sophisticated code to actually extract the zero-crossing angles.

A portion of the experimental data was collected with the butanol beads replaced by graphite beads to enable the background contamination level and asymmetry at the n-p elastic scattering asymmetry to be measured. The author assumed sole responsibility for analyzing the background data.

The data was analysed at the University of Alberta and concurrently at the University of Manitoba by two distinct groups. Only exchanges of advice and observations but not software were made between the groups. The results will be compared to assure that the final results were free of errors generated by software dependent effects. The author participated in many meetings between the two analysis groups to identify differences and to suggest appropriate corrections. As of writing the University of Manitoba analysis is not yet complete. Once both analyses are completed, a thorough comparison will be undertaken to resolve any differences in the final results.


Interest in charge symmetry breaking in the neutron-proton elastic scattering system remains quite high. The discrepancy between theory and experiment and between various calculations are quite large. At least three separate measurements at different energies are required to unravel the energy dependence of the various terms in the calculations. The completed experiment at 477 MeV, the ongoing effort at the Indiana University Cyclotron Facility at 188 MeV as well as the future TRIUMF experiment at 350 MeV will provide this energy dependence. The candidate authored the proposal to remeasure the extent to which charge symmetry was broken at 350 MeV and successfully defended it in front of the TRIUMF Experimental Evaluation Committee (EEC). The author was responsible for

identifying changes to be made to the experimental apparatus, estimating the time required for the measurement to be made, identifying sources of possible systematic errors at 350 MeV, as well as justifying the need for the CSB experiment to be repeated at a lower energy. The proposal itself has been reproduced in appendix C.

Several papers have been published relating to the TRIUMF measurement. The author's duties include the writing of the definitive paper on the experiment (a distillation of this thesis) and the writing of a separate paper devoted to the evaluation of the  $A_n$  and  $A_p$  zero - crossing angles (The experiment was not designed to measure the zero-crossing angles but the difference. An absolute measurement is much more susceptible to systematic errors and requires additional analysis techniques.). These values will be an important constraint on existing neutron - proton elastic scattering phase shift analyses.

Summarizing, the author participated fully in the experimental data collection and assumed complete control over the University of Alberta analysis. An accurate, self consistent, convincing result was obtained. The release of the definitive experimental paper now awaits the completion of the University of Manitoba half of the analysis. An experimental proposal was written for a similar, yet distinct, experiment measuring the extent to which charge symmetry is broken at 350 MeV.

## Appendix C

<b>TRIUMF - RESEARCH PROPOSAL</b> 		Experiment no	Sheet 1 of 31
Title of proposed experiment <b>Charge Symmetry Breaking in n-p Elastic Scattering at 350 MeV</b>			
Name of group R. Tkachuk L.G. Greeniaus W.T.H. Van Oers			
Spokesperson for group			
Members of group (name, institution, status) (For each member, include percentage of research time to be devoted to this experiment over some specified time period)			
	Department-Faculty-University	% of Total Research Time (1986-7)	
L.G. Greeniaus	University of Alberta/TRIUMF	15%	
R. Abegg	University of Alberta/TRIUMF	10	
J. Birchall	University of Manitoba	10	
C. Davis	University of Manitoba	15	
P.W. Green	University of Alberta/TRIUMF	10	
C. Lapointe	University of Alberta	10	
C.A. Miller	University of Alberta/TRIUMF	10	
W.J. McDonald	University of Alberta	10	
G.A. Moss	University of Alberta	15	
W.D. Ramsay	University of Manitoba	15	
R. Tkachuk	University of Alberta	50	
W.T.H. van Oers	University of Manitoba	15	
Date ready		Beam time requested	
Spring '87		12-hr shifts	Beam line/channel
Fall '87		6(test)	4A--9° Neutron Port
Total		44	4A--9° Neutron Port
		50	Polynized primary beam?
			No
			Yes



<b>BEAM REQUIREMENTS</b>	Sheet 2 of 31								
Experimental area  Proton Area Beam Line 4A Neutron Scattering Area									
Primary beam and target (energy, energy spread, intensity, pulse characteristics, emittance)   <table> <tr> <td>Proton Beam Energy</td> <td>370 MeV</td> </tr> <tr> <td>Average Proton Polarization</td> <td>0.7</td> </tr> <tr> <td>Average Proton Current</td> <td>1.5 <math>\mu</math>A</td> </tr> <tr> <td>LD<sub>2</sub> Target</td> <td></td> </tr> </table>		Proton Beam Energy	370 MeV	Average Proton Polarization	0.7	Average Proton Current	1.5 $\mu$ A	LD <sub>2</sub> Target	
Proton Beam Energy	370 MeV								
Average Proton Polarization	0.7								
Average Proton Current	1.5 $\mu$ A								
LD <sub>2</sub> Target									
Secondary channel									
Secondary beam (particle type, momentum range, momentum bite, solid angle, spot size, emittance, intensity, beam purity, target, special characteristics)   <table> <tr> <td>Neutron Port</td> <td>9° collimator</td> </tr> </table> 350 MeV-neutrons Neutron intensity at target $3.3 \cdot 10^{+6}$ n/sec on 2 cm wide x 5 cm high area Two spin precession dipoles as required in experiment #121.		Neutron Port	9° collimator						
Neutron Port	9° collimator								

## SUMMARY

Sheet 3 of 31

Do not exceed one page.

An experiment similar in most respects to the recently completed TRIUMF experiment #121 is proposed to test the validity of charge symmetry in the n-p system at a lower incident neutron energy of 350 MeV. Direct evidence of charge symmetry breaking (CSB) can be detected by measuring the analyzing power of a polarized neutron beam scattered from a proton target,  $A_n$ , and comparing the result to the analyzing power measured with an unpolarized neutron beam on a polarized proton target,  $A_p$ . Using a polarizable target, the analyzing powers can be measured in two concurrent experiments utilizing the identical equipment. Rather than measuring the difference  $\Delta A = A_n - A_p$  throughout a large angular range, it is proposed that  $\Delta A$  be measured at the zero crossing angle of the analyzing power. Such an experiment requires no knowledge of absolute target or beam polarizations. Scattered neutrons and protons will be detected in two sets of detection apparatus situated with mirror symmetry with respect to the neutron beam axis. Such an experimental arrangement reduces all systematic errors affecting the measurement of  $A_n$  and  $A_p$  to first order and those affecting  $\Delta A$  to second order. The experiment will attain an accuracy in the determination of the difference in the zero-crossing angles to  $\pm 0.026^\circ$ , corresponding to an accuracy in  $\Delta A$  of  $\pm 0.0008$ . The precision of this experiment will be better than the preliminary error of  $\pm 0.0018$  achieved by experiment #121.

## SAFETY

Sheet 4 of 31

Summarize possible hazards associated with the experimental apparatus, precautions to be taken, and other matters that should be brought to the notice of the Safety Officer. Details must be provided separately in a safety report to be prepared by the spokesperson under the guidance of the Safety Report Guide available from the Science Division Office.

Operation of  $LD_2$  target (800 cm<sup>3</sup> of liquid) in BL4A  
Operation of cryogenic polarized hydrogen target (35 cm<sup>3</sup>) in Neutron Area  
HV supply to Neutron Detector photomultipliers and delay line wire chambers  
Gas supply to delay line wire chambers

## DETAILED STATEMENT OF PROPOSED RESEARCH

Sheet 5 of 31

The following information should be included:

- (a) **Scientific value of the experiment:** Describe the importance of the experiment and its relation to previous work and to theory. All competitive measurements at other laboratories should be mentioned. Include examples of the best available theoretical calculations with which the data will be compared.
- (b) **Description of the experiment:** Techniques to be used, scale drawing of the apparatus, measurements to be made, data rates and background expected, sources of systematic error, results and precision anticipated. Compare this precision with that obtained in previous work and discuss its significance in regard to constraining theory. Give a precise list of targets to be used in order of their priority.
- (c) **Experimental equipment:** List all equipment to be used and indicate which is to be supplied by TRIUMF. Details of all equipment and services to be supplied by TRIUMF must be provided separately on the Technical Review Form available from the Science Division Office.
- (d) **Readiness:** Provide a schedule for assembly, construction and testing of equipment. Include equipment to be provided by TRIUMF.
- (e) **Beam time required:** State in terms of number of 12-hour shifts. Show details of the beam time estimates, indicate whether prime-user or parasitic time is involved, and distinguish time required for test and adjustment of apparatus.
- (f) **Data analysis:** Give details and state what data processing facilities are to be provided by TRIUMF.

### (a) Scientific Value of Experiment

An experiment similar in most respects to the recently completed TRIUMF experiment #121 is proposed to test the extent of the isospin mixing component of the neutron-proton interaction at 350 MeV. The experiment will measure the difference in analyzing powers  $A_n$  and  $A_p$  (where the subscript denotes the polarized nucleon) at the zero-crossing angle. Designed as a null measurement, the experiment will achieve an accuracy in  $\Delta A$  of  $\pm 0.0008$  or  $\pm 0.026^\circ$  in the crossover angle.

The extent to which charge symmetry is valid has been of fundamental interest ever since it was postulated soon after the discovery of the neutron. Much circumstantial evidence has accumulated over the years favouring the breaking of charge symmetry on the order of less than a percent. Although low energy nucleon studies have shown a slight inequality of the nn, np and pp scattering lengths<sup>1)</sup>, it has proved very difficult to remove experimental and theoretical uncertainties to unequivocally isolate charge symmetry breaking interactions. Evidence of CSB has surfaced in  $\pi$  scattering from  $^3\text{H}$  and  $^3\text{He}$ <sup>2)</sup> and in  $\pi^\pm$ -d cross section experiments<sup>3,4)</sup>. The  $\pi$ -d total cross section results have been interpreted in terms of mass splitting in the  $\Delta$  system. The large effect observed in reference<sup>2)</sup> may be due to purely geometric effects caused by coulomb repulsion combined with 3-body forces<sup>5)</sup>. Differences in the binding energies of mirror nuclei, the Nolen-Schiffer effect<sup>6)</sup>, hint at the presence of CSB terms in the interaction, but again, the isolation and removal of EM effects has proven to be difficult.

Charge symmetry implies the complete separation of the isoscalar and isovector components of the n-p interaction. This in turn leads to equal differential cross sections of polarized neutrons scattering from unpolarized protons and vice versa. As a result  $A_n(0) = A_p(0)$ . A nonvanishing analyzing power difference  $\Delta A$  is directly proportional to the isospin singlet-triplet mixing amplitude and therefore direct evidence of a CSB term in the interaction.

A measurement of  $\Delta A(\theta_p)$  at the zero-crossing angle at 477 MeV has yielded a preliminary result of  $\Delta A = A_n - A_p = (+3.4 \pm 1.8) \cdot 10^{-3}$ . This value should be compared to the theoretical result<sup>7)</sup> of  $-4.1 \cdot 10^{-3}$  which includes direct EM effects, the effect of the neutron-proton mass difference in one-pion exchange and the isospin mixing  $\rho$ - $\omega$  meson exchange. The contributions to  $\Delta A$  due to each of the above interactions, as well as the experiment #121 result, are illustrated in figures [1] and [2] for neutron beam energies of 350 and 477 MeV. The discrepancy between theory and experiment at 477 MeV encourages a repeat measurement at a different energy. At 350 MeV the theoretical prediction of  $\Delta A$  is  $-4.0 \times 10^{-3}$ . The calculations were done with phase shifts from Arndt et al.<sup>8)</sup> and the Paris potential.

The 188 MeV experiment at IUCF is progressing slowly and is expected to yield results similar to Experiment #121 within a year or so. The new theoretical prediction at that energy is shown in figure [3]. The magnitudes of the contributing terms are significantly different from those at both 350 MeV and 477 MeV. The discrepancy between theory and experiment at 477 MeV may be due to problems with the energy dependence of the terms included in the calculation, and/or to terms that have not been included. In any event, at least three separate measurements will be essential to clarify the theoretical interpretation. There are no theoretical predictions for the proposed experiment at LAMPF but the effect is probably of comparable size to that near 500 MeV.

#### (b) Description of the Experiment

As the proposed experiment is similar in most respects to the recently completed TRIUMF experiment #121 comparisons between it and the proposed experiment are frequently made. The experiment shall achieve an accuracy in the zero-crossing angle to  $\pm 0.026^\circ$ , corresponding to an accuracy in the analyzing power of  $\pm 0.0008$ . The only comparable measurement was taken during experiment #121 where the preliminary accuracy of  $\Delta A$  was  $\pm 0.0018$ . This preliminary result is based on analysis which has not yet included the effects of quasi-elastic background subtraction. Achieving the accuracy of  $\pm 0.0008$  will require less beam time than that used for experiment #121: fifty 12 hour shifts. The experimental parameters for the proposed experiment and those observed in the successfully completed experiment are summarized in table (1).

## DETAILED STATEMENT OF PROPOSED RESEARCH

Sheet 7 of 31

Table (i) Experimental Parameters

	Proposed	Experiment #12
Proton Energy	368 MeV	498 MeV
Reproducibility of Energy	$\pm 0.09$ MeV	$\pm 0.09$ MeV
Polarization	0.70	0.68
Proton Current Unpolarized	1.5 $\mu$ A	0.8 $\mu$ A
" " Polarized	1.5 $\mu$ A	0.4 $\mu$ A
Neutron Energy (spread)	350 MeV	477 MeV
	11 MeV FWHM	11 MeV FWHM
Neutron Polarization	0.57	0.50
Neutron Intensity on Target	$1.5 \times 10^5$ n/(sec cm <sup>2</sup> )	$3 \cdot 10^4$ n/(sec cm <sup>2</sup> )
Target Volume	35.0 cm <sup>3</sup>	50.0 cm <sup>3</sup>
Proton Angular Range (lab)	$45.1^\circ < \theta_p < 58.5^\circ$	$47.0^\circ < \theta_p < 57.0^\circ$
Neutron Angular Range (lab)	$27.0^\circ < \theta_n < 40.4^\circ$	$27.0^\circ < \theta_n < 37.0^\circ$
Estimated np Elastic Event Rate	27/sec	6/sec
Energy Resolution	$\sigma_{Ep} = 10$ MeV $\sigma_{En} = 17$ MeV	$\sigma_{Ep} = 10$ MeV $\sigma_{En} = 17$ MeV
Energy Sum Resolution	$\sigma_{Esum} = 21$ MeV	$\sigma_{Esum} = 21$ MeV
Angular Resolution	$\sigma_{\theta p} = 0.8^\circ$ $\sigma_{\theta n} = 0.3^\circ$	$\sigma_{\theta p} = 0.8^\circ$ $\sigma_{\theta n} = 0.2^\circ$
Opening Angle Resolution	0.8°	0.8°
Azimuthal Coplanarity Resolution	1.5°	1.4°

The laser pumped polarized ion source is assumed to be available to provide a polarized proton beam intensity of 1.5  $\mu$ A averaged over the duration of the experiment. This will significantly decrease the amount of beam time necessary to complete the experiment compared to that of experiment #121.

Proton beam energy and polarization will be monitored throughout the experiment with a modified version of the existing beam energy monitor and polarimeter. During experiment #121 relative proton beam energies were determined to  $\pm 0.10$  MeV within ten minutes of the initiation of each run. Absolute knowledge of the neutron beam energy is not crucial to the experiment, but the energy must be reproducible to within  $\pm 0.10$  MeV from one run to the next. Experiment #121 has shown that this criterion can be attained. The

proton polarimeter detects protons scattered from a kapton foil at  $17^\circ$  in coincidence with the recoil proton. Throughout the previous experiment the measured instrumental asymmetry of the polarimeter was constant within  $\pm 0.001$ . This apparatus will undergo modifications for use at a lower beam energy and higher intensities but no decrease in accuracy is foreseen. The anticipated proton beam currents would destroy the kapton foils in the existing polarimeter within 24 hours after their insertion.

For the polarized beam portion of the experiment a solenoid precesses the vertical polarization of the proton beam into the scattering plane, perpendicular to the direction of motion. This takes advantage of the large  $D(p,n)2p$  transverse polarization transfer coefficient  $([R_t^2 + R_t'^2]^{1/2} = 0.86)$  to attain the maximum neutron polarization. As  $R_t$  increases from 0.72 to 0.86 for the proposed experiment as compared to its value for experiment #121, the amount of beam time necessary to complete the experiment will be reduced. Minor deviations in the proton beam position on the  $LD_2$  target will be corrected continuously over the course of the experiment to maintain an accuracy in the position to  $\pm 0.2\text{mm}$  and to  $\pm 0.009^\circ$  in the incident angle, as in experiment #121. Asymmetries from two sets of x and y split plate secondary emission monitors (SEMs) situated before and after the spin precession solenoid are used to correct the settings of steering magnets located further upstream. The position of the proton beam on the SEMs can be made stable to  $\sigma_x = 0.1\text{mm}$ .

The n-p scattering cross section increases slightly at the lower energy. The intensity noted in table (1) was calculated by scaling the measured neutron intensity at 477 MeV by the ratio of the two differential cross sections-

Two dipole magnets, "Bonnie" and "Clyde", are to precess the neutron spin back into the vertical direction. Polarization components that do not change direction with beam polarization reversals are precessed into the direction of the neutron beam. Parity conservation forbids any contribution to a measured asymmetry from such spin components.

The TRIUMF frozen spin target (FST) is assumed to be available. The holding field (2.6kG) on such a target is lower than conventional types of polarized targets. The reduced effect of the target holding field on recoil proton tracks is gained at the expense of a four hour time period needed to re-polarize the target for each day of operation. The volume of the target will be reduced from  $50\text{ cm}^3$  to  $35\text{ cm}^3$  and the shape changed from cylindrical to rectangular to minimize the effects of multiple scattering in the target (see appendix).

After passing through the FST the neutron beam will pass through a profile monitor consisting of a charged particle veto counter, a scintillator converter and two delay line chambers (DLCs). In experiment #121 the centroids of the neutron beam were measured to be within  $\pm 0.5\text{ mm}$  of the symmetry axis. Such a deviation caused an angle error of less than  $\pm 0.03^\circ$ . Errors in the measurement of  $\Delta A$  due to such effects are cancelled when the analyzing powers are averaged over the left and right detection systems (see appendix). The profile monitor is immediately followed by the neutron polarimeter. The

polarimeter serves both to determine the proper settings for the dipole magnets and to monitor the neutron polarization throughout the experiment.

A schematic drawing of the detection apparatus is illustrated in figure [5]. The scattered neutrons are detected in a large  $105.0 \times 105.0 \times 30.0 \text{ cm}^3$  NE110 scintillator array 446 cm from the FST. Each array is composed of fourteen  $105.0 \text{ cm}$  long and  $15 \times 15 \text{ cm}^2$  cross section scintillator bars stacked two deep and seven high. Each bar is viewed on both ends with a photomultiplier. The neutron photomultiplier gains are to be monitored throughout the experiment by detecting passing protons in coincidence with small "button" counters located in the back of the arrays. The energies of passing the protons do not have to be known absolutely, only that the energy spectrum remains constant from run to run. A neutron detection efficiency of 29% has been estimated based on a Monte Carlo analysis.

The proton detection system consists of a thin proton time of flight start scintillator and two x-y DLCs situated close to the target, two other x-y DLCs further downstream, a  $\Delta E$  and E counter followed by an absorber and veto counter. During experiment #121, deviations between the four pairs of measured horizontal and vertical proton track co-ordinates and a straight line fit were within  $\pm 0.1 \text{ mm}$ . Efficiencies were typically  $> 99\%$  per chamber. All proton detection apparatus will be rigidly attached to a boom bolted to the floor of the neutron area to eliminate the possibility of movement during the experiment. Moving the detection apparatus closer to the target from the experiment #121 positions has increased the effective solid angle of the apparatus by 45% without a decrease in the ability to distinguish among elastic n-p events and  $^{12}\text{C}(n,np)$  background as compared to experiment #121. Experiment #121 also included a wedge-shaped absorber in front of the E-counter to reduce low energy background and to equalize the n-p elastic proton energies at the E-counter independent of the proton angle. At the lower energy of the proposed experiment the wedge must be removed. Monte Carlo simulations made before data taking of experiment #121 began showed that the trigger rate of  $^{12}\text{C}(n,np)^{11}\text{B}$  background would increase by a factor of two without the wedge. Approximately 0.5% of background slipped through the kinematic software cuts during experiment #121 analysis, but this is not expected to change. This level is within allowable limits (see appendix on systematic errors). A secondary target will be inserted just behind the FST to allow a more exhaustive analysis of background events in case unforeseen problems arise in eliminating the background under the new conditions.

An exhaustive summary of the magnitudes of possible systematic errors and their effects on direct asymmetry measurements and, more seriously, of their effects on the difference  $\Delta A = A_0 - A_p$  is presented in the appendix. The extent to which potential systematic errors can effect the difference  $\Delta A$  is briefly summarized below in table [2] with their experiment #121 counterparts.

Achieving an accuracy in  $\Delta A$  to the stated value will require two  $6 \times 12$ -hour shifts of unpolarized beam time to calibrate equipment and  $38 \times 12$ -hour shifts (calculations summarized in a later section) of beam time utilizing the polarized ion source. The actual experiment will be subdivided into a run measuring  $\Delta A$  for n-p elastic scattering, and a later run to measure  $^{12}\text{C}(n,np)^{11}\text{B}$  background with the FST filled with carbon beads.



Table (2) Effect on AA of Experimental Systematic Errors

Systematic	Parameters	477 MeV	350 MeV
(1) Inequality of Up and Down Polarization	$P^+=0.8, P^-=0.6$	0 at $A=0$ $8 \times 10^{-5}$ at $A=0.2$	0 at $A=0$ $8 \times 10^{-5}$ at $A=0.2$
(2) Unequal Left and Right Scattering Angle	$ \theta_L - \theta_R  = 0.1^\circ$	$< 10^{-5}$ at $A=0$	$< 10^{-5}$ at $A=0$
(3) Unequal Scattering Angles and unequal Polarization	$P^+=0.8, P^-=0.6$ $ \theta_L - \theta_R  = 0.1^\circ$	$< 10^{-5}$ at $A=0$ $10^{-4}$ at $A=0.2$	$< 10^{-5}$ at $A=0$ $10^{-5}$ at $A=0.2$
(4) Position modulation of Proton Beam at $LD_2$ target	$ x^+ - x^-  = 1 \text{ mm}$	$< 2 \times 10^{-4}$	$2 \times 10^{-4}$
(5) Movement of FST with Respect to Holding Field	$\Delta r = 1 \text{ mm}$	$< 4 \times 10^{-4}$	$5 \times 10^{-4}$
(6) Incorrect Precession of Proton Beam Spin	$\Delta \phi_p = 5^\circ$	$< 10^{-4}$	$< 10^{-4}$
(7) Incorrect Precession of Neutron Beam Spin	$\Delta \phi_n = 5^\circ$	$< < 10^{-4}$	$< < 10^{-4}$
(8) Residual Transverse Neutron polarization when FST polarised	$P_n < 0.035$	$2 \times 10^{-4}$ at $A=0$ 0 at $A=0$	$2 \times 10^{-4}$ at $A=0.2$ 0 at $A=0$
(9) Multiple Scattering in FST	$\theta_{rms} = 0.7^\circ$	$8 \times 10^{-4}$	$7 \times 10^{-4}$
(10) Irreproducibility of Target Holding Field	$\sigma_{hf} = 2.5G$	$< 10^{-4}$	$< 10^{-4}$
(11) Quasi-Free Scattering at FST Upper limit on ratio of back-ground to np elastic events: 0.01	$A_b = 0.012$	$10^{-4}$	$10^{-4}$
(12) Neutron Detector Instability	1% gain shift	$2 \times 10^{-5}$	$2 \times 10^{-5}$
(13) Proton Beam Energy Shift	$\Delta E = 0.1 \text{ MeV}$	$< < 10^{-4}$	$10^{-4}$
(14) Proton Beam Angle Modulation	$ \theta^+ - \theta^-  = 0.1^\circ$	$< 10^{-4}$	$< 10^{-4}$

**(c) Experimental Equipment**

- (i) It is assumed that the laser pumped polarized ion source will be available. Preliminary calculations have assumed an average polarized intensity of  $1.5 \mu\text{A}$  over the course of the experiment.
- (ii) Proton beam monitors with a 1 mm resolution will be required directly in front of the  $\text{LD}_2$  target.
- (iii) A proton beam polarimeter insensitive to small drifts in beam position and operable at beam currents of  $2 \mu\text{A}$  will be required.
- (iv) The frozen spin target with a volume of  $35 \text{ cm}^3$  is assumed to be available. This is the configuration planned for experiment #182 ( $A_{nn}$ ).
- (v) The 8 delay line multiwire proportional counters, range counters, thin scintillators and proton beam energy monitoring device will be provided by the experimenters.
- (vi) The 2 neutron scintillator arrays used for experiment #121 are assumed to be available.
- (vii) The electronics requirement for the proposed experiment is the same as for experiment #121 or the  $A_{nn}$  experiment.
- (viii) It is assumed that the DG Eclipse is available for data acquisition and online analysis.

**(d) Readiness**

The majority of the equipment needed is to be reused from experiment #121. The lower energy and larger expected beam currents do make alterations to a portion of the equipment necessary.

## DETAILED STATEMENT OF PROPOSED RESEARCH

Sheet 12 of 31

Equipment	Alterations	Date Ready
Frozen Spin Target	Reduction in Volume of existing target from 50 cm <sup>3</sup> to 35 cm <sup>3</sup> .	Spring '86
TOF Start System	Modifications to existing proton TOF system to allow viewing of secondary target.	Jan '87 for tests
Proton Booms	Modifications to existing system to enable moving the counter system closer to the target.	Jan '87 for tests
Proton Polarimeter/ Beam Energy Monitor	Modifications to existing apparatus to enable running at lower energy and higher beam currents.	Jan '87 for tests

The experiment will be ready for initial tests in early 1987, and calibrations and data-taking in fall 1987.

## (e) Beam Time Estimates

Values used to calculate the anticipated event rate are listed below:

Target Volume	35 cm <sup>3</sup>
Packing Fraction	70%
Hydrogen/unit volume	$4.6 \times 10^{22}/\text{cm}^3$
Average Differential Cross Section over detection region	6.5 mb
Neutron Intensity	$10^5/(\text{sec } \mu\text{A cm}^2)$
Defining Counter Dimensions	$67 \times 65 \text{ cm}^2$
Distance from FST	286 cm
Effective Solid Angle	40 msr
Neutron Detection Efficiency	29%
Deadtime	25%
Anticipated left + right Event Rate (deadtime subtracted)	$\approx 18/(\mu\text{A sec})$
Anticipated Background Rate	$\approx 50/(\mu\text{A sec})$

The effective solid angle is the angular range common to the left and right proton detectors.

The table below illustrates the anticipated parameters needed to achieve an accuracy in  $\Delta A$  of  $\pm 0.0008$  assuming an average beam current of 1.5  $\mu\text{A}$ .

## DETAILED STATEMENT OF PROPOSED RESEARCH

Sheet 13 of 31

	<u>Target Polarized</u>	<u>Beam Polarized</u>
Target/Beam Polarization	$0.80 \pm 0.03$	$0.60 \pm 0.02$
Measured Asymmetry Slope	$-0.024/\text{deg}$	$-0.017/\text{deg}$
Events over Angular Range (L + R)	$6 \times 10^6$	$8 \times 10^6$
Beam Time Needed	90 $\mu\text{A}$ hrs.	120 $\mu\text{A}$ hrs.
Beam Time	60 hrs.	80 hrs.

AA must be measured for the target holding field in the up and down times. We assume that data taking accounts for 16 hours each day (5 hours per day of target maintenance, neutron profile measurements and other systematic checks, as well as 3 hours per day as overhead). The number of 12-hour shifts needed to complete the experiment is summarized below:

(i) Equipment set up and testing	2 x 6	1 unpolarized beam
(ii) First Data taking run		
Setup and calibration	6	unpolarized beam
Data taking	18	polarized beam
(iii) Second data taking run		
Setup and calibration	6	unpolarized beam
Carbon background	8	polarized beam
Subtraction run		
<b>TOTAL</b>	<u>30</u>	

The carbon background runs will be taken with the FST filled with carbon beads.

## (f) Data Analysis

No computing facilities are to be provided by TRIUMF as data analysis will be completed at the University of Alberta VAX center.

References

- 1) E.M. Henley and G.A. Miller. **Mesons in Nuclei**, edited by M. Rho and D.H. Wilkinson. (North Holland, Amsterdam, 1979) 411
- 2) B.M.K. Nefkens et al., Phys. Lett 52 (1984) 735
- 3) E. Pedroni et al., Nucl. Phys. A300 (1978) 321
- 4) T.G. Masterson et al., Phys. Rev. C26 (1982) 2091
- 5) S. Barshay and L.M. Shegal, Phys. Rev. C31 (1985) 2133
- 6) J.A. Nolen, Jr. and J.P. Schiffer, Ann. Rev. Nucl. Sci. 19 (1969) 471
- 7) J. Svéne, Private Communications
- 8) R.A. Arndt et al. Phys. Rev. D28 (1983) 97

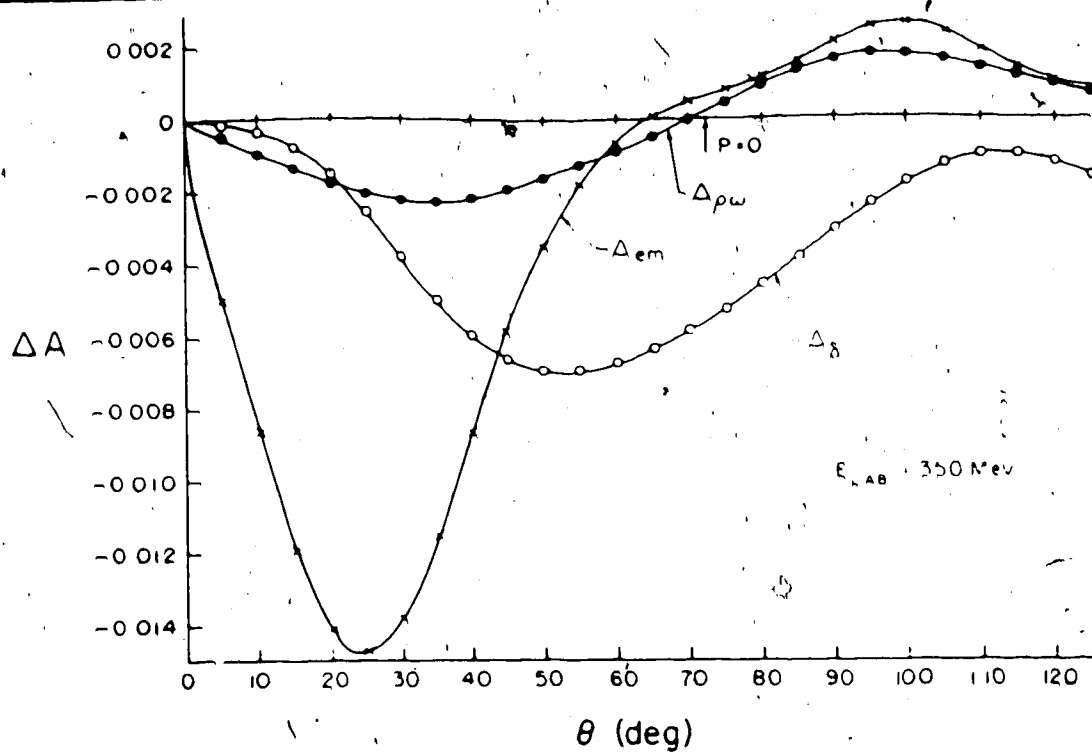


Figure 1

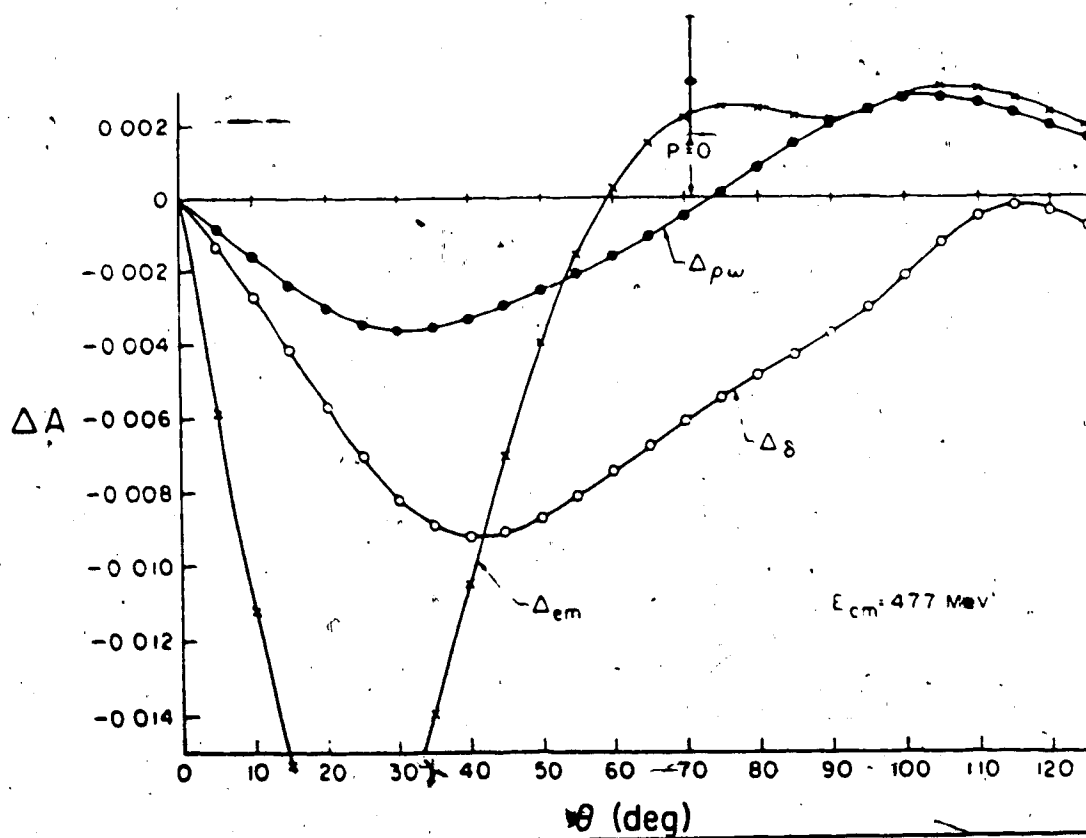


Figure 2

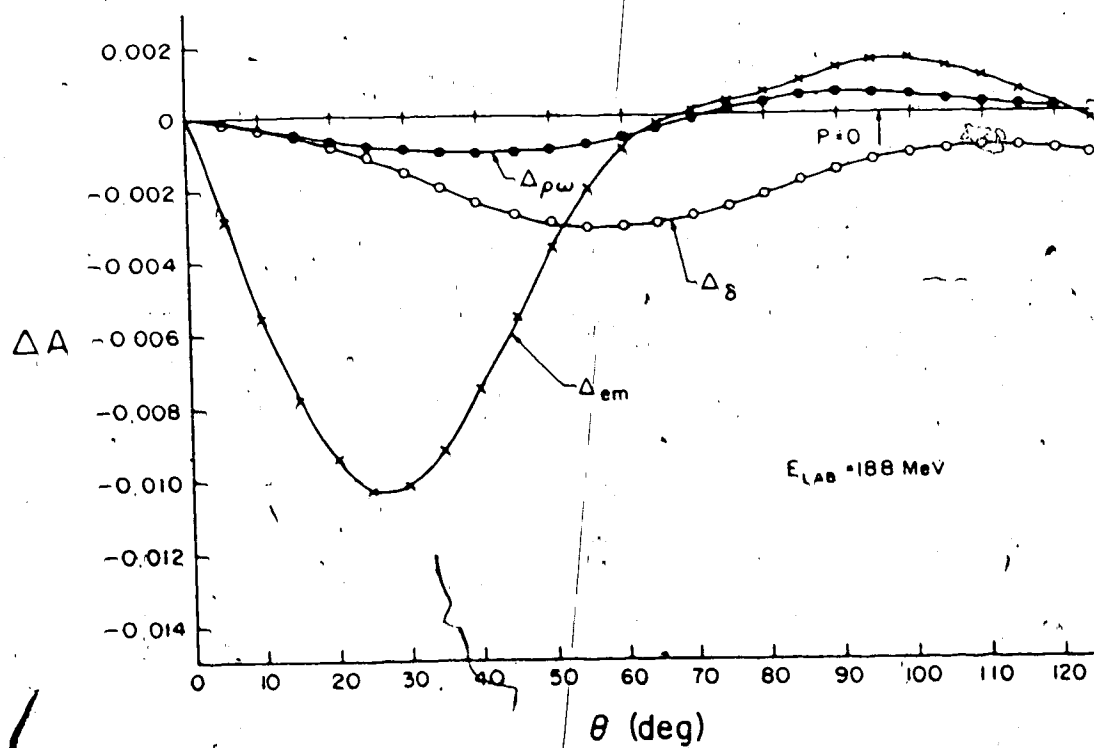


Figure 3

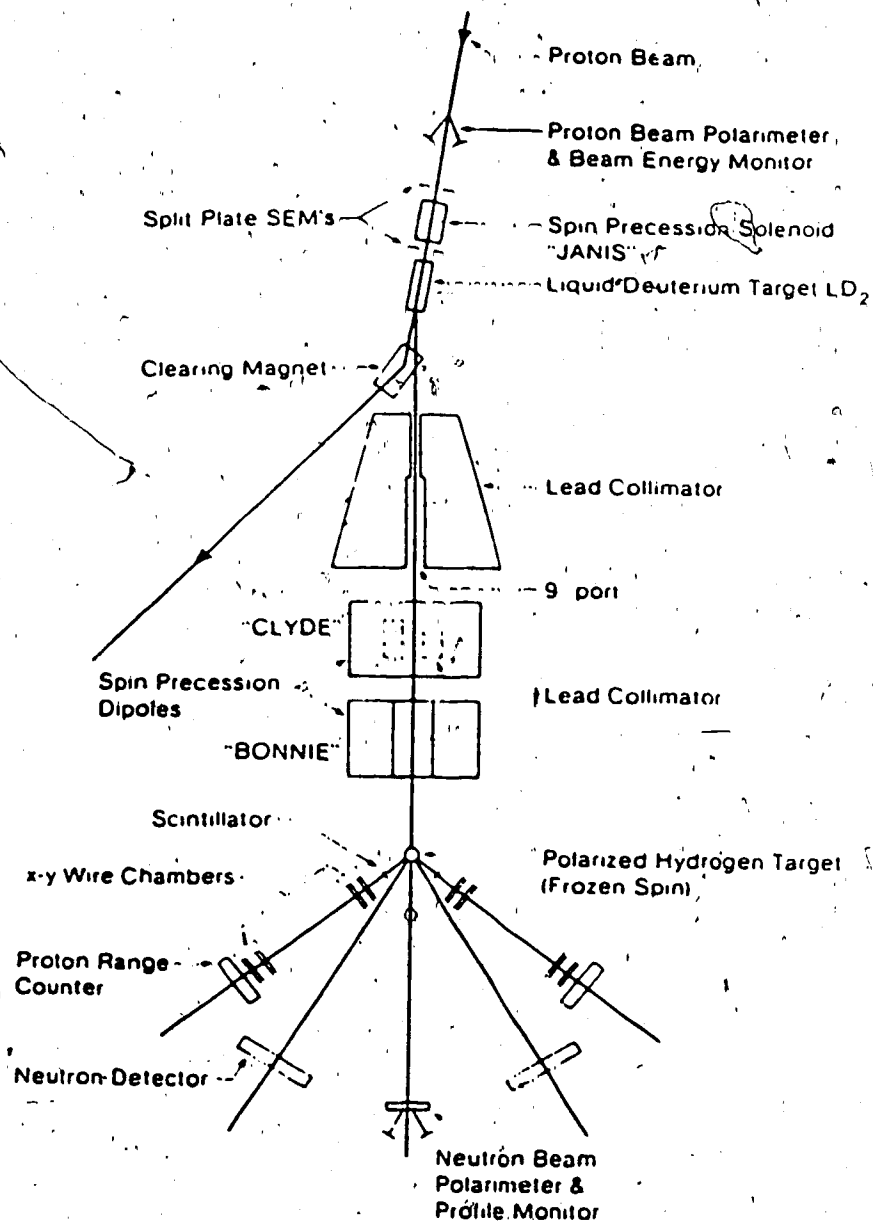
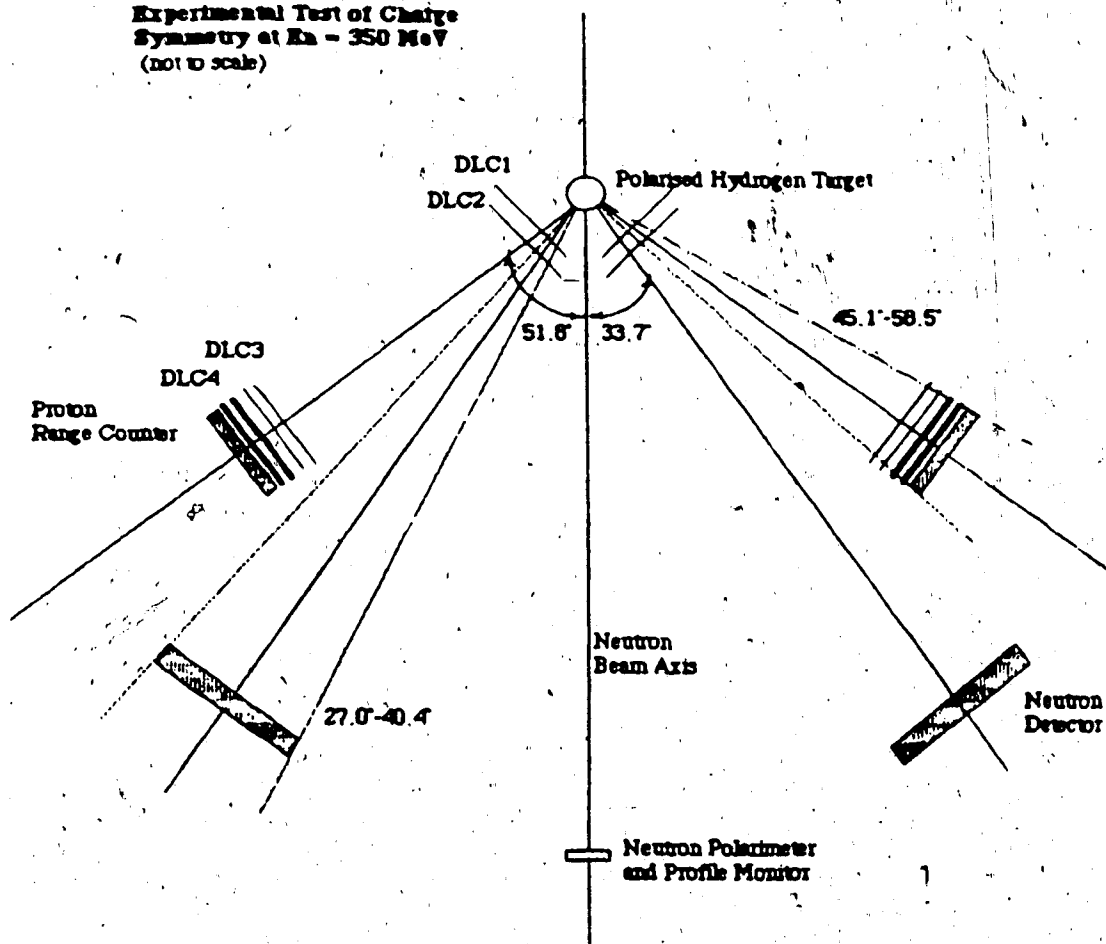


Figure 4



Figure (5)  
Experimental Test of Charge  
Symmetry at  $E_n = 350$  MeV  
(not to scale)



## COST OF THE EXPERIMENT

Sheet 19 of 31

Summarize, distinguishing salaries, major capital items and travel costs.  
Indicate the expected sources of funding

	Amount from NSERC for 1986 - 1987	Est. future requirements for completing project
1. Salaries and Stipends	\$ 0.00	\$ 9,600.00
2. Equipment	\$ 14,500.00	\$ 1,500.00
3. Travel		
(a) Conferences	\$ 5,500.00	\$ 5,500.00
(b) Field trips	\$ 15,713.00	\$ 32,200.00
4. Materials, supplies, incidentals	\$ 6,701.00	\$ 24,900.00
5. Computing costs	\$ 0.00	\$ 0.00
6. For use of TRIUMF facilities only:		
(a) Instrument rental	\$ 0.00	\$ 0.00
(b) Machine shop	\$ 0.00	\$ 0.00
(c) Electronics Shop	\$ 0.00	\$ 0.00
(d) Design office	\$ 0.00	\$ 0.00
<b>TOTAL</b>	<b>\$ 42,414.00</b>	<b>\$ 73,700.00</b>

## Appendix - Summary of Systematics

The nature of the experiment removes most errors to first order in the determination of the analyzing power,  $A$ , and to second order in the determination of  $\Delta A = A_n - A_p$ , where the subscript represents the polarized particle, at the zero-crossing angle. Absolute knowledge of beam intensity, target and beam polarization are not needed in the final calculations. Sources of error caused by differences between left and right detection apparatus are diminished by the manner in which the analyzing power is determined from experimental data. The following notes summarize the major sources of error and a calculation of their effects on the measured asymmetries under the most pessimistic of conditions. It must be stressed from the outset that  $A_n$  and  $A_p$  are independent quantities and are measured in two different, but concurrent, experiments utilizing the identical equipment. Systematic errors may affect one or both analyzing power measurements. With this in mind errors in individual asymmetries will be denoted  $\delta A_{n,p}$  and errors in the difference  $A_n - A_p$  will be identified as  $\delta \Delta A$ . The errors calculated herein follow the outline of a similar note written for an earlier CSB experiment at a higher incident neutron energy of 480 MeV by J. Birchall.

It is convenient to adopt a general notation which can be referred to throughout this note. The observed count rates in the left and right side detection apparatus can be written as

$$\begin{aligned} L^+ &= \sigma^+(1 + P^+ A_p^+) \\ R^+ &= \sigma^+(1 - P^+ A_p^+) \\ L^- &= \sigma^-(1 - P^- A_p^-) \\ R^- &= \sigma^-(1 + P^- A_p^-) \end{aligned} \quad (A1)$$

The '+' superscripts represent the direction of the target or beam polarization for measurements of  $A_p$  or  $A_n$ . The asymmetries are determined from the data as

$$\epsilon = (r-1)/(r+1) \quad (A2)$$

where  $r^2 = L^+ R^- / L^- R^+$

$$= [\sigma_p^+ \sigma_r^-(1 + P^+ A_p^+)(1 + P^- A_r^-)] / [\sigma_p^- \sigma_r^+(1 - P^- A_p^-)(1 - P^+ A_r^+)] \quad (A3)$$

In the complete absence of any experimental errors (A3) reduces to

$$r_0^2 = \left( \frac{1 + PA}{1 - PA} \right)^2 \quad (A4)$$

The differential cross section, as a function of angle, has been assumed to differ from its nominal value due to slight geometric or other imperfections as:

$$\sigma_{lr}^{\pm} = \sigma(1 + s_{lr}^{\pm}), \quad (A5)$$

and/or the observed asymmetry changes as

$$A_{lr}^{\pm} = A + a_{lr}^{\pm}, \quad (A6)$$

and the magnitude of the polarization changes between up and down states as

$$|P^{\pm}| = |P \pm \alpha|. \quad (A7)$$

Inserting the expanded expressions (A5), (A6) and (A7) into (A3) one finds that the parameter  $r^2$ , to second order in terms of the  $s$ ,  $a$  and  $\alpha$ , becomes

$$\begin{aligned} r^2 = r_0^2 & \left[ 1 + \frac{1}{\sigma}(s_l^+ + s_r^- - s_l^- - s_r^+) \right. \\ & + P(a_l^+ + a_r^- + a_l^- + a_r^+) - AP^2(a_l^+ + a_r^- - a_l^- - a_r^+) \\ & + \alpha(a_l^+ - a_r^- + a_l^- + a_r^+) - 2PA\alpha(a_l^+ - a_r^- - a_l^- + a_r^+) \\ & \left. + 4PA^3\alpha^2 + P^2(a_l^+ a_r^- + a_l^- a_r^+) \right]. \end{aligned} \quad (A8)$$

The error in the measured asymmetry can be rewritten as

$$\begin{aligned} \delta A = \frac{1}{4P} & \left[ \frac{1}{\sigma}(s_l^+ + s_r^- - s_l^- - s_r^+) \right. \\ & + P(a_l^+ + a_r^- + a_l^- + a_r^+) - AP^2(a_l^+ + a_r^- - a_l^- - a_r^+) \\ & + \alpha(a_l^+ - a_r^- + a_l^- + a_r^+) - 2PA\alpha(a_l^+ - a_r^- - a_l^- + a_r^+) \\ & \left. + 4PA^3\alpha^2 + P^2(a_l^+ a_r^- + a_l^- a_r^+) \right]. \end{aligned} \quad (A9)$$

#### Deviation of Beam Spot on LD<sub>2</sub> Target

A change of the proton beam spot position will alter the angle of the neutron beam on the frozen spin target (FST), which influences the direction of the scattered and recoil particles from the FST. The measured n-p asymmetry is not affected by minor drifts of the proton beam in the vertical direction, but deviations in the horizontal position are directly related to both the polar scattering angles of the elastic n-p pair and therefore the observed asymmetry.

The FST is situated 12.55 m from the center of the LD<sub>2</sub> target. A change in the x-position of 2mm could alter the angle of the neutron beam incident

on the FST by  $\psi = 1.5 \times 10^{-3}$  degrees. Since  $\psi$  will be very small the expansions of (A5) and (A6) need be taken to only first order:

$$\begin{aligned} a_L^+ &= \psi A', & A_L^+ &= -\psi A', \\ a_L^- &= \psi A', & a_L^- &= -\psi A', \\ s_L^+ &= \psi \sigma' / \sigma, & s_L^+ &= -\psi \sigma' / \sigma, \\ s_L^- &= \psi \sigma' / \sigma, & s_L^- &= -\psi \sigma' / \sigma \end{aligned} \quad (A10)$$

Here  $A' = -0.028/\text{deg}$ ,  $\sigma = 6.4 \text{ mb}$ , and  $\sigma' = -0.32 \text{ mb/deg}$  at the zero-crossing angle. Therefore, after substitution into (A9) one gets:  $\delta A = \delta \Delta A = 0$ .

If the a deviation of the beam spot on the  $LD_2$  target is correlated with beam polarization (A9) changes into

$$\delta A_n = \psi \sigma' + \psi A' = 10^{-4} \text{ at } A = 0. \quad (A11)$$

As  $A_p$  is not affected by correlated deviations in proton beam position with beam polarization reversals  $\delta A_p = 0$ . Therefore  $\delta \Delta A = \delta A_n = 10^{-4}$ . This value is likely a pessimistic over-estimation of the error as the neutron collimator defines the acceptance region of neutrons originating at the  $LD_2$  target.

Changes in the beam spot position also cause an energy change in the scattered neutron beam. The neutron collimator axis intersects the center of the  $LD_2$  target at nine degrees to the proton beam axis. The average length the proton beam passes through the target will depend on where the collimator axis intersects the proton beam. Protons of 350 MeV will lose approximately 0.04 MeV/mm. The asymmetry zero-crossing angle changes as a function of energy as  $\partial \theta_{zc} / \partial E = -0.025^\circ / \text{MeV (lab)}$ . Therefore, a change in the proton beam position on the  $LD_2$  target by 1.0 mm causes a change to the path lengths of those protons which produce the neutron beam by 6.3 mm thereby changing the neutron beam energy by 0.25 MeV. This results in a change in the zero-crossing angle of  $6.3 \times 10^{-3}$  degrees or, equivalently, a change in the asymmetry at the nominal zero-crossing angle by  $1.9 \times 10^{-4}$ . To keep  $\delta A < 10^{-4}$ , the proton beam position on the  $LD_2$  target must be kept to within  $\pm 0.50 \text{ mm}$ .

#### Modulation of Proton Beam on $LD_2$ Target

Changes in the direction of the proton beam on the  $LD_2$  target effectively alters the energy of the outgoing neutron beam. At 480 MeV the  $\theta_{zc}$ , and therefore the asymmetry, does not change appreciably with neutron energy. This situation changes at the lower energies. At 350 MeV  $\partial E / \partial \theta_{\text{recoil}} = -2.4 \text{ MeV/deg(lab)}$ ,  $\partial \theta_{zc} / \partial E = -0.025^\circ / \text{MeV}$  at  $A = 0$ , and  $\partial A / \partial \theta = -0.028/\text{deg}$  resulting in  $\partial A / \partial \theta_{\text{recoil}} = 1.8 \times 10^{-4} / \text{deg}$  at the nominal zero-crossing angle. A modulation of the beam direction on the  $LD_2$  target of  $|\theta^+ - \theta^-| = 0.1^\circ$  correlated with primary beam polarization results in systematic deviation of  $\delta \Delta A = 2 \times 10^{-5}$ . The direction of the proton beam was stable to  $\pm 0.009$  degrees during experiment #121.

### Inequality of Up and Down Polarization

If the beam or target polarization differs in magnitude between up and down states as  $P^\pm = P \pm \alpha$ , then one finds from (A9) that  $\delta A_{n,p} = A^3 \alpha^2$ . At  $A = 0$ ,  $\delta A_{n,p} = 0$  and  $\delta \Delta A = 0$ . At the limits of the detection apparatus the analyzing power approaches a value of  $A = 0.2$  and taking the difference in up and down beam or target polarization states as 0.2 (that is,  $\alpha = 0.1$ )  $\delta \Delta A = \delta A_{n,p} = 8 \times 10^{-5}$ .

### Misalignment of Apparatus

If the apparatus is misaligned by

$$\theta_L = \theta - \psi, \text{ and } \theta_R = \theta + \psi, \quad (A12)$$

then the variables of (A5) and (A6) are:

$$\begin{aligned} a_L^+ &= \psi A' + \psi^2 A''/2 & a_L^+ &= \psi A' + \psi^2 A''/2 \\ a_L^- &= -\psi A' + \psi^2 A''/2 & a_L^- &= -\psi A' + \psi^2 A''/2 \\ s_L^\pm &= \frac{1}{\sigma}(\psi \sigma' + \psi^2 \sigma''/2) & s_L^\pm &= \frac{1}{\sigma}(-\psi \sigma' + \psi^2 \sigma''/2). \end{aligned} \quad (A13)$$

All first order errors in the asymmetry cancel to first order leaving second order systematics

$$\delta A = \psi^2 A''/2, \quad (A14)$$

$$|A''| < 8 \times 10^{-4} \text{ deg}^{-2},$$

giving  $\delta A < 10^{-4}$  throughout the angular range for a misalignment of  $0.1^\circ$ . The proton and neutron detection apparatus were located to an accuracy of  $\pm 0.02^\circ$  and  $\pm 0.05^\circ$  respectively during experiment #121.

### Inequality of Up and Down Polarization and Misalignment of Apparatus

Let the detectors be misaligned as in (A12), and the beam or target polarizations differ in magnitude between opposite spin states as (A7). Substituting (A13) as well as (A7) into (A9) one finds that between opposite spin states

$$\delta A_{n,p} = -2A\alpha\psi A' + \frac{\psi^2}{2} A'' + A^3 \alpha^2. \quad (A15)$$

Since the proton and neutron detectors can be located to an accuracy of  $\pm 0.02^\circ$  and  $\pm 0.05$  respectively, in estimating the maximum effect on  $\Delta A$  a value of  $|\theta_L - \theta_R| = 0.1^\circ$  will be used. The asymmetry changes with angle as

$$A' = -0.028/\text{deg}$$

$$|A''| < 8 \times 10^{-4} \text{ deg}^{-2}.$$

At the extreme limits of detection the expression for  $\delta A$  is dominated by the term proportional to  $A$ . Inserting  $P = 0.7 \pm 0.1$ , that is  $\alpha = 0.1$ , into (A13) one finds that  $\delta A = (6 \times 10^{-4})A$ . As  $A$  approaches a value of 0.2 at the limits of the angular acceptance one finds that  $\delta A = 10^{-4}$ . Where  $A_n = 0$ , all terms in (A15) contribute since  $A_p$  is in the range of  $4 \times 10^{-3}$ . Here,  $\delta A < 10^{-5}$ .

There will be a slight contribution to  $\delta \Delta A$  as  $A_n' \neq A_p'$  due to slight CSB effects. The magnitude of the inequality can only be estimated on the basis of theoretical contributions to  $\Delta A$  illustrated in figure (1). One finds that

$$A_n' - A_p' = 6 \times 10^{-4} / \text{deg} (1.86).$$

One sees immediately that such contributions to  $\delta \Delta A$  are significant.

#### Reproducibility of Target holding Field

Small changes in the magnitude of the holding field cause changes in the extent to which the holding field bends recoil proton trajectories. The holding field will bend n-p elastic trajectories at the large angle limit of the detection system by  $1.8^\circ$  and to the small angle detection limit by  $1.2^\circ$ . The target holding field at the centre of the target is 2.57 kG and the line integral  $\int B \cdot dl$  seen by a proton originating in the center of the target is 44 kG-cm. One finds that at  $\theta_p = 53^\circ$ ,  $P_p = 476 \text{ MeV/c}$ . Also,  $\partial \theta_{hf} / \partial B_{hf} = 55 \times 10^{-4} \text{ deg/Gauss}$ . The magnitude of the holding field fluctuations can be estimated as  $\sigma_{hf} = 2.6 \text{ G}$  based on Experiment #121 experience. If holding field deviations are not concealed with spin direction,  $\delta A = \delta \Delta A = 0$ . If the holding field deviations are directly correlated with target polarization then  $\delta \theta_{zc} = 1.4 \times 10^{-3}$  degrees corresponding to  $\delta \Delta A = 4 \times 10^{-5}$  at  $A = 0$ .

#### Multiple Scattering

Multiple scattering smears the angles of recoil protons emerging from the target. Assuming that the multiple scattering has a Gaussian distribution, then

$$L^{\pm}(\theta) = \int \sigma(\theta + \delta) [1 \pm PA(\theta)] \exp(-\delta^2 / \delta_0^2) d\delta, \quad (\text{A16})$$

and a similar equation holds for  $R^{\pm}$ . The parameter  $\delta_0$  is related to the magnitude of multiple scattering by  $\delta_0 = \sqrt{2} \sigma_{\text{rms}}$ . Expanding  $\sigma(\theta)$  and  $A(\theta)$  as a function of  $\theta$  as

$$\sigma(\theta) = \sigma(\theta_0) + \delta\sigma(\theta_0) + \frac{\delta^2}{2} \sigma''(\theta_0) + \dots, \quad (A17)$$

and integrating the first three terms of the combined Taylor expansion of  $L^\pm$  and  $R^\pm$ , (A16) can be rewritten as

$$L^\pm(\theta) = L^\pm(\theta_0) + \frac{\delta_0^2}{4} (\sigma''(1 \pm PA) \pm \sigma PA'' \pm 2P\sigma'A') \quad (A18)$$

$$R^\pm(\theta) = R^\pm(\theta_0) + \frac{\delta_0^2}{4} (\sigma''(1 \mp PA) \mp \sigma PA'' \mp 2P\sigma'A'). \quad (A19)$$

These expressions can be expressed in terms of the more familiar notation of (A9) as

$$\begin{aligned} a_L^+ &= \frac{\delta_0^2}{4\sigma} (\sigma A'' + 2\sigma'A') \\ a_R^+ &= \frac{\delta_0^2}{4\sigma} (\sigma A'' + 2\sigma'A') \\ a_L^- &= \frac{\delta_0^2}{4\sigma} (\sigma A'' + 2\sigma'A') \\ a_R^- &= \frac{\delta_0^2}{4\sigma} (\sigma A'' + 2\sigma'A'). \end{aligned} \quad (A20)$$

Inserting the above results into the expression (A4), one gets

$$\delta A = \frac{\delta_0^2}{4} (A'' + \frac{2\sigma'}{\sigma} A'). \quad (A21)$$

Near the zero-crossing angle,

$$A' = -0.028/\text{deg}$$

$$|A''| < 8 \times 10^{-4} \text{ deg}^{-2}$$

$$\sigma = 6.4 \text{ mb(lab)}$$

$$\sigma' = -0.32 \text{ mb/deg(lab)}$$

$$\delta_0 = 1.0 (\approx \sqrt{2} \sigma_{\text{rms}})$$

Substituting into (A21) one gets  $\delta A = 7 \times 10^{-4}$ , at  $A = 0$ . Since  $\delta A_n = \delta A_p$ ,  $\delta \Delta A = 0$ .



### Incorrect Precession of Spin

Any residual proton polarization perpendicular to the horizontal plane left after the proton spin precession can only result in a neutron polarization also perpendicular to the horizontal plane. Such a neutron polarization component is rotated into the beam axis by the dipole magnets, Bonnie and Clyde, and cannot in itself result in a false asymmetry. However, an error in the proton spin precession leaving a residual vertical component coupled with an error in the neutron spin precession can cause an error in the measured asymmetry. Assuming an error in both the proton and neutron spin precession by  $\omega_p = 5^\circ$  and  $\omega_n = 5^\circ$ , there would exist an additional vertical component to the neutron polarization at the FST which would change sign with flips in the beam polarization,  $P_p$ , as

$$\Delta P_n^\pm = \frac{(P \pm D_t P_p \sin \omega_p)}{(1 \pm P_p A)} \sin \omega_n. \quad (A22)$$

The Wolfenstein depolarization transfer parameter  $D_t = 0.30$ , and the polarization, equal to the analyzing power,  $P = A = -0.06$ . One finds that the extra component to the neutron vertical polarization is exceedingly small. It has been shown earlier that differing up/down polarizations do not contribute to false asymmetries if  $|P^+ - P^-| < 0.1$  from (A15).

### Residual Neutron Polarization on Polarized Target

A residual vertical neutron polarization can couple to the target polarization and cause a false asymmetry measurement. The polarized target state left and right count rates would (after dropping common factors) be

$$\begin{aligned} L^+ &= (1 + P_p A + P_p P_n C_{nn}) \\ R^+ &= (1 - P_p A + P_p P_n C_{nn}) \\ L^- &= (1 - P_p A - P_p P_n C_{nn}) \\ R^- &= (1 + P_p A - P_p P_n C_{nn}). \end{aligned} \quad (A23)$$

The spin correlation parameter  $C_{nn}$  does not change sign on the left and right sides, i.e. it does not in itself cause a left-right asymmetry. Adopting the usual notation of (A6) one gets

$$a_L^+ = a_R^- = P_n C_{nn},$$

and

$$a_l = a_r^* = -P_n C_{nn}$$

resulting in the following expression for  $\delta A$

$$\delta A = P_p P_n C_{nn} A \quad (A24)$$

Neutrons created from an unpolarized proton beam on the LD<sub>2</sub> target have a maximum vertical polarization determined by the np asymmetry at 9°. A residual vertical polarization at the FST could only occur if this polarization was improperly precessed. An upper limit on the error of spin precession is 5°. The maximum possible vertical polarization available to the neutron at the FST would then be  $P_n = 0.06 \sin(5^\circ) = 0.0052$ . The spin correlation parameter is equal to  $C_{nn} = 0.24$  ( $E_n = 350$  MeV, 70° cm; Arndt/84 phase shifts). At the limits of detection  $A = 0.2$ , giving  $\delta A_p = 2 \times 10^{-4}$ . Since there is no similar effect for the polarized target case  $\delta A_n = 0$  and  $\delta \Delta A = 2 \times 10^{-4}$ . At  $A_p = 0$ ,  $A_n = 4 \times 10^{-4}$ , therefore  $\delta \Delta A \ll 10^{-4}$ .

#### Neutron Energy Stability

Asymmetry changes with incident neutron energy. At  $E_n = 350$  MeV, and  $\theta_n = 72.0^\circ$ .

$$\frac{\partial A}{\partial \theta} = -0.028/\text{MeV}(\text{lab})$$

$$\frac{\partial \theta}{\partial E} = -0.025 \text{ deg/MeV}(\text{lab})$$

Absolute knowledge of the beam energy is unimportant to a few MeV as long as it does not change between data taking runs. During Experiment #121 the primary proton beam energy was kept constant to  $\pm 0.09$  MeV.

#### Relative Position of Target and Holding Field with Respect to Symmetry Axis

Deviations in target position and/or the holding field with respect to the symmetry axis will cause shifts between actual scattering angles and those measured for the tracks. The main contributor to the resultant angular deviations is the different  $\int B \cdot dl$  which protons see due to the shifted holding field. As such, shifts of the target position are similar in effect to shifts in the holding field.

The position of the target cell was determined within  $\pm 0.5$  mm from X-rays of the FST taken at least once per data taking period. This procedure will be followed during the proposed experiment.

## (a) Lateral Target Deviations

Let the target move to one side by  $dx$ . Protons to one side will pass through a larger  $\int B \cdot dl$  and be bent through a larger angle, and those to the other side will pass through a smaller  $\int B \cdot dl$  and be deflected by a smaller angle. The left/right change in asymmetries and cross section of (A3) and (A4) are related by

$$a_L^+ = a_L^- = a_R^+ = a_R^- = a$$

and

$$s_L^+ = s_L^- = -s_R^+ = -s_R^- = s. \quad (A25)$$

Estimating the parameters  $a$  and  $s$  as from

$$a = \frac{\partial A}{\partial \theta} \frac{\partial \theta}{\partial x} hf \, dx, \quad s = \frac{1}{\sigma} \frac{\partial \sigma}{\partial \theta} \frac{\partial \theta}{\partial x} hf.$$

The change in magnetic field deflection can be easily determined to find that

$$\frac{\partial \theta}{\partial x} hf = 5 \times 10^{-3} \text{ deg mm}^{-1} \text{ at } \theta = 53^\circ \text{ and at the target center,}$$

and

$$\frac{1}{\sigma} \frac{\partial \sigma}{\partial \theta} = 5.1 \times 10^{-2} \text{ deg}^{-1},$$

to find that

$$\delta A = 1.5 \times 10^{-4} dx$$

throughout the angular range. Lateral deviations should be kept to within  $\pm 0.7 \text{ mm}$ .

## (b) Longitudinal Target Deviations

Target deviations along the symmetry axis cause recoil protons to have a larger or lower  $\int B \cdot dl$ , depending on the direction of the shift. One discovers that the angular shift is of the same magnitude for protons scattered to the left or right, but towards larger angles on one side and towards lesser angles on the other. Consequently in the notation of (A3):  $a_L^+ = -a_R^+$  and  $s_L^+ = s_R^+$ .

$$a_L^+ = \frac{\partial A}{\partial \theta} \frac{\partial \theta}{\partial l} dl$$

$$\text{at } 53^\circ, \frac{\partial \theta}{\partial l} = 5 \times 10^{-3} \text{ deg mm}^{-1}$$

Substituting into (A9) one finds that  $\delta A \ll 10^{-4}$  close to where  $A = 0$ . If such deviations are correlated with spin flips,  $\Delta A = 1.5 \times 10^{-4} d\ell$ . Therefore the upper limit on longitudinal displacements is  $\pm 0.7$  mm.

### (c) Vertical Target Displacement

For vertical displacements we have  $a_L^\dagger = -a_R^\dagger$ ,  $s_L^\dagger = s_R^\dagger$ . At the zero-crossing, fluctuations in vertical position are not critical. If vertical displacements are correlated with spin flips  $\Delta A = 1.2 \times 10^{-4} dy$  (in mm). Vertical deviations should be kept within  $\pm 0.8$  mm.

### Neutron Detection Stability

A higher threshold on neutron detection effectively discriminates against a percentage of otherwise detected np pairs. If the efficiency of a left or right neutron bar increases or decreases by a fixed specific percentage  $\epsilon$ , then

$$s_L^\dagger = s, \text{ and } s_R^\dagger = 0, \Delta A = 0. \quad (\text{A26})$$

If the efficiency changes randomly as  $\epsilon \pm \Delta\epsilon$  as the experiment progresses the estimation of  $\Delta A$  is somewhat more involved. If the spin of the beam or target is flipped  $N$  times (consider only the target at its polarization is flipped far less often), the average difference in the efficiency between the time with the target spin in the down direction and the target spin in the up direction is inversely proportional to the square root of the number of times the target spin was reversed and directly proportional to the standard deviation of the efficiency. The time scale at which the efficiency drifts is also important but, as this is not known, the worst case will be selected --that the efficiency drifts cyclically with a period comparable to that of the target polarization reversal. Then if all of the eight threshold discriminators on both of the neutron arrays have long term random instabilities  $\pm \Delta\epsilon$ , the uncertainty in each of the parameters  $s_{LR}^\dagger$  of eq. (A5) is

$$\Delta s_{LR}^\dagger = \frac{\Delta\epsilon}{(2\sqrt{N})}. \quad (\text{A27})$$

Substituting (A27) into (A9) one finds that

$$\delta A = \frac{\Delta\epsilon}{4P\sqrt{N}} \quad (\text{A28})$$

with  $P = 0.6$ ,  $N = 8$  target polarization flips,  $\delta A = 0.15 \Delta\epsilon$ .

The efficiency can change due to photomultiplier gain shifts. Estimates of  $\epsilon$  can be made based on results from Experiment #121. Experiment #121 had

neutron software cuts at roughly 3.2 MeV electron equivalent (MeVee). At this energy the neutron bar efficiency changes with respect to the energy threshold by 0.0039/MeV. The absolute efficiency of the neutron bars for the proposed experiment will be ~30%. To keep  $\delta A < 10^{-4}$ , changes in efficiency should be kept within  $\pm 6 \times 10^{-4}$  (eq. A15). Therefore the software cut at 3.2 MeVee must not change by 0.15 MeVee, or 5%. Since changes in software thresholds are directly proportional to photomultiplier gains, an equivalent condition to the stability of thresholds to  $\pm 5\%$  is that photomultiplier gains should also be kept to within  $\pm 5\%$ .

### Background

#### (i) Polarized Neutron Beam

Let  $f$  = the fraction of target nuclei which can cause quasifree scattering of cross section  $\sigma_b$ . If the analyzing power for the background is  $a_b$ , the count rates for a polarized neutron run are:

$$L^+ = \sigma(1+PA) + f\sigma_b(1+Pa_b)$$

$$R^+ = \sigma(1+PA) + f\sigma_b(1-Pa_b)$$

$$L^- = \sigma(1+PA) + f\sigma_b(1-Pa_b)$$

$$R^- = \sigma(1+PA) + f\sigma_b(1+Pa_b)$$

Adopting the notation of (A6) one gets

$$a_L^+ = \frac{f\sigma_b}{P\sigma} (1+Pa_b)$$

$$a_R^+ = \frac{f\sigma_b}{P\sigma} (1+Pa_b)$$

$$a_L^- = \frac{f\sigma_b}{P\sigma} (1+Pa_b)$$

$$a_R^- = \frac{f\sigma_b}{P\sigma} (1+Pa_b)$$

(A30)

Then, substituting the above into (A9):

$$\delta A_n = \frac{f\sigma_b}{\sigma} a_b$$

(A16)

To keep the effects on  $\delta A_n$  due to the background to within  $\pm 10^{-4}$ , the percentage of background counts to real n-p elastic counts multiplied by the background asymmetry must be kept within  $\pm 10^{-4}$ . An upper limit on the ratio of background to real n-p elastic events will be  $\sim 1\%$ . During experiment #121 the  $^{12}\text{C}(n, np)^{11}\text{B}$  background asymmetry was measured to be  $-0.012 \pm 0.013$ . Inserting these values into (A16) results in  $\delta A_n = 10^{-4}$ .

(ii) Polarized Target

A background merely serves to lessen the asymmetry since the contents of the target other than  $^1\text{H}$  cannot be polarized. One finds that  $\delta A_p = 0$ .